

**Thermal and mechanical properties of $\text{Mg}_2\text{Si}_{1-x}\text{Sn}_x$ ($x = 0 - 1$) for thermoelectric
generators**



DISSERTATION

submitted for the degree of

Doctor rerum naturalium

(Dr. rer. nat.)

By

Gustavo Castillo Hernández

Supervisor: Prof. Dr. Eckhard Müller

Institut für Anorganische und Analytische Chemie

Justus-Liebig-Universität Gießen

Gießen, 2022

Selbständigkeitserklärung

Hiermit versichere ich, die vorgelegte Thesis selbstständig und ohne unerlaubte fremde Hilfe und nur mit den Hilfen angefertigt zu haben, die ich in der Thesis angegeben habe. Alle Textstellen, die wörtlich oder sinngemäß aus veröffentlichten Schriften entnommen sind und alle Angaben die auf mündlichen Auskünften beruhen, sind als solche kenntlich gemacht. Bei den von mir durchgeführten und in der Thesis erwähnten Untersuchungen habe ich die Grundsätze guter wissenschaftlicher Praxis, wie sie in der ‚Satzung der Justus-Liebig-Universität zur Sicherung guter wissenschaftlicher Praxis‘ niedergelegt sind, eingehalten. Gemäß § 25 Abs. 6 der Allgemeinen Bestimmungen für modularisierte Studiengänge dulde ich eine Überprüfung der Thesis mittels Anti-Plagiatssoftware.

Datum

Unterschrift

Acknowledgements

I would like to express my sincere gratitude to my supervisors Dr Johannes de Boor and Prof. Dr Eckhard Müller, first for the amazing opportunity to join the research group and then for the continuous support that made this work possible. This work would have never been possible without the financial support from the Conacyt-DAAD PhD scholarship.

I would also like to thank my amazing colleagues Sahar, Prasanna, Julia, Mila, Aryan, Mohammad, Nader, Ngan, Nhi, Radhika, Kunal, Silvana, Nacho, Laura, Venkatesh, Antoine, Roberto, Gregor, Klaus, Severin, Matthias, Vidushi, Adina, and Christian for their support, and for the enjoyable working environment.

I would like to specially thank Mohammad for his mentorship and friendship throughout the PhD program, Sahar and Prasanna for the emotional support and the fruitful scientific and non-scientific discussions. I would like to acknowledge as well the role of Venkatesh and Roberto as interns during my work, their valuable input in experience, experiments and ideas was priceless for this thesis.

Further acknowledgement goes to Prof. Dr. Benedikt Klobes from the University of Applied Sciences Bremerhaven, who not only provided the measurements for RUS but also helped in the understanding of the phenomena around it. Prof. Dr. Marion Bartsch aided me immensely during the modelling and simulation.

I would also like to thank Family Keuth, Rene, Monique, Marcel and Michelle, for taking us in as further members of the family. Specially as the world descended into chaos during the pandemic, you helped us through in innumerable ways. From the bottom of our hearts, thank you very much.

Last but not least, I would like to thank my family, Cesar, Elvia, David and Marina for their love and support in all stages of my life, even from halfway across the planet. Above all I would like to thank my lovely wife Gaby, who not only supported me during the PhD, she even took on the adventure of moving to a foreign country with absolutely no knowledge of the language or culture. None of this would have been possible without her support.

Thank you all

List of figures

Figure 2–1 Charge carrier movement under a temperature difference	3
Figure 2–2 Thermoelectric uni-couple in both generation and heat pump modes	4
Figure 2–3 Dependence on carrier concentration of Seebeck coefficient, thermal and electrical conductivity, based on original work from [16].....	6
Figure 2–4 Thermoelectric module. Adapted from [18].....	7
Figure 2–5 Example of a body under external forces, resultant force on the point Q and diagram of the area with the three-dimensional axes system.....	9
Figure 2–6 Stress distribution for a three-dimensional body.....	10
Figure 2–7 Side view of the shear stresses acting on the xy face.....	11
Figure 2–8 Stress components acting on a tilted differential area	12
Figure 2–9 Stress as a function of rotation angle for the auxiliary axes.....	13
Figure 2–10 Planar normal strain.....	14
Figure 2–11 Planar shear strain.....	15
Figure 2–12 Stress and related strain for different directions.....	18
Figure 2–13 Plane stress and related expansion and constriction.....	19
Figure 2–14 Plane stress transformation using an auxiliary axis x'	20
Figure 2–15 Stress-strain diagram.....	21
Figure 2–16 a) original sample before deformation, b) ductile sample after extensive plastic deformation and fracture and c) brittle sample exhibiting almost no plastic deformation.....	22
Figure 2–17 Crack aperture modes, adapted from [31]	24
Figure 2–18 Representation of an infinite long plate under tensile stress without and with a crack inside, the lines represent the stress distribution within the material	25
Figure 2–19 Geometry of a Vickers indenter	27

Figure 2–20 Sketch of a multi-phase material being stretched with the inclusion aligned parallel to the force	29
Figure 2–21 Sketch of a multi-phase material being stretched with the inclusion aligned perpendicular to the force	30
Figure 2–22 Effective Young's modulus of a material as a function of volume fraction of the inclusion V_f if the inclusion has a Young's modulus 100 times higher than the matrix. Adapted from [43]	31
Figure 2–23 Lennard-Jones potential	32
Figure 2–24 Miscibility gap for the Mg_2Si - Mg_2Sn material system, taken from [63]. Gradient color indicates a full miscibility while striped color indicates the miscibility gap	35
Figure 2–25 Damage seen in several modules. Taken from [19, 95].....	41
Figure 4–1 Binary literature values and interpolated solid solution melting temperature for the Mg_2Si - Mg_2Sn material system	45
Figure 4–2 Basic X-ray diffractometer with the source, detector and sample holder.	48
Figure 4–3 Different crystallographic planes and their representation. Taken from [104].....	49
Figure 4–4 Backscatter coefficient as a function of gray value	53
Figure 4–5 Clemex hardness testing machine.....	54
Figure 4–6 Room temperature setup for the IET	58
Figure 4–7 High temperature setup for the IET.....	59
Figure 4–8 Sketch of the positioning of the supports (gray), the impact place (red) and the position of the microphone (blue) to perform a simultaneous Young's and shear modulus measurement	60
Figure 4–9 RUS spectrum showing the frequencies at which the material has a resonance against the root of the relative amplitude of displacement.	64
Figure 4–10 Dilatometer used and close-up of the sample holder.....	65

Figure 8–1 Composition dependent recovery resistance, total crack length (2c) and imprint size (2d) for $Mg_2Si_{1-x}Sn_x$	72
Figure 8–2 Comparison of the recovery resistance to the Young’s modulus over the solid solution series $Mg_2Si_{1-x}Sn_x$	73
Figure 8–3 X-ray diffractograms from samples obtained by pressing powder synthesized by different methods.....	74
Figure 8–4 Vickers hardness of samples pressed from powder synthesized by different processes.	75
Figure 8–5 SEM backscatter images for $Mg_2Si_{0.3}Sn_{0.665}Bi_{0.035}$ samples synthesized by a) melting + milling, b) ball milling and c) gas atomization. All samples were compacted at 66 MPa and 700 °C for 20 min.	76
Figure 8–6 Dimensions in mm and 3D geometry of the model employed for FEM analysis, with the n-type on the left and p-type on the right.....	78
Figure 8–7 Temperature distribution used for the simulation.....	79
Figure 8–8 Diagram showing the model and the mechanical constraints.....	81
Figure 8–9 Meshed model.....	81
Figure 8–10 von Mises stress distribution for material properties a) all RT constant and b) all temperature dependent 25 – 300°C.....	82
Figure 8–11 Distribution of the first principal stress for material properties a) all RT constant and b) all temperature dependent.....	84
Figure 8–12 Cut view from the shear stress τ_{yz} for material properties a) all RT constant and b) all temperature dependent at 300°C.....	86
Figure 8–13 Comparison between the CTE for the thermoelectric legs and the copper bridge.....	87
Figure 8–14 Temperature dependent Young’s modulus and CTE for the n-type material showing the compensating mechanical effects at higher temperatures.....	88
Figure 11–1 Exemplary image of a $Mg_2(Si,Sn)$ sample with a variety of gray values for a small area (red circle).	105
Figure 11–2 Raw data and fitting for the Young’s modulus of n-type $Mg_2Si_{0.3}Sn_{0.7}$	106

Figure 11–3 Raw data and fitting for the coefficient of thermal expansion of the n-type $Mg_2Si_{0.3}Sn_{0.7}$	107
Figure 11–4 Raw data and fitting for the total thermal conductivity of the n-type $Mg_2Si_{0.3}Sn_{0.7}$	108
Figure 11–5 Raw data and fitting for the Young’s modulus of the p-type $Mg_2Si_{0.3}Sn_{0.7}$	108
Figure 11–6 Raw data and fitting for the coefficient of thermal expansion of the p-type $Mg_2Si_{0.3}Sn_{0.7}$	109
Figure 11–7 Raw data and fitting for the total thermal conductivity of the p-type $Mg_2Si_{0.3}Sn_{0.7}$	110

List of symbols and abbreviations

- BSE – Back Scattered Electrons
- EDX – Energy Dispersive X-ray Spectroscopy
- SEM – Scanning Electron Microscopy
- XRD – X-ray Diffraction
- IET – Impulse Excitation Technique
- RUS – Resonant Ultrasound Spectroscopy
- FEM – Finite Element Model

Variable	Name	Unit
T_{sint}	Sintering temperature	K
t	Time	s
λ	Wavelength of incident ray	nm
n	Order of reflection	-
θ	Angle of incidence	°
zT	Figure of merit of the materials	-
ρ	Density	g/cm ³
σ	Stress	Pa
ε	Strain	-

E	Young's modulus	GPa
G	Shear modulus	GPa
ν	Poisson's ratio	-
H	Hardness	GPa
K_{Ic}	Fracture toughness under tensile conditions	$\text{MPa}\cdot\text{m}^{\frac{1}{2}}$
A	area	m^2
F	force	N
σ_u	Maximum tensile stress	Pa
σ_Y	Yield stress	Pa
σ_{eq}	Von Mises equivalent stress	Pa
V	volume	m^3
β	Volumetric coefficient of thermal expansion	1/K
α	Linear coefficient of thermal expansion	1/K
Z	Atomic number	-
M	Atomic mass	G
ω	Angular frequency	rad/seg
f	Vibration frequency	Hz
R_s	Recovery resistance	Pa

Abstract

Thermoelectric technology is a good option for electricity generation due to its capacity to turn waste heat directly into employable electrical energy. Thermoelectric modules are the basis of this technology and are fabricated from doped n- and p-type semiconductors.

$Mg_2(Si,Sn)$ thermoelectric material is one of the top candidates for module assembly due to its good thermoelectric properties coupled with low density and cost. The low toxicity and high availability of the precursor elements give this material system crucial advantages in comparison with other competitors.

Thermoelectric module operation requires a temperature difference, which inevitably causes differential thermal expansion within a module. Such an expansion in a device composed of different materials with different expansion coefficients could lead to failure due to stress-induced fracture, posing a serious threat to reliability and applicability of thermoelectric modules. It is therefore important for module design to take into account the different thermal and mechanical properties of the materials involved in the assembly.

Most of the research on thermoelectric applications, however, is focused on the optimization of the thermoelectric performance of the materials. Other properties like elastic modulus, hardness and coefficient of thermal expansion are studied with substantially lower intensity.

This thesis aims at filling the gap of missing information regarding the mechanical and thermal properties for the solid solutions $Mg_2Si_{1-x}Sn_x$ with $x = 0 - 1$.

This work starts with hardness measurement, Vickers indentations were performed on the sintered pellets to identify the effect of Sn content in $Mg_2(Si,Sn)$ on the hardness exhibited by the material. Increasing the amount of Sn in the solid solution decreases the hardness values in a linear relationship. Mg_2Si has the highest value at 5 GPa and Mg_2Sn the lowest at 2 GPa. The fracture toughness of the studied samples did not, however, follow the same trend, as the material $Mg_2Si_{0.6}Sn_{0.4}$ exhibited the highest value. It was found that Si-rich regions in the microstructure left over from the synthesis and pressing processes were strengthening the material by adding interfaces, which deflected or otherwise impeded the growth of the cracks produced by indentation.

The next step towards filling the gap in missing information was to characterize the elastic moduli of the solid solution series $Mg_2Si_{1-x}Sn_x$ with $x = 0 - 1$. Two non-destructive characterization methods were employed and compared, the Resonant Ultrasound Spectroscopy and the Impulse Excitation Method. This work innovates in the parallel measurement and comparison between the results provided by both of these techniques. The difference between the measurement results is below 9%, which suggests that using both techniques interchangeably is possible. The main

differences between the techniques are the sample size required for testing, as well as the ease at which high temperature measurements can be implemented.

This work presents the first ever report of Young's modulus of $\text{Mg}_2(\text{Si},\text{Sn})$ as a function of composition and temperature, finding a linear dependence of both. Using these results, a bilinear dependence was proposed to predict the Young's modulus of any material within the solid solution and at any temperature between 300 K and 623 K.

Joining a fast quantification method to estimate the local composition using back-scattered electron images to the bilinear equation, the effective Young's modulus of several samples was estimated. For this estimation both the Voigt and Reuss approximations for a composite material were used. The results show that the composite material approach and the bilinear equation can be used to accurately predict the effective elastic modulus of typical, not completely homogenized, $\text{Mg}_2(\text{Si},\text{Sn})$ material.

To test the effect of doping species on the thermal and mechanical properties of $\text{Mg}_2(\text{Si},\text{Sn})$, the materials $\text{Mg}_2\text{Si}_{0.3}\text{Sn}_{0.665}\text{Bi}_{0.035}$ and $\text{Mg}_{1.97}\text{Li}_{0.03}\text{Si}_{0.3}\text{Sn}_{0.7}$ were compared to undoped $\text{Mg}_2\text{Si}_{0.3}\text{Sn}_{0.7}$ and low doped $\text{Mg}_2\text{Si}_{0.3}\text{Sn}_{0.6925}\text{Bi}_{0.0075}$. This information is crucial for accurate module design as any possible effect has not been identified before.

Room and high temperature Young's modulus was measured for all the mentioned compositions. All of them exhibited a linear behavior, albeit with Bi containing samples having different slopes. Both materials of interest show, however, very similar values at application temperatures.

The coefficient of thermal expansion for all the aforementioned samples was measured from room temperature to 440 °C. It was proposed to use a linear fit and extrapolation to describe the temperature dependent thermal expansion of the material instead of the mean value usually given in literature. When the equation obtained from the extrapolation is used to estimate the room temperature value, the comparison to the mean value results in a difference <3%.

This work concludes with the simulation of a thermoelectric uni-couple using Finite Element Modelling. For this simulation, temperature dependent data presented in this work is used and compared to modeling results based on constant values. The stress distribution is described using three main stress components, the von Mises stress, the principal stress 1 and the shear stress along the contact surface. A comparison between constant values with temperature dependent data for $\text{Mg}_2(\text{Si},\text{Sn})$ shows that using constant room temperature or temperature averaged values gives similar results as full temperature dependent calculations. However, when only one of the main variables, Young's modulus or coefficient of thermal expansion, is employed with the correct temperature dependence, the stress values can be off by more than 10%.

Table of contents

Acknowledgements	iii
List of figures	iv
List of symbols and abbreviations.....	viii
Abstract	x
1. Introduction	1
2. Theoretical background.....	3
2.1. Thermoelectric effects	3
2.1.1. Seebeck and Peltier effect.....	3
2.1.2. Thermoelectric devices	4
2.1.3. Thermoelectric module	7
2.2. Mechanical properties	9
2.2.1. Stress	9
2.2.2. Stress transformation.....	11
2.2.3. Strain	14
2.2.4. Elasticity.....	16
2.2.5. Failure theories.....	22
2.2.6. Fracture toughness.....	23
2.2.7. Hardness.....	26
2.2.8. Temperature dependence of Young's modulus.....	27
2.2.9. Effective properties of multi-phase materials.....	28
2.2.10. Thermal expansion	31
2.3. Mg_2X	34
2.3.1. Mg_2X system	34
2.3.2. TE properties of $Mg_2(Si,Sn)$	36
2.4. Mechanical properties of TE materials	38
2.4.1. Non-silicide systems	38
2.4.2. $Mg_2(Si,Sn)$	39
2.5. Thermoelectric module evaluation.....	41

3. Summary of research.....	43
3.1. Research motivation.....	43
3.2. Thesis overview	43
4. Materials and Methods.....	45
4.1. Synthesis methods	45
4.1.1. Direct melting in the DSP.....	45
4.2. Characterization methods.....	48
4.2.1. Structural characterization.....	48
4.2.2. Mechanical characterization	53
5. Hardness and Fracture Toughness of Solid Solutions of Mg ₂ Si and Mg ₂ Sn	66
6. Room and high temperature mechanical properties of Mg ₂ Si, Mg ₂ Sn and their solid solutions	71
7. Impact of the dopant species on the thermomechanical material properties of thermoelectric Mg ₂ Si _{0.3} Sn _{0.7}	81
8. Discussion.....	97
8.1. The role of secondary phases	97
8.2. Relationship of Young's modulus with hardness and CTE	98
8.3. Influence of material synthesis method on microstructure and hardness ..	101
8.4. Mechanical modelling of a Mg ₂ (Si,Sn) pn-couple considering the temperature dependence of the material properties.....	105
9. Conclusions and outlook	118
9.1. Outlook	119
• Suggestion on determination of critical stress values.....	119
• Suggestion on improving the boundary conditions for the FEM	120
• Suggestion on determination of thermal stability of mechanical properties	120
• Suggestion on determining the thermal cycling resistance	121
10. References	123
11. Appendix.....	132
11.1. Limitations on the use of the rapid compositional analysis in Mg ₂ X.....	132

11.2. Material properties used for simulation.....	134
n-type $\text{Mg}_2\text{Si}_{0.3}\text{Sn}_{0.665}\text{Bi}_{0.035}$	134
p-type $\text{Mg}_{1.97}\text{Li}_{0.03}\text{Si}_{0.3}\text{Sn}_{0.7}$	136

1. Introduction

Space missions have a high demand for power. This holds especially in the lift-off phase and the way into orbit but as well for the rest of the mission time. The operation of launchers requires electrical power that is currently provided by heavy batteries.

Thermoelectric generators (TEG) have been successfully utilized to provide energy to space faring objects, such as probes, since the 1970's [1]. These generators can convert heat directly into usable electrical power with virtually no maintenance requirements [2].

This technology has been proposed further to use on Moon or other planets to provide electrical energy, working complementary or in tandem with photovoltaic (PV) panels [3], which utilize solar radiation to generate electricity. These PV modules are prone to deterioration by dust and solar radiation, as well as being inactive during planetary/lunar night. In contrast to these shortcomings of PV technology, TEG can function in the absence of light [4, 5].

Therefore, the Young Investigator Group "Thermoelectric generators for space applications", from in the department of "Thermoelectric Materials and Systems" at the German Aerospace Center aims for the development of thermoelectric (TE) generators based on light-weight and high-performance silicides. Development of such generators requires material testing and optimization as well as the development of contacting solutions, generator module design, and – as final and most prominent step – the fabrication and evaluation of the thermoelectric generator devices.

The development cycle of such devices must include a reliability test, in order to ensure that the hardships of space travel and operation under extreme environments is overcome. Early TEG technology relied on the trial-and-error approach, by building and then testing generators under challenging situations until they failed and studying the failure mode [6]. With the advent of technology and computer simulation software, these trials can be done in the virtual world with reduced time and money expenditure. Such a simulation can only yield meaningful results if proper material properties are used.

The use of finite element modeling (FEM) to mechanically optimize designs in TEG technology has been explored before [7–9]. The majority of previous studies have only dealt with room temperature mechanical behavior, mostly because this is the available information in literature. However, it remains to be tested whether or not the temperature difference of the mechanical behavior has an influence in the simulated results.

The focus of this work will be the measurement of different mechanical and thermal properties, needed for the correct design of a functioning silicide-based TEG. The aim is to provide a footwork in which to build, to assess the mechanical reliability of a TEG.

Both the effect of temperature and composition on the elastic moduli of $Mg_2(Si,Sn)$ material will be investigated, as well as the effect of doping species in the composition selected for technological use.

With the information about temperature and composition dependence of mechanical properties known, a simulation of a thermoelectric uni-couple will be presented and analyzed. This analysis will focus on the effect of temperature dependent properties compared to the usual constant room temperature values used in literature.

2. Theoretical background

2.1. Thermoelectric effects

2.1.1. Seebeck and Peltier effect

In 1821, Thomas J. Seebeck observed that whenever a material was heated on one side and kept at lower temperature on the other, a magnetic needle placed close to the circuit would move.

This effect is called Seebeck effect in his honor today, it is also now known that the effect is caused by the thermal diffusion of charge carriers from the hot side to the cold one [4].

The voltage buildup V and the temperature difference between the ends ΔT are related by a proportionality constant

$$V = -S\Delta T \quad (1)$$

where S is the Seebeck coefficient and T is temperature. The Seebeck coefficient can have a positive or a negative value, depending on the type of majority carriers within the material.

Materials with excess electrons are denominated as n-type, while materials with excess holes are called p-type. A sketch of electron movement is shown in **Figure 2–1**. The voltage will build up between the hot (T_h) and cold (T_c) sides of the material.

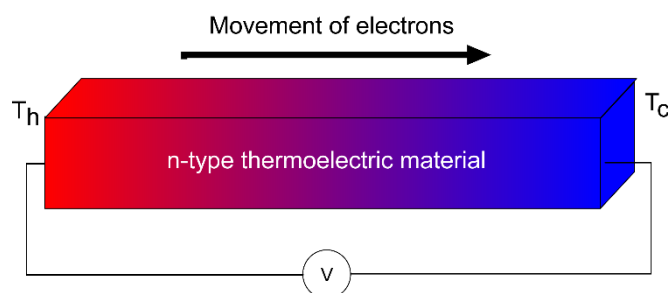


Figure 2–1 Charge carrier movement under a temperature difference

On the other hand, in 1834 a related effect was observed by Jean Charles Athanase Peltier. He observed that whenever current flowed through the junction of two materials A and B, this junction would heat up or cool down. The heat absorption or release depends on the material combination and the direction of the current flow [10]. Thus, the Peltier effect was described. The Peltier coefficient Π is defined as the relationship between the rate of heat flow \dot{Q} and current I following **Equation 2** [11]

$$\dot{Q} = \Pi \cdot I \quad (2)$$

The Peltier coefficient can be related to the Seebeck coefficient by the Kelvin relation:

$$\Pi_A - \Pi_B = (S_A - S_B)T \quad (3)$$

Single materials are of limited use technologically, they need to be assembled in pairs, one p- and one n-type. This is the basic unit of functioning for thermoelectric technology.

2.1.2. Thermoelectric devices

A thermoelectric couple in its most basic form is the connection of an n-type with a p-type semiconductor (also called legs) through a metallic bridge [5].

This couple can then function as a generator (using the Seebeck effect) or as a heat pump (using the Peltier effect), this is illustrated in **Figure 2-2**.

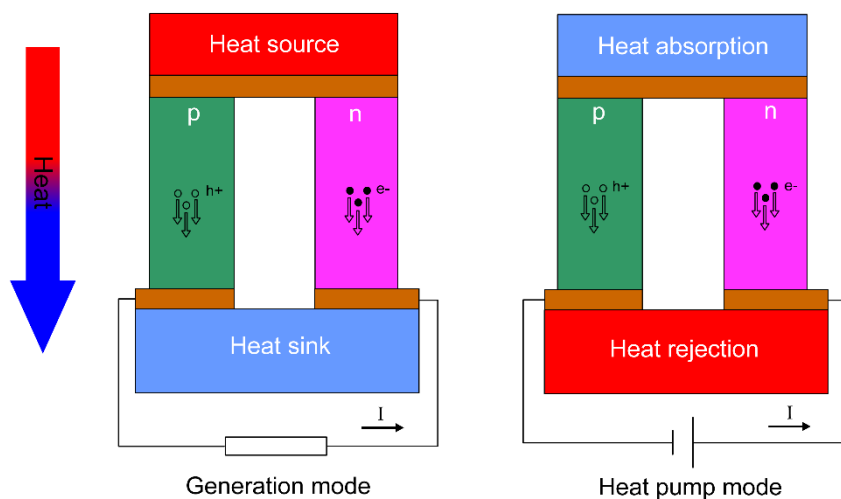


Figure 2-2 Thermoelectric uni-couple in both generation and heat pump modes

As can be seen from the picture, in the generation mode both materials have the same temperature difference (thermally connected in parallel) to provide the charge carrier movement necessary to produce the voltage. As they are electrically connected in series, the small voltages produced by each leg will add up.

The efficiency (η) of such a device is defined by the ratio of output power and heat flow going in $\eta = \frac{P}{\dot{Q}_{in}}$, where P is the power and \dot{Q}_{in} is the heat going in. Output power is expressed as $P = \dot{Q}_{out} - \dot{Q}_{in}$, where \dot{Q}_{out} is the heat going out of the device [2].

As any heat engine, a thermoelectric device is limited by the Carnot efficiency, defined as $\frac{\Delta T}{T_H}$ where T_H is the temperature on the hot side. The maximum efficiency of a thermoelectric generator can be expressed using **Equation 4** [2, 12].

$$\eta = \frac{\Delta T}{T_H} \frac{\sqrt{1+ZT}-1}{\sqrt{1+ZT}+T_C/T_H} \quad (4)$$

where T_C is the temperature on the cold side and ZT is the device figure of merit. This in turn is similar to the material figure of merit (zT) if the TE properties (see below) of both TE materials are similar and device effects like contact resistances are small.

This material figure of merit relates all main properties at a given temperature and is described by **Equation 5** [13]

$$zT = \frac{S^2\zeta}{\kappa} T \quad (5)$$

where ζ is the electrical conductivity and κ the total thermal conductivity. The term $S^2\zeta$ is also called the power factor. From **Equation 5** it is clear that increasing the Seebeck coefficient and the electrical conductivity, while keeping the thermal conductivity low is the key to increase the performance in TE materials.

Thermal conductivity κ is the rate at which a solid material can conduct heat when under a temperature difference between its ends. This heat flow is expressed by

$$\dot{Q} = A\kappa \frac{dT}{dx}$$

Heat transfer is done mainly by charge carriers (electrons and holes) and by lattice waves (phonons). These are the main components, the lattice κ_L and electronic κ_e contributions to the total thermal conductivity [14]. The unit in SI for thermal conductivity is W/m·K

The lattice thermal conductivity governs how thermal energy is transported through the lattice, and thus will be impacted by the type of bonding present in the material and the atomic weight of the component elements. A good estimation of this value can be obtained using the equation $\kappa_L = \frac{Cv}{3}l$ where C is the specific heat, v is the speed of sound and l is the mean free path for the phonons [15].

The electronic component of the thermal conductivity can be estimated, following the Wiedemann-Franz law, using the equation $\kappa_e = L\zeta T$ where L is the Lorenz number and ζ the electrical conductivity.

Electrical conductivity is the ease at which the charge carriers move through a material, producing electrical current. For a single carrier type, it is given by $\zeta = ne\mu$, where n is the charge carrier density, e is the electron charge and μ the charge carrier mobility. In the SI, the units used for electrical conductivity are S/m .

Both Seebeck coefficient and electrical conductivity are directly related to charge carrier concentration, and thermal conductivity is partly influenced (through the electronic component) by it. The interplay between these variables is shown in **Figure 2-3**.

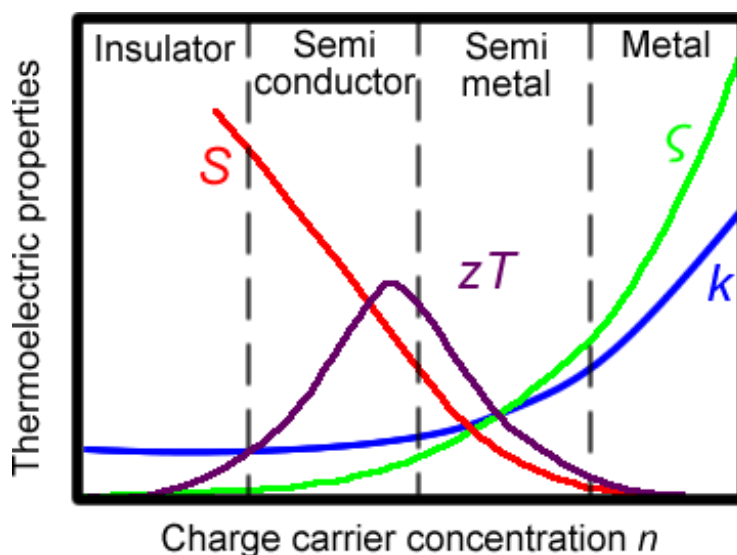


Figure 2-3 Dependence on carrier concentration of Seebeck coefficient, thermal and electrical conductivity, based on original work from [16]

Materials with too high (metals) or too small (insulators) carrier concentration tend to have poor qualities to be used as thermoelectrics [17], thus the class of semiconductors tends to be the focus of thermoelectric technology development.

2.1.3. Thermoelectric module

A thermoelectric module is composed of several uni-couples connected electrically in series and thermally in parallel.

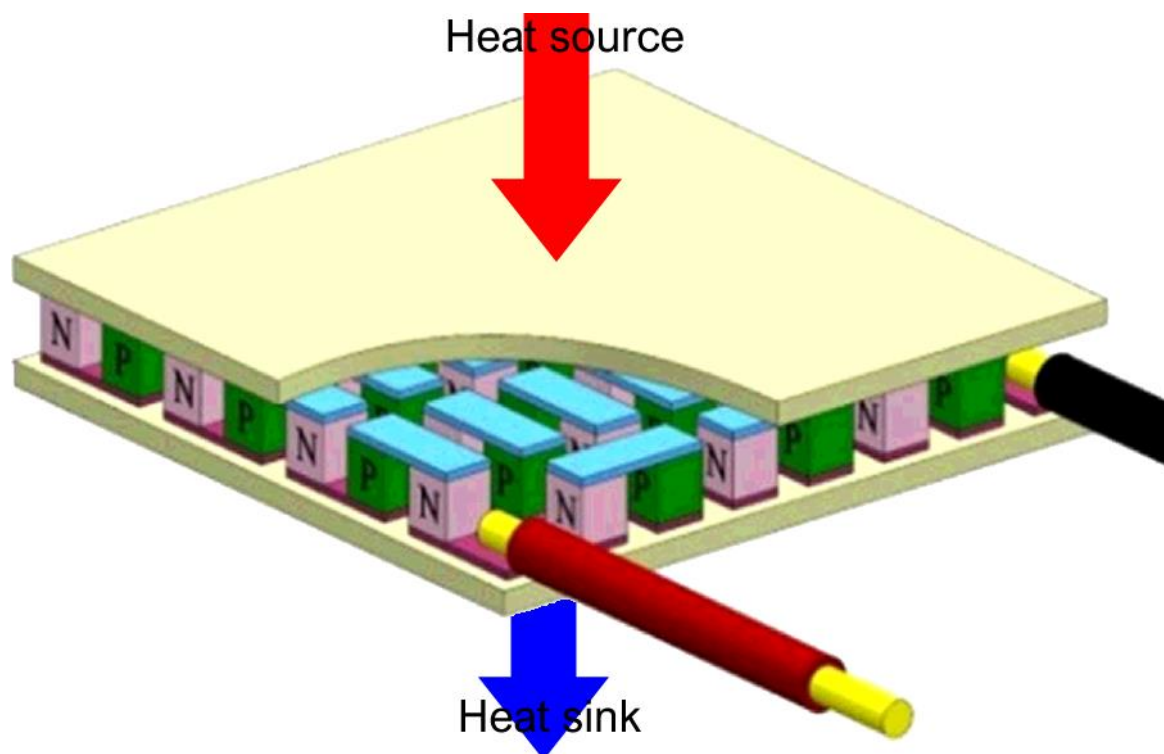


Figure 2–4 Thermoelectric module. Adapted from [18]

As can be seen from **Figure 2–4**, the mechanical support for the generator is given by insulator ceramic plates on top and bottom.

The TE materials need to be joined to the bridges; these are metallic connections between legs whose function is to provide electric continuity to the circuit.

Materials commonly used as legs do not join well with some of the most common bridge materials (Cu, Ni, Al, etc.) [2, 19] and thus an extra layer of metallization needs to be applied to the material in order to be soldered in the array. Electric connections to allow the current to flow into and out of the module also need to be provided.

The assembled module shall be placed within a temperature difference, and lower on the one end. The Seebeck effect will then enable the module to convert heat into electricity.

This combination of materials used to assemble a module creates an environment in which high temperatures can lead to several issues, the dominant one amongst them

being the thermal expansion within the module, although stability issues, oxidation or evaporation of the material, and various other degradation mechanisms are also present [20–22]

2.2. Mechanical properties

As previously described, a thermoelectric module is composed of different materials assembled together, thus, thermal expansion of said devices will exert thermally induced mechanical stress which will act upon the whole assembly.

Several properties need to be known to evaluate the performance of such materials under working conditions. These will be introduced in this section.

2.2.1. Stress

In order to analyze and understand what stress is, an example can be made using an arbitrary body. This body is assumed to be in equilibrium and external forces are assumed to be applied onto its surface. The flat cross-sectional area A can be defined as shown. Within this area, an arbitrary point Q can be positioned and the resulting force applied on this area can be defined as F . The 3D orthogonal coordinate system with the axes directions x , y , z can then be placed with their origin on the point Q and the components of the force along all three-axis computed, so that F_x , F_y and F_z are known. A diagram exhibiting the forces and surfaces is shown in **Figure 2–5**

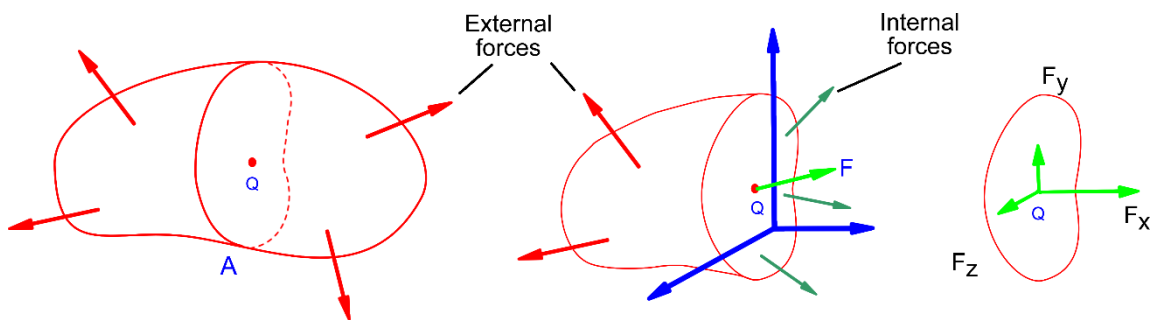


Figure 2–5 Example of a body under external forces, resultant force on the point Q and diagram of the area with the three-dimensional axes system

The resultant force will change if the point Q is moved. However, at the point Q pictured, the stresses are estimated by dividing the force by the area as follows [23].

$$\sigma_{xx} = \frac{F_x}{A}$$

$$\sigma_{xy} = \frac{F_y}{A} = \tau_{xy}$$

$$\sigma_{xz} = \frac{F_z}{A} = \tau_{xz}$$

Where the suffix denotes first the plane on which the stress acts, and then the direction in which it is acting. So, for example, the stress σ_{xx} acts on the x plane (perpendicular to the x direction) and in the direction of x, while τ_{xy} acts on the x plane and in the direction of y. Whenever the stresses act on the same direction and plane, they are called normal stresses. If the stresses act parallel to the surface, they are called shear stresses.

If, instead of taking only a differential surface on the body, a differential volume is taken, the three-dimensional stress state can be defined as shown in **Figure 2–6**.

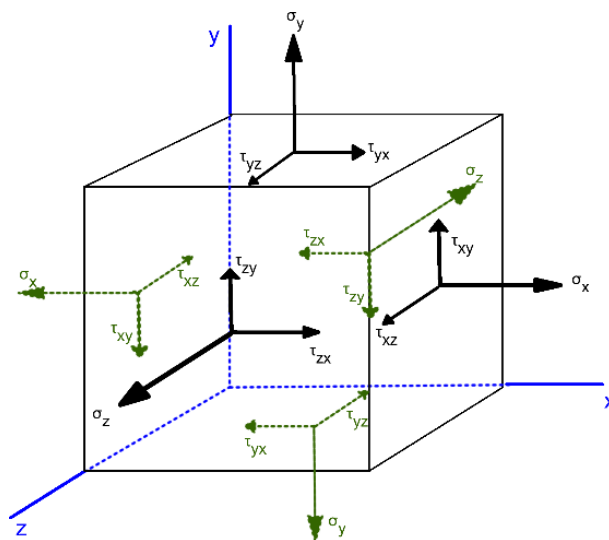


Figure 2–6 Stress distribution for a three-dimensional body

This stress state can be represented by a matrix (denominated Cauchy stress tensor) in the form [24]

$$\sigma_{ij} = \begin{bmatrix} \sigma_{xx} & \sigma_{xy} & \sigma_{xz} \\ \sigma_{yx} & \sigma_{yy} & \sigma_{yz} \\ \sigma_{zx} & \sigma_{zy} & \sigma_{zz} \end{bmatrix} = \begin{bmatrix} \sigma_x & \tau_{xy} & \tau_{xz} \\ \tau_{yx} & \sigma_y & \tau_{yz} \\ \tau_{zx} & \tau_{zy} & \sigma_z \end{bmatrix}$$

It can be seen that stress state of an arbitrary body can be defined by these nine components. The sign convention is as follows, when both the normal and the stress component point in the positive direction, the stress is positive. If normal and stress component both point to the negative side of the axis, the stress is positive. Otherwise, the stress is negative. It can be seen thus, that tensile stresses (pulling apart the body) are always positive, while compressive stresses are always negative

In order to check for symmetry, the plane xy will be analyzed, as shown in **Figure 2–7**. The system will be assumed to be in static equilibrium, so the sum of all torques must be zero and the distances from the application point to the origin are the same.

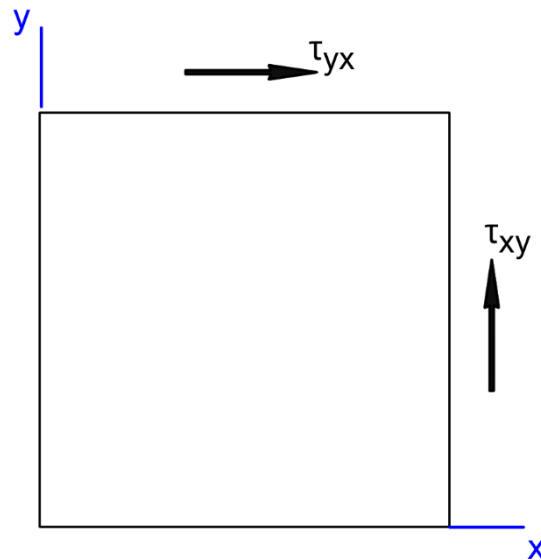


Figure 2–7 Side view of the shear stresses acting on the xy face

Thus, it can be established that $\tau_{xy} = \tau_{yx}$ and furthermore, doing the same on the xz and yz planes, it can also be found that $\tau_{xz} = \tau_{zx}$ and $\tau_{yz} = \tau_{zy}$.

2.2.2. Stress transformation

Stress is usually expressed in reference to the orthogonal axes xyz . However, it is sometimes convenient to use auxiliary axes to refer to stress.

The process to employ auxiliary axes is described next. Taking a differential 2D element AOB subjected to stress along the y and x axes and slicing it an angle θ (inclined at the same angle as the auxiliary axes) yields an element AOB. Area AOB will be assumed to be the unity [23]. The stress components need to be rewritten in the new coordinate system and yield a diagram as shown in **Figure 2–8**,

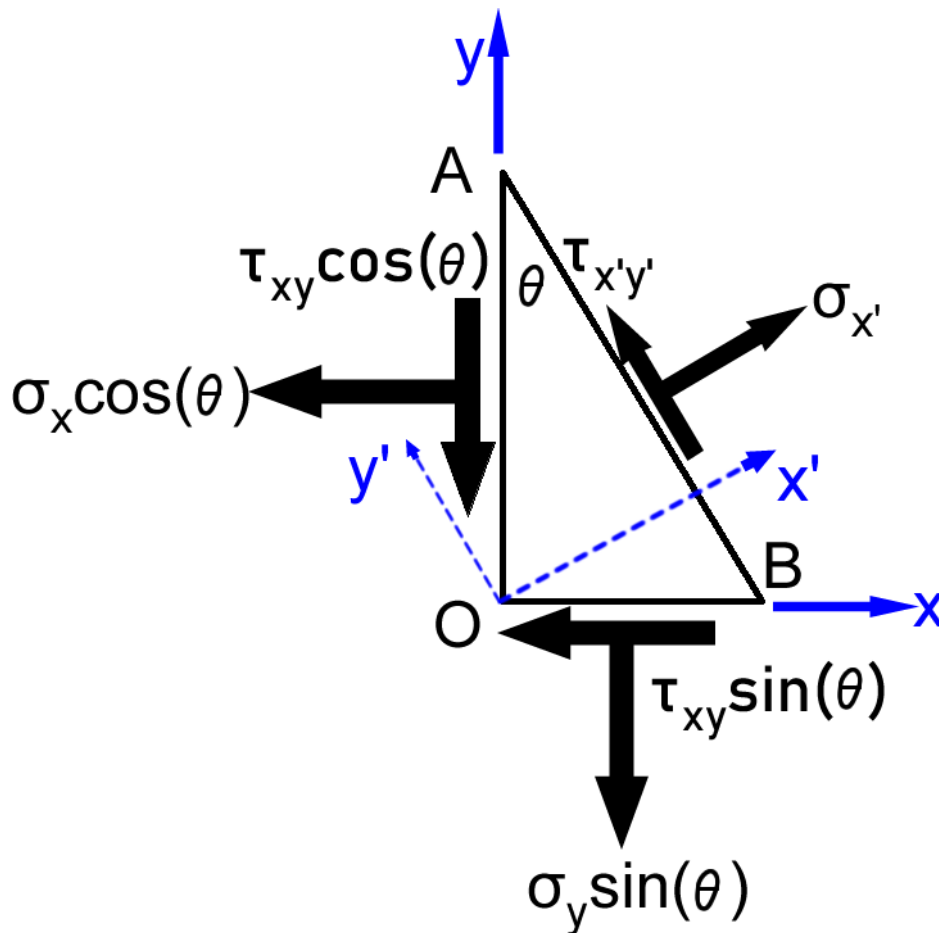


Figure 2–8 Stress components acting on a tilted differential area

In order to find the normal and shear stress $\sigma_{x'}$ and $\tau_{x'y'}$ respectively, the sum of forces on x' and y' needs to be equal to 0, these forces will be calculated as the stress component multiplied by the area AOB.

The sums are defined as $\sum F_{x'} = 0 = \sigma_{x'} - \tau_{xy} \sin(\theta) \cos(\theta) - \tau_{xy} \cos(\theta) \sin(\theta) - \sigma_y \sin(\theta) \sin(\theta) - \sigma_x \cos(\theta) \cos(\theta)$ and $\sum F_{y'} = 0 = \tau_{x'y'} + \tau_{xy} \sin(\theta) \sin(\theta) - \tau_{xy} \cos(\theta) - \sigma_y \sin(\theta) \cos(\theta) + \sigma_x \cos(\theta) \sin(\theta)$.

The resulting equations are

$$\sigma_{x'} = \sigma_x \cos^2(\theta) + \sigma_y \sin^2(\theta) + \tau_{xy} (2 \cdot \sin(\theta) \cos(\theta))$$

$$\tau_{x'y'} = (\sigma_y - \sigma_x) \cdot (2 \cdot \sin(\theta) \cos(\theta)) + \tau_{xy} (\cos^2(\theta) - \sin^2(\theta))$$

By employing trigonometric identities, the equations are finally found as

$$\sigma_{x'} = \frac{1}{2}(\sigma_x + \sigma_y) + \frac{1}{2}(\sigma_x - \sigma_y) \cdot \cos(2\theta) + \tau_{xy} \cdot \sin(2\theta) \quad (6)$$

$$\tau_{x'y'} = -\frac{1}{2}(\sigma_x - \sigma_y) \cdot \sin(2\theta) + \tau_{xy} \cdot \cos(2\theta) \quad (7)$$

By plotting shear and normal stress as a function of the varied angle, a graph can be constructed to find the maximum values for these stresses. Such a graph is exemplified in **Figure 2–9**.

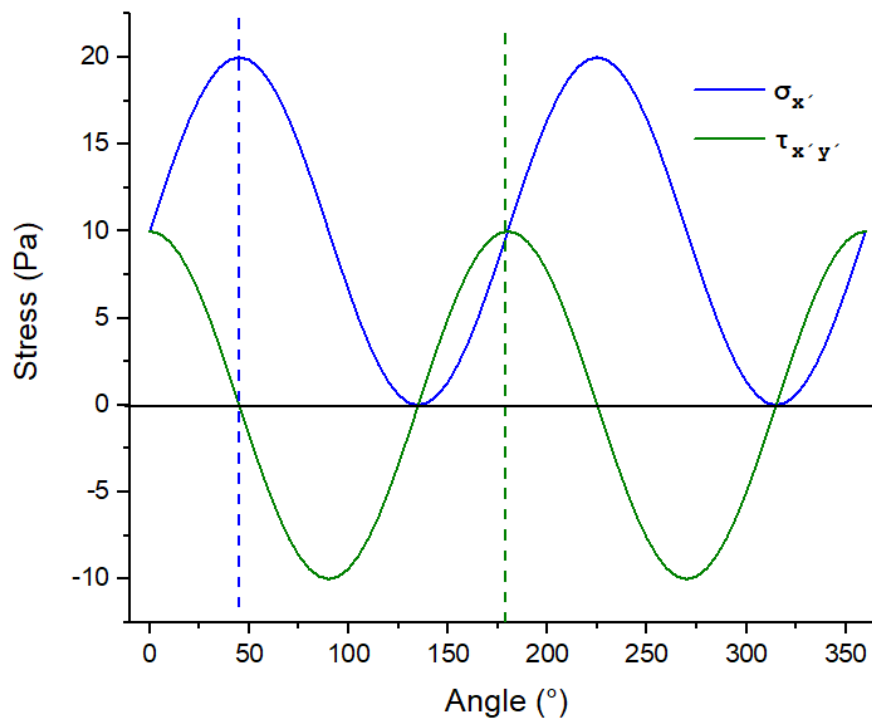


Figure 2–9 Stress as a function of rotation angle for the auxiliary axes

As can be seen from the figure, and deduced from the **Equations 6** and **7**, the maximum shear and maximum normal stress are separated by 45° . It is also important to note that when the maximum normal is achieved, shear stress vanishes and when the maximum shear is achieved, the normal stress will be at the median value.

It is also convenient to know the values for these stresses. In order to achieve this, the first derivative of **Equations 6** and **7** needs to be equaled to 0. The resulting equations are

$$\sigma_{1,2} = \frac{\sigma_x + \sigma_y}{2} \pm \sqrt{\left(\frac{\sigma_x - \sigma_y}{2}\right)^2 + \tau_{xy}^2} \quad (8)$$

$$\tau_{\max} = \sqrt{\left(\frac{\sigma_x - \sigma_y}{2}\right)^2 + \tau_{xy}^2} \quad (9)$$

where $\sigma_{1,2}$ are the maximum and minimum stresses, also called principal stresses and sometimes referred to as $\sigma_{p1,p2}$ [23, 25]

the angle at which the principal stresses are located can be estimated using the expression $\tan(2\theta_p) = \frac{2\tau_{xy}}{\sigma_x - \sigma_y}$, while the angle at which the maximum shear stress is located will be calculated using the equation $\tan(2\theta_s) = \frac{\sigma_x - \sigma_y}{2\tau_{xy}}$.

2.2.3. Strain

A body can be considered to be strained when the relative positions of two arbitrary points are altered after being subjected to an external force.

As in the case of stresses, strain can be normal (due to forces perpendicular to the plane) and shear (due to forces parallel to the plane). Normal strain will be introduced first. Following **Figure 2–10**, let there be a body with length dx , width dy and a thickness equal to one unit, in which the points A, B, C and D are defined at the corners, point A will be assumed to be fixed.

After being subjected to external normal forces, the new points B', C' and D' can be found as shown.

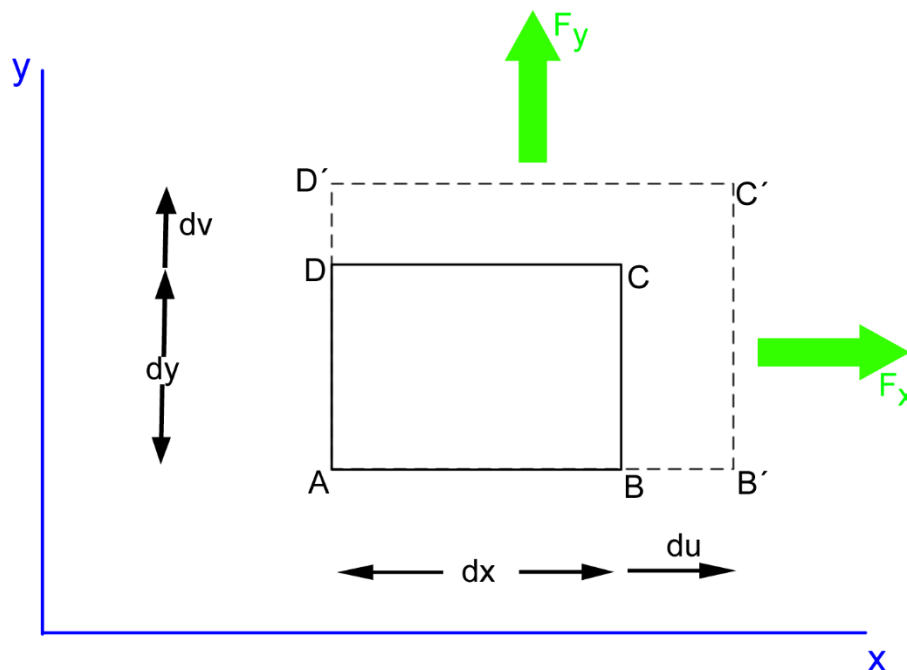


Figure 2–10 Planar normal strain

It can be seen that the point B' was moved from its x position by du due to F_x and point D' has moved dv in the y axis due to F_y .

Normal strain can be defined as the change of length divided by the original length as $\varepsilon = \frac{L-L_0}{L_0}$, thus the strain along the x axis would be defined by $\varepsilon_{xx} = \frac{du}{dx}$ while the strain along the y axis is described by $\varepsilon_{yy} = \frac{dv}{dy}$ [23, 26].

Shear strain is typically represented as a change in angle of the original shape. This is better represented in **Figure 2–11**.

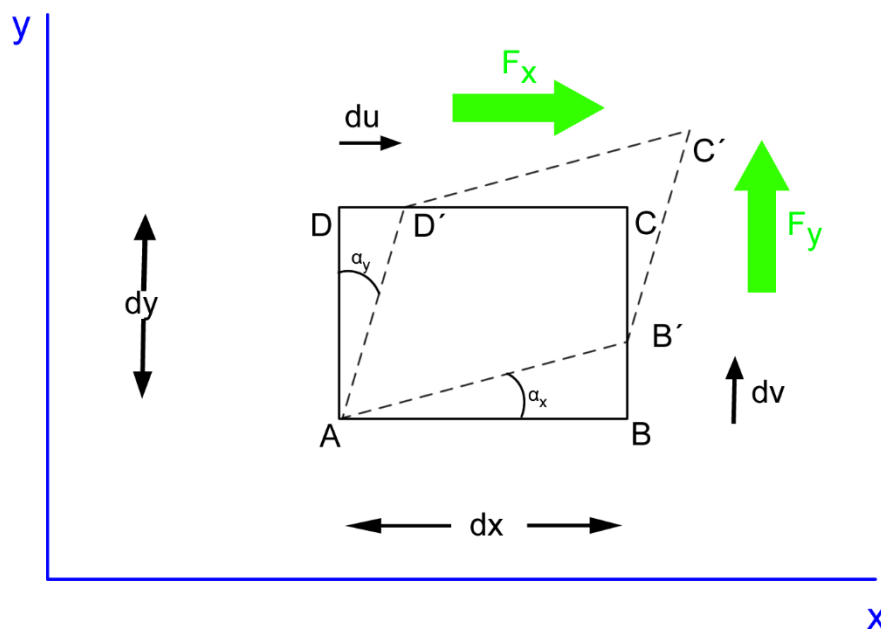


Figure 2–11 Planar shear strain

Point D' will move along the x axis due to the action of force F_x , and point B' will move on the y axis due to F_y . Assuming that the longitudinal deformation is small ($AB \approx AB'$), and that the angles α_x (BAB') and α_y (DAD') are small enough so that $\tan \alpha = \alpha$, then both angles can be expressed as $\alpha_x = \frac{dv}{dx}$ and $\alpha_y = \frac{du}{dy}$. The resulting strain can be calculated using $\gamma_{xy} = \alpha_x + \alpha_y = \frac{du}{dy} + \frac{dv}{dx}$. Just as in the case of shear stresses, the shear strain is symmetrical and thus $\gamma_{xy} = \gamma_{yx}$.

In the case of 3D, the introduction of w as the displacement and dz as the original length in the z axis is necessary. The equations, however, remain the same and the final three-dimensional strain can be expressed using the following equations

$$\varepsilon_{xx} = \frac{du}{dx} \quad \varepsilon_{yy} = \frac{dv}{dy} \quad \varepsilon_{zz} = \frac{dw}{dz} \quad \text{for normal strain}$$

$\gamma_{xy} = \frac{du}{dy} + \frac{dv}{dx}$ $\gamma_{xz} = \frac{du}{dz} + \frac{dw}{dx}$ $\gamma_{yz} = \frac{dv}{dz} + \frac{dw}{dy}$ for engineering shear strain

In a more general form, strains can be estimated using **Equation 10** [23]

$$\varepsilon_{kl} = \frac{1}{2} \left(\frac{du_k}{dx_l} + \frac{du_l}{dx_k} \right) \quad (10)$$

Where k, l can take the values x, y, z , and thus $du_y = dv$ and $dx_z = dz$, for example. Following this equation means that the real shear strain is half the engineering shear strain following $\varepsilon_{xy} = \frac{1}{2}\gamma_{xy}$. The measurement of engineering strains predates the development of the mathematical tool to analyze tensors, thus the real shear strain was defined and a factor of 0.5 included to keep the equality [23].

Once all the strains have been defined, the matrixial form can be obtained in the form

$$\varepsilon_{kl} = \begin{bmatrix} \varepsilon_{xx} & \varepsilon_{xy} & \varepsilon_{xz} \\ \varepsilon_{yx} & \varepsilon_{yy} & \varepsilon_{yz} \\ \varepsilon_{zx} & \varepsilon_{zy} & \varepsilon_{zz} \end{bmatrix} = \begin{bmatrix} \varepsilon_x & \frac{1}{2}\gamma_{xy} & \frac{1}{2}\gamma_{xz} \\ \frac{1}{2}\gamma_{yx} & \varepsilon_y & \frac{1}{2}\gamma_{yz} \\ \frac{1}{2}\gamma_{zx} & \frac{1}{2}\gamma_{zy} & \varepsilon_z \end{bmatrix}$$

2.2.4. Elasticity

In 1660, Robert Hooke discovered that the elongation (x) of a spring fixed on one side and with a set of weights on the other end would be proportional to the amount of weight (F) tied to it [27].

$$F \propto x$$

The proportionality was held through the use of a constant that he denominated k , this is the stiffness constant.

A similar relationship can be established for the analysis of materials under loads as well, as long as the strains are small enough (typically below 2% for most materials), the proportionality is given by the matrix **Equation 11** [28]

$$\sigma = C\varepsilon \quad (11)$$

Or in the alternative form in **Equation 12**

$$\sigma_{ij} = C_{ijkl}\varepsilon_{kl} \quad (12)$$

Where i, j, k, l can take the values x, y, z and C is the elastic tensor that relates stress and strain. It can be seen then that this tensor will have 4 dimensions ($3 \times 3 \times 3 \times 3$) and a size of 81 elements [27].

Since the elastic tensor is also affected by the symmetries mentioned for both stress and strain ($ij = ji, kl = lk$), the original 81 elements can be reduced to 36. Further simplification can be done by using the Voigt notation, this is done by using the following substitutions [28]

$$xx = 1 \quad yy = 2 \quad zz = 3 \quad yz, zy = 4 \quad zx, xz = 5 \quad xy, yx = 6$$

The elastic tensor can then be written as

$$C = \begin{bmatrix} C_{11} & C_{12} & C_{13} & C_{14} & C_{15} & C_{16} \\ C_{21} & C_{22} & C_{23} & C_{24} & C_{25} & C_{26} \\ C_{31} & C_{32} & C_{33} & C_{34} & C_{35} & C_{36} \\ C_{41} & C_{42} & C_{43} & C_{44} & C_{45} & C_{46} \\ C_{51} & C_{52} & C_{53} & C_{54} & C_{55} & C_{56} \\ C_{61} & C_{62} & C_{63} & C_{64} & C_{65} & C_{66} \end{bmatrix} \quad (13)$$

If the generalized Hooke's equation in matrix form is written, the following form will be obtained

$$\begin{bmatrix} \sigma_1 \\ \sigma_2 \\ \sigma_3 \\ \sigma_4 \\ \sigma_5 \\ \sigma_6 \end{bmatrix} = \begin{bmatrix} C_{11} & C_{12} & C_{13} & C_{14} & C_{15} & C_{16} \\ C_{21} & C_{22} & C_{23} & C_{24} & C_{25} & C_{26} \\ C_{31} & C_{32} & C_{33} & C_{34} & C_{35} & C_{36} \\ C_{41} & C_{42} & C_{43} & C_{44} & C_{45} & C_{46} \\ C_{51} & C_{52} & C_{53} & C_{54} & C_{55} & C_{56} \\ C_{61} & C_{62} & C_{63} & C_{64} & C_{65} & C_{66} \end{bmatrix} \begin{bmatrix} \varepsilon_1 \\ \varepsilon_2 \\ \varepsilon_3 \\ \varepsilon_4 \\ \varepsilon_5 \\ \varepsilon_6 \end{bmatrix} \quad (14)$$

However, the simplified nomenclature σ_x instead of σ_{xx} or σ_1 will be used for the rest of this work to avoid confusion with principal stresses.

It is possible to subdivide the matrix into 4 areas, following the dotted lines, the upper left area responds to normal stresses, the lower right area responds to shear stresses and the other two to mixed stresses.

Following **Figure 2–10** and **Figure 2–11**, as well as experimental evidence shows that mixed stress state does not exist (as normal stresses do not produce shear strain and vice versa), these regions are considered to be 0, off-diagonal shear stresses are also

non-existent and thus $C_{45} = C_{46} = C_{54} = C_{56} = C_{64} = C_{65} = 0$ [23]. Further conditions may be applied, according to the specific crystal structure for example.

Cubic crystals have identical properties along axes x, y and z , thus $C_{11} = C_{22} = C_{33}$, $C_{44} = C_{55} = C_{66}$ and $C_{12} = C_{13} = C_{21} = C_{23} = C_{31} = C_{32}$

The Hooke's law for a cubic crystal is then expressed by the following equation

$$\begin{bmatrix} \sigma_x \\ \sigma_y \\ \sigma_z \\ \tau_{yz} \\ \tau_{xz} \\ \tau_{xy} \end{bmatrix} = \begin{bmatrix} C_{11} & C_{12} & C_{12} & 0 & 0 & 0 \\ C_{12} & C_{11} & C_{12} & 0 & 0 & 0 \\ C_{12} & C_{12} & C_{11} & 0 & 0 & 0 \\ 0 & 0 & 0 & C_{44} & 0 & 0 \\ 0 & 0 & 0 & 0 & C_{44} & 0 \\ 0 & 0 & 0 & 0 & 0 & C_{44} \end{bmatrix} \begin{bmatrix} \varepsilon_x \\ \varepsilon_y \\ \varepsilon_z \\ \frac{1}{2}\gamma_{yz} \\ \frac{1}{2}\gamma_{xz} \\ \frac{1}{2}\gamma_{xy} \end{bmatrix} \quad (15)$$

In this case C_{11} relates the stress along an axis when a strain is applied in that same axis, C_{44} relates the shear stress in the material when a shear strain is applied to it, and finally, C_{12} relates the transverse deformation caused by a stress along the perpendicular axis as shown in **Figure 2–12**.

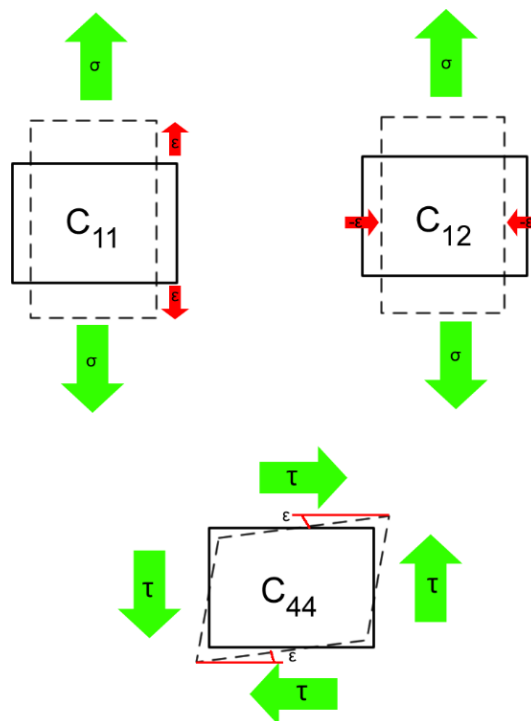


Figure 2–12 Stress and related strain for different directions

In an isotropic material, a directional behavior of the material under stress is not found. This is because the properties are the same in all directions. The material will however, still deform similar to what is shown in **Figure 2–12**. When in longitudinal deformation,

the Young's modulus E will act as analogous of C_{11} , while during shear deformation, the shear modulus G will act as analogous of C_{44} . The constriction perpendicular to the stress direction is not described by any individual variable, however the relationship to the longitudinal deformation is described by the Poisson's ratio.

To better understand this, a 2D element can be examined. Stress on the x and y axes are present and both will cause expansion on their respective directions and constriction on the perpendicular axis as shown in **Figure 2–13**. The total strain along the x axis is the sum of the strains $\epsilon_x = \frac{\sigma_x}{E} - \nu \frac{\sigma_y}{E}$

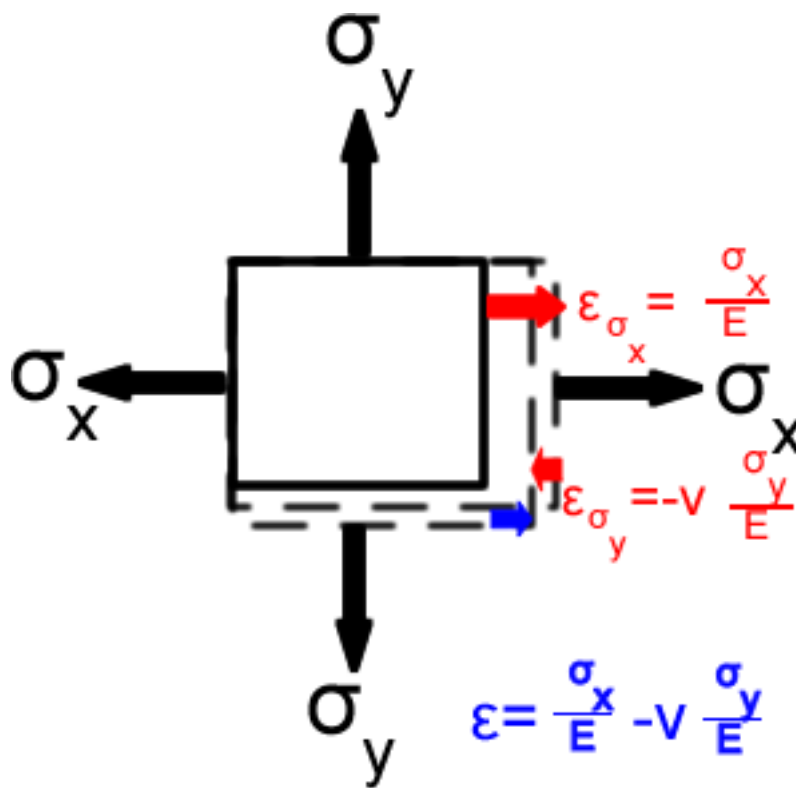


Figure 2–13 Plane stress and related expansion and constriction

Similar equations can be derived for the y axis. Moreover, this is valid for 3D as well, thus the total strain in 3D can be estimated using

$$\epsilon_x = \frac{1}{E} [\sigma_x - \nu(\sigma_y + \sigma_z)]$$

$$\epsilon_{xy} = \frac{1}{2} \gamma_{xy} = \frac{\tau_{xy}}{G}$$

$$\epsilon_y = \frac{1}{E} [\sigma_y - \nu(\sigma_x + \sigma_z)]$$

$$\epsilon_{yz} = \frac{1}{2} \gamma_{yz} = \frac{\tau_{yz}}{G}$$

$$\epsilon_z = \frac{1}{E} [\sigma_z - \nu(\sigma_y + \sigma_x)]$$

$$\epsilon_{xz} = \frac{1}{2} \gamma_{xz} = \frac{\tau_{xz}}{G}$$

The maximum shear stress is located at 45° with respect to the horizontal axis x [23] as shown by **Equation 7** and plane stress transformation can be used to estimate the normal strain along an auxiliary axis x' inclined 45° as shown in **Figure 2–14**.

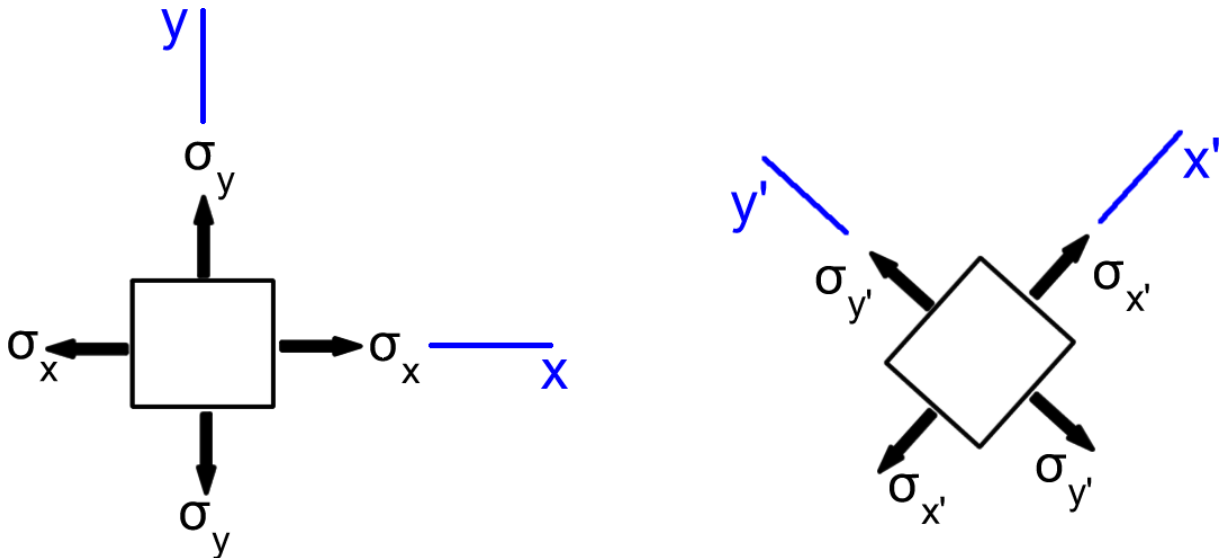


Figure 2–14 Plane stress transformation using an auxiliary axis x'

The equation found is $\varepsilon_{x'} = \frac{\tau_{xy}}{E} (1 + \nu)$ [23]. On the other hand, when under pure shear $\varepsilon_{x'} = \varepsilon_{xy} = \frac{\tau_{xy}}{2G}$, so by combining these two equations, the relationship between E, G and ν is found.

$$G = \frac{E}{2(1+\nu)} \quad (16)$$

Combining the 3D strain equations with **Equation 16** and rearranging to get the stress, the generalized Hooke's law for isotropic materials is found

$$\begin{aligned} \sigma_x &= 2G\varepsilon_x + \Lambda(\varepsilon_x + \varepsilon_y + \varepsilon_z) & \tau_{xy} &= G\gamma_{xy} = 2G\varepsilon_{xy} \\ \sigma_y &= 2G\varepsilon_y + \Lambda(\varepsilon_x + \varepsilon_y + \varepsilon_z) & \tau_{xz} &= G\gamma_{xz} = 2G\varepsilon_{xz} \\ \sigma_z &= 2G\varepsilon_z + \Lambda(\varepsilon_x + \varepsilon_y + \varepsilon_z) & \tau_{zy} &= G\gamma_{zy} = 2G\varepsilon_{zy} \end{aligned}$$

Λ is the Lamé constant [23] and is defined as $\Lambda = \frac{E\nu}{(1+\nu)(1-2\nu)}$. The generalized Hooke law can also be written as

$$\begin{bmatrix} \sigma_x \\ \sigma_y \\ \sigma_z \\ \tau_{yz} \\ \tau_{xz} \\ \tau_{xy} \end{bmatrix} = \begin{bmatrix} 2G + \Lambda & \Lambda & \Lambda & 0 & 0 & 0 \\ \Lambda & 2G + \Lambda & \Lambda & 0 & 0 & 0 \\ \Lambda & \Lambda & 2G + \Lambda & 0 & 0 & 0 \\ 0 & 0 & 0 & 2G & 0 & 0 \\ 0 & 0 & 0 & 0 & 2G & 0 \\ 0 & 0 & 0 & 0 & 0 & 2G \end{bmatrix} \begin{bmatrix} \varepsilon_x \\ \varepsilon_y \\ \varepsilon_z \\ \varepsilon_{yz} \\ \varepsilon_{xz} \\ \varepsilon_{xy} \end{bmatrix} \quad (17)$$

Stress-strain diagrams and fracture

Stress and strain can be related in a graph, which is usually obtained through a traction test, in which a sample material is fixed on one end and pulled on the other uniaxially. This test will then display normal stress and strain.

These kinds of diagrams show different areas, as shown in **Figure 2–15**. The region before the yield point is denominated as the elastic part. Deformation undergone in this area will disappear after the load is removed and the material will return to the original shape [29].

In other words, the energy applied to the system is low enough so that it can return to the original state.

The region after the yield point is called the plastic zone. Deformation in this region will not completely disappear after the load is removed and thus, the material will not return to the original shape. In this case, atomic movement can be seen as slipping or cracking.

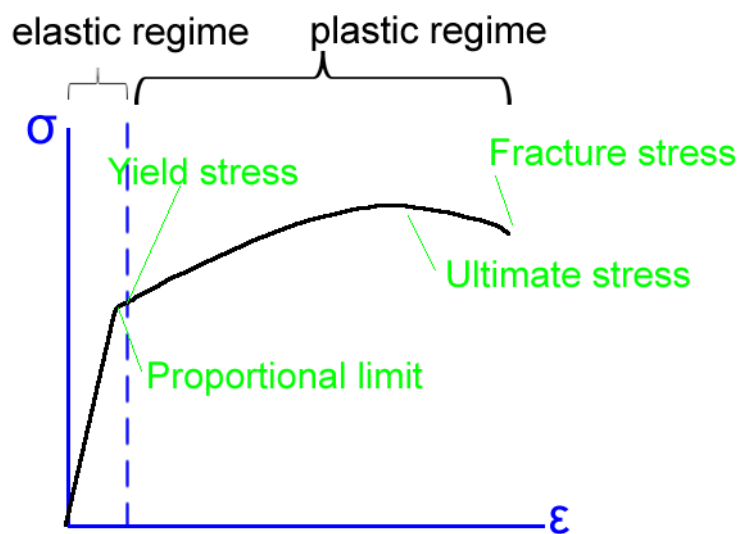


Figure 2–15 Stress-strain diagram

Materials can generally be classified according to the curve shape in these diagrams. Those that break after a relatively large plastic region are denominated ductile materials. Metals and polymers are an example of these. Materials that break with little to no plastic deformation are denominated brittle. Ceramics are the best known materials with brittle nature [30]. As can be seen in **Figure 2–16**, ductile materials after fracture have increased in length more extensively, while brittle materials have barely changed.

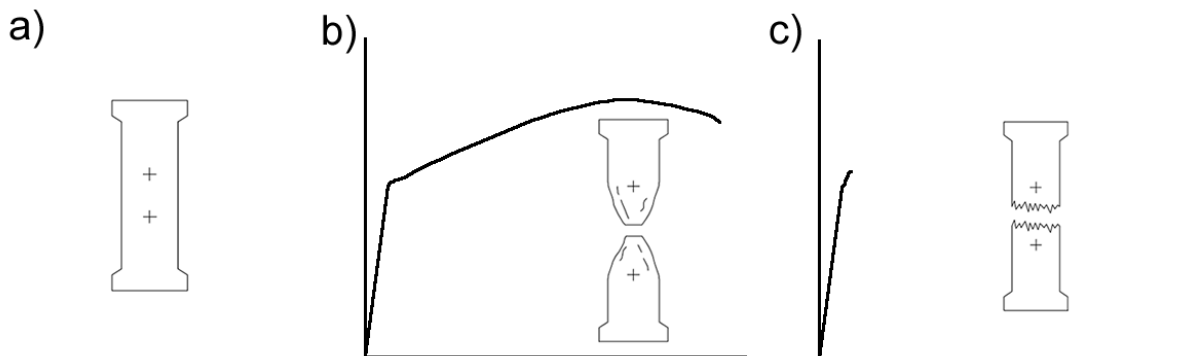


Figure 2–16 a) original sample before deformation, b) ductile sample after extensive plastic deformation and fracture and c) brittle sample exhibiting almost no plastic deformation

In engineering and materials testing, Young's modulus is measured using a traction test in which the sample is pulled on one side and kept stiff on the other. This test does not produce shear stress and thus G can be disregarded. Before the proportional limit, constriction due to normal stress (and thus Poisson effects) are very small and can also be disregarded. Therefore, Young's modulus can also be referred as the slope of the stress-strain diagrams before the proportional limit [29]. Thus, **Equation 11** can be rewritten as

$$\sigma = E\varepsilon \quad (18)$$

2.2.5. Failure theories

According to Ugural and Fenster, failure of an element comes when said element cannot perform the task for which it was designed [23]. This can mean different failure modes, like deformation beyond a certain limit or fracture.

Several theories have been proposed, many of which are specialized in specific materials, like the Coulomb-Mohr theory for rocks and concrete.

The maximum principal stress concept was developed by William John Macquorn Rankine, Gabriel Lamé, and Claude-Louis Navier. According to this theory, the material is characterized by its tensile and compressive strengths. Failure will then come whenever one of the principal stresses goes over the value of one of these limits. As this theory was developed to describe ceramic materials, and these typically have compressive strengths 5-10 times larger than tensile strengths, the usual failure criteria used is the first principal stress described by **Equation 8** [26]. This principal stress must be lower than the maximum tensile stress σ_{ut} of a material.

$$\sigma_1 < \sigma_{ut}$$

Behavior of ductile materials is described by the von Mises theory. This theory was formulated by Richard von Mises in 1913.

According to the von Mises theory, failure by yielding will occur whenever the combined stress state has the amount of energy equal to that of yielding of the material under pure tensile testing [23]. In order to make the comparison, an equivalent stress called the von Mises stress needs to be estimated.

$$\sigma_{eq} = \sqrt{\frac{1}{2} \left([\sigma_x - \sigma_y]^2 + [\sigma_y - \sigma_z]^2 + [\sigma_z - \sigma_x]^2 + 6[\tau_{xy}^2 + \tau_{yz}^2 + \tau_{zx}^2] \right)} \quad (19)$$

$$\sigma_{eq} = \sqrt{\frac{1}{2} [\sigma_1 - \sigma_2]^2 + [\sigma_2 - \sigma_3]^2 + [\sigma_3 - \sigma_1]^2} \quad (20)$$

Thus, the criterion rests on the equivalent von Mises stress being smaller than the yield stress σ_Y of a particular element to avoid failure.

$$\sigma_{eq} < \sigma_Y$$

2.2.6. Fracture toughness

A fracture occurs when the material separates into two or more parts. This in principle means that the bonds between the constituent atoms are broken. Fracture occurs when a crack propagates through the material. Stress is usually the driving factor behind crack appearance and growth; however, it is aided by defects in the lattice.

Crack nucleation can happen within the grain or at the grain boundaries. In the first type, transcrystalline cracks happen when dislocations pile up at any obstacle. This pile-up leads to bonding separation and cracks. The cracking occurs most of the time

along preferred directions within a grain and can change direction as it jumps from grain to grain, following preferred directions in each subsequential grain [26].

Intracrystalline crack nucleation happens when the boundaries are weaker than the grains, in this case pile-up and grain sliding are the main factors driving the nucleation.

Both processes are brittle in nature, which means that little plastic deformation is involved around the new surfaces

Crack opening can happen in three forms, as shown in **Figure 2–17**, mode I is related to tensile stress, modes II and III are related to shear stresses [31].

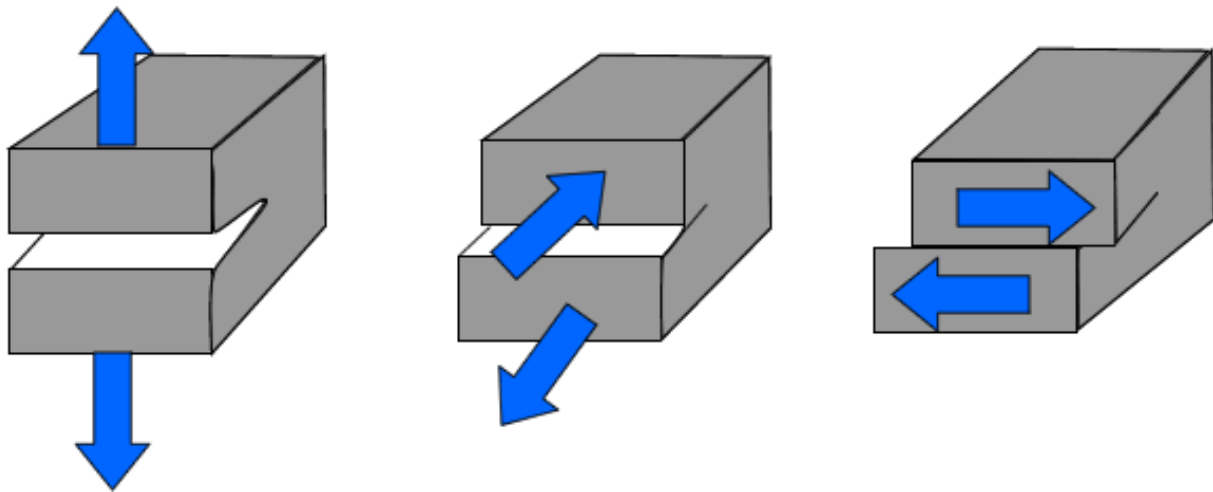


Figure 2–17 Crack aperture modes, adapted from [31]

This work will focus on mode I, as it is the most relevant in general and particularly for thermoelectric generator applications as previous research has shown that the tensile stresses tend to be the most prominent in the module assembly [7] due to the fact that most materials have compressive strengths 2-10 times higher than the tensile strength.

The appearance of a crack in a material means that less area is available to spread the force acting on the element. It can be seen then, that the stress distribution will change. A stress concentration will occur, following the example shown in **Figure 2–18** [31].

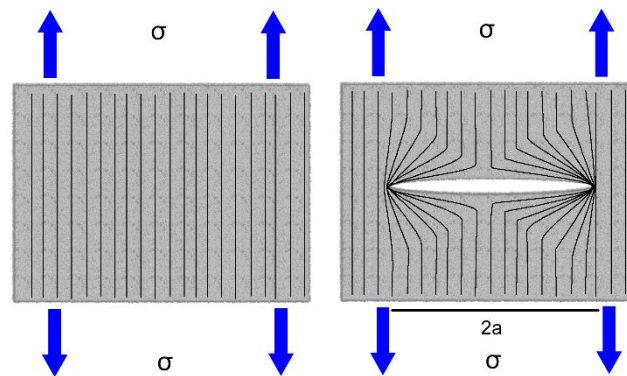


Figure 2–18 Representation of an infinite long plate under tensile stress without and with a crack inside, the lines represent the stress distribution within the material

The reduction in area will increase the amount of stress on the material. This concentration of stress is represented by K_I and is expressed in **Equation 21** [26, 31]

$$K_I = \psi \sigma \sqrt{\pi a} \quad (21)$$

where ψ is a geometry factor dependent on the ratio of the width of the plate to the size of the crack. Higher values (longer cracks or shorter plates) will produce higher geometric factors to account for the increased area loss in a relatively smaller plate. K_I will then have the unit MPa m^{1/2} and is a representation of how much area is lost due to the appearance of a discontinuity in the material.

Cracks do not necessarily grow when under stress. For this to happen a specific critical load needs to be applied to the material. When this happens the stress concentration factor reaches a value called fracture toughness, also represented as K_{Ic} [32].

Determination of such a property is usually done through standardized tests called single edge notched beam (SENB) [33]. This test includes a tensile or bending test of a sample manufactured in a specific size and with a notch that serves as crack initiator. K_{Ic} is then estimated from the stress, crack length and load.

On ceramic materials with low plasticity, estimating fracture toughness is possible by the use of the cracks produced after indentation with a Vickers diamond punch [34].

When the indenter penetrates an isotropic material, it will create two opposing effects. The first one will be a compressive force that will leave an imprint on the material, the second effect will act upon release of the force and is a tensile component that will tear open cracks on the areas that have the highest stress concentrations (edges) of the

imprint [35]. The crack produced will have a semicircular shape, centered around the imprint and can be then expressed by **Equation 22**

$$K_r = \chi_r \frac{F}{c^{3/2}} \quad (22)$$

where K_r is the stress intensity factor driving the crack opening, F is the applied load, c is the median half-length of the crack and χ_r depends on the relationship between hardness (H) and Young's modulus as shown in **Equation 23**

$$\chi_r = \zeta \left(\frac{E}{H} \right)^{1/2} \quad (23)$$

where ζ is a geometrical correction factor whose value is 0.016 [35] when using a Vickers indenter. Substituting χ_r from **Equation 21** into **Equation 22**, the expression

to estimate fracture toughness from Vickers indentation can be found as $K_r = \frac{P\zeta\left(\frac{E}{H}\right)^{1/2}}{c^{3/2}}$.

Further descriptions of hardness, and more specifically Vickers indentations will be discussed in the following section.

2.2.7. Hardness

Hardness can be defined as the resistance to localized and permanent deformation. This deformation can be applied through scratching, wear, bending or indentation, however it is the last one that has received the most attention as it is also the easiest to perform in a reproducible manner [36].

Indentation can be done on a macro scale, as well as micro and nano, depending on the amount of the load. Forces from 2 N and up to 30 kN are used in macro testing, micro testing on the other hand uses loads below 2 N and indentation depths larger than 0.2 μm . Nanoindentation on the other hand, uses anywhere between a few μN to about 200 mN [37].

Different scales exist, however the one used in this work is Vickers Hardness.

Vickers Hardness (HV)

Developed by the British corporation Vickers Ltd. in 1920, it relies on the use of a pyramidal indenter with a specific geometry.

The indenter has an angle of 136° between opposing edges of the pyramid, as shown in **Figure 2–19**.

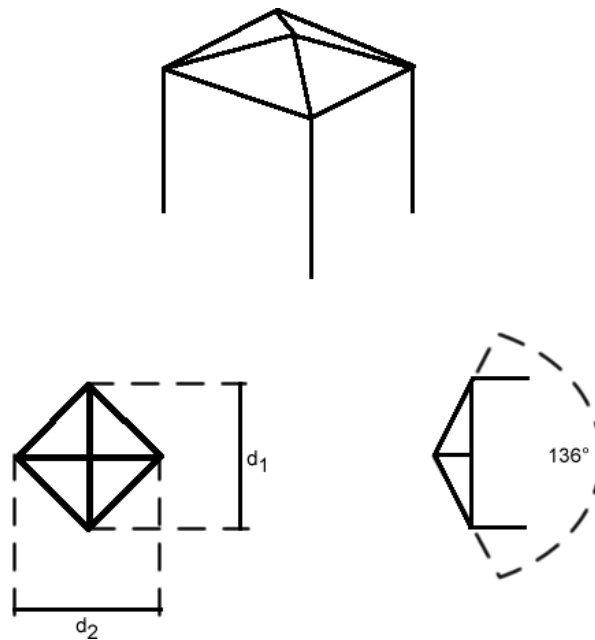


Figure 2–19 Geometry of a Vickers indenter

The hardness estimation is then calculated with the force divided by the real imprint area, this area in turn is estimated by measuring the diagonals d using an optical microscope [38]. This process is summed up in **Equation 24**

$$H = \frac{L}{A_r} = \frac{2L}{d^2} \sin \frac{136^\circ}{2} = 1.854 \frac{L}{d^2} \quad (24)$$

Loads used in this technique range from 1 to 120 kgf (9.8 N-1.2 kN) when macro-hardness is being measured, while microhardness testing allows for loads as low as 100 gf. If the force is measured in gf, the hardness is reported as hardness Vickers units (HV), if the force is measured in newtons, the hardness is reported in Pascals.

The load application is done in 2-8 s, and then held for 10-15 s.

The American ASTM E92-16 and the international ISO 6507 are the standards used for this kind of testing [39, 40].

2.2.8. Temperature dependence of Young's modulus

As thermoelectrics have to work in an environment where the temperature is high, their properties will change in comparison to room temperature behavior. Mechanical

properties are not an exception and thus, it is convenient to know what the state of the art is in models for temperature dependence of mechanical properties.

Wachtman *et al.* [41] published a paper where they found that on many ceramic materials, the temperature dependence of Young's modulus obeyed the equation $E(T) = E_0 - BT e^{-\frac{T_0}{T}}$, where E_0, B and T_0 were experimentally determined values. Moreover as T_0 is reported to be 0.3-0.5 of the Debye temperature, for T values $T \gg T_0$, $e^{-\frac{T_0}{T}}$ tends to 1 and thus, the temperature dependence of E becomes linear. Temperatures close to the melting point are not covered by this equation, however, as every material has a particular behavior at such high temperatures.

More recently, Rahemi and Li [42] developed an equation from the Lennard-Jones potential to describe the bonds between atoms in the lattice and thus, explain the temperature dependence of E . They found an equation in the form $E(T) = \beta \left[\varphi_0 - \vartheta \frac{(k_B T)^2}{\varphi_0} \right]^6$ where β , φ_0 and ϑ are constants determined experimentally. This model takes into account not only the interaction with the closest neighboring atom, but the 2nd and 3rd closest neighbors as well. This equation has been only tested on pure metal samples.

This work performed high temperature measurements of Young's modulus. Further analysis for this data was performed using the Wachtman equation since it was developed for ceramic materials and it is proven to be accurate for such material systems.

2.2.9. Effective properties of multi-phase materials

Many materials, thermoelectric amongst them, can have several phases present in their structure. This happens as a consequence of processing or intentionally, e.g. to improve the TE properties by increased phonon scattering or to strengthen a material by adding strain fields in the lattice.

Room temperature $Mg_2(Si,Sn)$ solid solutions are no exception to this, given the known solubility gap between both ends of the spectrum. This will be discussed more in detail in chapter 2.4.1. however, it is important to state that a material composed of phases with different properties will behave differently in comparison with the pure

materials. A composite-material approach will be used in this work and therefore, information about composites is needed beforehand.

A composite material is defined by Taya and Arsenault as a man-made material that is composed of at least two materials chemically different from each other, assembled in a 3D manner with properties that would not be achieved by their individual components [43].

Mechanical properties in these kinds of materials are, thus, different from the matrix (main component) and the inclusions. These inclusions will be addressed as “fibers” however they can be any material that has different enough properties compared to the matrix. This work will focus on the Young’s modulus of such materials.

The first model used to describe the effective properties in a composite is the law of mixtures, first proposed by Waldemar Voigt and sometimes called after him.

The law of mixtures works in an iso-strain environment, in which all the particles in the material are deformed by the same amount under stress. A simple 3 element model can be used to envision strain in Voigt’s approximation, this is shown in **Figure 2–20**.

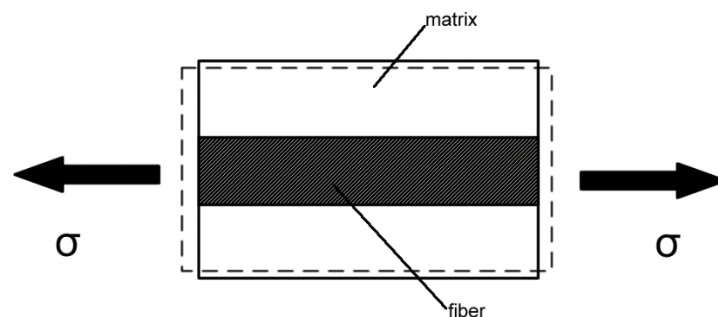


Figure 2–20 Sketch of a multi-phase material being stretched with the inclusion aligned parallel to the force

In this case since the strain is the same in the complete material, and since the total volume V on which the stress is acting is the sum of the matrix V_m and the inclusion V_f following $V = V_f + V_m$ and since the total energy that can be absorbed by the material is defined as σV [43] the equation for this energy in the composite becomes $\bar{\sigma}V = \sigma_f V_f + \sigma_m V_m$. Following Equation 13 this can be rewritten as $\bar{E}\bar{\epsilon}V = E_f \epsilon_f V_f + E_m \epsilon_m V_m$. But $\bar{\epsilon} = \epsilon_m = \epsilon_f$, so the equation is reduced to $\bar{E}V = E_f V_f + E_m V_m$ in the case of a two-material system. This can be generalized to an n element material as shown in

$$\bar{E} = \sum E_i V_i \quad (25)$$

where V_i is the volume percentage fraction of a given phase and E_i is the Young's modulus exhibited by that specific phase.

The second approximation was proposed by Andras Reuss to complement Voigt's work, this model in comparison works with the iso-stress condition. **Figure 2–21** shows a diagram of a three-element material under these conditions.

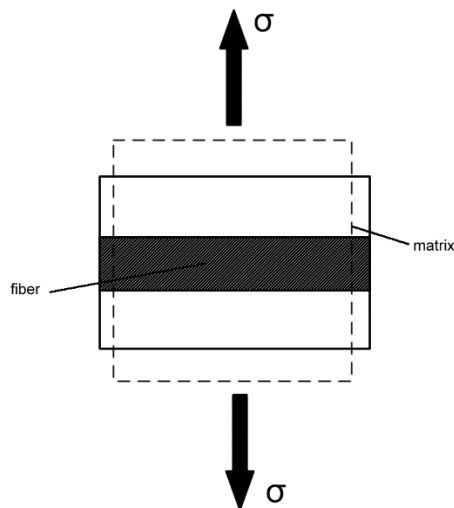


Figure 2–21 Sketch of a multi-phase material being stretched with the inclusion aligned perpendicular to the force

Similar to the previous case, the volume is subjected to the same stress, the strain however will be different as e.g. the matrix is softer than the inclusion and will deform further. In this case the total volumetric strain is $\bar{\varepsilon}V = \varepsilon_f V_f + \varepsilon_m V_m$ [43], and just as the previous case, using **Equation 18**, the total strain expression can be rewritten as $\frac{\bar{\sigma}V}{\bar{E}} = \frac{V_f \sigma_f}{E_f} + \frac{V_m \sigma_m}{E_m}$, but since $\bar{\sigma} = \sigma_f = \sigma_m$, the expression reduces to $\frac{V}{\bar{E}} = \frac{V_f}{E_f} + \frac{V_m}{E_m}$. This equation can be expanded to a material with n elements using

$$\bar{E} = \left(\sum \frac{V_i}{E_i} \right)^{-1} \quad (26)$$

Both the Voigt and Reuss approximations work on the premise that the inclusions are perfectly aligned with the stress. However, in most cases the inclusions are aligned in a random pattern and the material will not behave exactly as these previous models predict. Instead, they will be the limits of the mechanical behavior exhibited by the composite as shown in **Figure 2–22**.

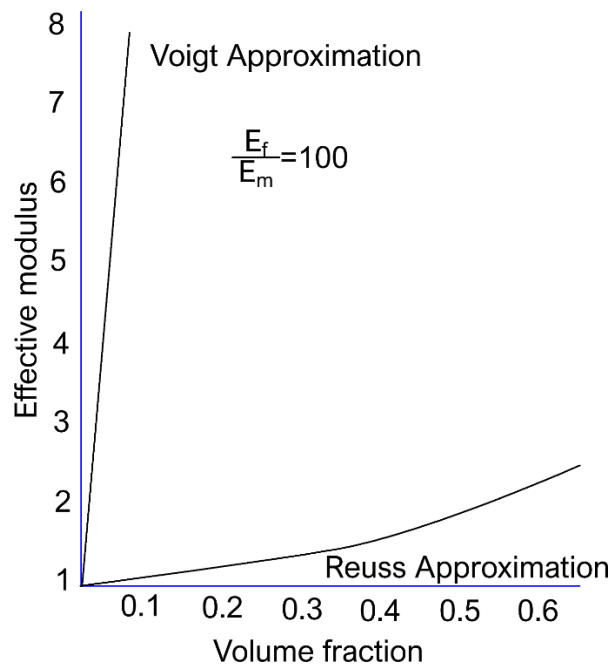


Figure 2–22 Effective Young's modulus of a material as a function of volume fraction of the inclusion V_f if the inclusion has a Young's modulus 100 times higher than the matrix. Adapted from [43]

As Naslain describes [44], several authors have introduced correction factors to better approximate the real behavior of a composite with randomly oriented reinforcing fibers.

2.2.10. Thermal expansion

The materials within the module assembly will inevitably expand under the high module operation temperature.

Whenever a material is heated, the atomic distances will increase because of the rising repulsive forces between atoms due to a higher overlap between electron distributions. A more detailed description of this overlap is given next.

Within the bond, two competing forces act upon the atoms, the dispersing force and the repulsive force. The dispersing force (also called London dispersing force) acts to bring atoms together through the attraction exerted by the creation of instantaneous dipoles, these in turn, caused by the rearrangement of electrons in an atom because of the fluctuation in the position of the electrons in its closest neighborhood.

However, as they become closer together their electron charge distributions start to overlap. Based on Pauli's exclusion principle, atoms repulse each other to prevent electrons from occupying prohibited energetic states [28].

This interplay between forces is expressed in the Lennard-Jones potential, denoted as $U(r) = 4\epsilon \left[\left(\frac{\xi}{r} \right)^{12} - \left(\frac{\xi}{r} \right)^6 \right]$, where U is the energy of the system, r the distance between atoms, ϵ and ξ are experimental values representing the dispersion energy and distance at which the interatomic potential energy is 0. The exponent 6 for the attractive term was described by London and later proved to be correct by quantum chemical calculations [45], since the attractive forces decay with the relationship $\left(\frac{1}{r} \right)^6$. The repulsion force has an exponent 12, which does not have a real physical meaning but approximates the Pauli repulsion well and is easily expressed as the square of the attractive forces.

The form of the Lennard-Jones potential curve is shown in **Figure 2–23**

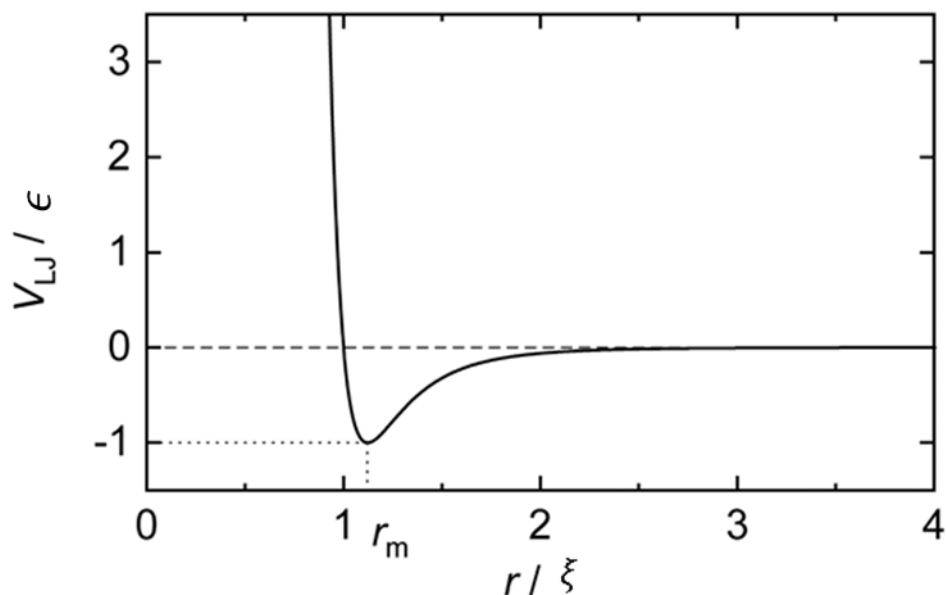


Figure 2–23 Lennard-Jones potential

The minimum value is found at $2^{1/6}\xi$, which corresponds to the energy minimum $-\epsilon$.

The Lennard-Jones potential is a simplified model that does not take into account interactions with the 2nd or third closest neighbors, however it is the best simple model that describes an interaction between atoms in a realistic way.

It can be seen that providing thermal energy to the bond increases the distance between atoms to prevent further overlap between electron charge distributions.

Thermal volumetric expansion relates how much a material changes in volume by exposing it to a different temperature than its original state. This change in volume can be expressed by

$$\frac{V_f - V_i}{V_i} = \beta(T_f - T_i) \quad (27)$$

where the subscripts i and f refer to initial and final states respectively, V refers to volume and β is the volumetric coefficient of thermal expansion.

Linear expansion on the other hand, is a similar concept that relates how much a material changes in length upon being heated or cooled. The rate at which this happens is called the coefficient of thermal expansion (CTE or α) [46]. In this case, the elongation due to temperature change can be expressed as

$$\frac{l_f - l_i}{l_i} = \alpha(T_f - T_i) \quad (28)$$

where l refers to length. Note also that $\beta = 3\alpha$.

Whenever this change in size is restricted, a pressure or tension will build up in the material. These stresses bring about the possibility of failure to an assembly. It is therefore imperative to keep them at the lowest possible level [7].

Materials need to be paired with contacts and bridges in a way that the CTE is as similar as possible. Failing to do so will lead to bigger stresses and more possibilities to fail [21].

2.3. Mg_2X

2.3.1. Mg_2X system

The material system Mg_2X ($X = Si, Ge, Sn$) is a good thermoelectric material, known since the 1960's. It has been in recent years, however, that the attention of the scientific community has returned to these materials.

All the materials having an Mg_2X formula exhibit a $Fm\bar{3}m$ antiferroite crystal structure, with an FCC arrangement. Mg atoms sit on the eight tetrahedral positions (Wyckoff positions 8c), while the X atoms fill the corners and face centers (Wyckoff positions 4a). This identical crystal structure favors the alloying between materials as the X position can be filled by either element, or a combination of them [47].

Special attention has been given to the solid solution $Mg_2(Si,Sn)$, which in comparison to Ge-containing material has a better cost/performance ratio. All elements present in the material are highly abundant in the earth's crust and pose little to no danger to life or environment. The added benefit of a very low density also makes it a very good candidate for TE technology.

Mg_2Si

The best studied member of the family of Mg_2X materials has a lattice parameter of 6.354 Å and a density of 2 g/cm³. It has a natural n-type conduction, however adding elements belonging to the IA group in the Mg position can lead to p-type materials [48–55].

It has a melting temperature above 1373 K, however material degradation due to Mg oxidation can be seen from 1073 K [56].

Mg_2Sn

This material has a lattice parameter of 6.764 Å and a density of 3.6g/cm³. Its melting temperature is 1050 K, however oxidation has been observed from 773 K [47, 52, 57, 58].

$Mg_2(Si,Sn)$

The solid solution benefits from having two different types of atoms in the X position, as such, the thermal conductivity will drop [59] as phonon scattering is increased through alloying.

The lattice parameter and density also obey Vegard's law and they can be estimated using a linear interpolation between the binaries [60]. One very common way to define the stoichiometry in the solid solution is $Mg_2Si_{1-x}Sn_x$.

The solid solution has a solubility gap. The extend depends on temperature but the reported results differ between different publications, as shown in **Figure 2–24**, however most agree that the compositions around $x = 0.5$ are outside the solubility range for the material system at room temperature and up to 700 °C. This creates a potential issue for material stability as the material will tend to remain in a metastable state [61–64]. Whether or not the compositions with different x Sn content than the nominal composition can be considered as secondary phases has been challenged during the course of this work. A more detailed description will be done in the discussion part.

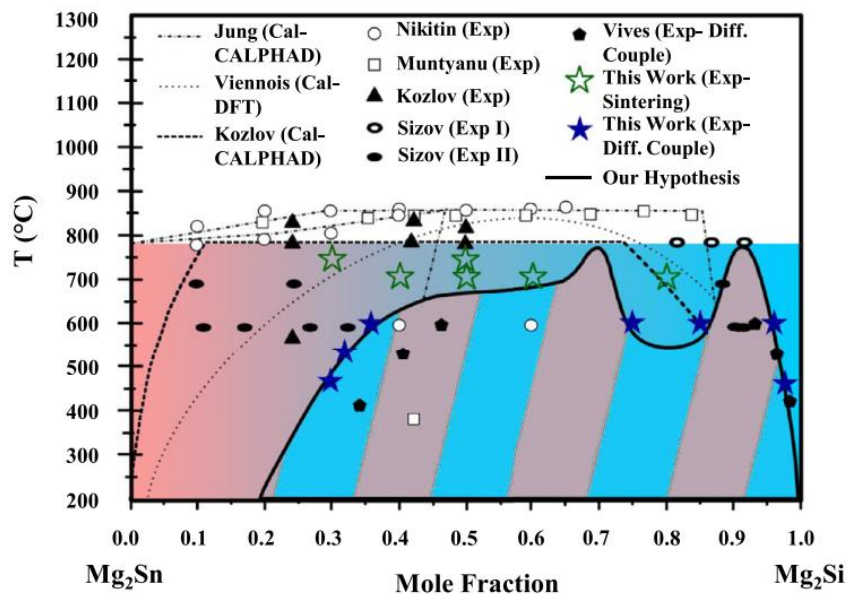


Figure 2–24 Miscibility gap for the Mg_2Si - Mg_2Sn material system, taken from [63]. Gradient color indicates a full miscibility while striped color indicates the miscibility gap

Another interesting feature in the solid solution is the convergence of the two lowest lying conduction bands, which according to most authors happens around the

composition $\text{Mg}_2\text{Si}_{0.4}\text{Sn}_{0.6}$. This effect produces favorable electric properties for the n-type material and, according to some recent research, good thermal properties through the lowered speed of sound [65–67].

Synthesis of these materials is not a trivial process. The difference in melting points for the precursors (923 K for Mg, 505 K for Sn and 1683 K for Si) as well as the high Mg vapor pressure make the synthesis through traditional melting challenging. In this regard, several process routes have been tried, e.g. induction melting [68, 69], melt spinning [70–72]. Other methods like ball milling have been developed and yield material with good properties ($zT = 1.2\text{--}1.4$), albeit with material quantity limited to some 10's of grams as published by [73–76].

Mixed synthesis methods, e.g. melting + milling, have also been developed to produce larger (>50 g) amounts of precursor material with consistent zT values of 1.3 [77].

2.3.2. TE properties of $\text{Mg}_2(\text{Si},\text{Sn})$

In contrast to most work performed on thermoelectric materials this work will not be focusing on the thermoelectric properties exhibited by them. A small introduction to highlight the good performance achieved by $\text{Mg}_2(\text{Si},\text{Sn})$ is given in the following paragraphs nonetheless.

Mechanical properties exhibited by thermoelectrics in general, and more specifically $\text{Mg}_2(\text{Si},\text{Sn})$ will be introduced in chapter 2.5.

n-type

n-type $\text{Mg}_2(\text{Si},\text{Sn})$ is typically doped with elements belonging to the VA group like Sb and Bi. It is known, in the case of Bi, that the solubility limit in the binary Mg_2Si is around 2 at% [49]. The solid solution does not have a reported limit on the solubility for Bi, however Seebeck coefficient values reported previously in material with $x = 0.7$ place this value between 3.5 and 4 at% [78].

Optimized thermoelectric properties have been found for the material $\text{Mg}_2\text{Si}_{0.3}\text{Sn}_{0.665}\text{Bi}_{0.035}$. This composition exploits the band convergence effect and the high solubility limit of Bi in the material. The maximum zT achieved by this material was 1.25 at 700 K [77].

p-type

The doping is usually done by substituting Li in the Mg sites [60, 79, 80], however work with Na, Ag and Ga has also been published [70, 81].

Experimental values, as well as calculations to find the optimum p-type composition is the focus of some recent work by Kamila *et al.* [82]

This work will focus on the material $\text{Mg}_{1.97}\text{Li}_{0.03}\text{Si}_{0.3}\text{Sn}_{0.7}$. Such a composition is known to have relatively good thermoelectric properties.

2.4. Mechanical properties of TE materials

2.4.1. Non-silicide systems

Mechanical properties of TE materials are a subject that has been recently re-visited by researchers. It is still far behind in comparison with the material optimization for TE performance.

One of the material systems that has been studied is Half Heusler compounds (HH). These kinds of materials have the general formula XYZ, where X and Y are transition metals and Z is an element whose valence electrons come from the p orbital.

Half Heusler materials are most commonly used in the middle to high temperature ranges (700-1000 K) [12].

As a family of very diverse materials, it is also expected to find a wide range of mechanical properties amongst them. So, for example materials like ZrNiSn with a hardness of 14 GPa can be found. In contrast, some softer materials like $Zr_{0.5}Hf_{0.5}Co_{0.1}Rh_{0.9}Sn_{0.01}Sb_{0.99}$ with merely 3.8 GPa also exist. The median values for hardness as reported by Rogl *et al.* is 10 GPa [83].

The elastic modulus values of such materials are as diverse as their hardness and therefore it is found that VCoSn has a Young's modulus of 243 GPa and $ZrNiSn_{0.95}Sb_{0.05}$ has 71.8 GPa. The median values reported are 200 GPa [83].

A more direct comparison of Mg_2X can be made to Skutterudites. These materials have an application in the mid-temperature range (between 400 and 800 K), just as the aforementioned material.

Skutterudites are based on the general formula XY_3 , where X can be Co, Fe and Ni, while Y corresponds to As or Sb. Their crystal structure is Im-3, composed normally of 8 Co cubes, 6 of which are filled by Sb square shaped rings [12].

Extra elements can be added to fill these empty cube cells, whenever the Skutterudite material has these fillers, they are denominated "filled Skutterudites". Such elements contribute to a lower thermal conductivity by scattering phonons by rattling inside the icosahedral voids in the lattice as a point defect [17, 84].

Just as with the HH, Skutterudites form a very wide family of materials and their mechanical properties are varying, although not as much as with the previous case. Hardness values are found in literature ranging from 2 GPa for the hand milled $\text{DD}_{0.25}\text{Fe}_{2.5}\text{Ni}_{1.5}\text{Sb}_{12}$ (DD, or Didymium is an alloy from Praseodymium and Neodymium), while $\text{Ba}_{0.075}\text{Sr}_{0.025}\text{Yb}_{0.1}\text{Co}_4\text{Sb}_{12}$ shows a hardness of 5.6 GPa. The median values reported are around 5 GPa [85, 86].

The Young's modulus exhibited by skutterudites ranges from 100 to 148 GPa, with the aforementioned Didymium filled material being the softest and CoSb_3 being the stiffest.

2.4.2. $\text{Mg}_2(\text{Si},\text{Sn})$

Magnesium silicide, magnesium stannide and the solid solutions have also received some attention in regard to their mechanical properties.

Magnesium silicide, the most studied of them, has a reported hardness value of 5 GPa [87], while the reports for Young's modulus vary between 85 and 145 GPa [50, 55, 87–91]. The wide range of values for the Young's modulus depends on the type of measurement done on it. While ultrasound methods yield a value more consistent with the median, other methods like nanoindentation and compressive testing yield values off the median.

Magnesium stannide has been, on the other hand, the main point only for very few publications. One paper reports the hardness of the material to be 1.7 GPa [92], further publications address the elastic constants and the Young's modulus, this last value was reported to be 82 GPa [57, 58].

A solid solution has also been researched, $\text{Mg}_2\text{Si}_{0.4}\text{Sn}_{0.6}$ was studied by Gao *et al.* [92] and Gelbstein *et al.* [93] finding a hardness value of 3.06 GPa and a Young's modulus of 88 GPa for the former, the latter study found a hardness of 3.57 GPa and elastic modulus of 83 GPa.

Other compositions within the solid solutions whose mechanical properties are known are $\text{Mg}_2\text{Si}_{0.6}\text{Sn}_{0.4}$, in a very recent paper that was published during the course of this work, Mejri *et al.* [94] report a hardness value of 4.5 GPa and a Young's modulus of 90 GPa. They also performed temperature dependent measurements on the elastic properties and found a linear influence of temperature in the Young's modulus.

Lattice dynamics were studied to understand the effect of the Si/Sn ratio for some compositions along the solid solution [67]. Results were published during the experimental work on this study. Klobes *et al.* found that the Si-Mg bond has a more covalent nature compared to Mg-Sn, and thus increasing the Si content in the material the strength of the bonding becomes larger. This substitution has the consequence of stronger mechanical properties and higher thermal stability.

2.5. Thermoelectric module evaluation

Mechanical evaluation of the performance achieved by a thermoelectric module is not usually done, with the electric power output being the most important parameter to study.

However it has been proved before that mechanical degradation can lead to a reduction in TE performance as the electrical resistance increases [22].

In practice, mechanical stability of a thermoelectric module is evaluated qualitatively by producing the module, submitting it to thermal annealing or cycling and observing the damage on the module [19, 22, 95, 96] **Figure 2–25** shows published pictures of damage on TE modules. Both images are from modules built with HMS p-type and $Mg_2(Si,Sn)$ n-type legs.

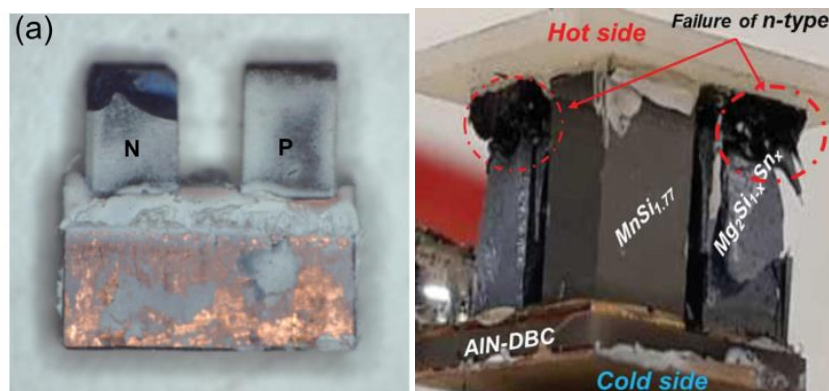


Figure 2–25 Damage seen in several modules. Taken from [19, 95]

The use of computational methods to predict areas susceptible to damage by means of a finite element model (FEM) simulation has spread to the field of thermoelectricity as well.

The role of a FEM simulation is to provide insight into the mechanical and/or also TE performance of a module without the need to actually build it. It can be used to test different parameters such as leg geometry, metallization material, bridge material and size, etc. [7, 97–99].

The effectiveness of such a simulation will be influenced mainly by two factors, how precise the properties of the materials involved are characterized and how realistic/adequate the boundary conditions are selected [8].

One of the main goals of this work is to produce a precise database of mechanical properties to be used in FEM simulation. This will increase the usefulness of software usage in the development of a Mg_2X based thermoelectric module.

3. Summary of research

3.1. Research motivation

The development cycle of TE modules involves the optimization of material for the legs, the metallization of said legs to facilitate assembly and the soldering of the functionalized legs to the bridges.

These processes require the material to undergo loads, both mechanical and thermal. As previously described in chapter 2, loading of the material will produce stress, which depending on the magnitude might be enough to damage the leg.

Stresses caused by mechanical and thermal loads will continue to be present in the module even when it is placed in working conditions, due to the principle under which TE technology works. It is therefore important to add a step in the development cycle to assess the mechanical stability of any design intended for a TE module.

First principles calculations and measurements of mechanical properties have been reported for the $\text{Mg}_2(\text{Si},\text{Sn})$ solid solution, however in most cases the information provided is very specific to a composition and only at room temperature.

Furthermore, mechanical stability of TE modules is still in the process of migrating from the trial-and-error used in previous decades to the fully digital FEM simulation. This step can decrease costs and time to a large extent, however appropriate data needs to be provided in order to produce a meaningful result.

3.2. Thesis overview

The aim of this work is to provide temperature and composition dependent mechanical properties for the solid solution series $\text{Mg}_2(\text{Si},\text{Sn})$.

Chapter 5 describes the experimental determination of hardness and fracture toughness of $\text{Mg}_2\text{Si}_{1-x}\text{Sn}_x$ solid solutions with $x = 0, 0.4, 0.5, 0.6, 0.7, 1$. The hardness values follow a linear trend between the binaries, with the Si-rich $\text{Mg}_2\text{Si}_{0.6}\text{Sn}_{0.4}$ composition deviating from the expected values.

This trend continued in the fracture toughness, as the $\text{Mg}_2\text{Si}_{0.6}\text{Sn}_{0.4}$ sample exhibited fracture toughness values above the binary Mg_2Si material. This was attributed to the

strengthening factor of the Si-rich inhomogeneities that dotted the sample due to an incomplete reaction from the elemental precursors.

Chapter 6 describes the temperature- and composition-dependent behavior of Young's and shear moduli for the same compositions as studied in chapter 5. For this part of the study, the synthesis method had to be expanded since the samples for mechanical characterization were required to be larger.

The samples showed a linear behavior both with composition and temperature, thus a bi-linear equation was proposed to predict the elastic properties (both Young's and shear modulus) of any composition within the solid solution and at any temperature up to 623 K.

Chapter 7 moves to samples with different doping concentration and species, all in the $\text{Mg}_2\text{Si}_{0.3}\text{Sn}_{0.7}$ composition. This material is close to the electronic band convergence and has good thermoelectric properties.

Room and high temperature Young's moduli are determined and temperature dependent coefficient of thermal expansion values are measured. Using these results, the potential thermally induced stress and an analytical estimation of stress under homogeneous heating are estimated.

This last chapter gives evidence of a very good compatibility of mechanical properties and thermal expansion values between n- and p-type $\text{Mg}_2(\text{Si},\text{Sn})$ and provides proof that a module entirely made of this material is mechanically feasible.

Chapter 8 includes a description of structural and mechanical properties exhibited by samples obtained using powder synthesized by different methods.

The last section of this work is reserved to present mechanical modelling using the data obtained in the course of this work, showing the positions on the pn couple assembly (n-type, p-type and Cu interconnections) where the highest stresses will be found and providing a hint at the possible zones where a failure can be expected.

4. Materials and Methods

4.1. Synthesis methods

4.1.1. Direct melting in the DSP

The synthesis method employed throughout this work is based on the work previously done by Farahi *et al.* [77] on the $Mg_2Si_{0.3}Sn_{0.7}$ thermoelectric material.

The method was expanded to cover the whole solid solution series of Mg_2Si – Mg_2Sn . The melting points of both binary compounds were used for a linear interpolation (following Vegard's law) to find the numerical estimates of melting points of several interesting points within the solid solution as shown in **Figure 4–1**. Literature results previously published show a good agreement with a linear behavior [100].

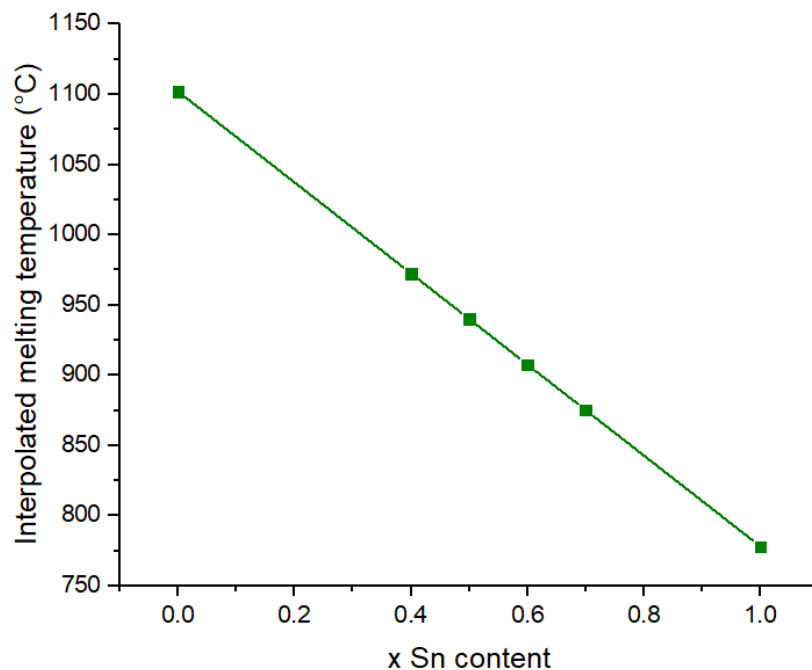


Figure 4–1 Binary literature values and interpolated solid solution melting temperature for the Mg_2Si – Mg_2Sn material system

The original method was divided in three melting cycles, each one divided in three temperature steps. This is displayed in **Table 4-1**.

Table 4-1 Details of the melting route used to synthesize $Mg_2Si_{0.3}Sn_{0.7}$

	Temperature step 1	Temperature step 2	Temperature step 3
<i>Melting step 1</i>	300 °C for 10 min	600 °C for 20 min	800 °C for 20 min
<i>Melting step 2</i>	300 °C for 10 min	600 °C for 20 min	850 °C for 20 min
<i>Melting step 3</i>	300 °C for 10 min	600 °C for 20 min	900 °C for 20 min

The temperature of the first step in each melting cycle is set above the melting point of Sn (232 °C), the second one slightly below the melting temperature of Mg (650 °C) and the last target temperature changes slightly on each sequential step.

The first step ends ~25 °C above the melting temperature of Mg_2Sn (778 °C), while the 3rd step ends ~25 °C above the melting temperature of the intended final composition $Mg_2Si_{0.3}Sn_{0.7}$ (875.2 °C). The middle step is set halfway through both of these.

In order to expand this method for the other compositions, the first melting step was always left at 800 °C, while the last step was set using the melting temperatures presented in **Figure 4–1** and adding 25 °C. The middle melting step was set to the average between 800 °C and the maximum temperature previously established.

Binaries were treated as an exception. Mg_2Sn had three steps of melting at 800 °C, while Mg_2Si had three reaction steps at 1100 °C (maximum temperature achievable with the used setup).

Once the material was obtained in an ingot form after all three cycles, it was removed from the crucible, cleaned using ethanol to remove BN contamination and transferred inside an Ar filled glovebox for further processing.

The ingot was broken into smaller pieces using hammer and chisel, then put inside a milling jar with balls in a ratio of 0.81 (one 8.1-gram ball to 10 g of material). The jar was then sealed and transferred outside to mill in a SPEX D8000 ball mill for 30 minutes.

The resulting powder was then transferred to a container inside the glovebox.

Pressing conditions, as well as structural and mechanical properties are discussed in chapter 5.

Direct melting has some advantages compared to ball milling as a synthesis method for the material system studied in this work, namely, a larger batch of material available, shorter synthesis times and comparable quality. Chapter 6 includes microstructural characterization to prove good material quality.

Several publications have been based on material synthesized with this method [101–103].

4.2. Characterization methods

4.2.1. Structural characterization

XRD

The X-Ray Diffractometer is a device that shines high energy photons (20-50 keV) onto a material in a specific angle and then collects the diffracted ones. In its most basic form, it is composed of an X-ray source, a working table and a detector, a scheme shown in **Figure 4–2**

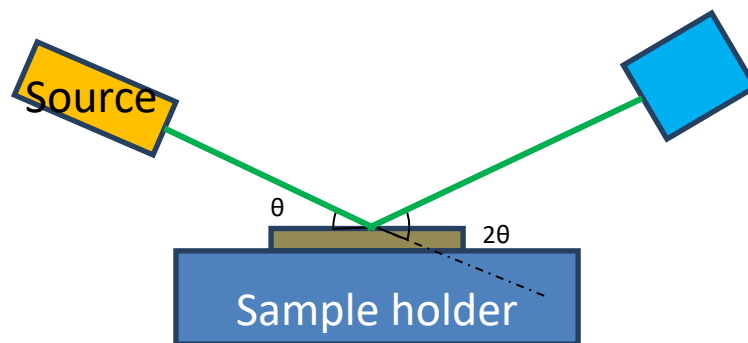


Figure 4–2 Basic X-ray diffractometer with the source, detector and sample holder.

The basics of X-ray diffraction will be presented in the following paragraphs.

Crystals, as discussed in section 2.1, are a set of atoms arranged in a periodical array. As such, they can diffract light incident on them. Since atoms are closely packed together in the lattice, a source with a very small wavelength is needed in order to be useful. The light whose photons have the wavelength in the desired range are X-rays produced with 20-50 kV.

Whenever light impacts an atom and it coherently scatters the incident energy, this energy will be redistributed in all directions with the same wavelength as the original, also called an elastic scattering [104]. When this happens in an array of atoms, like a crystalline lattice, the waves from the scattered photons from each individual atom will undergo interference. This interference can be positive or negative. If the interference is negative, it is called destructive and its intensity is reduced to a minimum. On the other hand, if the interference is positive, its intensity will increase.

At this point it is convenient to underline certain aspects from the irradiated material which will diffract light. A crystallographic plane is an imaginary construct that can be

used to explain the phenomenon of diffraction. They need to intersect all lattice points, be parallel to each other and equally spaced. Their distance is called the interplanar distance and is represented as d . Each of the planes is defined by a set of integers called the Miller indices (hkl). These will divide each lattice vector a , b and c into a specific number of parts. Such representation is better visualized in **Figure 4–3**

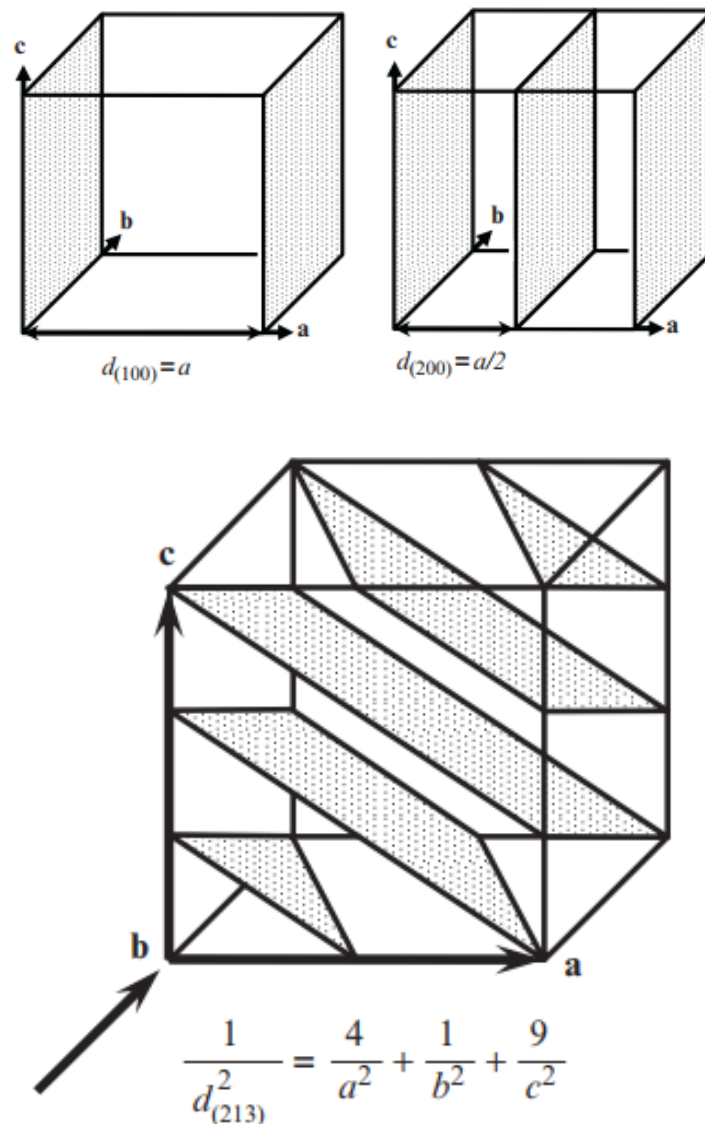


Figure 4–3 Different crystallographic planes and their representation. Taken from [104].

It can be seen from the pictures that a Miller index of 2 divides the axis in 2, while higher order miller indices will further divide the unit.

Interplanar distance is related to the angle at which the positive interference appears. This relationship is called the Bragg equation and is expressed as

$$n\lambda = 2 d \sin\theta \quad (29)$$

The interplanar distance is also related to the lattice parameter a , in the case of a cubic crystal the relationship is described by

$$d = \frac{a}{\sqrt{h^2+k^2+l^2}} \quad (30)$$

where h, k, l are the Miller indices.

This work will use XRD to identify the phases present in the material obtained. **Equation 30** will be further employed to estimate the lattice parameter to corroborate that the nominal phase is obtained.

SEM

The Scanning Electron Microscope (SEM) uses a magnetically directed fine electron beam to characterize materials. This beam is pointed at a particular spot similar to the cathode televisions, illuminating an area. The interactions of the electrons with the material will produce several effects: secondary electrons, backscatter electrons, Auger electrons, as well as continuous X-rays and characteristic X-rays [105].

Secondary electrons have usually a very low energy (3-5 eV) and are collected in a detector that is charged typically with +200 V. This kind of electrons are produced when the highly accelerated electron beam hits the surface of the specimen and an inelastic collision occurs with the nucleus of the atoms present near the surface. They are usually employed to observe the topography of the sample. this is done through counting the number of secondary electrons that arrive to the detector. Surfaces inclined in the direction of the detector will reflect more than a surface inclined away from the detector, and thus will appear brighter on the image. Materials with heavier elements will also reflect more electrons, as the probability of collision with larger nuclei is greater.

Backscatter electrons are produced similarly to the secondary electrons, in this case the collision is elastic and the electrons retain most of their energy. Thus, energy values of 16-18 keV are not uncommon. They are collected by a detector charged with -50 V, this is enough to divert any secondary electrons. Backscattered electrons travel only in straight lines, so only those that travel directly from the point of contact between the beam and the specimen, and the detector are effectively counted.

The ratio of electrons that are backscattered to the incident electrons is called the backscatter coefficient η . This coefficient varies with the atomic number Z approximately as $\eta = \frac{\ln(Z)}{6} - \frac{1}{4}$ [106].

The backscatter coefficient is thus sensitive to composition, as materials with different atomic numbers (and homogeneous mixtures of materials with different atomic percentages) will have different backscatter coefficients.

Continuous x-rays are produced when a specimen is bombarded by an electron beam with low acceleration voltage ($\sim 20\text{kV}$), the specimen will then emit a constant and continuous (within the wavelength limit) x-ray radiation. Increasing the voltage above the short wavelength limit will make the characteristic K_α and K_β lines.

EDX

Energy dispersive X-ray spectroscopy or EDX uses the characteristic K_α and K_β emission lines to identify elemental species present in the sample.

When an electron with high energy interacts with the inner K shell of electrons, some of these will be ejected, then one electron from the outer L shell will fill in this gap and in the process emit an X-ray photon of a particular energy [105]. This is called a K_α interaction, while an electron from the K shell being ejected and another electron from the M level filling in is called a K_β interaction. The energy emitted is particular to every element in the periodic table, however elements lighter than boron ($Z = 5$) cannot be identified by this method for most setups. Likewise, elements lighter than sodium ($Z = 11$) and heavier than Boron can usually only be qualitatively identified.

Fast quantification method

Since EDX mapping usually takes a long time (>20 min) Yasseri *et al.* developed a technique to use backscatter electron images as a quantification tool to estimate the x value in $\text{Mg}_2\text{Si}_{1-x}\text{Sn}_x$ [106].

The method is based on the dependency of the backscatter coefficient on the composition being studied. This coefficient can be expressed as

$$\bar{\eta} = \sum_i \eta_i C_i \quad (31)$$

Where η_i is the backscatter coefficient of the i th element present in the material, while C_i is the weight fraction of said element. This fraction, can be expressed by the atomic fractions n_i with

$$C_i = \frac{M_i n_i}{\sum_i M_i n_i} \quad (32)$$

Where M_i is the atomic mass of the i th element.

Yasseri *et al.* noticed that for the case of $Mg_2Si_{1-x}Sn_x$, the Mg atomic percentage would remain 66.66%, leaving the rest to be divided between Si and Sn, thus creating a system with only one degree of freedom, the Sn content value x . This was mentioned as a prerequisite for the method to work properly.

They proceeded to rewrite **Equation 31** using this condition and arrived to the following expression

$$\bar{\eta} = \frac{n_{Mg} M_{Mg} \eta_{Mg} + n_{Si} M_{Si} \eta_{Si} + (1 - n_{Mg} - n_{Si}) M_{Sn} \eta_{Sn}}{n_{Mg} M_{Mg} + n_{Si} M_{Si} + (1 - n_{Mg} - n_{Si}) M_{Sn}} \quad (33)$$

Since n_{Mg} is known, and M values are known for all samples, and $\eta_i = \frac{\ln(Z)}{6} - \frac{1}{4}$ [107], the only variables left unknown are n_{Si} and $\bar{\eta}$.

The mean backscatter coefficient $\bar{\eta}$ can be estimated by taking advantage of another observation done by Yasseri *et al.* The gray value (0-255) as read in the image from SEM is assumed to be related linearly with the aforementioned mean backscatter coefficient. This is approximately valid if contrast and brightness settings of the picture remain constant and a couple of other conditions are fulfilled [106]. Thus, only a couple of EDX points are needed as calibration to relate them to each other as shown in **Figure 4-4**.

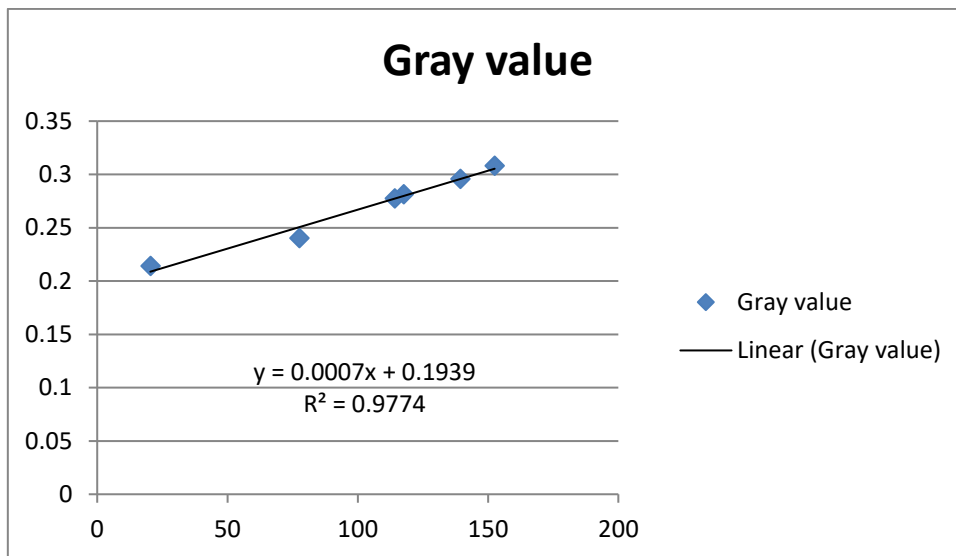


Figure 4–4 Backscatter coefficient as a function of gray value

In the end the gray value, known for each point in the image obtained through SEM, can be related to a specific n_{Si} and from there to the x Sn content value in the material $Mg_2Si_{1-x}Sn_x$.

4.2.2. Mechanical characterization

Hardness

Samples subjected to hardness measurements were tested in a Clemex hardness testing machine shown in **Figure 4–5**. The sample holder for this machine has a standard 45 mm allocation for an embedded sample.



Figure 4–5 Clemex hardness testing machine

The embedding was done on a Struers hot press using the sensitive mode, by heating at 180 °C and pressing with 25 bar for 2 minutes and then increasing to 100 bar, then holding for 5 minutes. Then a cooling process of 2 minutes was performed on the samples.

For Vickers indentation [39], samples were polished. The first step was grinding with SiC paper in an ATM Saphir grinding machine with a designation of 1200, 2500 and 4000. This grinding was done under water and at a constant speed of 150 rpm, turning the sample 90° each time the SiC paper was changed.

After the last grinding step, the samples were thoroughly dried to avoid oxidation due to the remaining water.

Four polishing steps were introduced, all of them under ethanol and for 6 minutes in an ATM Saphir sample moving machine. The first step used a diamond suspension with a particle size of 3 μm , the consecutive steps used particle sizes of 1, 0.25 and 0.05 μm .

In between the polishing steps, samples were rinsed with ethanol to remove diamonds still sticking to the surface. At the end of the last polishing step, a 10 min ultrasound bath in ethanol was performed to remove as many diamonds as possible, then a 10-minute cleaning run in the machine under pure ethanol.

Polished and clean samples were installed in the hardness testing machine, then using the included software an array of 6 x 6 indentations was made, keeping the distance between the center of each indentation at 100 μm . The standard requires a distance between centers of at least $4d$ [39]. This distance is smaller than the one programmed into the array.

Indentations done on the sample were carried out at 100 gf (0.981 N) for 10 s, the diagonals were measured with the in-built microscope and software. Crack length was also measured using this procedure, albeit with the manual correction to re-position the length markers.

Using **Equation 24**, hardness values were estimated, while fracture toughness was estimated using **Equation 22**. Both properties were estimated for each individual indentation, then the mean value and variation were estimated.

IET

The impulse excitation technique (IET) relies on the free vibration of a beam after it has been hit with a small projectile. This free vibration can be expressed by [108]

$$EI \frac{\partial^4 y}{\partial x^4} + \rho A \frac{\partial^2 y}{\partial t^2} = 0 \quad (34)$$

Where E is the Young's modulus, A the transversal area and I is the second moment of area. The second moment of area is a property of said area that reflects how points are distributed around an axis. In the case of a rectangle with base b and height h , this value is $I = \frac{b^3 h}{12}$.

Equation 34 relates the sum of total energy in the beam, both potential (deformation based) and kinetic (movement based). The wave produced by the impact will travel longitudinally through the sample causing deflection in the perpendicular direction.

The 4th order partial differential equation has a solution in the form $y(x, t) = u(x)v(t)$. This is the characteristic equation of a standing wave.

A standing wave is a phenomenon that occurs when interference happens between a wave traveling from the origin of the vibration and the wave being reflected off the end of the vibrating material. This generates a wave whose nodes (maximum amplitude) and anti-nodes (minimum amplitude) are fixed at certain positions along the length of the element. The function that governs the oscillation pattern for this kind of waves is [109]

$$y(x, t) = 2y_{\max} \sin(kx) \cos(\omega t) \quad (35)$$

where y_{\max} is the maximum amplitude of the wave, ω the angular frequency, equal to $2\pi f$, and k is the wavenumber, which denotes the number of radians traveled per unit distance and is defined as $\frac{2\pi}{\lambda}$. Note also that from **Equation 34** the relationship between them is

$$\omega^2 = \frac{EI}{\rho A} k^4 \quad (36)$$

The characteristic equation $y(x, t) = u(x)v(t)$ can be separated into the time and displacement components as follows

$$u(x) = C_1 \sin(kx) + C_2 \cos(kx) + C_3 \sinh(kx) + C_4 \cosh(kx) \quad (37)$$

$$v(t) = d_1 \sin(\omega t) + d_2 \cos(\omega t) . \quad (38)$$

Only the displacement-based equation can be subjected to boundary conditions. In order to do this, it is convenient to know what the derivatives of this equation mean.

The first derivative of **Equation 37** in relation to the length x will be the slope of the deformation, the second derivative the bending moment and the third will be the shear stress. With this information and the free vibration constraints (no bending or shear stress at both ends), it follows that $u''(0) = u'''(0) = u''(L) = u'''(L) = 0$ [109]

Substituting in **Equation 37**, it follows that

$$u''(L) = -C_1 \sin(kL) - C_2 \cos(kL) + C_3 \sinh(kL) + C_4 \cosh(kL) = 0 \quad (39)$$

$$u'''(L) = -C_1 \cos(kL) + C_2 \sin(kL) + C_3 \cosh(kL) + C_4 \sinh(kL) = 0 \quad (40)$$

$$u''(0) = -C_2 + C_4 = 0 \quad (41)$$

$$u'''(0) = -C_1 + C_3 = 0 \quad (42)$$

Substituting **Equation 41** and **Equation 42** in **Equation 39** and **Equation 40**, then rearranging in a matrix form, the expression turns to

$$\begin{bmatrix} \sinh(kL) - \sin(kL) & \cosh(kL) - \cos(kL) \\ \cosh(kL) - \cos(kL) & \sinh(kL) + \sin(kL) \end{bmatrix} \begin{bmatrix} C_1 \\ C_2 \end{bmatrix} = \begin{bmatrix} 0 \\ 0 \end{bmatrix} \quad (43)$$

Now in order to get a solution, the term $\cosh(kL) \cos(kL) = 1$ needs to be found. There is not an analytical solution, so a few numerical solutions are presented in **Table 4-3**

Table 4-3 First three numerical solutions to the vibration of a free beam

Order of solution n	$k_n L$
1	4.73
2	7.853
3	10.995

With the help of **Equation 36**, the resonant frequency can be found.

The standard ASTM E1876 includes the most important parameters and equations, based on numerical solutions to the previously presented equations, to measure both Young's modulus and shear modulus in different geometries [110]. Since this work focuses on flat pellets cut into bars, the methodology for rectangular bars of material will be presented.

The samples can be characterized at either room temperature or high temperature. The equipment used to perform the measurements for this work is an Integrated Material and Control Engineering HT1600 device. The room temperature set is composed of a sample holder with elastic supports, projectile and microphone as shown in **Figure 4-6**

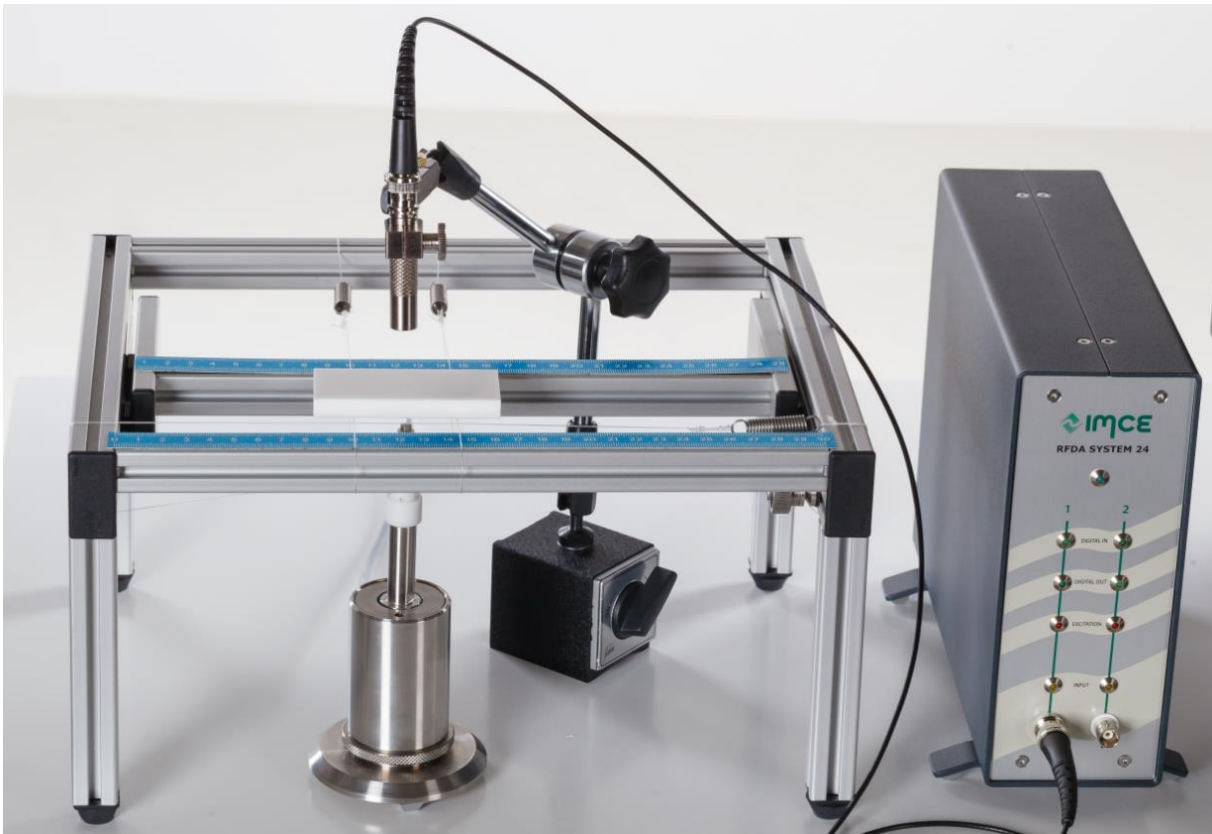


Figure 4–6 Room temperature setup for the IET

The high temperature setup consists of a ceramic sample holder with titanium supports, ceramic projectile and infrared position sensor shown in **Figure 4–7**. These elements are inside an oven that reaches 1600 °C, however without the possibility to connect a vacuum pump or perform measurements under inert atmosphere.



Figure 4-7 High temperature setup for the IET

The samples intended for IET measurements all had a length of 40-43 mm, a width of 12 mm and a thickness of 2.5-3 mm. It is paramount for a successful measurement to have parallel faces with a precision of 0.01 mm thus, after cutting the samples, they were grinded with a special sample holder to size.

The prepared samples were placed on the room temperature setup as shown in **Figure 4-8**. The distance between the supports depends on the sample size and is given by the control software when typing in the required data.

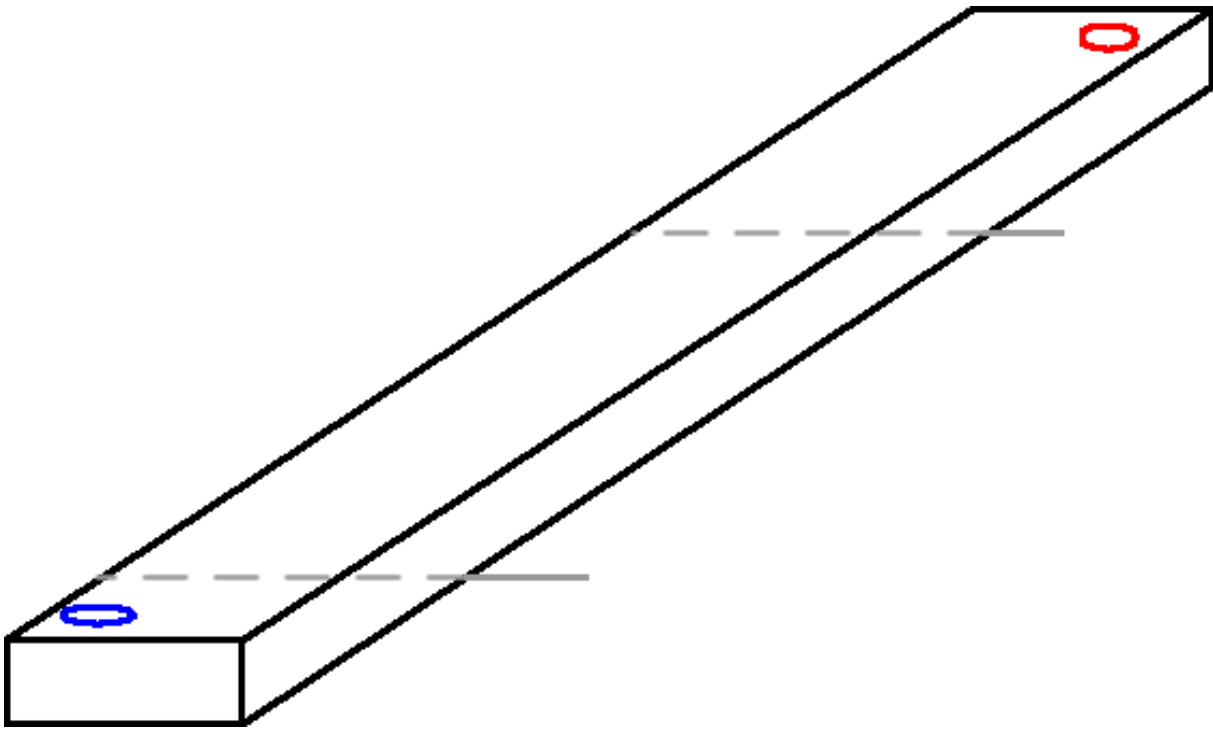


Figure 4–8 Sketch of the positioning of the supports (gray), the impact place (red) and the position of the microphone (blue) to perform a simultaneous Young's and shear modulus measurement

From this setup two sets of frequencies are registered by the microphone, a longitudinal and a transversal component. These are related to the elastic properties using the following set of equations.

Young's modulus estimation is done using

$$E = 0.9465 \left(\frac{mf^2}{b} \right) \left(\frac{L^3}{t^3} \right) T_1 \quad (44)$$

Where m is the mass of the sample, f the fundamental (lowest) frequency; b , t and L the width, thickness and length of the sample and T_1 is a correction factor for the finite thickness of the sample and the Poisson ratio expressed by .

$$T_1 = 1 + 6.585(1 + 0.0752\nu + 0.8109\nu^2) \left(\frac{t}{L} \right)^2 - 0.969 \left(\frac{t}{L} \right)^4 - \left[\frac{8.34(1+0.2023\nu+2.173\nu^2) \left(\frac{t}{L} \right)^4}{1+6.338(1+0.1408\nu+1.536\nu^2) \left(\frac{t}{L} \right)^2} \right] \cdot \quad (45)$$

The shear modulus, on the other hand is estimated by

$$G = \frac{4Lmf_t^2}{bt} B \quad (46)$$

where f_t is the transversal resonant frequency, B is a geometrical correction factor defined by

$$B = \frac{\frac{b+t}{t+b}}{4\left(\frac{t}{b}\right) - 2.52\left(\frac{t}{b}\right)^2 + 0.21\left(\frac{t}{b}\right)^6} \quad (47)$$

For testing at high temperatures, the equations remain the same, however the positioning of the sample and the area of impact change due to the sample holder being different.

Measurements at room temperature were made using 48% of the maximum energy of the projectile to avoid sample damage and to prevent the sample from moving away from the supports. This excitation was done for 0.2 s. The lower end sensitivity excitation voltage for the microphone was set at 0.05 V to pick up second harmonics for both longitudinal and transversal frequencies.

Samples measured at high temperature had the same parameters. However, the distance between nodes is fixed, as the supports cannot be moved. The only frequencies picked up are longitudinal as the transversal frequencies are dampened out. The high temperature program was set to have a maximum temperature of 623 K with a heating and cooling ramp of 1 K/min. Measurements were taken every 30 s. Upon reaching the maximum temperature, a 60 min holding time was programmed.

RUS

Resonant Ultrasound Spectroscopy is based on the forced vibration of a small sample clamped between a pair of transducers. While one of these transducers is excited to vibrate with changing frequencies, the other one is used to detect any vibration transmitted through the sample. As such mechanical vibrations are usually strongly damped, only resonance frequencies of the sample are transmitted.

Resonant frequencies of solid materials depend on sample geometry and size, as well as on the elastic moduli exhibited by the material [108]. Thus, known resonance frequencies can be used to determine elastic constants, the principle of which will be described in the following paragraphs.

Following **Equation 12**, the elastic tensor relates the stress and strain present in a three-dimensional sample. The equation that describes motion generated by the vibration is [111]

$$\frac{\partial \sigma_{ij}}{\partial x_j} = \rho \frac{\partial^2 u_i}{\partial t^2} \quad (48)$$

where u_i are the displacement vectors.

So, by substituting **Equation 12** into **Equation 48**, the new form is

$$\frac{C_{ijkl} \partial^2 u_k}{\partial x_j \partial x_l} = \rho \frac{\partial^2 u_i}{\partial t^2} \quad (49)$$

The solutions to **Equation 49** are complicated to find, however Migliori *et al.* [112] have proposed an approximation.

By taking advantage of the fact that the displacements $u_i(x_k)$ with free boundaries are both a solution to **Equation 49** and points where the derivative of the elastic Lagrangian is at a minimum, the possible solution starts to take form in

$$L = \frac{1}{2} \int (\rho \omega^2 u_i^2(r) - C_{ijkl} u_{ij}(r) u_{kl}(r)) dV \quad (50)$$

where the first half of the equation denotes the kinetic energy and the second half the strain energy.

The displacement vectors in **Equation 50** can be expanded to a different base by using appropriate expansion coefficients a_i and base functions $\phi(r)$

$$u_i = a_i \phi(r) . \quad (51)$$

The base functions are chosen depending on the geometry of the sample, thus for parallelepipeds, a good choice are the Legendre polynomials due to their orthogonality. In a more general case, the expansion can be done using basis power functions in the form $\sum_0^R \phi_\alpha = x^l y^m z^n$. Where $l + n + m = \alpha$ and R is the limiting factor of the series.

Substituting **Equation 51** in **Equation 50** yields

$$L = \frac{1}{2} \left(\rho \omega^2 a_i a_j \int (\delta_{ij} \phi(r)) dV - a_i a_j \int C_{ijkl} \phi_j(r) \phi_l(r) dV \right) \quad (52)$$

Which can be re-written in matrix form by grouping the elements in the integrals into matrices.

$$L = \frac{1}{2} (\rho \omega^2 \mathbf{a}^T \mathbf{E} \mathbf{a} - \mathbf{a}^T \mathbf{\Gamma} \mathbf{a}) \quad (53)$$

Now the minimum values of the derivative of **Equation 53** with respect to the displacement vectors can be found, which are the extreme values of the Lagrangian (where the value is 0) and the result is

$$\Gamma \mathbf{a} = \rho \omega^2 \mathbf{E} \mathbf{a} . \quad (54)$$

Equation 54 is a generalized eigenvalue problem that can be solved to find the eigenvalues ($\rho \omega^2$). The eigenvector \mathbf{a} of displacements can also be estimated, however this is not normally done as the technique is mostly interesting to estimate elastic constants.

The values of the matrices Γ and \mathbf{E} will be estimated with **Equation 52**, with the left side of the integral constituting the kinetic energy part assigned to matrix \mathbf{E} and the right side constituting the potential energy and assigned to matrix Γ .

As can be seen from **Equation 52**, the kinetic energy matrix is estimated using also the Kronecker symbol, and will thus be a diagonal matrix. If the displacements are expanded using the Legendre polynomials, the orthogonality of said expressions will make it a unity matrix.

Since the expansion series has an infinite number of elements, the matrices can also have an infinite number of elements. This is the reason behind the limiting factor R , for $R = 10$, the matrices have an element number of 858.

Using **Equation 54** and given the dimensions and density of a sample, it is possible to estimate the resonant frequencies assuming an initial value for the elastic constants by finding the eigenvalue and using $f = \omega / 2\pi$.

The estimation method *per se* is based on the comparison and fitting of the predicted resonant frequencies estimated by the process earlier described, and the measured values obtained from the transducers, shown in **Figure 4–9**.

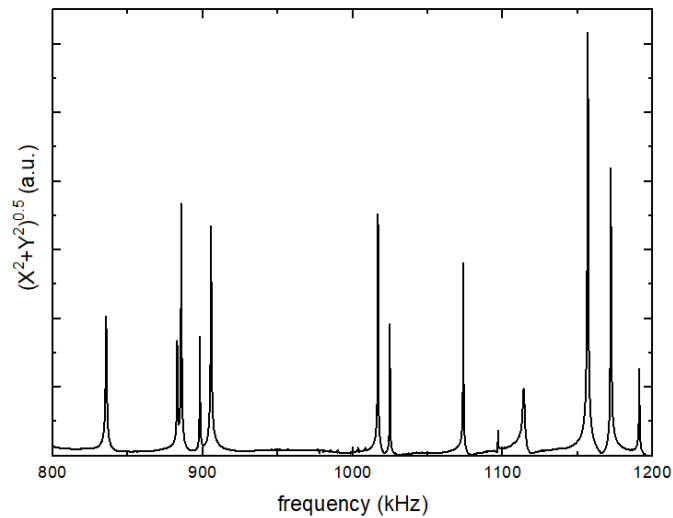


Figure 4–9 RUS spectrum showing the frequencies at which the material has a resonance against the root of the relative amplitude of displacement.

For this work, a Python script developed in the University of Applied Sciences Bremerhaven was used. The first 20-25 resonances were fit using a least squares method.

Spectra were taken using an in-house build RUS in a range of 300 kHz to 1.2 MHz. The range of frequencies was adjusted after a trial-and-error search depending on the sample geometry.

All samples presented in this work had a size of $3 \times 4 \times 5 \text{ mm}^3$, were cut using a diamond saw and ground to a parallel face, with a maximum deviation of 0.01 mm.

CTE

The coefficient of thermal expansion was measured in an analog dilatometer from Bähr Analytics.

The dilatometer is composed of a ceramic sample holder where the slabs can rest. On one side of the sample holder, two ceramic rods can be found. These are connected to the displacement sensor and are used to measure thermal expansion as shown in **Figure 4–10**. The whole assembly fits into an oven that can reach $1200 \text{ }^\circ\text{C}$. This oven is also connected to a vacuum pump, so measurements in the absence of air can be done.



Figure 4–10 Dilatometer used and close-up of the sample holder

Samples to be measured in this equipment had a size of $3 \times 5 \times 40 \text{ mm}^3$. They were measured from room temperature up to $440 \text{ }^\circ\text{C}$ (713 K) under vacuum ($<1 \times 10^{-4} \text{ bar}$) using a heating ramp of 1 K/min .

5. Hardness and Fracture Toughness of Solid Solutions of Mg_2Si and Mg_2Sn

One of the most studied mechanical properties is hardness, due to the relative ease at which it can be measured in comparison with other destructive and non-destructive characterization [36].

Several other works have reported on the hardness of thermoelectric materials $Mg_2(Si,Sn)$. However, most works focus on a single composition [74, 85, 87, 89, 91, 92, 113].

In this first paper, the relationship between Sn content in the solid solution and the hardness of said material is investigated. Additional characterization was made to measure the crack length in order to estimate fracture toughness.

The effect of Si-rich phases in the deflection and shortening of cracks is investigated through SEM and discussed. The relationship between hardness and composition is also discussed and the first ever proposedly-made Mg_2Sn hardness value is presented.

THERMOELECTRICS
AND THEIR APPLICATIONS

Hardness and Fracture Toughness of Solid Solutions of Mg₂Si and Mg₂Sn

Gustavo Castillo Hernandez^{a,b}, Mohammad Yasseri^{a,b}, Sahar Ayachi^{a,*},
Johannes de Boor^a, and Eckhard Müller^{a,b}

^a Institute of Materials Research, German Aerospace Center, Cologne, 51170 Germany

^b Institute of Inorganic and Analytical Chemistry, Justus Liebig University Giessen, Giessen, 35392 Germany

*e-mail: Sahar.ayachi@dlr.de

Received May 15, 2019; revised June 3, 2019; accepted June 3, 2019

Abstract—Thermoelectric material development typically aims at maximizing produced electrical power and efficiency of energy conversion, even though sometimes, this means adding expensive or toxic materials. An alternative is to use highly available and low toxic silicides. In fact, magnesium silicide and magnesium stannide have low densities (1.99 and 3.49 g/cm³, respectively), and exhibit good thermoelectric properties with their thermoelectric figure of merit $zT > 1$ for *n*-type and near 0.6 for *p*-type Mg₂Si–Mg₂Sn solid solutions in the range of 723–773 K. These properties turn the materials into logical candidates for light-weight and efficient thermoelectric generators (TEG). The research on their mechanical properties is however lagging behind and little effort has been put into understanding them. In this work we study the effect of the composition over the Mg₂Si–Mg₂Sn solid solution series on hardness and fracture toughness values. Hardness ranges from 2.44–5.56 GPa whereas fracture toughness values are in a tighter range (0.64–0.88 MPa m^{1/2}). However, the highest value does not belong to binary Mg₂Si but a composition within the solid solution that exhibits secondary phase nanostructuring.

Keywords: magnesium silicide thermoelectrics, fracture toughness, hardness

DOI: 10.1134/S1063782619130098

1. INTRODUCTION

Thermoelectric materials have been studied for a long time as a means of reusing waste heat and converting it to electricity. From the variety of materials available for such effect, magnesium alloys such as Mg₂Si, Mg₂Sn, and Mg₂Ge [1] started to attract attention lately because of their light weight, high abundance, negligible toxicity [2, 3] and their similar crystal structure. They form solid solutions with improved thermoelectric properties compared to the corresponding binary compounds [1, 4]. Most of the materials research is focused on improving thermoelectric properties [5–11], whereas mechanical properties received little attention to date even though they are also crucial for the development of durable thermoelectric generators (TEG).

Thermoelectric materials in TEG operation are subjected to a variety of mechanical and thermal stresses [12, 13] caused by thermal expansion coefficient mismatch, thermal cycling, and static and dynamic mechanical loads. Materials must be able to withstand such stresses for a long service life.

Mechanical loading of the material is expected to create micro-cracking within the material [14], and previous studies show that crack appearances in the

material lead to performance decay [15, 16]. Moreover, the failure mode for brittle materials has been described as the appearance and growth of such cracks [17]. Therefore it is of utmost importance to characterize the mechanical properties exhibited by thermoelectrics on-par with their energy conversion optimization.

It is commonly established that elastic properties such as Young's modulus and shear modulus, as well as the surface hardness and fracture toughness, are good indicators of a material's ability to withstand loads [18].

Magnesium silicide is a well-known material whose mechanical properties have been predicted using First principles calculations (110 GPa for the Young's modulus) [19] and experimentally studied using resonant ultrasound spectroscopy [20, 21], hardness testing [22], and compression tests [23]. These methods yielded several Young's modulus values, ranging from 76 GPa for induction melted cast material up to 145 GPa for SPS, with their corresponding hardness values of 4 and 5.4 GPa. The difference was attributed by the authors to differences in grain size, as spark plasma sintering produces very

Table 1. Pressing parameters and achieved density of compacted $\text{Mg}_2\text{Si}_{1-x}\text{Sn}_x$ pellets

$\text{Mg}_2\text{Si}_{1-x}\text{Sn}_x$	Temperature (K)	Time (s)	Density (g/cm^3)
0	1073	600	1.959
0.4	998	1800	2.597
0.5	973	1200	2.744
0.6	973	1200	2.909
0.7	973	600	3.012
1	873	600	3.425

small grains while cast material promotes grain growth.

On the other hand, research for Mg_2Sn has a more limited literature than Mg_2Si . First principles calculations for this binary show a Young's modulus of 82 GPa [24] and a hardness of 1.7 GPa [25]. The solid solutions Mg_2Si – Mg_2Sn are attracting attention due to the reported band convergence, the known miscibility gap and the increased performance compared to the binary compounds [1, 5, 7, 26]. However this interest has yet to be more widely extended towards the mechanical properties. Gao et al. report the hardness and Young's modulus in $\text{Mg}_2\text{Si}_{0.4}\text{Sn}_{0.6}$ as 3.07 GPa and 90 GPa, respectively.

This lack of information coupled with the ever better thermoelectric properties obtained for the material system prompts this work to study the mechanical properties exhibited by the binaries Mg_2Si and Mg_2Sn , as well as some compositions along the solid solution series by micro hardness testing using Vickers indentation. By describing the effect of the variation of Si:Sn ratio within the solid solutions we aim at another possibility of nano-structuring that will produce a mechanically stable and robust material for TE generation. Potential candidates from the wide range of compositions were identified through previous research [27, 28].

2. MATERIALS AND METHODS

Undoped $\text{Mg}_2\text{Si}_x\text{Sn}_{1-x}$ solid solutions with $x = 0, 0.4, 0.5, 0.6, 0.7, 1$ were synthesized by mechanical alloying, employing high energy ball milling (SPEX 8000D). The precursors (Mg turnings (Merck), Si (<6 mm, ChemPUR), Sn (<71 μm , Merck)) were weighed according to stoichiometry. 5% excess of Mg was added as to account for any type of Mg loss during processing and pressing for all compositions, except Mg_2Sn , which had 7.5% excess. The desired elements were transferred into a stainless steel jar with a ball to powder ratio 1.7:1. All the procedures were conducted inside a glove box under Ar atmosphere to prevent oxidation and contamination.

The elements were milled with constant rotation speed (~ 800 rpm) for 10–12 h until fine and homogeneous powders were obtained. Details for the complete milling are given elsewhere [27]. The obtained powders were transferred to a graphite die ($\varnothing 10$ mm) and sintered at 873–1073 K by utilizing a direct sinter press DSP 510 SE, Dr. Fritsch GmbH, Fellbach, Germany under vacuum condition ($\sim 10^{-5}$ bar), at a sintering pressure of 66 MPa with a heating rate of 1 K/s. Table 1 contains the pressing conditions for all samples as well as densities measured by Archimedes method in ethanol.

Pellets were cut using a precision diamond wire cutter (Well Diamond Wire Saws SA) into pieces measuring 2 mm in thickness and then embedded in conductive polymer in pairs. Each pair displayed both the cross section and the surface of the pellet (parallel and perpendicular to the pressing direction). The embedded samples were then ground using SiC paper and polished with ethanol based diamond suspension down to a polish particle size of 0.25 μm .

Hardness testing was done using a Vickers micro hardness machine (Clemex SMT-X7) for 10 s and 0.98 N. Each sample was indented 20 times for each surface orientation (parallel and perpendicular to pressing) for a total of 40 indentations per composition. Imprint analysis was done using the in-built microscope and software, and calculations were done following Oliver and Pharr methodology [29] using Eq. (1) to estimate sample hardness

$$H = \frac{1.854P}{(2d)^2}, \quad (1)$$

where P is the load exerted by the machine and d being the half length of the plastic imprint left by the indentation. Fracture toughness was estimated using Eq. (2):

$$K_{Ic} = \frac{\zeta(E/H)^{1/2}P}{c^{3/2}}, \quad (2)$$

where ζ is a geometrical constant estimated to be 0.016 for the Vickers indenter by previous research [29], and H is the hardness obtained from Eq. (1). P is the load, c is the half average crack length measured from the center of the imprint, and E is the Young's modulus estimated in this work by linearly interpolating between theoretical values obtained from previous first principles calculations [19, 24] as shown in Table 2. It is assumed that a linear behavior will be dominant since previous research shows this trend for other properties [30].

Microstructure analysis was carried out using a Scanning Electron Microscope Zeiss Ultra 55 SEM with a Zeiss QBSE detector, also equipped with an Oxford energy dispersive X-ray (EDX) detector (PentaFET $\times 3$).

3. RESULTS

As first observation in this study, we found no significant change between measurements done on the cross section and the base face of the pellet as shown in Fig. 1. This is mainly because of the cubic isotropic nature of the material. Therefore results shall be addressed as a function of composition only.

Using the in-built software, each of the diagonals in every indentation was measured. Afterwards hardness values were calculated using the known force applied. Figure 2 shows an optical micrograph of an indentation showing the typical radial crack appearance at the tips of the imprint.

Given the brittle nature of the material, scarce strengthening effects are noted in Fig. 2. Intrinsic strengthening, acting ahead of the crack tip is seldom found in ceramic materials since it relies on the material's ability to plastically deform, therefore weak when present. It is however possible to induce crack deviation by using secondary phases or by reducing grain size [31].

As expected from the known behavior in other properties like lattice parameter [30], hardness has a mainly linear behavior with the increase of the Sn content over the solid solution as shown in Fig. 3; except for the points $x = 0.5$ and 0.4 . As the material forms by diffusion of Si into the Mg_2Sn matrix; the secondary phases are smaller in size and number in low Si content samples. However, increasing the Si:Sn ratio also increases this Si-rich areas in both size and number, also increasing both the hardness and fracture toughness.

Figure 4 shows the fracture toughness of some compositions along the solid solution series. Here the difference between the binaries is smaller compared to hardness and is related to the tradeoff between the

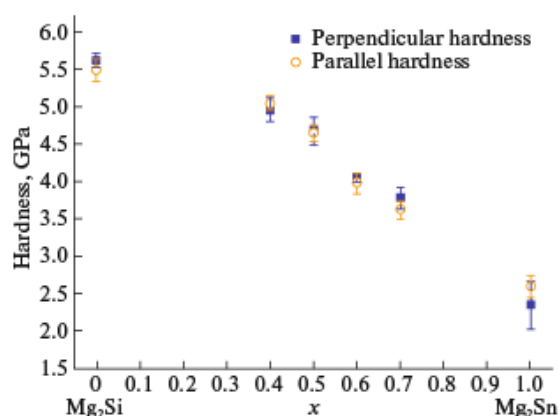


Fig. 1. Comparison between all compositions and the directional (parallel and perpendicular to pressing direction) characterization.

Table 2. Young's modulus used to estimate fracture toughness

$Mg_2Si_{1-x}Sn_x$, X	Young's modulus (GPa)
0	110
0.4	98.8
0.5	96
0.6	93.2
0.7	90.4
1	80

amounts of plastic deformation as compared to the crack length.

These values have a peculiar behavior around $x = 0.5-0.4$ which can be attributed to the strengthening effect exerted by the Si rich areas in the material as shown in Fig. 5.

The area around EDX point 3 has the composition $Mg_2Si_{0.6}Sn_{0.4}$; while two areas with clear contrast difference can be seen near points 1 and 4. These regions have composition that ranges between $Mg_2Si_{0.75}Sn_{0.25}$ (dark gray area) and $Mg_2Si_{0.51}Sn_{0.48}$ (light gray). The dark areas visible near point 2 are $Mg_2Si_{1-x}Sn_x + MgO$, and the dark spots in the center of the picture are MgO particles.

4. DISCUSSION

Deviation from linearity in hardness with composition (Fig. 3) can be expected in non-uniform material with secondary phases. SEM images show regions within the homogenous material that retain a higher content of silicon that was not diffused into the matrix during the high energy ball mill and the following current assisted sintering. Previous reports also show an influence of both milling time and sintering parameters on the thermoelectric properties [27, 30]. Prevalence of these Si rich areas was observed with lower milling time in the same material system where they did not cause any significant change in either the thermal conductivity or electrical properties. Their influence on the mechanical properties is however higher due to the stress fields they produce around the area where they are located.

DSP sintered materials show a slightly larger grain size compared to SPS reports [32] and the mechanical

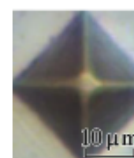


Fig. 2. Optical micrograph of an Mg_2Si indentation.

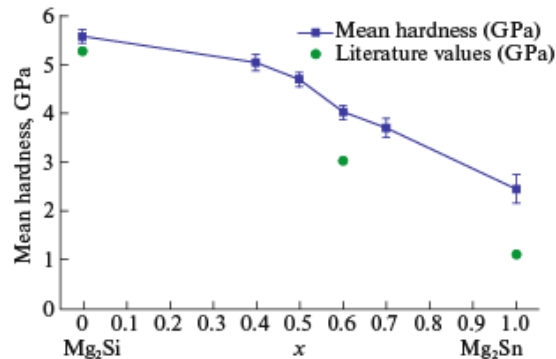


Fig. 3. Measured hardness values (black squares) compared to literature values (green circles) for Mg₂Si [20], Mg₂Sn [24], and Mg₂Si_{0.4}Sn_{0.6} [25].

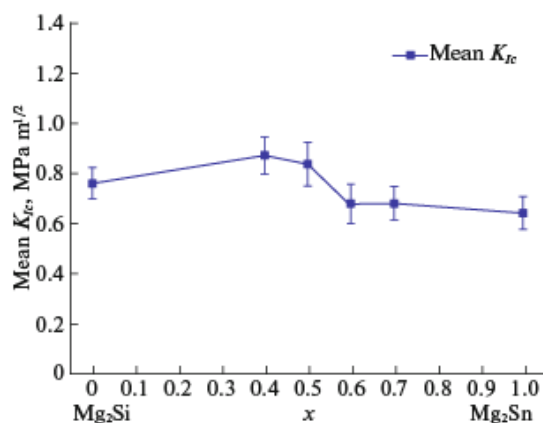


Fig. 4. Fracture toughness over the solid solution series as a function of composition.

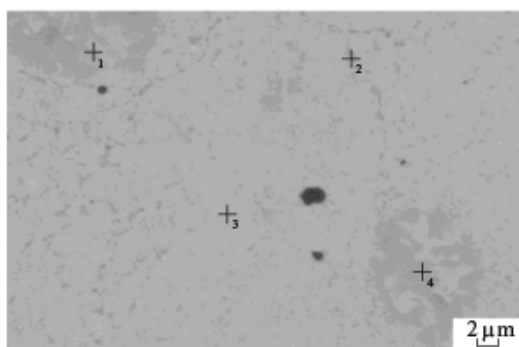


Fig. 5. SEM picture and EDX points of a nominally Mg₂Si_{0.6}Sn_{0.4} sample with secondary phases present.

properties decrease accordingly. However, they are better compared to cast material with a typical large grain size [23]. Therefore material synthesis and pressing plays a critical role in the properties exhibited by thermoelectric materials.

Literature values for the hardness of the binary Mg₂Si vary with a low estimate being 3.96 GPa [23], while most values are around 5 GPa [20–22, 32]. In our case, the value of 5.56 ± 0.14 GPa is within a reasonable range. Previous studies have shown that hardness is influenced by grain size; and that smaller grain size results in a higher hardness value. This is related to the amount of plastic deformation allowed by the system. In fact, smaller grains have lower possibility to deform further and are restrained from moving, therefore hardening the material.

Mg₂Sn literature values for hardness are scarce and one study [33] gives a value of 1.17 GPa. Our measured value, however, was comparatively higher with 2.44 ± 0.28 GPa, which is a 100% increase from the literature value. This after mentioned study was done on a magnesium alloy with tin inclusions and not an intentionally synthesized binary stannide for thermoelectric applications, which might be the cause of the deviation.

Fracture toughness values were obtained using the interpolated value for Young's modulus from first principles calculations. It is possible that a variation in the concentration of secondary phases within the material influenced the elastic properties. Therefore this is another source of variation for the results presented in this work.

Values for K_{Ic} in the binary Mg₂Si range between 0.8 and 1.7 MPa m^{1/2} for pristine material [20–22, 32] where our material falls within the lower part of the interval at 0.76 ± 0.06 MPa m^{1/2}. Current-assisted sintering produces larger grains (1–10 μm) compared to an SPS previous report [32] and it is known that a smaller grain size prevents crack growth [22, 31] which might be behind this lower value.

In pristine binary Mg₂Sn, there are, to the best of our knowledge, no values reported for fracture toughness. Our samples exhibited a value of 0.64 ± 0.06 MPa m^{1/2}. This value is very similar to Mg₂Si, which might be caused by the lower brittleness exhibited by the material. The work being applied to the material by the indentation can either be released as plastic deformation (imprint) or as new surfaces (cracks). The value for Young's modulus is reduced in a similar ratio to the hardness, thus, according to Eq. (2), the fracture toughness will remain comparatively high.

Crack lengths for both silicide (22.7 ± 2.1 μm) and stannide (26.99 ± 3.54 μm) remained similar. The imprint size, however, was not. Magnesium silicide

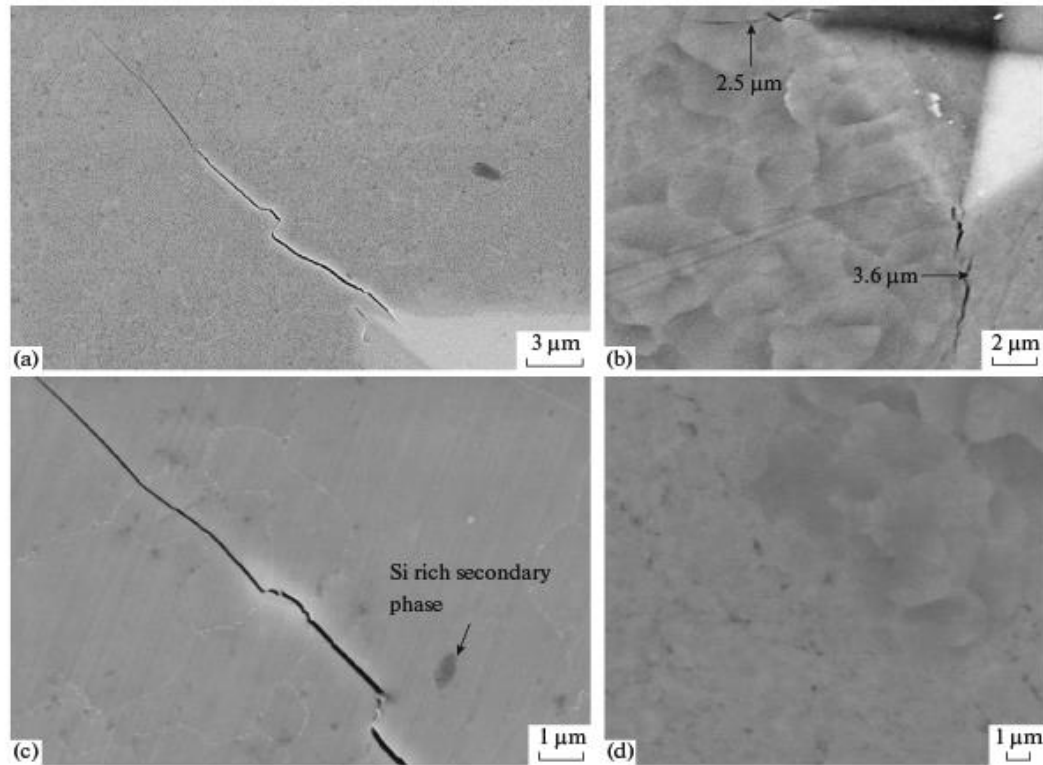


Fig. 6. SEM pictures showing the comparison between a homogenous $\text{Mg}_2\text{Si}_{0.3}\text{Sn}_{0.7}$ material (a, c) compared to an $\text{Mg}_2\text{Si}_{0.6}\text{Sn}_{0.4}$ material with secondary phases (b, d). Note the difference in crack length.

has a noticeably smaller residual deformation ($1.80 \pm 0.02 \mu\text{m}$) compared to the magnesium stannide ($27.41 \pm 0.46 \mu\text{m}$).

Brittle materials like magnesium silicide-stannide have a very low plastic deformation capability and therefore, the only way to strengthen them intrinsically is to include flaws in the lattice. A change in direction due to a pinned stress field caused by the grain boundary is the main strengthening factor in a single phase material with no inclusions [31] (Fig. 6c). The coexistence of several phases in the material strengthens it against crack growth by this very same method, as the crack is forced to go through several stress fields (phase boundaries) caused by the phase mismatch (Fig. 6b).

Magnesium silicide-stannide ranks somewhere in the middle within other thermoelectric material families regarding hardness values. They are clearly above tellurides which exhibit a value ranging from 0.7–1.5 GPa [34, 35], have a comparable hardness value to Skutterudites (3–7 GPa) [35, 36], and are below half-Heuslers which can surpass 10 GPa [35, 37].

When comparing fracture toughness exhibited by different thermoelectric materials, we find the Mg_2Si – Mg_2Sn system to be at the lower end, having a lower value than half-Heuslers (1.8 – $2 \text{ MPa m}^{1/2}$) [37] and tellurides ($1.1 \text{ MPa m}^{1/2}$) [38]. However, they are comparable to Skutterudites (0.4 – $0.8 \text{ MPa m}^{1/2}$) [39].

5. CONCLUSIONS

Different compositions of magnesium silicide-magnesium stannide solid solutions were successfully synthesized and characterized. They exhibited medium to low hardness and low fracture toughness when compared to other thermoelectric materials. In this work, the first ever report of the fracture toughness in magnesium stannide binary compound was discussed.

Magnesium silicide is a very brittle material with a high hardness value, whereas magnesium stannide has a lower brittleness. However, both have similar fracture toughness due to the fact that Mg_2Sn is capable of more plastic deformation compared to Mg_2Si .

Considerable strengthening effect of secondary phases was observed in higher silicon content samples. This was credited to interphase stress shortening and deflecting crack growth. Secondary phases that do not interfere with thermoelectric properties can thus exert a beneficial effect of a shortened material preparation.

Further work is needed to strengthen the material through microstructure optimization or nano-inclusions, and complement the low density and low toxicity properties that make it an attractive TE material. Mechanical properties should be tailored to the application desired. This in turn, prompts the scientific community to deepen the knowledge in the subject, to be able to engineer the material to specification both in thermoelectric and mechanical properties.

This study shed light on the material mechanical properties and its place among other potential candidates for TE generator materials in relation to how well they manage crack nucleation and growth.

ACKNOWLEDGMENTS

The authors would like to thank Dr. Ulises Alfaro Mercado and Reinhard Sottong for the technical support, as well as Alexander Francke for sample preparation and Dr. Alexander Burkov for the kind invitation to the conference. We would also like to acknowledge the endorsement for the DLR executive Board Members for Space Research and Technology, as well as the financial support from the Young Research Group Leader Program.

FUNDING

Financial support for M.Y is provided by the DFG via the GRK (Research Training Group) 2204 "Substitute Materials for Sustainable Energy Technologies". GCH would like to thank the Mexican science and technology council (CONACYT) and the German academic exchange service (DAAD) for the PhD fellowship.

REFERENCES

- J. Mao, H. S. Kim, J. Shuai, Z. H. Liu, R. He, U. Saparamadu, F. Tian, W. S. Liu, and Z. F. Ren, *Acta Mater.* **103**, 633 (2016).
- S. LeBlanc, S. K. Yee, M. L. Scullin, C. Dames, and K. E. Goodson, *Renewable Sustainable Energy Rev.* **32**, 313 (2014).
- R. Santos, S. A. Yamini, and S. X. Dou, *J. Mater. Chem. A* **6**, 3328 (2018).
- H. Kasai, L. R. Song, H. L. Andersen, H. Yin, and B. B. Iversen, *Acta Crystallogr., Sect. B* **73**, 1158 (2017).
- M. I. Fedorov, V. K. Zaitsev, and G. N. Isachenko, *Solid Compd. Trans. Elem.* **170**, 286 (2011).
- V. K. Zaitsev, M. I. Fedorov, E. A. Gurieva, I. S. Eremin, P. P. Konstantinov, A. Y. Samunin, and M. V. Vedernikov, *Phys. Rev. B* **74**, 045207 (2006).
- V. K. Zaitsev, M. I. Fedorov, E. A. Gurieva, I. S. Eremin, P. P. Konstantinov, A. Y. Samunin, and M. V. Vedernikov, in *Proceedings of the 24th International Conference on Thermoelectrics ICT'2005*, p. 189.
- U. Saparamadu, J. de Boor, J. Mao, S. W. Song, F. Tian, W. S. Liu, Q. Y. Zhang, and Z. F. Ren, *Acta Mater.* **141**, 154 (2017).
- J. de Boor, C. Compere, T. Dasgupta, C. Stiewe, H. Kolb, A. Schmitz, and E. Mueller, *J. Mater. Sci.* **49**, 3196 (2014).
- J. de Boor, S. Gupta, H. Kolb, T. Dasgupta, and E. Muller, *J. Mater. Chem. C* **3**, 10467 (2015).
- B. Klobes, J. de Boor, A. Alatas, M. Y. Hu, R. E. Simon, and R. P. Hermann, *Phys. Rev. Mater.* **3** (2019).
- T. Sakamoto, T. Iida, Y. Ohno, M. Ishikawa, Y. Kogo, N. Hirayama, K. Arai, T. Nakamura, K. Nishio, and Y. Takahashi, *J. Electron. Mater.* **43**, 1620 (2014).
- G. Skomedal, L. Holmgren, H. Middleton, I. S. Eremin, G. N. Isachenko, M. Jaegle, K. Tarantik, N. Vlachos, M. Manoli, T. Kyratsi, D. Berthebaud, N. Y. D. Truong, and F. Gascoin, *Energy Convers. Manage.* **110**, 13 (2016).
- T. J. Lu and N. A. Fleck, *Acta Mater.* **46**, 4755 (1998).
- E. D. Case, *J. Electron. Mater.* **41**, 1811 (2012).
- A. B. Zhang, B. L. Wang, J. Wang, J. K. Du, and C. Xie, *J. Appl. Phys.* **121** (2017).
- J. P. Singh, C. Shih, and D. P. H. Hasselman, *J. Am. Ceram. Soc.* **64**, C106 (1981).
- M. Edwards and K. Brinkfeldt, in *Proceedings of the 14th International Conference on Thermal, Mechanical and Multi-Physics Simulation and Experiments in Microelectronics and Microsystems (Eurostme)*, 2013.
- Z. W. Huang, Y. H. Zhao, H. Hou, and P. D. Han, *Phys. B (Amsterdam, Neth.)* **407**, 1075 (2012).
- R. D. Schmidt, E. D. Case, J. Giles, J. E. Ni, and T. P. Hogan, *J. Electron. Mater.* **41**, 1210 (2012).
- R. D. Schmidt, X. F. Fan, E. D. Case, and P. B. Sarac, *J. Mater. Sci.* **50**, 4034 (2015).
- S. Muthiah, R. C. Singh, B. D. Pathak, and A. Dhar, *Mater. Res. Express* **4**, (2017).
- V. Milekhine, M. I. Onsoien, J. K. Solberg, and T. Skaland, *Intermetallics* **10**, 743 (2002).
- W. B. W. L. C. Davis, and G. C. Danielson, *J. Phys. Chem. Solids* **28**, 9 (1967).
- P. Gao, I. Berkun, R. D. Schmidt, M. F. Luzenski, X. Lu, P. B. Sarac, E. D. Case, and T. P. Hogan, *J. Electron. Mater.* **43**, 1790 (2014).
- X. D. Luo, H. Liu, W. L. Xu, and Y. X. Zhu, *Adv. Res. Mater. Sci., Environ. Sci. Comput. Sci.* **886**, 71 (2014).
- A. Sankhla, A. Patil, H. Kamila, M. Yasserli, N. Farahi, E. Mueller, and J. de Boor, *Appl. Energy Mater.* **1**, 11 (2018).
- H. Kamila, P. Sahu, A. Sankhla, M. Yasserli, H. N. Pham, T. Dasgupta, E. Mueller, and J. de Boor, *J. Mater. Chem. A* **7**, 1045 (2019).

29. W. C. Oliver and G. M. Pharr, *J. Mater. Res.* **7**, 1564 (1992).
30. H. Kamila, M. Yasseri, Hoang, N. Farahi, J. de Boor, and E. Mueller, *Mater. Today Proc.* **8**, 9 (2019).
31. M. E. Launey and R. O. Ritchie, *Adv. Mater.* **21**, 2103 (2009).
32. P. Vivekanandhan, R. Murugasami, and S. Kumaran, *Mater. Lett.* **231**, 109 (2018).
33. B. H. Kim, J. J. Jeon, K. C. Park, B. G. Park, Y. H. Park, and I. M. Park, *Int. J. Cast Met. Res.* **21**, 186 (2008).
34. A. Schmitz, J. de Boor, K. Mull, and E. Muller, *J. Mater. Sci.* **51**, 6933 (2016).
35. R. He, S. Gahlawat, C. F. Guo, S. Chen, T. Dahal, H. Zhang, W. S. Liu, Q. Zhang, E. Chere, K. White, and Z. F. Ren, *Phys. Status Solidi A* **212**, 2191 (2015).
36. L. Zhang, G. Rogl, A. Grytsiv, S. Puchegger, J. Koppensteiner, F. Spieckermann, H. Kabelka, M. Reinecker, P. Rogl, W. Schranz, M. Zehetbauer, and M. A. Carpenter, *Mater. Sci. Eng. B* **170**, 26 (2010).
37. G. Rogl, A. Grytsiv, M. Gurth, A. Tavassoli, C. Ebner, A. Wunschek, S. Puchegger, V. Soprunyuk, W. Schranz, E. Bauer, H. Muller, M. Zehetbauer, and P. Rogl, *Acta Mater.* **107**, 178 (2016).
38. L. D. Zhao, B. P. Zhang, J. F. Li, M. Zhou, W. S. Liu, and J. Liu, *J. Alloys Compd.* **455**, 259 (2008).
39. J. Eilertsen, M. A. Subramanian, and J. J. Kruzic, *J. Alloys Compd.* **552**, 492 (2013).

6. Room and high temperature mechanical properties of Mg_2Si , Mg_2Sn and their solid solutions

Following the characterization of composition dependent hardness, the next step was to continue the measurement of mechanical properties in the $Mg_2(Si,Sn)$ material.

A relatively new method called Impulse Excitation Technique was used to estimate the room and high temperature Young's modulus in the solid solution. These measurements were compared to the more established Resonant Ultrasound Spectroscopy similar to previous studies comparing both techniques [114].

Following the composition and temperature dependent results, a new equation to predict both Young's and shear modulus was proposed. With the help of said equation and a quick phase determination process proposed earlier by Yasseri *et al.* [106] the effective Young's modulus of a composite $Mg_2(Si,Sn)$ material with different Si-content was estimated. These values were in turn, very similar to the measured values in all samples.



Contents lists available at ScienceDirect

Journal of Alloys and Compounds

journal homepage: <http://www.elsevier.com/locate/jalcom>

Room and high temperature mechanical properties of Mg₂Si, Mg₂Sn and their solid solutions



Gustavo Castillo-Hernandez^{a,b,*}, Mohammad Yasseri^{a,b}, Benedikt Klobes^c, Sahar Ayachi^a, Eckhard Müller^{a,b}, Johannes de Boor^{a,**}

^a Institute of Materials Research, German Aerospace Center, 51170, Cologne, Germany

^b Institute of Inorganic and Analytical Chemistry, Justus Liebig University Giessen, Heinrich-Buff-Ring 17, 35392, Giessen, Germany

^c University of Applied Sciences Bremerhaven, Bremerhaven Institute of Nanotechnology, An der Karlstadt 8, 27568, Bremerhaven, Germany

ARTICLE INFO

Article history:

Received 9 March 2020

Received in revised form

8 June 2020

Accepted 23 June 2020

Available online 8 July 2020

Keywords:

Thermoelectric
Mechanical properties
Magnesium silicide
Magnesium stannide
Mg₂Si
Mg₂Sn

ABSTRACT

Knowledge of the mechanical properties of thermoelectric materials at high temperature is required for the modelling and optimization of a thermoelectric generator under application conditions. We present room and high temperature characterization of Young's modulus for Mg₂Si, Mg₂Sn and their solid solutions establishing a linear dependence, both on composition and on temperature.

Through the comparison of Resonant Ultrasound Spectroscopy and free vibration techniques, we measure the elastic moduli with high precision. The comparison of our results ($E = 110$ GPa for Mg₂Si and 78 GPa for Mg₂Sn) to first principles calculations and experimentally reported data shows good agreement. Additionally, by estimating the Poisson ratio, we calculate the temperature-dependent shear modulus G and finally provide a simple bilinear function for Young's and shear moduli as a function of temperature and composition.

© 2020 Elsevier B.V. All rights reserved.

1. Introduction

Thermoelectric generators (TEG) for thermal-to-electric energy conversion in their most basic form consist of both n- and p-type doped semiconductor materials (commonly referred to as legs) electrically connected by a metallic bridge. Such devices have attracted the attention of researchers due to their inherent advantages such as simple construction, free scalability, lack of moving parts, and reduced maintenance cost and effort [1–3]. Their ability to perform under vacuum and in the absence of light also makes them perfect candidates for space mission energy supply, as exemplified by the Voyager missions and numerous further deep space and lander missions from the 1970's [4]. TEGs can also be used in/are also candidates for terrestrial applications, such as

waste heat recovery in industrial facilities, combustion engines and mobile or autarkic current supply e.g. for sensors.

Current TEG technology is mainly based on rare or toxic materials such as Te or Sb, which makes the “en masse” application of thermoelectric generators unattractive [5]. In this context, research on light, inexpensive, and more importantly environmentally benign materials becomes a priority to facilitate the technology's inclusion into the market. One of such materials is the Mg₂(Si,Sn) system, composed of a solid solution of Mg₂Si and Mg₂Sn. Both binaries and their solid solutions form a family of light and highly available (therefore inexpensive) materials [1,2].

Mg₂(Si,Sn) has shown a good thermoelectric performance, as indicated by the high dimensionless figure of merit zT defined as $zT = S^2 \alpha \kappa^{-1} T$, where S , α , κ , and T represent Seebeck coefficient, electrical conductivity, total thermal conductivity, and absolute temperature, respectively. n-type Mg₂(Si,Sn) achieved a $zT > 1.2$ at temperatures close to 973 K [6–12], while p-type materials reached 0.55 around the same temperatures [11,13–17].

Several other factors besides TE performance have to be taken into account when building a functional generator, such as the electrode that connects the functional material to the electrical bridge. Further progress has been made in this regard with possible

* Corresponding author. Institute of Materials Research, German Aerospace Center, 51170, Cologne, Germany.

** Corresponding author.

E-mail addresses: Gustavo.castillo-hernandez@dlr.de (G. Castillo-Hernandez), Mohammad.yasseri@dlr.de (M. Yasseri), bklobes@hs-bremerhaven.de (B. Klobes), Sahar.ayachi@dlr.de (S. Ayachi), Eckhard.mueller@dlr.de (E. Müller), Johannes.deBoor@dlr.de (J. de Boor).

candidates already selected and tested. Cu and Ag seem to be feasible options for the Sn-rich solid solutions given their compatible coefficient of thermal expansion (CTE) values [18,19], while Ni appears to be a solution for binary Mg_2Si [20–22].

The selection of the TE material, the contacting electrode and the bridging electrical conductor is not trivial. In fact, CTE mismatches between these materials will produce thermal stresses at working temperature that could potentially threaten the mechanical integrity of the module. Using the same material system for both n- and p-type legs is one way to reduce the CTE mismatch; it will, however, not completely eliminate the issue. Therefore, thermal stress and its potentially destructive effects cannot be avoided [23].

It is, thus, imperative to know the room and high temperature mechanical behavior of the materials in order to design the module in a way that minimizes possible mechanical failure.

The mechanical properties of the binary magnesium silicide were predicted using first principles calculations, obtaining a value of 110 GPa for the Young's modulus [24,25], and were measured using several techniques. Among these techniques, we find dynamic methods like Resonant Ultrasound Spectroscopy (RUS) and traditional static characterizations like micro-hardness and compression tests [26–29]. These previous studies reported a wide range of values for the elastic behavior of Mg_2Si , ranging from 76 GPa to 145 GPa, with hardness values ranging from 4 to 5.4 GPa. The authors put great emphasis on the effect of grain size distribution on the mechanical properties in these studies.

In contrast, reported data on Mg_2Sn is more limited. First principles calculations for this binary yield a Young's modulus of 67–82 GPa [25,30,31], and an experimental hardness value of 1.7 GPa was reported [12].

Recent work in our research group was done on the mechanical properties of the solid solutions $Mg_2Si_{1-x}Sn_x$ (with $x = 0-1$), finding a mostly linear influence of the Sn content on the hardness. However, $Mg_2Si_{0.6}Sn_{0.4}$ showed an increased value compared to what the interpolation between binaries suggests and above the linear behavior characteristic in the low Si content material. Such behavior was attributed to secondary phases strengthening the material [32]. Room temperature measurements of the elastic constants have also been carried out on the solid solution [33], and the study found a strengthening of the material as the Si amount increased. However, the composition $Mg_2Si_{0.4}Sn_{0.6}$ showed diminished elastic properties, which was attributed by the authors to a possible connection between electronic and vibrational properties.

On the other hand, high temperature values are scarce. One recent paper reported the Young's modulus of the $Mg_2Si_{0.6}Sn_{0.4}$ material [34] where a linear decrease with temperature was found. The material had a reduction of ~10% in its total elasticity during the heating phase; however, no further information was given on the cooling phase.

One complication of the Mg_2Si – Mg_2Sn material system is the miscibility gap, which, depending on the author, can be found in different compositional ranges [35,36]. The gap also depends heavily on temperature, as it widens at lower temperatures. It was observed in previous studies that homogenized samples decompose into separate phases after being annealed. Due to the phase separation at high temperatures, it is of utmost importance to know the material stability while being subjected to temperature.

Therefore, this work focuses on the microstructural and Young's modulus characterizations of $Mg_2Si_xSn_{1-x}$ materials ($x = 0-1$), at both room and high temperatures using different techniques: Resonant Ultrasound Spectroscopy (RUS) and Impulse Excitation Technique (IET).

Table 1
Sintering parameters for $Mg_2Si_{1-x}Sn_x$.

x	Pressure (MPa)	Temperature (°C)	Time (min)
0	66	800	10
0.4	66	750	30
0.5	66	700	20
0.6	66	700	20
0.7	66	700	10
1	66	600	10

2. Materials and methods

Undoped $Mg_2Si_{1-x}Sn_x$ samples were synthesized using commercially available precursor elements, namely Mg turnings (Merck), Si chunks (<6 mm, ChemPur), and Sn (<71 μ m, Merck) with high purity >99.5%. Elemental materials were put in a graphite crucible and melted into an ingot using a previously described method [11]. The obtained ingot was then ball milled in a SPEX 8000D Shaker Mill for an hour to obtain a homogenous powder, and pellets were synthesized by pressing the powder in a direct current press DSP 510 SE from Dr. Fritsch GmbH. The temperature and time used to press each composition have been reported previously [6,11,19,36,37] and are detailed in Table 1. These reports showed very good thermoelectric properties for both n and p-type materials. Samples of compositions $Mg_2Si_{1-x}Sn_x$ $x = 0.4, 0.5, 0.6$ require extra time for pressing conditions due to the slow process of phase formation. It was previously observed that if Mg_2Sn and Mg_2Si formations are competing, Mg_2Sn forms first and then Si diffuses slowly into the matrix [6,36].

The pellets obtained measured 50 mm in diameter and ~3 mm in thickness. They were then subsequently cut using a diamond disc saw (DISCO Co) into pieces measuring $12 \times 45 \times 3.0$ mm for the IET experiments and $3.0 \times 4.0 \times 5.0$ mm for the RUS characterization. Two separate samples were cut and tested for each composition and technique. The remaining circular segments were embedded in conductive resin, grinded with SiC paper and polished with diamond suspension for microstructure analysis.

Resonant ultrasound spectroscopy (RUS) utilizes mechanical resonance frequencies of a given sample to determine the elastic tensor of a material. Parallelepiped shaped polycrystalline samples of 60 mm³ were investigated by a custom made spectrometer similar to the setup described in Ref. [38]. Using the first 20 resonances, C_{11} and C_{44} were determined following the analytical scheme described in Refs. [39] and implemented in Python. In all cases, the root-mean-square residual between calculated and measured resonance frequencies was below 0.5%.

Independent elastic constants C_{11} , C_{12} and C_{44} [40] characterized by RUS can then, be related to the elastic moduli. The bulk B modulus can be estimated by the relationship

$$3B = C_{11} + 2C_{12} \quad (1)$$

The shear modulus G can be described by Equation (2) for materials with cubic crystal structure.

$$G = C_{44} \quad (2)$$

Finally Young's modulus can be estimated using Equation 3

$$E = \frac{9B \cdot G}{3B + G} \quad (3)$$

RUS experiments were carried out in a self-built setup at room temperature sweeping frequencies between 300 kHz and 1 MHz. Characterization was done repeatedly while changing the position of the sample between transducers to maximize the amount of

resonant frequencies registered for the fitting.

The Impulse Excitation Technique (IET) relies on the free vibration of a bar shaped sample set on top of supports. A microphone picks up the resulting vibration frequency. A simple set of equations are then used to compute the Young's and shear modulus.

$$E = 0.9465 \frac{mF_l^2 L^3}{b t^3 T_1} \quad (4)$$

$$G = \frac{4LmF_t^2}{bt} \frac{B}{1-A} \quad (5)$$

Where m is the mass of the sample, L , b and t are the length, width and thickness respectively; F_l is the longitudinal resonant frequency and F_t the transverse resonant frequency. T_1 , B and A are all geometrical correction factors described in the standard ASTM E 1876 – 01 [41]. In such a case, it is important to ensure that the fundamental (lowest resonant frequency) has been identified. The ratio to higher order frequencies can be used to determine if the fundamental is present, and whether we measured longitudinal or transverse. For longitudinal frequencies the ratio to the fundamental is 1:2.757:5.404:8.933 ...; meanwhile, for the transverse, the relationship is simpler, 1:2:3:4 ...

Slight variations in the thickness of the samples during preparations alter the precision of the method following Eq. (4), therefore we grinded all samples to get a $\Delta E < 1$ GPa.

IET characterization was done employing a system from IMCE NV at room temperature with an automatic excitation time of 30 ms. High temperature measurements were done in air until 623 K, and then the sample was held at this temperature for 30 min. Heating and cooling ramp was 5 K per minute, and one data point was collected every 60 s during both processes. The oven can only control the cooling ramp down to 423 K; afterwards the cooling through natural convection happens slower.

Phase identification was done using X-ray diffraction, which was performed on sample pellets utilizing a Siemens D5000 Bragg-Brentano diffractometer with a secondary monochromator. Spectra were taken using Cu K_α radiation (1.5406 Å) in the 2θ range 20° – 80° with a step size of 0.01° , and the lattice parameters were estimated using the Bragg equation. Microstructure analysis was carried out using a Scanning Electron Microscope Zeiss Ultra 55 SEM with a Zeiss QBSE detector, also equipped with an Oxford energy dispersive X-ray (EDX) detector (PentaFETx3). The grain size was observed from SEM pictures and estimated using ImageJ software.

Density measurements needed for the RUS and IET calculations were obtained using the Archimedes method in ethanol. All samples exhibited relative densities higher than 96%. The solid solution relative density was taken as linear interpolation between the binaries.

3. Results

Most pressed pellets exhibit high phase purity, as shown by the XRD patterns in Fig. 1. Samples with $x = 0.5$ and 0.4 exhibit a shoulder or peak bifurcation. Which could be an indicator that secondary phases are present in the material. Only phases with a composition of $Mg_2Si_{1-x}Sn_x$ were found, i.e. no MgO or elemental Si or Sn (see Fig. 1 in SI).

Using the main peaks (111) and (220), the Bragg equation was used to estimate the lattice parameter for each sample. The results were then averaged and shown together with density and composition in Table 2.

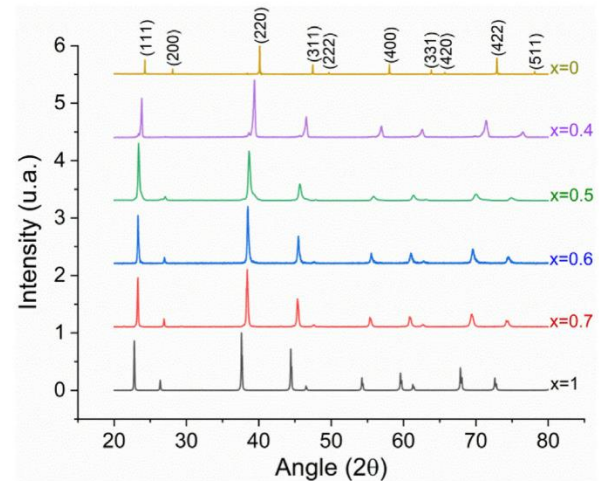


Fig. 1. XRD Spectra for the solid solution $Mg_2Si_{1-x}Sn_x$, $x = 0-1$.

The grain sizes were estimated using image processing software and were found to be very similar for all compositions; this is presumably because of the preparation procedure. While the melting temperature is different between the compositions, the final step before compaction is a 1-h ball milling of the ingot, which is the same for all samples. This similarity between samples means any differences in mechanical properties will not come from grain size difference, but from other sources i.e. Sn–Si ratio, secondary phases amount, etc.

Room temperature IET measurements for $Mg_2Si_{1-x}Sn_x$ (Fig. 2 a) show a linear influence of the tin content in the solid solution on the Young's modulus, with the exception of $x = 0.4$. This composition does not follow the linear behavior observed for the other compositions.

RUS allows us to characterize the elastic constants (see Table 1 in SI), and then, by using Eq. (1), Eq. (2) and Eq. (3), the moduli were calculated for the samples studied in this work (Fig. 2 a). These results also exhibit a linear behavior as the Sn content increases, and go well in accordance with previously reported values [33]. Nevertheless, we observed a reduced elastic constant value at $x=0.6$, as also previously reported in the same paper.

Using previously reported hardness data [32], the fracture toughness of the studied composition along the solid solution was estimated using Equation (6) [32].

$$K_{Ic} = \frac{\zeta \left(\frac{E}{H} \right)^{\frac{1}{2}} P}{c^{3/2}} \quad (6)$$

where H is the measured hardness, P the load used for the indentation and c the length of the crack as measured from the center of the indentation, ζ is a geometrical correction factor set to be 0.016 [43]. Crack length and diagonal needed for hardness estimation were measured using the in-built microscope as described in Refs. [32].

Fig. 2b shows the difference in K_{Ic} between using first principles and experimental values recorded by RUS and IET measurements for the estimation. $Mg_2Si_{0.6}Sn_{0.4}$ exhibited the highest fracture toughness in the original study with the interpolated Young's modulus. Using the measured value instead does not change the trend.

Table 2
Structural parameters for $Mg_2Si_{1-x}Sn_x$.

x	Density (g/cm ³)	Relative density	Lattice parameter (Å)	Grain size (μm)
0	1.97	0.99	6.35	7 ± 1
0.4	2.65	1.00	6.46	8 ± 2
0.5	2.83	1.01	6.58	7 ± 2
0.6	2.97	1.00	6.58	8 ± 2
0.7	3.09	0.99	6.62	7 ± 3
1	3.46	0.96	6.76	7 ± 1

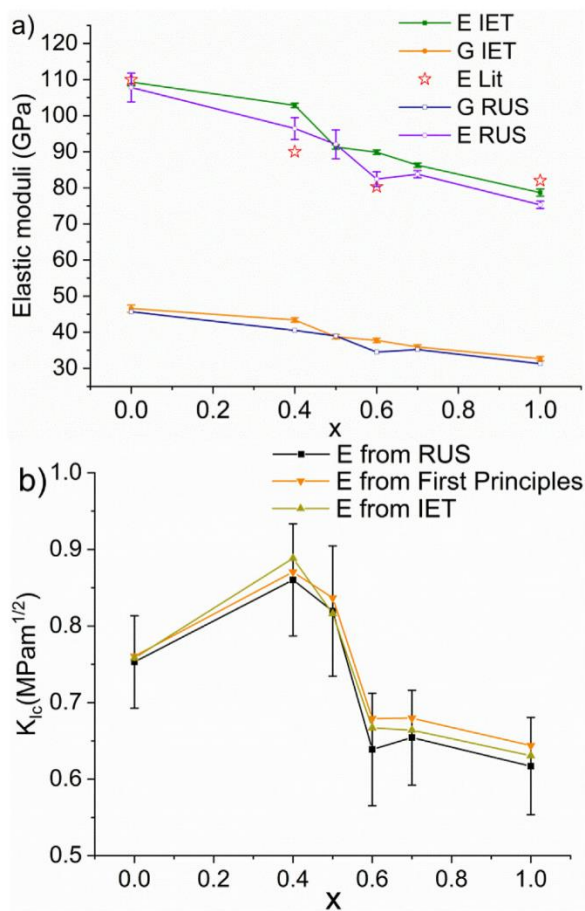


Fig. 2. a) Comparison between elastic constants obtained by RUS and IET with literature data [12,25,30,34,42] and b) Estimation of fracture toughness using (i) values of Young's modulus obtained by linear interpolation between first principles calculation [32] and (ii) experimental observation.

Previous work predicted a linear decrease in elastic constants above room temperature [25]. This work confirms this behavior, as all the samples show a linear dependence of Young's modulus with increasing temperature (Fig. 3a).

Mg_2Sn exhibits the highest percentage of softening at high temperature (623 K) with 11%, while the samples containing Si (solid solutions and binary Mg_2Si) only lose 7–8% of their total strength. Such behavior does not come as a surprise as the stiffening of the $Mg_2(Si,Sn)$ solid solutions were previously described by Klobes *et al.* [33] as the effect of the covalent Mg–Si bond.

Once the material reaches the holding temperature, a small

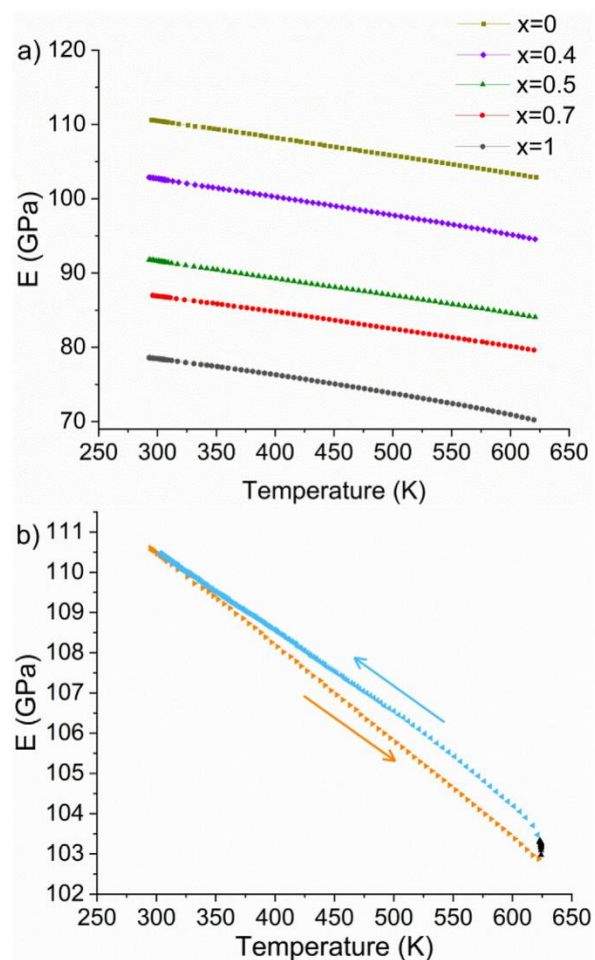


Fig. 3. a) Heating curve for high temperature measurements of Young's modulus showing all compositions tested and b) heating and cooling curve for Mg_2Si , showing a noticeable hysteresis.

strengthening takes place (<1%), which continues when the cooling process starts, as shown in Fig. 3 b). The hysteresis behavior was observed for all samples and is typical of a micro crack healing mechanism that takes place at higher temperatures. Once the material starts to cool down, the thermal stress re-opens micro cracks and the material returns to its original state [44]. It cannot be excluded, however, that the micro-crack healing process starts before the holding temperature. However, with the employed measurement approach, it is noticeable only when the maximum testing temperature is reached, and the temperature-induced

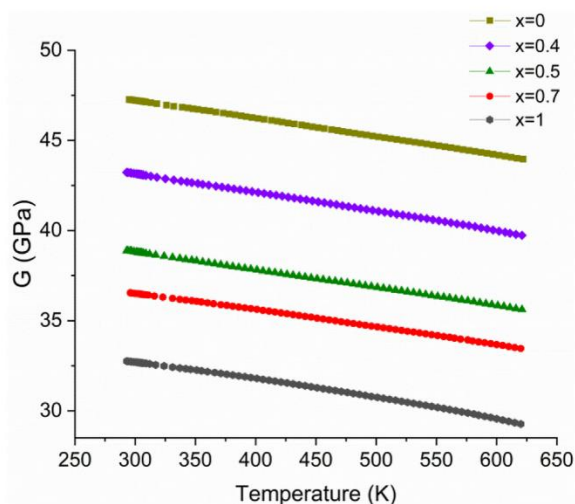


Fig. 4. Temperature dependent shear modulus obtained from $E(T)$ and the Poisson ratio at room temperature.

decrease in Young's modulus ceases.

The integrity of the microstructure after the measurement cycle can be attested by the fact that the initial value is reached again at room temperature. Furthermore, previous work in the research group has proven that long time annealing of samples obtained through the very same method retains the microstructure [11].

The setup used to test high temperature Young's modulus does not permit the easy characterization of shear modulus. However, it can be derived using the Poisson ratio, which is defined as $\nu = \frac{E}{2G} - 1$.

In this regard, we find one previous report of Poisson's ratio measurement for the solid solution $x = 0.6$ [12] which shows a small increase from 0.197 to 0.215 in the temperature range from 300 K to 600 K. Meanwhile, a calculation made with data obtained from first principles calculations [25] yields values for the binary materials that range from 0.173 to 0.176 for Mg_2Si and 0.20–0.198 for Mg_2Sn in the same temperature range. Therefore, assuming a constant Poisson ratio which was obtained from the room temperature measurements, we calculated the temperature-dependent shear modulus for the complete range of compositions tested in this work, as seen in Fig. 4.

The phase purity can be assessed from the microstructure shown in Fig. 5. Secondary phases are present to some degree in all solid solution samples. However, only the samples with $x = 0.4$ and 0.5 have secondary phases in such size and concentration as to be observable in XRD patterns; this is confirmed by the displayed SEM pictures.

Fig. 5 c), d) and e) show the typical microstructure for the solid solution Mg_2Si-Mg_2Sn with secondary phases rich in Si, typical for a melting route synthesis. The appearance of such secondary phases is due to the incomplete diffusion, which is a consequence of a short pressing time during sintering [6,36]. Longer sinter times produce purer samples with fewer amounts of Si-rich phases. However, excessive time can also induce Mg loss, which is detrimental to phase formations [36].

Phase quantification in backscatter SEM pictures was done following the methodology described in Ref. [45] for two samples, $Mg_2Si_{0.6}Sn_{0.4}$ and $Mg_2Si_{0.3}Sn_{0.7}$, and the results are presented in Fig. 6.

The sample $x = 0.4$ is shown in Fig. 6 a). It shows a bifurcated

peak in XRD, and phase quantification confirms the incomplete phase homogenization. Sn-rich phases can be seen surrounding phases with greater Si content creating many interfaces, which will introduce further strain into the matrix according to the inclusion theory [46]. These additional strains might be the reason for the observed increase in Young's modulus. On the other hand, the sample with $x = 0.7$ shown in Fig. 6 b) has a better phase purity, confirming the XRD measurements. The matrix (orange) is noticeable in the picture, and embedded within it, we can identify particles with higher Si content (shown as darker shade of red) and reddish diffusion zones around them. The cumulative percentage of phases belonging to specific compositions (see Fig. 5. In SI) shows that the target phase with $\Delta x = 0.2$ composes more than 90% of the area. These diffusion zones confirm the observations done by Yaseri *et al.* [36] that Si-rich $Mg_2(Si,Sn)$ remnant from the synthesis reacts in the sintering phase as the Si slowly substitutes Sn in the matrix, dissolving the Mg_2Si . Additionally, binary Mg_2Si can also be identified in both pictures.

Given the comparatively low variation in Young's modulus values for $Mg_2Si_{1-x}Sn_x$ and, assuming the area depicted in the SEM picture is representative of the volume fraction of secondary phases in the rest of the material, we can expect very little change in the effective Young's modulus measured. This is because to estimate the elastic modulus in composite materials the contributions of each phase are considered linearly in the Voigt approximation ($\bar{E} = \sum_i n_i E_i$) and approximately linearly in the Reuss approximation ($\bar{E} = \sum_i n_i / E_i^{-1}$) [47].

Previous studies on $Mg_2(Si,Sn)$ obtained through the same method described in this work have shown no indication of microstructural change after annealing at 723K for more than 700 hours [11]. It is therefore assumed that the thermal cycle experienced by the samples during the measurement did not affect the microstructure present in the pristine samples.

4. Discussion

Previous reports for the Young's modulus of Mg_2Si show similar values to what we report, 109 GPa [26–29], except for a value of 145 GPa obtained through nano-indentation [28]. With regard to that characterization technique, Radison *et al.* [48] proved that nano-indentation is a good method to characterize the Young's modulus of a material, yet it was also prone to overestimate the value. This might be the reason for the considerable discrepancy between what we present in this work for the binary material and previous reports by Muthiah *et al.* [28].

RUS and IET were compared in the past by Radovic *et al.* [48]. The paper describes thickness as the main source of uncertainty in IET. As much as 9% variation in elastic moduli can be expected with a variation of thickness below 3%. In our study, the maximum variation for the samples following the linear behavior was 5%, which is well within the previously reported precision for the techniques used. The outliers from linearity are probably due to different effects, such as the inhomogeneity for the $x = 0.4$ composition and the possible influence of the band convergence on the vibrational properties for the $x = 0.6$ sample, rather than technique-dependent uncertainties.

Fracture toughness values do not deviate widely from each other due to the fact that the Young's modulus measurements agree with the linear interpolation used in the first study [32]. Said work also described the effect of secondary phases and particle sizes as strengthening factors in the material. Such mechanisms can be observed in samples with $x < 0.5$. In this case, the high concentration of interfaces is likely to deflect or shorten cracks due to the

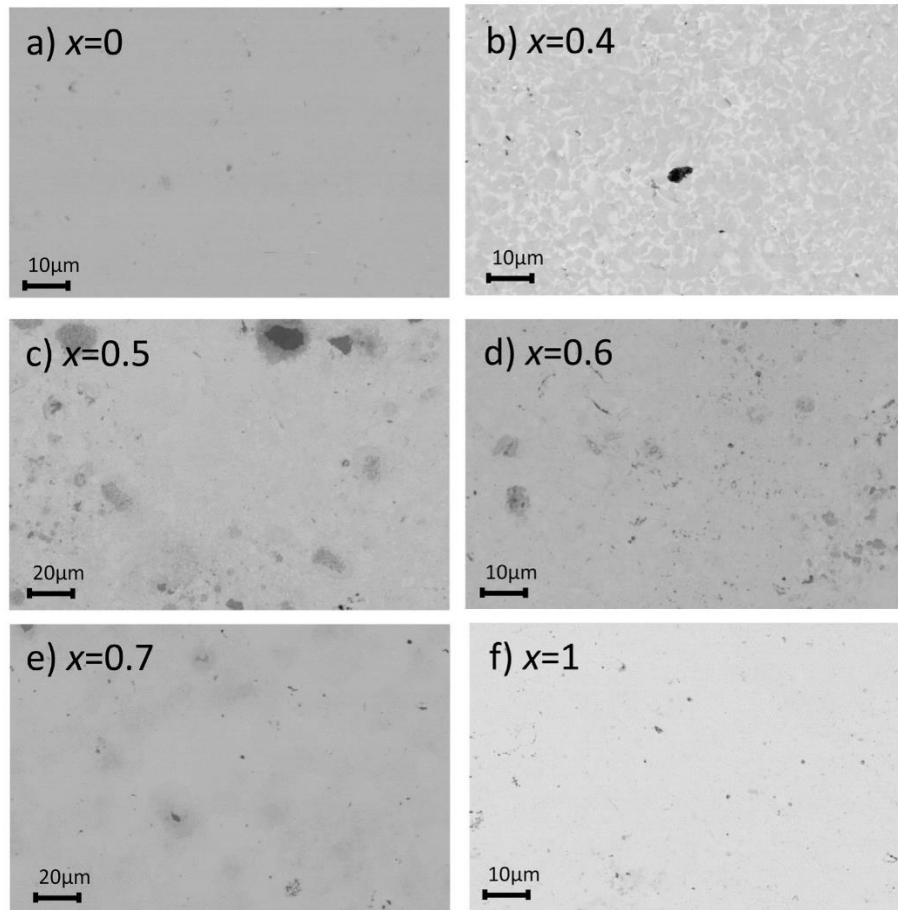


Fig. 5. Backscatter SEM images of a) Mg_2Si , b) $\text{Mg}_2\text{Si}_{0.6}\text{Sn}_{0.4}$, c) $\text{Mg}_2\text{Si}_{0.5}\text{Sn}_{0.5}$, d) $\text{Mg}_2\text{Si}_{0.4}\text{Sn}_{0.6}$, e) $\text{Mg}_2\text{Si}_{0.3}\text{Sn}_{0.7}$ and f) Mg_2Sn , dark areas show the secondary Si rich phases in the solid solution.

intergranular energy at the particle boundaries [49].

The temperature dependent elastic behavior in polycrystalline materials, in general, can be divided into three regions, of which the first two can be described by the empirical Wachtman equation $E = E_0 - bTe^{-\frac{T}{T_0}}$ where E_0 is the Young's modulus at 0 K, b and T_0 are constants [50]. Previous work has set T_0 to 0.3–0.5 Debye temperature (θ_D) [51].

Beginning at the low temperature of $\sim 0.3 \theta_D$, the slope dE/dT decreases as $e^{-\frac{T}{T_0}}$ increases gradually with temperatures falling down to 0 K, where $E = E_0$. Above $0.3 \theta_D$ we find the linear region where dE/dT remains constant as $e^{-\frac{T}{T_0}}$ approaches unity. Finally, the high temperature regime can no longer be described by the Wachtman equation, because the slope deviates from linearity as it gradually increases. The onset of such slope change depends on the material and can be obtained experimentally [51]. Thus, in order to identify the region where this experiment takes place, we estimated the Debye temperature.

For that, the average acoustic sound velocity was calculated using Equation 7

$$v_m = \left(\frac{1}{3} \left[\frac{2}{v_s^3} + \frac{1}{v_l^3} \right] \right)^{-1/3} \quad (7)$$

Where v_s is the transverse acoustic velocity ($v_s = \sqrt{\frac{G}{\rho}}$) and v_l is the longitudinal acoustic velocity ($v_l = \sqrt{\frac{E}{\rho}}$) [52]. Then the acoustic Debye temperature was estimated as

$$\theta_D = \frac{h}{k_B} \left(\frac{3q N_A \rho}{4\pi M} \right)^{1/3} v_m, \quad (8)$$

where h and k_B are the Plank and Boltzmann constants, q is the number of atoms per molecule, M the molecular weight, N_A the Avogadro number and ρ the material density. Results for v_l , v_s , v_m and θ_D are shown in Table 3. The presented data has an uncertainty of 20 m/s for sound velocities and 5 K for the Debye temperature.

With the Debye temperature and the Wachtman model, we can expect the high temperature values for Young's modulus to be linear, as 0.3 – $0.5 \theta_D$ is well below the temperature range of this study for all compositions.

The high temperature behavior of elastic moduli was predicted [25] and experimentally observed to be a linear decrease for

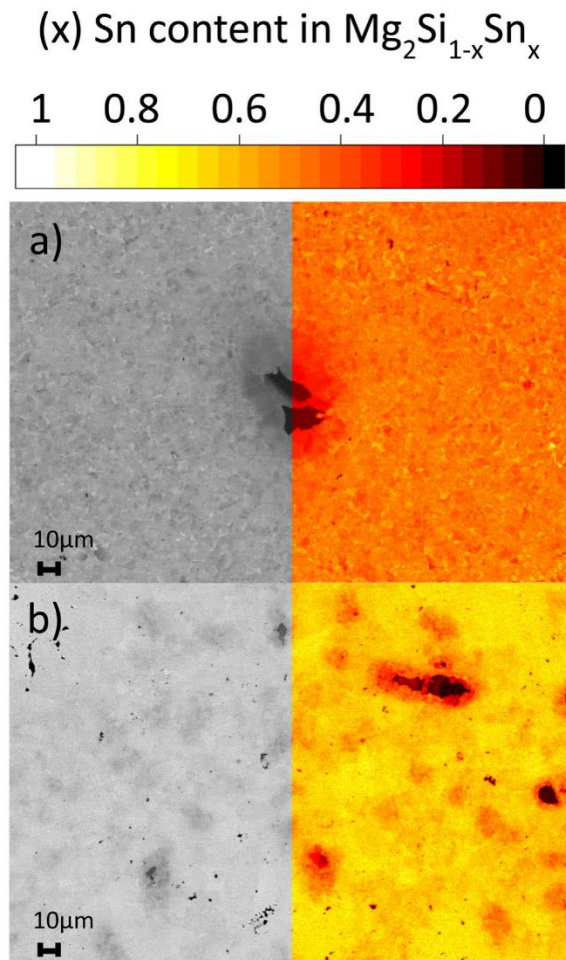


Fig. 6. Backscatter SEM pictures and their respective phase quantification for the samples a) $\text{Mg}_2\text{Si}_{0.6}\text{Sn}_{0.4}$ and b) $\text{Mg}_2\text{Si}_{0.3}\text{Sn}_{0.7}$.

Table 3

Room temperature sound velocities: Longitudinal (v_l) shear (v_s) and average (v_m); as well as Debye temperature (θ_D) for the solid solution $\text{Mg}_2\text{Si}_{1-x}\text{Sn}_x$.

x	V_l (m/s)	V_s (m/s)	V_m (m/s)	θ_D (K)
0	7730	4860	5350	570
0.4	6510	4040	4460	460
0.5	5920	3700	4080	420
0.6	5760	3560	3930	400
0.7	5560	3410	3760	380
1	5040	3080	3400	340

$\text{Mg}_2\text{Si}_{0.4}\text{Sn}_{0.6}$ [12] and $\text{Mg}_2\text{Si}_{0.6}\text{Sn}_{0.4}$ [34], which is in agreement with our results. Both previous studies report a reduction of 5–10% in the characterized elastic constants. In the previous work [34], the behavior of the $\text{Mg}_2\text{Si}_{0.4}\text{Sn}_{0.6}$ sample was fitted using a linear function and had a very good coefficient of determination ($R^2 = 0.995$) in the temperature range 300–600 K.

Our results, as well as previous literature reports, therefore indicate the validity of using a bilinear function in the form $A(x, T) = A_r + bT + cx$.

For this linear equation, A_r is either modulus at 0 K, Young's

Table 4

Values used to fit the model from room temperature up to 600K

Modulus	A_r (GPa)	b (GPa K^{-1})	c (GPa)	R^2
Young's modulus	116.55	-0.0234	-32.032	0.99
Shear modulus	49.77	-0.0098	-14.513	0.99

modulus (E) or shear modulus (G). The values used to fit the equation are detailed in Table 4 including the coefficient of determination obtained as described in Ref. [53]. Here the sample with $x = 0.4$ was excluded from the fitting due to the observed poor phase quality. However, as can be seen for the results including $x = 0.4$ (see SI), the coefficient of determination was very lightly modified.

Table 4 allows for the thermomechanical modelling of a TEG under operational conditions, and for an optimization with respect to composition, taking mechanical properties into account. The prediction of lattice thermal conductivities can also benefit from more precise data of the mechanical properties. A previous work on $\text{Mg}_2\text{Si}_{1-x}\text{Sn}_x$ materials [54] estimated the lattice thermal conductivity using the Debye approximation in the form

$$\kappa_l = \frac{k_B}{2\pi^2 v_m} \left(\frac{k_B T \pi}{h} \right)^3 \frac{x^4 e^x}{(e^x - 1)^2} T c$$

where we see the average sound velocity v_m . The approximation also depends on the Boltzmann constant k_B , the Plank constant h and the reduced phonon energy y which in turn is estimated with $y = \frac{2\hbar\omega}{k_B T \pi}$ where ω is the phonon frequency.

Knowledge of the elastic constants is also important for the modelling of the electronic properties. Scattering by acoustic phonons is the dominant scattering mechanism for electrons above room temperature for most materials [9,55]. This interaction is characterized by the deformation potential E_{Def} which is related to the carrier mobility by $\mu \propto \frac{C_i}{E_{\text{Def}}^2 \cdot m^{*2.5}}$, where m^* is the carrier effective mass and C_i is given by $C_i = E - G$ for cubic crystals [40]. Practically, E_{Def} is usually obtained from the measured mobility at high temperature using room temperature values for E and G [37,55–58]. However, as both exhibit clear temperature dependence, this leads to incorrect values of E_{Def} and should be considered as a fair approximation only.

5. Conclusion

High temperature elastic constants, as well as hardness and fracture toughness, are important parameters to predict the mechanical behavior of a certain material under load. Knowledge of said parameters will allow to thermo-mechanically model a possible TEG manufactured using $\text{Mg}_2\text{Si}_{1-x}\text{Sn}_x$, with correct values for the mechanical properties under application conditions.

Elastic moduli E and G are presented for several compositions along the $\text{Mg}_2\text{Si}_{1-x}\text{Sn}_x$ ($x = 0 - 1$) solid solution series at both room and high temperatures. The first ever experimental value for binary polycrystalline Mg_2Sn is presented and is in good agreement with first principles calculations. It was also shown that both the temperature and composition have a linear influence on both the moduli, which facilitates the description of the behavior by a simple bilinear equation.

Additionally, we describe that, besides a prominence of secondary phases, phase distribution can also affect the elastic behavior by stiffening the material, as was the case with the Si-rich ($x = 0.4$) $\text{Mg}_2\text{Si}_{1-x}\text{Sn}_x$. $\text{Mg}_2\text{Si}_{0.6}\text{Sn}_{0.4}$ was the only sample to deviate from the linear decrease in Young's modulus in the IET measurements. Such behavior is closely related to the microstructure found in the material, where small Si-rich areas are found surrounded by Sn-rich phases, creating a biphasic material with a great amount of

interfaces.

Mg₂Si_{0.4}Sn_{0.6}, on the other hand, deviated from the linear behavior in the RUS characterization. This is well in agreement with previous reports and possibly a consequence of the convergence of the conduction bands in this composition.

A better estimation of the temperature dependent elastic moduli is not only beneficial for mechanical design and modelling, but also for electronic and thermal properties of the thermoelectric materials.

CRedit authorship contribution statement

Gustavo Castillo-Hernandez: Investigation, Writing - original draft. **Mohammad Yasseri:** Conceptualization, Formal analysis. **Benedikt Klobes:** Formal analysis. **Sahar Ayachi:** Conceptualization, Writing - review & editing. **Eckhard Müller:** Supervision, Project administration. **Johannes de Boor:** Writing - review & editing, Supervision.

Declaration of competing interest

The authors declare that they have no known competing financial interests or personal relationships that could have appeared to influence the work reported in this paper.

Acknowledgements

The authors would like to acknowledge the endorsement for the DLR executive Board Members for Space Research and Technology, as well as the financial support from the Young Research Group Leader Program.

Financial support for M.Y is provided by the DFG via the GRK (Research Training Group) 2204 "Substitute Materials for Sustainable Energy Technologies". GCH would like to thank the Mexican science and technology council (CONACyT) and the German academic exchange service (DAAD) for the PhD fellowship.

Appendix A. Supplementary data

Supplementary data to this article can be found online at <https://doi.org/10.1016/j.jallcom.2020.156205>.

References

- X.D. Luo, H. Liu, W.L. Xu, Y.X. Zhu, Progress on Mg₂Si thermoelectric materials, *Adv Mater Res-Switz* 886 (2014) 71–74.
- R. Santos, S.A. Yamini, S.X. Dou, Recent progress in magnesium-based thermoelectric materials, *J. Mater. Chem.* 6 (8) (2018) 3328–3341.
- D.M. Rowe, Thermoelectric-Power generation, *IEE Rev.* 125 (Nov) (1978) 1113–1136.
- D.M. Rowe, Applications of nuclear-powered thermoelectric generators in space, *Appl. Energy* 40 (4) (1991) 241–271.
- S. LeBlanc, S.K. Yee, M.L. Scullin, C. Dames, K.E. Goodson, Material and manufacturing cost considerations for thermoelectrics, *Renew. Sustain. Energy Rev.* 32 (2014) 313–327.
- A. Sankhla, A. Patil, H. Kamila, M. Yasseri, N. Farahi, E. Mueller, J. de Boor, Mechanical alloying of optimized Mg₂(Si,Sn) solid solutions: understanding phase evolution and tuning synthesis parameters for thermoelectric applications, *ACS Appl. Energy Mater.* 1 (2) (2018) 531–542.
- V.K. Zaitsev, M.I. Fedorov, E.A. Gurieva, I.S. Eremin, P.P. Konstantinov, A.Y. Samunin, M.V. Vedernikov, Highly effective Mg₂Si_{1-x}Sn_x thermoelectrics, *Phys. Rev. B* 74 (4) (2006), 045207.
- W. Liu, X.J. Tan, K. Yin, H.J. Liu, X.F. Tang, J. Shi, Q.J. Zhang, C. Uher, Convergence of conduction bands as a means of enhancing thermoelectric performance of n-type Mg₂Si_{1-x}Sn_x solid solutions, *Phys. Rev. Lett.* 108 (16) (2012) 166601.
- W. Liu, H. Chi, H. Sun, Q. Zhang, K. Yin, X. Tang, Q. Zhang, C. Uher, Advanced thermoelectrics governed by a single parabolic band: Mg₂Si_{0.3}Sn_{0.7}, a canonical example, *Phys. Chem. Phys.* 16 (15) (2014) 6893–6897.
- T. Dasgupta, C. Stiewe, J. de Boor, E. Müller, Influence of power factor enhancement on the thermoelectric figure of merit in Mg₂Si_{0.4}Sn_{0.6} based materials, *Phys. Status Solidi* 211 (6) (2014) 1250–1254.
- N. Farahi, C. Stiewe, D.Y.N. Truong, J. de Boor, E. Muller, High efficiency Mg₂(Si,Sn)-based thermoelectric materials: scale-up synthesis, functional homogeneity, and thermal stability, *RSC Adv.* 9 (40) (2019) 23021–23028.
- P. Gao, I. Berkun, R.D. Schmidt, M.F. Luzenski, X. Lu, P.B. Sarac, E.D. Case, T.P. Hogan, Transport and mechanical properties of high-ZT Mg₂0.8Si_{0.4-x}Sn_{0.6}Sb_x (x) thermoelectric materials, *J. Electron. Mater.* 43 (6) (2014) 1790–1803.
- H. Kamila, A. Sankhla, M. Yasseri, P. Hoang, N. Farahi, E. Mueller, J. de Boor, Synthesis of p-type Mg₂Si_{1-x}Sn_x with x = 0–1 and optimization of the synthesis parameters, *Mater. Today: Proceedings* 8 (2019) 9.
- J. de Boor, T. Dasgupta, U. Saparamadu, E. Müller, Z.F. Ren, Recent progress in p-type thermoelectric magnesium silicide based solid solutions, *Materials Today Energy* 4 (2017) 105–121.
- P. Gao, J.D. Davis, V.V. Poltavets, T.P. Hogan, The p-type Mg₂LixSi_{0.4}Sn_{0.6} thermoelectric materials synthesized by a B2O₃ encapsulation method using Li₂CO₃ as the doping agent, *J. Mater. Chem. C* 4 (5) (2016) 929–934.
- P. Nieroda, A. Kolezynski, M. Oszajca, J. Milczarek, K.T. Wojciechowski, Structural and thermoelectric properties of polycrystalline p-type Mg_{2-x}Li_xSi, *J. Electron. Mater.* 45 (7) (2016) 3418–3426.
- U. Saparamadu, J. de Boor, J. Mao, S.W. Song, F. Tian, W.S. Liu, Q.Y. Zhang, Z.F. Ren, Comparative studies on thermoelectric properties of p-type Mg₂Sn_{0.75}Ge_{0.25} doped with lithium, sodium, and gallium, *Acta Mater.* 141 (2017) 154–162.
- S. Ayachi, G. Castillo-Hernandez, M. Yasseri, J. de Boor, E. Müller, Developing contacting solutions for Mg₂Si_{1-x}Sn_x-Based thermoelectric generators: Cu and Ni₄₅Cu₅₅ as potential contacting electrodes, *ACS Appl Mater Inter* 11 (43) (2019), <https://doi.org/10.1021/acsami.9b12474>.
- N.P. Pham, N. Farahi, H. Kamila, A. Sankhla, S. Ayachi, E. Müller, J. de Boor, Ni and Ag electrodes for magnesium silicide based thermoelectric generators, *Materials Today Energy* 11 (2019).
- J. De Boor, D. Droste, C. Schneider, J. Janek, E. Mueller, Thermal stability of magnesium silicide/nickel contacts, *J. Electron. Mater.* 45 (10) (2016) 5313–5320.
- J. de Boor, C. Gloanec, H. Kolb, R. Sottong, P. Ziolkowski, E. Muller, Fabrication and characterization of nickel contacts for magnesium silicide based thermoelectric generators, *J. Alloys Compd.* 632 (2015) 348–353.
- K. Mitra, S. Mahapatra, T.J. Dasgupta, Fabrication of nickel contacts for Mg₂Si based thermoelectric generators via an induction assisted, Rapid Monoblock Sintering Technique 48 (3) (2019) 1754–1757.
- X.D. Jia, Y.W. Gao, Estimation of thermoelectric and mechanical performances of segmented thermoelectric generators under optimal operating conditions, *Appl. Therm. Eng.* 73 (1) (2014) 335–342.
- Z.W. Huang, Y.H. Zhao, H. Hou, P.D. Han, Electronic structural, elastic properties and thermodynamics of Mg₁₇Al₁₂, Mg₂Si and Al₂Y phases from first-principles calculations, *Physica B* 407 (7) (2012) 1075–1081.
- S. Ganeshan, S.L. Shang, Y. Wang, Z.K. Liu, Temperature dependent elastic coefficients of Mg₂X (X = Si, Ge, Sn, Pb) compounds from first-principles calculations, *J. Alloys Compd.* 498 (2) (2010) 191–198.
- R.D. Schmidt, E.D. Case, J. Giles, J.E. Ni, T.P. Hogan, Room-temperature mechanical properties and slow crack growth behavior of Mg₂Si thermoelectric materials, *J. Electron. Mater.* 41 (6) (2012) 1210–1216.
- R.D. Schmidt, X.F. Fan, E.D. Case, P.B. Sarac, Mechanical properties of Mg₂Si thermoelectric materials with the addition of 0–4 vol% silicon carbide nanoparticles (SiCNP), *J. Mater. Sci.* 50 (11) (2015) 4034–4046.
- S. Muthiah, R.C. Singh, B.D. Pathak, A. Dhar, Mechanical properties of thermoelectric n-type magnesium silicide synthesized employing in situ spark plasma reaction sintering, *Mater. Res. Express* 4 (7) (2017).
- V. Milekhine, M.I. Onsoien, J.K. Solberg, T. Skaland, Mechanical properties of FeSi (epsilon), FeSi₂ (zeta(alpha)) and Mg₂Si, *Intermetallics* 10 (8) (2002) 743–750.
- W.B.W.L.C. Davis, G.C. Danielson, Elastic constants and calculated lattice vibration frequencies of Mg₂Sn, *J. Phys. Chem. Solid.* 28 (3) (1967) 9.
- X. Li, H. Xie, B. Yang, S.M. Li, Elastic and thermodynamic properties prediction of Mg₂Sn and MgTe by first-principle calculation and quasi-harmonic Debye model, *J. Electron. Mater.* 49 (1) (2019), <https://doi.org/10.1007/s11664-019-07682-w>.
- G. Castillo-Hernandez, M. Yasseri, S. Ayachi, J. de Boor, E. Müller, Hardness and Fracture Toughness of Solid Solutions of Mg₂Si and Mg₂Sn, *Fizika I Tehnika Poluprovodnikov (Semiconductors)*, 2019.
- B. Klobes, J. de Boor, A. Alatas, M.Y. Hu, R.E. Simon, R.P. Hermann, Lattice dynamics and elasticity in thermoelectric Mg₂Si_{1-x}Sn_x, *Phys Rev Mater* 3 (2) (2019).
- M. Mejri, Y. Thimont, B. Malard, C. Estournes, Characterization of the thermo-mechanical properties of p-type (MnSi_{1.77}) and n-type (Mg₂Si_{0.6}Sn_{0.4}) thermoelectric materials, *Scripta Mater.* 172 (2019) 28–32.
- R. Viennois, P. Jund, C. Colinet, J.C. Tedenac, Defect and phase stability of solid solutions of Mg₂X with an antifluorite structure: an ab initio study, *J. Solid State Chem.* 193 (2012) 133–136.
- M. Yasseri, A. Sankhla, H. Kamila, R. Orenstein, D.Y.N. Truong, N. Farahi, J. de Boor, E. Mueller, Solid solution formation in Mg₂(Si,Sn) and shape of the miscibility gap, *Acta Mater.* 185 (15) (2019), <https://doi.org/10.1016/j.actamat.2019.11.054>.
- H. Kamila, A. Sankhla, M. Yasseri, N.P. Hoang, N. Farahi, E. Mueller, J. de Boor, Synthesis of p-type Mg₂Si_{1-x}Sn_x with x = 0–1 and optimization of the

- synthesis parameters, *Mater. Today: Proceedings* 8 (2019) 546–555.
- [38] D. Bessas, E. Bruck, A versatile Lock-In digital Amplifier (LIdA): the case of mechanical resonances, *Eur. J. Phys.* 38 (3) (2017).
- [39] A. Migliori, J.L. Sarrao, W.M. Visscher, T.M. Bell, M. Lei, Z. Fisk, R.G. Leasure, Resonant ultrasound spectroscopic techniques for measurement of the elastic-moduli of solids, *Physica B* 183 (1–2) (1993) 1–24.
- [40] M. Jamal, S.J. Asadabadi, I. Ahmad, H.A.R. Aliabad, Elastic constants of cubic crystals, *Comput. Mater. Sci.* 95 (2014) 592–599.
- [41] Astm, Dynamic Young's Modulus, Shear Modulus, and Poisson's Ratio by Impulse Excitation of Vibration, 2001.
- [42] W.B. Whitten, P.L. Chung, G.C. Danielson, Elastic constants and lattice vibration frequencies of Mg₂Si, *J. Phys. Chem. Solid.* 26 (1965).
- [43] W.C. Oliver, G.M. Pharr, An improved technique for determining hardness and elastic-modulus using load and displacement sensing indentation experiments, *J. Mater. Res.* 7 (6) (1992) 1564–1583.
- [44] J.E. Ni, E.D. Case, R.D. Schmidt, C.I. Wu, T.P. Hogan, R.M. Trejo, E. Lara-Curzio, M.G. Kanatzidis, Fracture mode, microstructure and temperature-dependent elastic moduli for thermoelectric composites of PbTe–PbS with SiC nanoparticle additions, *Philos. Mag. A* 93 (35) (2013) 4412–4439.
- [45] M. Yasseri, N. Farahi, K. Kelm, E. Mueller, J. de Boor, Rapid determination of local composition in quasi-binary, inhomogeneous material systems from backscattered electron image contrast, *Materialia* 2 (2018).
- [46] T. Mura, *Micromechanics of Defects in Solids*, 2nd, rev. ed., M. Nijhoff.
- [47] B. Liu, X. Feng, S.M. Zhang, The effective Young's modulus of composites beyond the Voigt estimation due to the Poisson effect, *Compos. Sci. Technol.* 69 (13) (2009) 2198–2204.
- [48] M. Radovic, E. Lara-Curzio, L. Riestler, Comparison of different experimental techniques for determination of elastic properties of solids, *Mat Sci Eng A-Struct* 368 (1–2) (2004) 56–70.
- [49] M.E. Launey, R.O. Ritchie, On the fracture toughness of advanced materials, *Adv. Mater.* 21 (20) (2009) 2103–2110.
- [50] M.L. Nandanpawar, S. Rajagopalan, Wachtman equation and temperature-dependence of bulk moduli in solids, *J. Appl. Phys.* 49 (7) (1978) 3976–3979.
- [51] R.D. Schmidt, E.D. Case, J.E. Ni, J.S. Sakamoto, R.M. Trejo, E. Lara-Curzio, Temperature-dependent Young's modulus, shear modulus and Poisson's ratio of p-type Ce_{0.9}Fe_{3.5}Co_{0.5}Sb₁₂ and n-type Co_{0.95}Pd_{0.05}Te_{0.05}Sb₃ skutterudite thermoelectric materials, *Philos. Mag. A* 92 (6) (2012) 727–759.
- [52] L. Zhang, G. Rogl, A. Grytsiv, S. Puchegger, J. Koppensteiner, F. Spieckermann, H. Kabelka, M. Reinecker, P. Rogl, W. Schranz, M. Zehetbauer, M.A. Carpenter, Mechanical properties of filled antimonide skutterudites, *Mater Sci Eng B-Adv* 170 (1–3) (2010) 26–31.
- [53] C.R. Rao, *Linear Statistical Inference and its Applications*, John Wiley & Sons, Inc., 1973.
- [54] G.Y. Jiang, J. He, T.J. Zhu, C.G. Fu, X.H. Liu, L.P. Hu, X.B. Zhao, High performance Mg₂(Si,Sn) solid solutions: a point defect chemistry approach to enhancing thermoelectric properties, *Adv. Funct. Mater.* 24 (24) (2014) 3776–3781.
- [55] J. de Boor, T. Dasgupta, H. Kolb, C. Compere, K. Kelm, E. Mueller, Microstructural effects on thermoelectric efficiency: a case study on magnesium silicide, *Acta Mater.* 77 (2014) 68–75, 0.
- [56] H. Kamila, P. Sahu, A. Sankhla, M. Yasseri, H.-N. Pham, T. Dasgupta, E. Mueller, J. de Boor, Analyzing transport properties of p-type Mg₂Si–Mg₂Sn solid solutions: optimization of thermoelectric performance and insight into the electronic band structure, *J. Mater. Chem.* 7 (3) (2019) 1045–1054.
- [57] A.F. May, E. Flage-Larsen, G.J. Snyder, Electron and phonon scattering in the high-temperature thermoelectric La₃Te₄-zMz (M=Sb,Bi), *Phys. Rev. B* 81 (12) (2010).
- [58] X.H. Liu, T.J. Zhu, H. Wang, L.P. Hu, H.H. Xie, G.Y. Jiang, G.J. Snyder, X.B. Zhao, Low electron scattering potentials in high performance Mg₂Si_{0.45}Sn_{0.55} based thermoelectric solid solutions with band convergence, *Adv. Energy Mater.* 3 (9) (2013) 1238–1244.

7. Impact of the dopant species on the thermomechanical material properties of thermoelectric $\text{Mg}_2\text{Si}_{0.3}\text{Sn}_{0.7}$

With the composition and temperature dependent elastic properties known, the next step into the module simulation was the study of whether or not the doping influenced the mechanical properties.

This chapter is focused on the composition $\text{Mg}_2\text{Si}_{0.3}\text{Sn}_{0.7}$, as this is reported to have excellent TE properties [60, 73, 77]. The effect of doping with Bi (for the n-type) and Li (for the p-type) was studied against the undoped sample from the previous chapter.

For this chapter, also the coefficient of thermal expansion was studied, which is essential for module simulation.

Using both the Young's modulus and the CTE, the potential to develop thermal stresses ($E \cdot a$) was estimated and compared to other material systems like Skutterudites and Half Heusler.

Finally, a small comparison between thermally induced stress is presented. This stress was estimated using a combination of temperature dependent and constant properties. The difference observed in these comparisons serves as base for the modelling presented later in the discussion part of this thesis

Article

Impact of the Dopant Species on the Thermomechanical Material Properties of Thermoelectric $\text{Mg}_2\text{Si}_{0.3}\text{Sn}_{0.7}$

Gustavo Castillo-Hernández ^{1,2}, Eckhard Müller ^{1,2} and Johannes de Boor ^{1,3,*}

¹ Institute of Materials Research, German Aerospace Center, 51170 Cologne, Germany; gustavo.castillo-hernandez@dlr.de (G.C.-H.); eckhard.mueller@dlr.de (E.M.)

² Institute of Inorganic and Analytical Chemistry, Justus Liebig University Giessen, Heinrich-Buff-Ring 17, 35392 Giessen, Germany

³ Institute of Technology for Nanostructures (NST), Faculty of Engineering, University of Duisburg-Essen, Bismarckstreet 81, 47057 Duisburg, Germany

* Correspondence: johannes.deboor@dlr.de

Abstract: Thermoelectric generators are an excellent option for waste heat reuse. Materials for such devices have seen their thermoelectric properties improving constantly. The functioning of a generator, however, does not only depend on thermoelectric properties. Thermal and mechanical properties play a decisive role in the feasibility of any thermoelectric generator. To shed light on the properties exhibited by thermoelectric materials, we present the temperature dependent characterization of Young's modulus and coefficient of thermal expansion for $\text{Mg}_2\text{Si}_{0.3}\text{Sn}_{0.7}$. Comparing undoped to Bi-doped n-type and Li-doped p-type material, we investigated the influence of doping in the relevant temperature regime and found the influences to be minor, proving similar properties for n- and p-type. We found a Young's modulus of 84 GPa for the p-type and 83 GPa for the n-type, similar to that of the undoped compound with 85 GPa. The thermal expansion coefficients of undoped, as well as n- and p-type were equally similar with values ranging from 16.5 to 17.5×10^{-6} 1/K. A phase analysis was performed to further compare the two materials, finding a similar phase distribution and microstructure. Finally, using the gathered data, estimations on the possible thermally induced stresses under a temperature difference are provided to evaluate the relevance of knowing temperature dependent thermal and mechanical properties.

Keywords: mechanical properties; thermoelectric; Mg_2Si ; Mg_2Sn ; thermal expansion

Citation: Castillo-Hernández, G.; Müller, E.; de Boor, J. Impact of the Dopant Species on the Thermomechanical Material Properties of Thermoelectric $\text{Mg}_2\text{Si}_{0.3}\text{Sn}_{0.7}$. *Materials* **2022**, *15*, 779. <https://doi.org/10.3390/ma15030779>

Academic Editors: Amir Pakdel and David Berthebaud

Received: 14 December 2021

Accepted: 18 January 2022

Published: 20 January 2022

Publisher's Note: MDPI stays neutral with regard to jurisdictional claims in published maps and institutional affiliations.



Copyright: © 2022 by the authors. Licensee MDPI, Basel, Switzerland. This article is an open access article distributed under the terms and conditions of the Creative Commons Attribution (CC BY) license (<http://creativecommons.org/licenses/by/4.0/>).

1. Introduction

Thermoelectric generators (TEG) are solid state devices that can convert waste heat into usable electricity [1]. TEG have several advantages compared to other electrical power generation technologies in that they have no mobile parts and thus have low maintenance costs and high reliability and can function in the absence of light, in contrast to photovoltaic technology.

TEG can be manufactured from a wide range of materials, some of which are light and inexpensive [2,3]. The basic unit of such a TEG is a pair of doped semiconductors called legs, one n-type and the other p-type. Both legs are joined to a metallic connector usually denominated as the bridge. The legs are thus connected electrically in series and thermally in parallel [1,4], allowing to convert a fraction of the heat flowing through the legs into electricity.

The legs are ranked according to the power generating capabilities they possess. This classification is summed up in the dimensionless figure of merit zT , which is defined as $zT = S^2\rho\kappa^{-1}T$, where S , ρ , κ , and T represent the Seebeck coefficient, electrical resistivity, total thermal conductivity, and absolute temperature, respectively.

Among the materials that show good zT values, as well as other desirable properties like low density and cost, are the Mg_2Si - Mg_2Sn solid solutions. These materials have been thoroughly studied before, with zT values of 1.2–1.4 at 973 K for the n-type [5–11], while the p-type value is about 0.55 at the same temperature [12–17]. In conjunction with a density ranging from 1.99–3.5 g/cm³, the material system becomes a prime candidate for low-cost and non-toxic TEG technology development.

For TEG design, not only is the development of the thermoelectric properties important, but several other challenges need to be tackled as well. In particular, progress on contact technology and mechanical stability is also important. Contacting technology for Mg_2Si - Mg_2Sn has shown substantial progress as several candidate schemes have been evaluated [18–22] and their thermal stability assessed [23]. Mechanical properties have been studied, with our previous work detailing the temperature and composition dependent elastic behavior for the whole solid solution series [11,24–26].

Silicide-based TEG have traditionally been manufactured with an n-type $Mg_2(Si,Sn)$ and an higher manganese silicide (HMS) p-type leg because of the poor properties exhibited by p-type $Mg_2(Si,Sn)$ [25,27,28]. HMS has, on the other hand, quite different mechanical properties compared to $Mg_2(Si,Sn)$. In recent developments, however, both p-materials have achieved similar thermoelectric (TE) performance [12], and modules using only $Mg_2(Si,Sn)$ seem to be a realistic possibility now. Using n- and p-type legs from the same material class with similar compositions can be highly advantageous as the thermal and mechanical properties are expected to show similarity. This similarity is especially important since it has been proven that differences in the coefficient of thermal expansion (CTE) for the materials used in the legs may cause high thermally induced mechanical stresses, potentially damaging or destroying the module [29]. Moreover, the effect of damage caused by mechanical stress in modules, even if not destroying the module completely by a fracture, has been shown to decrease the device figure of merit to less than half the original value [20,30].

Having the same CTE for both leg materials is, however, not a guarantee that the module will have mechanical integrity, as other effects such as bridge or substrate expansion need to be considered. Previous work has been done on modeling the mechanical behavior of a Bi_2Te_3 module, where the said module employed legs that had the same CTE and Young's modulus, but high stresses were found in the TEG module [31].

Since the thermal expansion will cause stresses even if the CTE of the TE materials is similar, it is important not to design a module only based on the CTE, but take into account Young's modulus and Poisson's rate of the materials as well.

Mechanical properties of materials with similar compositions and an identical microstructure are expected to be equally similar. However, doping species have been known to alter the mechanical response in some TE materials. Skutterudites, in particular, typically have a Young's modulus of $E > 140$ GPa for n-type materials, while p-type materials rarely exhibit higher values than 130 GPa [32]. Within the same doping type, we see slight differences as well. P-type didymium (mixture of praseodymium and neodymium) filled material $DD_{0.86}Fe_4Sb_{12}$ shows a Young's modulus of 123 GPa, while the composition $DD_{0.68}Fe_3CoSb_{12}$ reaches 127 GPa. $DD_{0.68}Fe_4Sb_{12}$ has also been tested and shows a Young's modulus of 105 GPa, but here it remains unclear if the difference is due to changes in composition or mainly due to a modified synthesis approach.

Mg_2X material belongs to space group $Fm\bar{3}m$ with Mg filling the 8c Wyckoff position and X the 4a position. X can be filled with Si and Sn to produce the $Mg_2(Si,Sn)$ solid solution. Doping for n-type is also done in this position. The typical n-type dopants Bi and Sb substitute X, as discussed e.g., in [33]. Bi-doped $Mg_2(Si,Sn)$ shows good thermoelectric properties [10,34,35] and thus, the effect of Bi on other properties has received more attention lately. The hardness in a Bi-doped Mg_2Si material was reported to increase [26] from 327 Hv in undoped material to 475 Hv with an atomic dopant percentage of 2.5%. The authors of this work attribute the hardness increase to the substitution of Si by Bi in the

materials crystal lattice. Note that the original work reports the change in composition as 0.0025 at%, which is very likely a typographical error.

The lattice parameter of the Bi-doped cubic $\text{Mg}_2(\text{Si},\text{Sn})$ has been studied as well. Previous work details the effect of up to $x = 4$ at% Bi in a $\text{Mg}_2\text{Si}_{0.35}\text{Sn}_{0.65-x}\text{Bi}_x$ material. In this case, the lattice parameter increased from 6.607 Å to 6.632 Å with no indication of a solubility limit [34]. The authors attribute the increase to Bi occupancy of Si, Sn place in the lattice.

As most previous studies have focused on the effect of Bi on the thermoelectric properties of said materials, little is reported about the CTE and the Young's modulus, which are important for the stress formation in TEG modules in service. As high stresses may result in damages impairing the thermoelectric efficiency and finally may affect the structural integrity of the TEG, we performed the first ever characterization of CTE and Young's modulus for a p-type $\text{Mg}_2(\text{Si},\text{Sn})$ material, in comparison with the n-type and undoped material. A discussion of the potential consequences for TEG development is also presented.

2. Materials and Methods

$\text{Mg}_2\text{Si}_{0.3}\text{Sn}_{0.7}$ samples with different doping levels and species were synthesized using a mixed method described elsewhere [10]. The doping amount for n-type (3.5% Bi) and p-type (3% Li) was chosen according to previous work [10,12]; these compositions yield the best possible thermoelectric properties for the synthesis route. The low 0.75% Bi sample was chosen as initially, Bi segregation was deemed likely to happen and the effect of this was to be studied. However, as described later, no Bi-rich secondary phases were observed.

Precursor materials were Mg turnings (Merck, Darmstadt, Germany), Si chunks (<6 mm, ChemPur, Karlsruhe, Germany), Sn (<71 µm, Merck) with high purity > 99.5%, Li and Bi. A pellet was pressed from the powder in a direct current sinter press DSP 510 SE (Dr. Fritsch GmbH, Fellbach, Germany). The parameters of temperature (T_{sinter}) and pressure (p_{sinter}) used to sinter each sample are detailed in Table 1. Samples containing no Li were synthesized using extra Mg to account for losses in the process due to evaporation in the synthesis and pressing steps. These samples require, thus, extra time in the sintering step.

Table 1. Composition and sintering time for the employed $\text{Mg}_2\text{Si}_{0.3}\text{Sn}_{0.7}$ samples. We furthermore employed $T_{\text{sinter}} = 973$ K and $p_{\text{sinter}} = 66$ MPa.

Nominal Composition	Time (min)
$\text{Mg}_{1.97}\text{Li}_{0.03}\text{Si}_{0.3}\text{Sn}_{0.7}$	10
$\text{Mg}_{2.06}\text{Si}_{0.3}\text{Sn}_{0.7}$	10
$\text{Mg}_{2.06}\text{Si}_{0.3}\text{Sn}_{0.6925}\text{Bi}_{0.0075}$	20
$\text{Mg}_{2.06}\text{Si}_{0.3}\text{Sn}_{0.665}\text{Bi}_{0.035}$	20

The pellets obtained had a diameter of 50 mm and a thickness of 3.5 mm. They were cut using a diamond disc saw (DISCO Corp., Tokyo, Japan) into pieces measuring $(12 \times 45 \times 3.0)$ mm³ for the Young's modulus measurement and $(5 \times 40 \times 3.0)$ mm³ for the CTE measurement. Small semi-circular segments of the pellets were embedded in conductive resin, grinded with SiC paper, and polished with diamond suspension for microstructure analysis.

The Impulse Excitation Technique (IET) was used to determine the Young's modulus. Its measuring principle is based on the free vibration of a sample (bar or pellet) set on top of supports. It has been extensively described by other authors, as well as in our previous work [24,36]. Young's modulus measurement was done using a device from Integrated Material Control Engineering NV (Genk, Belgium). High temperature characterization was done in air from RT until 673 K with a heating and cooling rate of 1 K/min, and

a holding step of 60 min at maximum temperature was established. One data point was obtained every 30 s throughout the whole process. The cooling process can be controlled by the device down to 423 K; afterwards the cooling happens through natural convection. Two independent measurements were done per composition, the variation between them was lesser than the measurement precision and thus, this precision is reported.

The coefficient of thermal expansion was measured on a Bähr thermoanalysis dilatometer (Hüllhorst, Germany) in the temperature range of 300–720 K, using a sapphire calibration. The measurement was performed under vacuum ($<1 \times 10^{-4}$ bar) with a heating ramp of 1 K/min.

X-ray diffraction was used to identify the phases present. Such a measurement was performed on pieces of the obtained pellets utilizing a Bruker D8 advance diffractometer (Billerica, MA, USA) using Cu-K α radiation (1.5406 Å) in the 2θ range 20° – 80° with a step size of 0.01° . The Bragg equation was employed to estimate lattice parameters using the main diffraction peaks (111) and (220). Microstructure analysis was carried out using a Scanning Electron Microscope (SEM) Zeiss Ultra 55 SEM (Oberkochen, Germany) with a Zeiss QBSE detector, also equipped with an Oxford energy dispersive X-ray (EDX) detector (PentaFETx3) (Milpitas, CA, USA). The grain size was observed through SEM pictures and estimated using ImageJ on an average of 30 grains.

The electronic transport properties were measured utilizing an in-house developed facility utilizing a four-probe technique [37,38]. Density measurements were obtained using the Archimedes method in ethanol.

3. Results

XRD patterns shown in Figure 1 along with standard Mg₂Si and Mg₂Sn patterns confirm the presence of phases belonging to Mg₂(Si,Sn) for the Li doped sample where there is also one unidentified impurity peak ($\sim 30^\circ$ theta). The peak could be related to Li₂O or SiO₂ but cannot be identified with certainty.

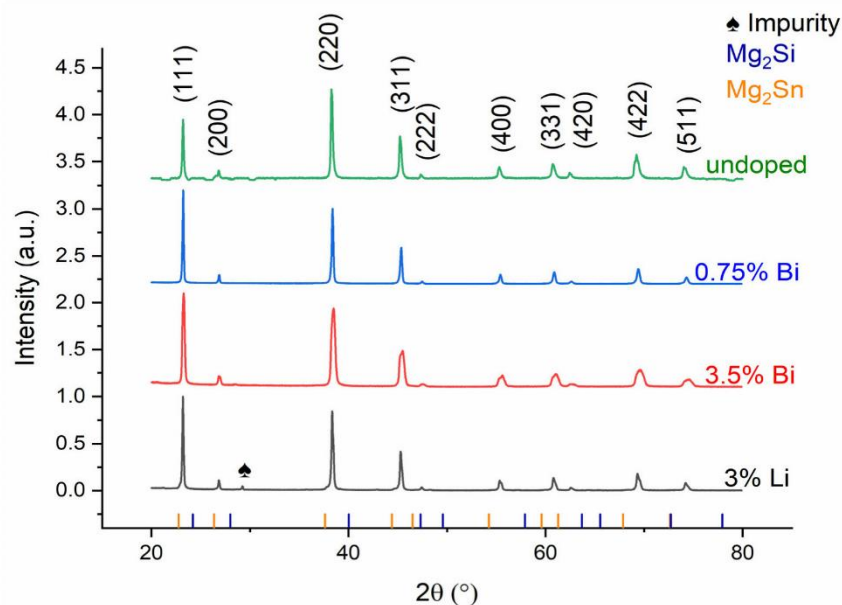


Figure 1. X-ray diffractograms of the samples studied.

As can be seen from Table 2, we do not see a systematic change of the lattice parameter with a change in doping species or with an increasing Bi content. Previous work, in comparison, shows a systematic increase with increasing Bi substitution in the lattice [26,35,39,40] in the range of 0.01–0.03 Å, depending on the Bi amount. This apparent inconsistency could be related to the broadness of the peaks. The n-type with 3.5% Bi has broader XRD peaks compared to other compositions, possibly indicating the presence of several similar phases or compositional variations within one phase. An exemplary deconvolution into two different compositions, see Supporting Information (SI) Figure S1, shows that the (220) peak is composed of 2 main components positioned at $2\theta = 38.379^\circ$ and 37.586° (Table S1 in SI), which correspond to material having an x (Sn content) for $\text{Mg}_2\text{Si}_{1-x}\text{Sn}_x$ of 0.67 and 0.59, respectively. Our research focuses on upscaled material with a higher yield. It is thus not unexpected to find a range of compositions in such a big sample.

The position and occupation fraction of the dopants can thus not be determined from the XRD pattern directly, but it is clear from the thermoelectric properties discussed later on that doping has been successful, i.e., Bi occupies the $4a$ positions, while Li tends to go to the $8c$ position as discussed e.g., in [41].

Table 2. Summary of structural properties for the $\text{Mg}_2\text{Si}_{0.3}\text{Sn}_{0.7}$ samples

Composition	Density (g/cm ³)	Lattice Parameter (Å)	Grain Size (μm)
$\text{Mg}_{1.97}\text{Li}_{0.03}\text{Si}_{0.3}\text{Sn}_{0.7}$	3.10 ± 0.01	6.61 ± 0.01	7 ± 3
$\text{Mg}_{2.06}\text{Si}_{0.3}\text{Sn}_{0.7}$	3.11 ± 0.01	6.63 ± 0.01	7 ± 3
$\text{Mg}_{2.06}\text{Si}_{0.3}\text{Sn}_{0.6925}\text{Bi}_{0.0075}$	3.09 ± 0.01	6.62 ± 0.01	6 ± 2
$\text{Mg}_{2.06}\text{Si}_{0.3}\text{Sn}_{0.665}\text{Bi}_{0.035}$	3.11 ± 0.01	6.61 ± 0.01	5 ± 3

The grain size of all samples is comparable, which is most likely due to the similar preparation route. An example can be seen in SI Figure S2.

Samples obtained using the same method and the same parameters have recently been shown to have state-of-the-art thermoelectric properties with $zT_{\text{max}} = 1.3$ at 773 K for the n-type [10]. The high carrier concentrations reported in these works $n \sim 10^{20} \text{cm}^{-3}$ prove that the dopants have been incorporated and are active. The charge carrier density was estimated assuming a single parabolic band model and using the measured Seebeck coefficient as well as an effective mass of $m_D^* = 1.43$ for the p-type material, while $m_D^* = 2.5$ was used for the n-type and undoped materials [13,42]. The mobility (μ) was estimated using the equation $\zeta = ne\mu$ where ζ is the electrical conductivity, n is the charge carrier density, and e is the charge of an electron. Electronic transport properties of the samples are shown in Table 3

Table 3. Electronic transport properties shown by the $\text{Mg}_2\text{Si}_{0.3}\text{Sn}_{0.7}$ samples at 25 °C.

Composition	Seebeck (μV/K)	Electrical Conductivity (S/cm)	n (cm ⁻³)	Mobility (cm ² /Vs)
$\text{Mg}_{1.97}\text{Li}_{0.03}\text{Si}_{0.3}\text{Sn}_{0.7}$	101	644	1.7×10^{20}	24
$\text{Mg}_{2.06}\text{Si}_{0.3}\text{Sn}_{0.7}$	−453	29	3.7×10^{18}	50
$\text{Mg}_{2.06}\text{Si}_{0.3}\text{Sn}_{0.6925}\text{Bi}_{0.0075}$	−157	1178	1.4×10^{20}	53
$\text{Mg}_{2.06}\text{Si}_{0.3}\text{Sn}_{0.665}\text{Bi}_{0.035}$	−114	2138	2.8×10^{20}	48

Our previous work has proven that the material shows a linear dependence of elastic moduli on x [24]; this work also provides evidence on the little difference in the mechanical properties we would expect for such small differences in composition.

Previous work on Bi-doped $\text{Mg}_2(\text{Si},\text{Sn})$ shows that the lattice parameter keeps on increasing beyond 3 at.% Bi, however, the solubility limit can be assumed to be between 3

at.% and 4 at.% from the Seebeck and electrical conductivity values reported in [34]. It is therefore highly plausible that the range of Bi content within this study is within the solubility limit of Bi in $\text{Mg}_2(\text{Si},\text{Sn})$. Comparison with the work of Nieroda *et al.* [16] furthermore indicates that the Li-content in our sample is well below the solubility limit. The room temperature mechanical properties exhibited by the samples are shown in Figure 2. Samples without Bi have a slightly higher Young's modulus.

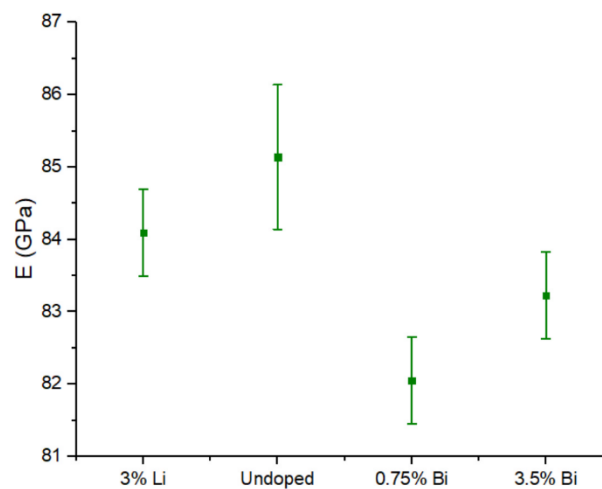


Figure 2. Room temperature Young's modulus of the $\text{Mg}_2\text{Si}_{0.3}\text{Sn}_{0.7}$ samples.

All materials studied in this work exhibit a general similarity in mechanical properties. This behavior is presumably due to the overall similarity in composition but the minor differences in composition lead to some small differences in high temperature Young's modulus. Such differences can be seen in Figure 3. Undoped and p-type Li-doped samples show the same slope of temperature dependency and a small difference in absolute values.

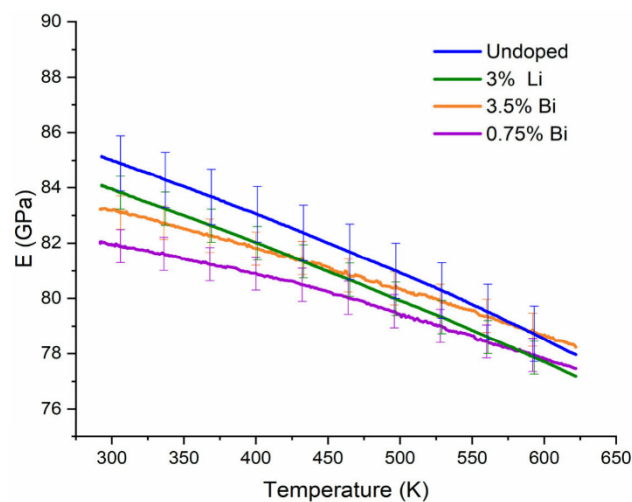


Figure 3. High temperature Young's modulus of the $\text{Mg}_2\text{Si}_{0.3}\text{Sn}_{0.7}$ samples.

We can thus prove that at relevant application temperatures, undoped and both n- and p-type doped $\text{Mg}_2\text{Si}_{0.3}\text{Sn}_{0.7}$ show similar absolute values and similar temperature dependence of the Young's moduli. The minor amount of impurity found in the 3% Li doped sample did not affect the room temperature values of the said material significantly.

In our previous work, we provided information about the Poisson ratio and argued that the value could be considered as constant in the temperature region studied by this work [24]. The room temperature measurement results for the shear modulus G are shown in Table 4, as well as the values for Poisson's ratio estimated using the equation $\nu = \frac{E}{2G} - 1$.

Table 4. Room temperature shear modulus and Poisson's ratio.

Composition	Shear Modulus (GPa)	Poisson Ratio
$\text{Mg}_{1.97}\text{Li}_{0.03}\text{Si}_{0.3}\text{Sn}_{0.7}$	35.2 ± 0.3	0.193 ± 0.002
$\text{Mg}_{2.06}\text{Si}_{0.3}\text{Sn}_{0.7}$	35.7 ± 0.3	0.191 ± 0.002
$\text{Mg}_{2.06}\text{Si}_{0.3}\text{Sn}_{0.6925}\text{Bi}_{0.0075}$	32.7 ± 0.3	0.217 ± 0.003
$\text{Mg}_{2.06}\text{Si}_{0.3}\text{Sn}_{0.665}\text{Bi}_{0.035}$	34.6 ± 0.3	0.209 ± 0.002

The coefficient of thermal expansion (α) data as a function of temperature is given in Figure 4 and shows two distinct parts: A strongly non-linear behavior from room temperature to ~400 K, which according to literature, stems from thermal inertia originated from internal stress [43], followed by an almost perfectly linear correlation between temperature and α . The raw data and extrapolation process are shown in the Supplementary Information figure S3.

Previous first principles calculations performed by Ganeshan *et al.* on the binaries Mg_2X ($\text{X} = \text{Si}, \text{Sn}$) predict a linear behavior of both the cell volume and CTE above room temperature [44]. These values were derived from the vibrational free energy per atom calculated from the phonon density of states [44]. Assuming the same linear behavior for our material and taking the values of the second region as well, the CTE values for low temperatures were derived by extrapolating the linear function $\alpha(T)$ from the high temperature regime between 450 and 700 K, and these values are shown in Figure 4. CTE values for the samples range between room temperature and 700 K. The linear function $\alpha(T)$ will be used in subsequent estimations, however an example of raw data for elongation and CTE is available in Supporting Information Figure S4.

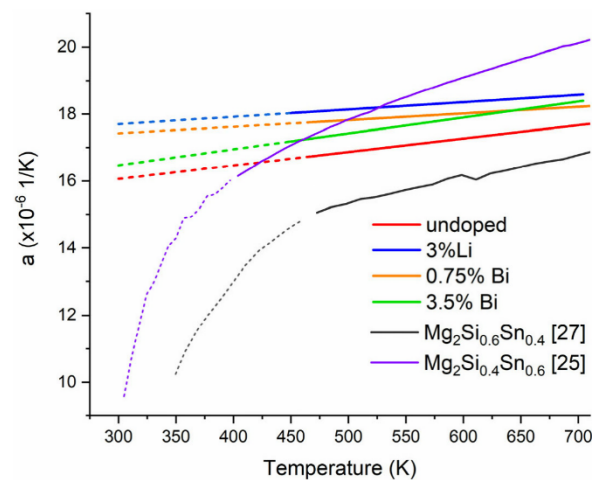


Figure 4. CTE between room temperature and 700 K for all samples of this study and selected literature results. Values for comparison are adapted from [25,27] in purple and black, respectively. Full

lines depict linear behavior range, dashed lines show the extrapolation to room temperature of our measurements, and dotted lines indicate the strongly non-linear region in the reference data.

The α values from the $\text{Mg}_2\text{Si}_{0.4}\text{Sn}_{0.6}$ are consistent with our data. The work done on this material reports a mean value of 17×10^{-6} 1/K [25]. The temperature dependence of the CTE in this work was obtained by dividing the reported elongation value by the temperature at which the data was obtained.

In the case of the $\text{Mg}_2\text{Si}_{0.6}\text{Sn}_{0.4}$, the slope is similar to what we report, albeit with lower absolute values. This can be explained by the increased Si content in the material, as it is known that binary Mg_2Si has an α value of 14×10^{-6} 1/K [45], and therefore a material with a higher Si content would be expected to have a lower CTE, closer to the binary.

4. Discussion

Previous work has detailed the effect of Bi doping on binary Mg_2Si and the Mg_2Si - Mg_2Sn solid solutions; the solubility limit of Bi in the material, as well as its effects on the thermoelectric properties were described in [34,35,39,46], while different mechanical properties of the material with different Bi concentrations were detailed in [26].

The authors of some of the previous works have reported phases outside the Mg_2Si - Mg_2Sn solid solution like MgO , Mg_3Bi_2 , and SiO_2 in the samples, some of which increase systematically as the Bi content increases.

These phases, as well as regions with different x Sn content could affect the mechanical response of the material [47]. Our XRD patterns show a very minor phase not belonging to the Mg_2Si - Mg_2Sn material system, which seems to have no effect on the microstructure or mechanical properties measured.

However, the width of the peaks in the sample with 3.5% Bi is larger than that of the others. The compositions found through deconvolution of the peak have a x Sn content difference below 0.1, which, according to previous work on the dependence of the Young's modulus on the Bi content, would yield a difference in the Young's modulus of < 3 GPa.

Previous studies have described phase formation from the elements into $\text{Mg}_2(\text{Si},\text{Sn})$ under milling, where, in the presence of both Si and Sn, Mg_2Sn tends to form first and then Si from brittle elemental debris slowly diffuses into the $\text{Mg}_2(\text{Si},\text{Sn})$ matrix [48]. This process might be influenced by the miscibility gap in the Mg_2Si - Mg_2Sn quasibinary system which is controversially discussed [49,50]. However, as discussed in [48], this could be the reason for the observed sharp contrast between regions of different Si content.

Longer sintering processes, studied in [44], were found to reduce the size and number of the Si-rich areas. However, a short process is technologically desirable, moreover the interfaces related to these inclusions are also known to act as phonon scatterers, reducing the thermal conductivity [13]. Inclusions with different mechanical properties also influence the mechanical properties. They are an intrinsic way to strengthen a material [51] and thus, a small number of areas with different x Sn content can be beneficial for the overall performance of the TE material.

The phase quantification was done following the procedure described in [52] on the four investigated materials. As detailed in the original publication, the Mg content is taken as constant (66.6 at%) and Si and Sn account for the difference to unity. The only degree of freedom is thus, the Si:Sn ratio.

The gray value obtained from the backscatter electron image was related to a composition measured by EDX, this relationship was then used to estimate the composition in the complete area observed through SEM.

Figure 5 displays SEM images of the four investigated materials. On half of each image, the Sn concentration is displayed as a color-coded overlay.

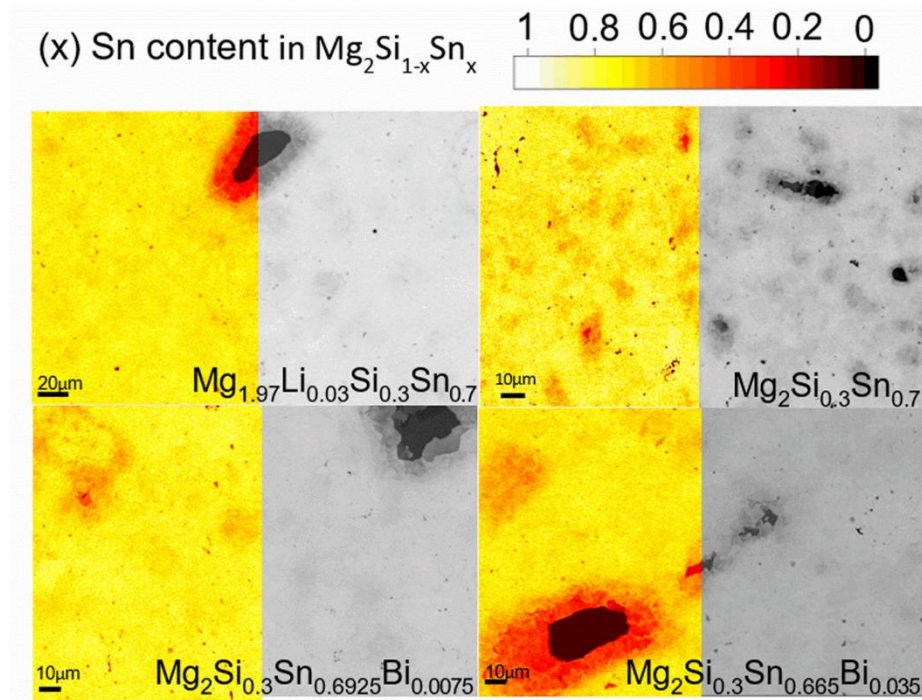


Figure 5. SEM images of the four studied materials; partly overlaid with color-coded plots visualizing the Sn concentration. For undoped material the same SEM picture shown in [24] was used as a base for the analysis.

From the compositional distribution estimated and shown in Figure 5, the mean composition was determined by plotting a histogram of the individual point compositions and fitting a Gaussian peak to the distribution (see SI figure S5). The peak center and full width at half maximum (FWHM) were taken as mean phase composition and its variation respectively. The results are shown in Table 5 whereas the graphs corresponding to the fitting can be found in the Supplementary Information.

Table 5. Mean phase composition as calculated from the grey values from the SEM images by backscattered electrons for $Mg_2Si_{1-x}Sn_x$.

Sample	Sn Content x and FWHM
$Mg_{1.97}Li_{0.03}Si_{0.3}Sn_{0.7}$	0.72 ± 0.11
$Mg_{2.06}Si_{0.3}Sn_{0.7}$	0.73 ± 0.21
$Mg_{2.06}Si_{0.3}Sn_{0.6925}Bi_{0.0075}$	0.74 ± 0.15
$Mg_{2.06}Si_{0.3}Sn_{0.665}Bi_{0.035}$	0.69 ± 0.13

It can be seen that all samples are located around $x = 0.7$ for $Mg_2Si_{1-x}Sn_x$, with similar variation in their composition. This is partially due to the similarity in the preparation method that is melting followed by crushing the ingot in a high energy ball mill. As the mean and distribution width values are estimated from the grey value of the BSE micrographs, the method tends to overestimate the variation in composition.

The composition histogram calculated through the phase quantification was used as a simple base for the calculation of effective mechanical properties, for the following

estimations, the whole histogram (SI) was used and we can define n_i as the fraction of the total material that has a specific i Sn content.

We used the linear equation to predict elastic moduli that we proposed in a previous work: $E(T, x) = E_r + bT + cx$ where $E_r = 116.5 \text{ GPa}$, $b = -0.0234 \text{ GPaK}^{-1}$, and $c = -32.032 \text{ GPa}$. Since the calculations are done at room temperature, we set $T = 300\text{K}$ [24].

Values for x Sn content were taken from the compositional percentages calculated (see SI) and thus the elastic modulus characteristic to that specific composition E_i is defined, we find that both the Voigt ($\bar{E} = \sum_i n_i E_i$) and Reuss ($\bar{E} = (\sum_i n_i / E_i)^{-1}$) approximations yield a theoretical elastic modulus of $87 \pm 2 \text{ GPa}$ for all samples. This is in line with the measured value for the undoped material of 85.14 GPa . The difference to the actual values of the doped samples (which are between 4% and 6% larger) stems probably from using the relation of $E(x)$ for the undoped material, obtained in our previous work whereas the slightly overestimated variation in composition is caused by the quantification method. This variation in turn is within the same range as the precision of the measurement presented.

Mechanical properties are heavily influenced by the nature of the bonding between atoms and hence the composition, in this case the Si:Sn ratio, is known to have an effect on the Young's modulus [24,53].

Similar changes might be expected due to doping, however on a smaller scale due to a smaller change of composition. Such a change is material specific and not clear a priori. Having established that our material is secondary-phase free and confirmed through local composition estimation that the Si:Sn ratio is similar, we can prove that both n- and p-type materials behave similarly at application temperatures. Moreover, the drastic hardness differences reported for Mg₂Si in [26] are most likely linked to secondary phases, not the intrinsic material properties.

In an application, the thermoelectric materials will be assembled in a generator, being soldered or otherwise joined to metallic contact bridges fixed to insulating, often ceramic substrates. In this configuration and with a variation of temperature, stresses will arise due to the different expansion of TE material and bridge.

The magnitude of the stresses occurring in the TEG depend on the design, the operating conditions of the TEG, and the thermal and mechanical properties of the TEG materials. For stationary conditions, the material parameters CTE, Young's modulus and Poisson's ratio are sufficient to calculate the stresses.

For example, the maximum stress σ in a fully restrained material sample, which has been subjected to a temperature change, is defined by Equation (1) [54].

$$\sigma = \frac{Ea(T_0 - T_1)}{1 - \nu} \quad (1)$$

where T_0 and T_1 are the temperatures before and after heating the material sample, ν is the Poisson's ratio, and a is the coefficient of thermal expansion.

If we analyze the case where we are at the threshold of failure, where the fracture tensile stress σ_u is reached, and using Equation (1), we can identify the maximum sudden temperature change $T_0 - T_1$ that a material can withstand [54,55]. This parameter is also called the thermal shock resistance R , which is defined by Equation (2) [54,56]:

$$T_0 - T_1 = \frac{\sigma_u(1-\nu)}{Ea} = R. \quad (2)$$

This equation is valid when the surface temperature of the material sample changes instantaneously.

If the heat transfer is not instant but kept at a constant rate, then the speed at which the heat flows from the core to the outer layer in a cylinder-shaped sample, and from there to the ambient, will also play a decisive role in the stress distribution. In this case, a second thermal resistance parameter, R' , is employed, whose governing equation is:

$$R' = \frac{\kappa\sigma_u(1-\nu)}{Ea} \quad (3)$$

In both cases, the product $E \cdot a$ is an important parameter to characterize a material subjected to temperature differences.

We, therefore, used a linear fit for the thermal dependence of E (as shown in Figure 3) and a (as shown in Figure 4) and plotted the behavior of the product $E \cdot a$ in the target application temperature range 400–620 K as shown in Figure 6. Note that not $E \cdot a / (1 - \nu)$ but $E \cdot a$ is plotted, the order of the curves is slightly modified, see Figure S6 in SI. However, it is still the p-type that develops the highest stress among the optimized TE materials.

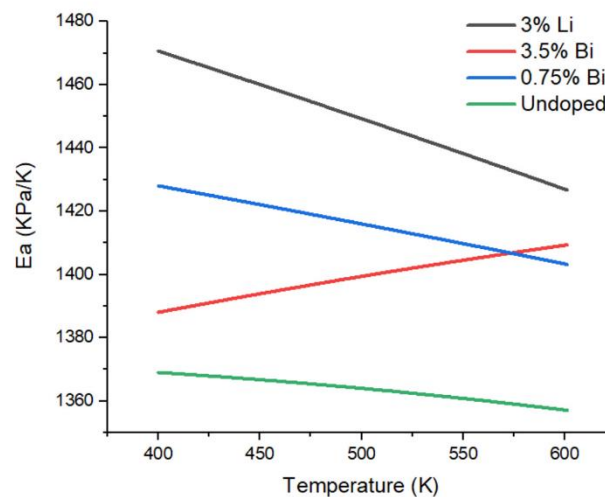


Figure 6. Temperature dependence of ($E \cdot a$), the product of Young's modulus and CTE.

The temperature dependence of $E \cdot a$ in the thermoelectric optimized materials exhibits a convergent behavior. Both n- (3.5% Bi) and p-type (3% Li) exhibit a very similar value at application temperature and thus, are expected to develop similar thermally induced stresses.

Other thermoelectric material systems have comparable $E \cdot a$ values for the temperature range between 400 and 600 K: $\text{Ba}_8\text{Ga}_{16}\text{Ge}_{30}$ shows a value of 1462 kPa/K, while $\text{Sr}_8\text{Ga}_{16}\text{Ge}_{30}$ has a value of 1198 kPa/K. Tellurides show a lower value, with 1148 and 674 for PbTe and Bi₂Te₃, respectively [55]. A more direct comparison can be done to Skutterudites, the mechanical properties of these materials are also well known [32,57] and thus their $E \cdot a$ values can be estimated. Such values range from 1129 kPa/K for $\text{DD}_{0.76}\text{Fe}_{3.4}\text{Ni}_{0.6}\text{Sb}_{12}$ to >1700 kPa/K for CoSb₃. Silicide-based TEG have thus an $E \cdot a$ product comparable to skutterudites, with the added advantage of a lower density and toxicity.

Using the previously detailed parameters, it is also possible to predict the thermally induced stress the material of a single leg of a thermoelectric module could have if it would be confined in length and heated from a homogenous temperature T_0 to higher homogenous temperature T_1 . Using Equation (1) and the data presented in this work, we estimated the theoretical stress the leg would undergo for T_1 values between 400 and 600 K if T_0 is 325 K.

To visualize the effect of using temperature dependent data, this is compared to the hypothetical stress when the room temperature values of E and/or a are employed instead of the temperature dependent data, see Figure 7.

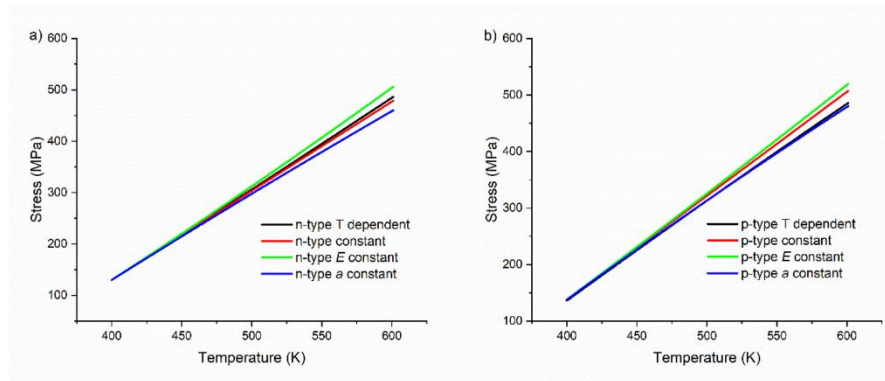


Figure 7. Comparison of thermal stress with both E and a as temperature dependent variables (black), both as constant with RT values (red), only E as constant (green) and only CTE as constant (blue) in material containing (a) 3.5% Bi and (b) 3% Li.

As can be seen from both graphs, the values estimated for thermal stress are at a maximum when the Young's modulus is considered constant. These values ignore the reducing of E with increasing temperature. The temperature dependence of the CTE has a small influence on the thermal stress as $\frac{da}{dT} \approx 10^{-9} K^{-2}$.

By using the temperature dependent elastic modulus, however, the difference in stress at the temperatures studied is close to 10% in comparison to the use of room temperature values.

These thermal stress values, however, only depict the effect of thermal expansion of a single leg and can be taken as an indication for the relevance of T -dependent mechanical properties. For a complete picture, it is necessary to consider, additionally, the effects of the expansion in the bridge and substrate.

5. Conclusions

We presented the temperature dependent elastic properties exhibited by $Mg_{1.97}Li_{0.03}Si_{0.3}Sn_{0.7}$ and $Mg_2Si_{0.3}Sn_{0.665}Bi_{0.035}$ and compared it to undoped and low doped n-type material $Mg_{2.06}Si_{0.3}Sn_{0.6925}Bi_{0.0075}$. We observed a similarity between these values with a relative difference to the values of the undoped material of less than 4% at room temperature. The Young's modulus is for all materials decreasing with an increasing temperature. Microstructural analysis shows that local fluctuation in Si:Sn observed for all samples does not affect their mechanical properties strongly. Furthermore, they can be predicted with good accuracy using the linear equation proposed and the composition range estimated through SEM pictures.

The CTE values for both of these materials were measured. They all share similar values with differences between the n- and p-type being 6% at operating temperature.

The comparison between analytic stress estimation using room temperature measurements and temperature dependent data shows a $\sim 10\%$ difference at $T_0 = 325$ K and $T_1 = 600$ K due to the overestimation of the Young's modulus in the constant data estimation, emphasizing the need for temperature dependent measurements if high accuracy is required.

We found that the difference in elastic moduli behavior in $Mg_{1.97}Li_{0.03}Si_{0.3}Sn_{0.7}$ and $Mg_2Si_{0.3}Sn_{0.665}Bi_{0.035}$ is partially accounted for with the difference in CTE, as the thermal stress developed by the legs is very similar. The similarity of both Young's modulus and CTE in n- and p-type further confirms the viability of using $Mg_2Si_{0.3}Sn_{0.7}$ for TEG development.

The data presented in this work expands the knowledge of mechanical behavior in TE materials, indispensable for developing a functional TEG with long life expectancy. The information is, however, not complete as the fracture stress of the materials is yet to be measured, as are the fatigue limits.

Supplementary Materials: The following supporting information can be downloaded at: www.mdpi.com/1996-1944/15/3/779/s1, Figure S1: Exemplary deconvolution of the (220) peak exhibited by the $Mg_{2.06}Si_{0.3}Sn_{0.665}Bi_{0.035}$ sample; Table S1: Fitted peaks for the XRD spectrum belonging to the sample doped with 3.5% Bi with peaks near the 38° mark highlighted; Figure S2: SEM backscatter image of the $Mg_{2.06}Si_{0.3}Sn_{0.665}Bi_{0.035}$ sample with markings for some grains used to estimate average grain size; Figure S3: (a) Coefficient of thermal expansion for an undoped $Mg_2Si_{0.3}Sn_{0.7}$ after calibration showing the linear and non-linear regimes. (b) fitting and extrapolation done on the same data; Figure S4:(a) Raw data corresponding to elongation and (b) raw data corresponding to CTE, the CTE values were obtained by dividing elongation by temperature; Figure S5: Histograms for local composition quantification showing the mean composition and distribution; Figure S6: Sensitivity to thermal stress in all materials studied.

Author Contributions: Conceptualization, G.C.-H. and J.d.B.; Investigation, G.C.-H.; Writing—Original Draft, G.C.-H.; Writing—Review & Editing, J.d.B.; Writing—Review & Editing, E.M.; Supervision, J.d.B.; Project administration, E.M. All authors have read and agreed to the published version of the manuscript.

Funding: This research received no external funding

Institutional Review Board Statement: Not applicable.

Informed Consent Statement: Not applicable.

Data Availability Statement: The data presented in this study are available on request from the corresponding authors.

Acknowledgments: The authors would like to acknowledge the endorsement of the DLR executive Board Members for Space Research and Technology, as well as the financial support from the Young Research Group Leader Program. GCH would like to thank the Mexican Science and Technology Council (CONACyT) and the German Academic Exchange Service (DAAD) for the PhD fellowship. The authors would also like to acknowledge the contributions of Nicole Knoblauch in measuring CTE, as well as Mohammad Yasseri and Sahar Ayachi for their fruitful discussions. Furthermore, the authors would like to thank Marion Bartsch for the invaluable input in the writing of this manuscript.

Conflicts of Interest: The authors declare no conflict of interest.

References

- Rowe, D.M. General Principles and Basic Considerations. In *Thermoelectrics Handbook Macro to Nano*; Taylor and Francis: Boca Raton, FL, USA, 2006; pp. 1–14.
- Santos, R.; Yamini, S.A.; Dou, S.X. Recent Progress in Magnesium-Based Thermoelectric Materials. *J. Mater. Chem. A* **2018**, *6*, 3328–3341. <https://doi.org/10.1039/C7TA10415D>.
- LeBlanc, S.; Yee, S.K.; Scullin, M.L.; Dames, C.; Goodson, K.E. Material and Manufacturing Cost Considerations for Thermoelectrics. *Renew. Sustain. Energy Rev.* **2014**, *32*, 313–327. <https://doi.org/10.1016/j.rser.2013.12.030>.
- El-Genk, M.S.; Saber, H.H.; Caillat, T. Efficient Segmented Thermoelectric Unicouples for Space Power Applications. *Energy Convers. Manag.* **2003**, *44*, 1755–1772. [https://doi.org/10.1016/S0196-8904\(02\)00217-0](https://doi.org/10.1016/S0196-8904(02)00217-0).
- Sankhla, A.; Patil, A.; Kamila, H.; Yasseri, M.; Farahi, N.; Mueller, E.; de Boor, J. Mechanical Alloying of Optimized $Mg_2(Si, Sn)$ Solid Solutions: Understanding Phase Evolution and Tuning Synthesis Parameters for Thermoelectric Applications. *ACS Appl. Energy Mater.* **2018**, *1*, 531–542. <https://doi.org/10.1021/acs.aem.7b00128>.
- Zaitsev, V.K.; Fedorov, M.I.; Gurieva, E.A.; Eremin, I.S.; Konstantinov, P.P.; Samunin, A.Y.; Vedernikov, M.V. Highly Effective $Mg_2Si_{1-x}Sn_x$ Thermoelectrics. *Phys. Rev. B* **2006**, *74*, 045207. <https://doi.org/10.1103/PhysRevB.74.045207>.
- Liu, W.; Tan, X.; Yin, K.; Liu, H.; Tang, X.; Shi, J.; Zhang, Q.; Uher, C. Convergence of Conduction Bands as a Means of Enhancing Thermoelectric Performance of N-Type $Mg_2Si_{1-x}Sn_x$ Solid Solutions. *Phys. Rev. Lett.* **2012**, *108*, 166601. <https://doi.org/10.1103/PhysRevLett.108.166601>.
- Liu, W.; Chi, H.; Sun, H.; Zhang, Q.; Yin, K.; Tang, X.; Zhang, Q.; Uher, C. Advanced Thermoelectrics Governed by a Single Parabolic Band: $Mg_2Si_{0.3}Sn_{0.7}$, a Canonical Example. *Phys. Chem. Chem. Phys.* **2014**, *16*, 6893–6897. <https://doi.org/10.1039/C4CP00641K>.

9. Dasgupta, T.; Stiewe, C.; de Boor, J.; Müller, E. Influence of Power Factor Enhancement on the Thermoelectric Figure of Merit in Mg₂Si_{0.4}Sn_{0.6} Based Materials. *Phys. Status Solidi A* **2014**, *211*, 1250–1254. <https://doi.org/10.1002/pssa.201300196>.
10. Farahi, N.; Stiewe, C.; Truong, D.Y.N.; de Boor, J.; Müller, E. High Efficiency Mg₂(Si, Sn)-Based Thermoelectric Materials: Scale-up Synthesis, Functional Homogeneity, and Thermal Stability. *RSC Adv.* **2019**, *9*, 23021–23028. <https://doi.org/10.1039/C9RA04800F>.
11. Gao, P.; Berkun, I.; Schmidt, R.D.; Luzenski, M.F.; Lu, X.; Sarac, P.B.; Case, E.D.; Hogan, T.P. Transport and Mechanical Properties of High-ZT Mg₂0.8Si_{0.4}-xSn_{0.6}Sbx Thermoelectric Materials. *J. Electron. Mater.* **2014**, *43*, 1790–1803. <https://doi.org/10.1007/s11664-013-2865-8>.
12. Kamila, H.; Sankhla, A.; Yasseri, M.; Hoang, N.P.; Farahi, N.; Mueller, E.; de Boor, J. Synthesis of P-Type Mg₂Si_{1-x}Sn_x with x = 0–1 and Optimization of the Synthesis Parameters. *Mater. Today Proc.* **2019**, *8*, 546–555. <https://doi.org/10.1016/j.matpr.2019.02.052>.
13. Kamila, H.; Sahu, P.; Sankhla, A.; Yasseri, M.; Pham, H.-N.; Dasgupta, T.; Mueller, E.; de Boor, J. Analyzing Transport Properties of P-Type Mg₂Si-Mg₂Sn Solid Solutions: Optimization of Thermoelectric Performance and Insight into the Electronic Band Structure. *J. Mater. Chem. A* **2019**, *7*, 1045–1054. <https://doi.org/10.1039/C8TA08920E>.
14. de Boor, J.; Dasgupta, T.; Saparamadu, U.; Müller, E.; Ren, Z.F. Recent Progress in P-Type Thermoelectric Magnesium Silicide Based Solid Solutions. *Mater. Today Energy* **2017**, *4*, 105–121. <https://doi.org/10.1016/j.mtener.2017.04.002>.
15. Gao, P.; Davis, J.D.; Poltavets, V.V.; Hogan, T.P. The P-Type Mg₂LixSi_{0.4}Sn_{0.6} Thermoelectric Materials Synthesized by a B₂O₃ Encapsulation Method Using Li₂CO₃ as the Doping Agent. *J. Mater. Chem. C* **2016**, *4*, 929–934. <https://doi.org/10.1039/C5TC03692E>.
16. Nieroda, P.; Kolezynski, A.; Oszejca, M.; Milczarek, J.; Wojciechowski, K.T. Structural and Thermoelectric Properties of Polycrystalline P-Type Mg₂-xLixSi. *J. Electron. Mater.* **2016**, *45*, 3418–3426. <https://doi.org/10.1007/s11664-016-4486-5>.
17. Saparamadu, U.; de Boor, J.; Mao, J.; Song, S.; Tian, F.; Liu, W.; Zhang, Q.; Ren, Z. Comparative Studies on Thermoelectric Properties of P-Type Mg₂Sn_{0.75}Ge_{0.25} Doped with Lithium, Sodium, and Gallium. *Acta Mater.* **2017**, *141*, 154–162. <https://doi.org/10.1016/j.actamat.2017.09.009>.
18. Ayachi, S.; Castillo Hernandez, G.; Pham, N.H.; Farahi, N.; Müller, E.; de Boor, J. Developing Contacting Solutions for Mg₂Si_{1-x}Sn_x-Based Thermoelectric Generators: Cu and Ni₄₅Cu₅₅ as Potential Contacting Electrodes. *ACS Appl. Mater. Interfaces* **2019**, *11*, 40769–40780. <https://doi.org/10.1021/acsami.9b12474>.
19. Pham, N.H.; Farahi, N.; Kamila, H.; Sankhla, A.; Ayachi, S.; Müller, E.; de Boor, J. Ni and Ag Electrodes for Magnesium Silicide Based Thermoelectric Generators. *Mater. Today Energy* **2019**, *11*, 97–105. <https://doi.org/10.1016/j.mtener.2018.10.016>.
20. Biswas, K.; Subramanian, M.A.; Good, M.S.; Roberts, K.C.; Hendricks, T.J. Thermal Cycling Effects on the Thermoelectric Properties of N-Type In, Ce-Based Skutterudite Compounds. *J. Electron. Mater.* **2012**, *41*, 1615–1621. <https://doi.org/10.1007/s11664-012-1975-z>.
21. de Boor, J.; Gloanec, C.; Kolb, H.; Sottong, R.; Ziolkowski, P.; Müller, E. Fabrication and Characterization of Nickel Contacts for Magnesium Silicide Based Thermoelectric Generators. *J. Alloys Compd.* **2015**, *632*, 348–353. <https://doi.org/10.1016/j.jallcom.2015.01.149>.
22. Camut, J.; Pham, N.H.; Nhi Truong, D.Y.; Castillo-Hernandez, G.; Farahi, N.; Yasseri, M.; Mueller, E.; de Boor, J. Aluminum as Promising Electrode for Mg₂(Si, Sn)-Based Thermoelectric Devices. *Mater. Today Energy* **2021**, *21*, 100718. <https://doi.org/10.1016/j.mtener.2021.100718>.
23. de Boor, J.; Droste, D.; Schneider, C.; Janek, J.; Mueller, E. Thermal Stability of Magnesium Silicide/Nickel Contacts. *J. Electron. Mater.* **2016**, *45*, 5313–5320. <https://doi.org/10.1007/s11664-016-4716-x>.
24. Castillo-Hernandez, G.; Yasseri, M.; Klobes, B.; Ayachi, S.; Müller, E.; de Boor, J. Room and High Temperature Mechanical Properties of Mg₂Si, Mg₂Sn and Their Solid Solutions. *J. Alloys Compd.* **2020**, *845*, 156205. <https://doi.org/10.1016/j.jallcom.2020.156205>.
25. Gelbstein, Y.; Tunbridge, J.; Dixon, R.; Reece, M.J.; Ning, H.; Gilchrist, R.; Summers, R.; Agote, I.; Lagos, M.A.; Simpson, K.; et al. Physical, Mechanical, and Structural Properties of Highly Efficient Nanostructured n- and p-Silicides for Practical Thermoelectric Applications. *J. Electron. Mater.* **2014**, *43*, 1703–1711. <https://doi.org/10.1007/s11664-013-2848-9>.
26. Vivekanandhan, P.; Murugasami, R.; Kumaran, S. Microstructure and Mechanical Properties of Magnesium Silicide Prepared via Spark Plasma Assisted Combustion Synthesis. *Mater. Lett.* **2018**, *231*, 109–113. <https://doi.org/10.1016/j.matlet.2018.08.017>.
27. Mejri, M.; Thimont, Y.; Malard, B.; Estournès, C. Characterization of the Thermo-Mechanical Properties of p-Type (MnSi_{1.77}) and n-Type (Mg₂Si_{0.6}Sn_{0.4}) Thermoelectric Materials. *Scr. Mater.* **2019**, *172*, 28–32. <https://doi.org/10.1016/j.scriptamat.2019.06.037>.
28. Nakamura, T.; Hatakeyama, K.; Minowa, M.; Mito, Y.; Arai, K.; Iida, T.; Nishio, K. Power-Generation Performance of a π -Structured Thermoelectric Module Containing Mg₂Si and MnSi_{1.73}. *J. Electron. Mater.* **2015**, *44*, 3592–3597. <https://doi.org/10.1007/s11664-015-3910-6>.
29. Ni, J.E.; Case, E.D.; Schmidt, R.D.; Wu, C.-I.; Hogan, T.P.; Trejo, R.M.; Kirkham, M.J.; Lara-Curzio, E.; Kanatzidis, M.G. The Thermal Expansion Coefficient as a Key Design Parameter for Thermoelectric Materials and Its Relationship to Processing-Dependent Bloating. *J. Mater. Sci.* **2013**, *48*, 6233–6244. <https://doi.org/10.1007/s10853-013-7421-7>.
30. Barako, M.T.; Park, W.; Marconnet, A.M.; Asheghi, M.; Goodson, K.E. Thermal Cycling, Mechanical Degradation, and the Effective Figure of Merit of a Thermoelectric Module. *J. Electron. Mater.* **2013**, *42*, 372–381. <https://doi.org/10.1007/s11664-012-2366-1>.

31. Karri, N.K.; Mo, C. Reliable Thermoelectric Module Design under Opposing Requirements from Structural and Thermoelectric Considerations. *J. Electron. Mater.* **2018**, *47*, 3127–3135. <https://doi.org/10.1007/s11664-017-5934-6>.
32. Zhang, L.; Rogl, G.; Grytsiv, A.; Puchegger, S.; Koppensteiner, J.; Spieckermann, F.; Kabelka, H.; Reinecker, M.; Rogl, P.; Schranz, W.; et al. Mechanical Properties of Filled Antimonide Skutterudites. *Mater. Sci. Eng. B* **2010**, *170*, 26–31. <https://doi.org/10.1016/j.mseb.2010.02.022>.
33. Farahi, N.; VanZant, M.; Zhao, J.; Tse, J.S.; Prabhudev, S.; Botton, G.A.; Salvador, J.R.; Borondics, F.; Liu, Z.; Kleinke, H. Sb- and Bi-Doped Mg₂Si: Location of the Dopants, Micro- and Nanostructures, Electronic Structures and Thermoelectric Properties. *Dalton Trans.* **2014**, *43*, 14983–14991. <https://doi.org/10.1039/C4DT01177E>.
34. Macario, L.R.; Cheng, X.; Ramirez, D.; Mori, T.; Kleinke, H. Thermoelectric Properties of Bi-Doped Magnesium Silicide Stannides. *ACS Appl. Mater. Interfaces* **2018**, *10*, 40585–40591. <https://doi.org/10.1021/acsami.8b15111>.
35. Ioannou, M.; Polymeris, G.S.; Hatzikraniotis, E.; Paraskevopoulos, K.M.; Kyratsi, T. Effect of Bi-Doping and Mg-Excess on the Thermoelectric Properties of Mg₂Si Materials. *J. Phys. Chem. Solids* **2014**, *75*, 984–991. <https://doi.org/10.1016/j.jpcs.2014.04.008>.
36. ASTM Standard E1876-01, 2017, "Method for Dynamic Youngs Modulus, Shear Modulus, and Poissons Ratio by Impulse Excitation of Vibration," ASTM International, West Conshohocken, PA, 2017, DOI: 10.1520/E1876-01.
37. de Boor, J.; Stiewe, C.; Ziolkowski, P.; Dasgupta, T.; Karpinski, G.; Lenz, E.; Edler, F.; Mueller, E. High-Temperature Measurement of Seebeck Coefficient and Electrical Conductivity. *J. Electron. Mater.* **2013**, *42*, 1711–1718. <https://doi.org/10.1007/s11664-012-2404-z>.
38. de Boor, J.; Müller, E. Data Analysis for Seebeck Coefficient Measurements. *Rev. Sci. Instrum.* **2013**, *84*, 065102. <https://doi.org/10.1063/1.4807697>.
39. Nieroda, P.; Leszczynski, J.; Kolezynski, A. Bismuth Doped Mg₂Si with Improved Homogeneity: Synthesis, Characterization and Optimization of Thermoelectric Properties. *J. Phys. Chem. Solids* **2017**, *103*, 147–159. <https://doi.org/10.1016/j.jpcs.2016.11.027>.
40. Fiameni, S.; Battiston, S.; Boldrini, S.; Famengo, A.; Agresti, F.; Barison, S.; Fabrizio, M. Synthesis and Characterization of Bi-Doped Mg₂Si Thermoelectric Materials. *J. Solid State Chem.* **2012**, *193*, 142–146. <https://doi.org/10.1016/j.jssc.2012.05.004>.
41. Ayachi, S.; Deshpande, R.; Ponnusamy, P.; Park, S.; Chung, J.; Park, S.; Ryu, B.; Müller, E.; Boor, J. On the Relevance of Point Defects for the Selection of Contacting Electrodes: Ag as an Example for Mg₂ (Si, Sn)-Based Thermoelectric Generators. *Mater. Today Phys.* **2021**, *16*, 100309. <https://doi.org/10.1016/j.mtphys.2020.100309>.
42. Farahi, N.; Prabhudev, S.; Botton, G.A.; Salvador, J.R.; Kleinke, H. Nano- and Microstructure Engineering: An Effective Method for Creating High Efficiency Magnesium Silicide Based Thermoelectrics. *ACS Appl. Mater. Interfaces* **2016**, *8*, 34431–34437. <https://doi.org/10.1021/acsami.6b12297>.
43. Pluta, Z.; Hryniewicz, T. Thermal Expansion of Solids. *J. Mod. Phys.* **2012**, *3*, 793–802. <https://doi.org/10.4236/jmp.2012.38104>.
44. Ganeshan, S.; Shang, S.L.; Wang, Y.; Liu, Z.-K. Temperature Dependent Elastic Coefficients of Mg₂X (X = Si, Ge, Sn, Pb) Compounds from First-Principles Calculations. *J. Alloys Compd.* **2010**, *498*, 191–198. <https://doi.org/10.1016/j.jallcom.2010.03.153>.
45. Imai, M.; Isoda, Y.; Udono, H. Thermal Expansion of Semiconducting Silicides β-FeSi₂ and Mg₂Si. *Intermetallics* **2015**, *67*, 75–80. <https://doi.org/10.1016/j.intermet.2015.07.015>.
46. You, S.-W.; Kim, I.-H.; Choi, S.-M.; Seo, W.-S. Thermoelectric Properties of Bi-Doped Mg₂Si_{1-x}Sn_x prepared by Mechanical Alloying. *J. Korean Phys. Soc.* **2013**, *63*, 2153–2157. <https://doi.org/10.3938/jkps.63.2153>.
47. Mura, T. *Micromechanics of Defects in Solids*, 2nd ed.; Mechanics of Elastic and Inelastic Solids; Springer: The Netherlands, Heidelberg, Germany, 1987; ISBN 978-90-247-3256-2.
48. Yasserli, M.; Sankhla, A.; Kamila, H.; Orenstein, R.; Truong, D.Y.N.; Farahi, N.; de Boor, J.; Mueller, E. Solid Solution Formation in Mg₂ (Si, Sn) and Shape of the Miscibility Gap. *Acta Mater.* **2020**, *185*, 80–88. <https://doi.org/10.1016/j.actamat.2019.11.054>.
49. Yasserli, M.; Mitra, K.; Sankhla, A.; de Boor, J.; Müller, E. Influence of Mg Loss on the Phase Stability in Mg₂X (X = Si, Sn) and Its Correlation with Coherency Strain. *Acta Mater.* **2021**, *208*, 116737. <https://doi.org/10.1016/j.actamat.2021.116737>.
50. Orenstein, R.; Male, J.P.; Toriyama, M.; Anand, S.; Snyder, G.J. Using Phase Boundary Mapping to Resolve Discrepancies in the Mg₂Si–Mg₂Sn Miscibility Gap. *J. Mater. Chem. A* **2021**, *9*, 7208–7215. <https://doi.org/10.1039/D1TA00115A>.
51. Launey, M.E.; Ritchie, R.O. On the Fracture Toughness of Advanced Materials. *Adv. Mater.* **2009**, *21*, 2103–2110. <https://doi.org/10.1002/adma.200803322>.
52. Yasserli, M.; Farahi, N.; Kelm, K.; Mueller, E.; de Boor, J. Rapid Determination of Local Composition in Quasi-Binary, Inhomogeneous Material Systems from Backscattered Electron Image Contrast. *Materialia* **2018**, *2*, 98–103. <https://doi.org/10.1016/j.mtla.2018.06.014>.
53. Klobes, B.; de Boor, J.; Alatas, A.; Hu, M.Y.; Simon, R.E.; Hermann, R.P. Lattice Dynamics and Elasticity in Thermoelectric Mg₂Si_{1-x}Sn_x. *Phys. Rev. Mater.* **2019**, *3*, 025404. <https://doi.org/10.1103/PhysRevMaterials.3.025404>.
54. Kingery, W.D. Factors Affecting Thermal Stress Resistance of Ceramic Materials. *J. Am. Ceram. Soc.* **1955**, *38*, 3–15. <https://doi.org/10.1111/j.1151-2916.1955.tb14545.x>.
55. Case, E.D. Thermal Fatigue and Waste Heat Recovery via Thermoelectrics. *J. Electron. Mater.* **2012**, *41*, 1811–1819. <https://doi.org/10.1007/s11664-012-2083-9>.
56. Lanin, A.; Fedik, I. *Thermal Stress Resistance of Materials*; Springer: Berlin/Heidelberg, Germany, 2008; ISBN 978-3-540-71399-9.
57. Rogl, G.; Zhang, L.; Rogl, P.; Grytsiv, A.; Falmbigl, M.; Rajs, D.; Kriegisch, M.; Müller, H.; Bauer, E.; Koppensteiner, J.; et al. Thermal Expansion of Skutterudites. *J. Appl. Phys.* **2010**, *107*, 043507. <https://doi.org/10.1063/1.3284088>.

8. Discussion

This chapter will aim at joining the information presented in chapters 5, 6 and 7 with additional original non-published information on the topic to get a better overview of the goals achieved by this work.

As detailed in chapter 3, our general objective with this work is to provide information that facilitates module design from a mechanical performance point of view.

This work aims at bridging the gap between the existing scarce knowledge on mechanical properties and the progress in TE performance research by providing not only detailed information about mechanical properties of $\text{Mg}_2(\text{Si},\text{Sn})$, but also describing a methodology that can be followed to obtain temperature dependent data for other material systems.

A mechanically sound TE module is described in literature as one composed of legs having similar CTE values [21]. However, expansion of the bridge, and the bending stress it imposes on the TE legs, is rarely taken into account in these kinds of studies. It is thus important, as detailed in chapter 6 and 7, to also characterize the elasticity shown by the TE material.

8.1. The role of secondary phases

With respect to the areas where the contrast is different in the SEM pictures presented in previous chapters when compared to the matrix, chapter 5 refers to them as “secondary phases” where the composition is different from the matrix. However, this is as of yet challenged, as the composition in the material is still Mg_2X , the desired material, and fluctuations within the Sn:Si ratio are expected in this system when process times are low. More accurate examples of a secondary phase would be MgO or elemental Si or Sn, as they do not belong to the solid solution.

The role of these areas is detailed in chapter 5 as strengthening of the matrix against crack propagation, by introducing an interphase between the mean composition of the material and a Si-rich region. These regions exhibit a different lattice parameter and general Si:Sn ratio compared to the matrix. The increased Si content in the material

creates a stiffer bond between Mg and Si and thus, these regions exhibit higher hardness than Sn-richer zones.

However, in the case of macro-properties, such as the Young's modulus, the effect of local compositional fluctuations within the material seems to be less pronounced. This is evident in chapter 6, where the relationship between composition and Young's moduli values for all samples fit very well into a linear model. In this case, although the Si-rich areas are present, they correspond to a very small percentage of the volume within the sample.

This behavior can be explained using a composite material approach, by employing the Reuss and Voigt models for estimation of the effective Young's modulus. Using an estimation of the percentage of material belonging to a specific composition and using the equation $A(T) = A_r + bT + cx$, derived from chapter 6, the Young's modulus expected for that specific mixture of material was estimated. Both approximations yielded good agreement with the measured values.

This situation was not altered when the doping species and amount was varied. Chapter 7 shows that even though the Young's modulus slightly varies with doping, the effective properties can still be predicted with reasonable precision (~4%). Secondary phases out of the Mg_2X system, in the case of the unidentified contamination in the p-type sample shown in Figure 1 Chapter 7 has a negligible effect on the Young's modulus, however it might be due to the fact that this phase was only found in traces amount and cannot be generalized.

8.2. Relationship of Young's modulus with hardness and CTE

It has been established in literature that a higher stiffness (high Young's modulus) is generally accompanied by a higher hardness [115]. However as described in [116], no definite rule can be established to generally encompass all materials. Instead, the relationship between the indenter mechanical properties and those of the sample can be employed by using the reduced modulus E_r , defined as $\frac{1}{E_r} = \frac{(1-\nu^2)}{E} + \frac{(1-\nu_i^2)}{E_i}$ where the subscripts i denote the indenter.

Most indenters for microhardness testing are made of diamond, whose E_i and ν_i values are known to be 1141 GPa and 0.07 respectively.

That same work details that through the use of Oliver and Pharr method [117], there are only two independent variables involved in the amount of energy dissipated or recovered during an indentation process. These being the hardness and the reduced modulus mentioned before. They are related to each other through the recovery resistance R_s defined as $R_s = 2.263 \frac{E_r^2}{H}$ [116]. This resistance parameter is related to the energy that can be dissipated during an indentation, either through a larger imprint or through cracking.

These values, as well as the hardness and Young's modulus are presented in **Table 8-1**

Table 8-1 Hardness, moduli and recovery resistance for $Mg_2Si_{1-x}Sn_x$

X Sn content in $Mg_2Si_{1-x}Sn_x$	Hardness (GPa)	Young's Modulus (GPa)	Reduced Modulus (GPa)	Recovery resistance (GPa)
1	2.45	78.70	91.51	7746.33
0.7	3.69	86.30	99.21	6029.46
0.6	4.02	89.88	101.81	5832.91
0.5	4.67	91.33	101.90	5028.26
0.4	5.02	102.88	114.47	5903.47
0	5.56	109.30	119.42	5801.92

Using the data gathered in chapters 5 through 7, the recovery resistance was compared to imprint size ($2d$) and total crack length ($2c$) as shown in **Figure 8-1**

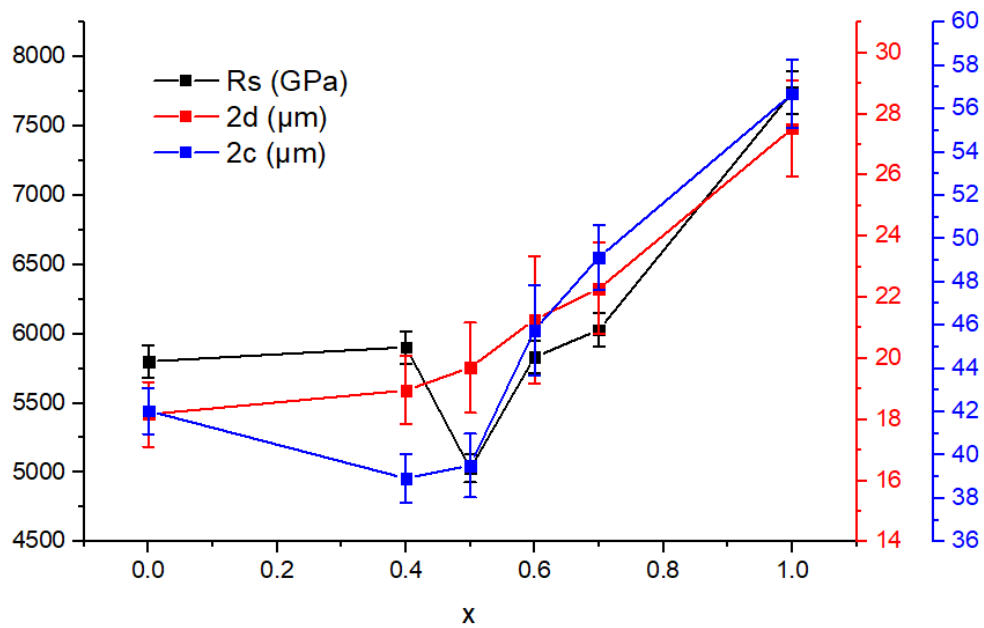


Figure 8–1 Composition dependent recovery resistance, total crack length ($2c$) and imprint size ($2d$) for $Mg_2Si_{1-x}Sn_x$

It can be seen that the samples with greater amounts of inhomogeneity XRD wise ($x = 0.4-0.5$) have a disproportionately small total crack length in comparison with the imprint size. This was attributed to the role of Si-rich areas deflecting cracks and strengthening the material. This confirms that a desired unmixing of the Mg_2X over the miscibility gap would not only improve the material by reducing thermal conductivity but also by improving its mechanical properties.

The recovery resistance also remains roughly constant for all solid solution samples and the binary Mg_2Si . Binary Mg_2Sn has a disproportionately large recovery energy, that comes in agreement to the observations made in chapter 5 about the fracture toughness of the materials studied.

When comparing the recovery resistance to the Young's modulus shown in **Figure 8–2**, both values at $x = 0.4$ are high. This is probably due to the phase separation present in this sample. Si-rich phases would then make the material stiffer (elevating the Young's modulus value) as well as shorten and deflect cracks and prevent plastic deformation through indentation.

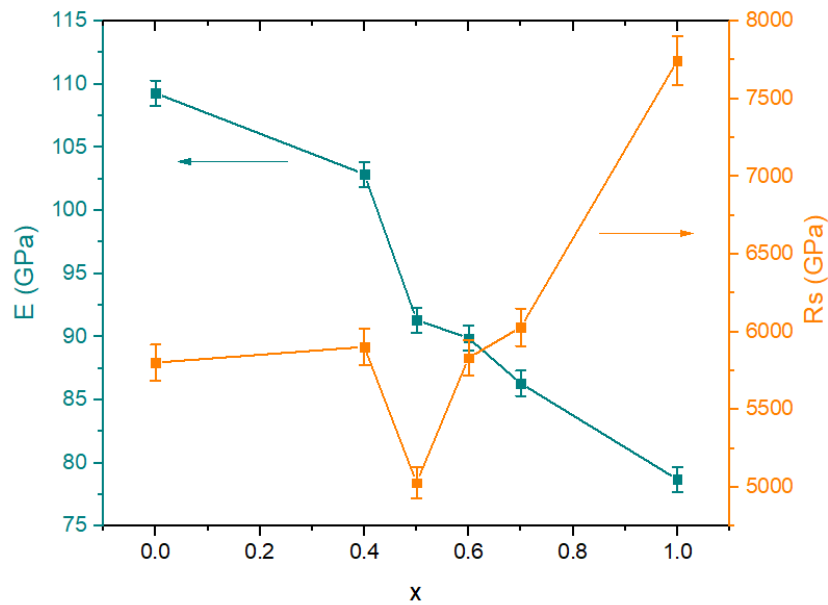


Figure 8–2 Comparison of the recovery resistance to the Young's modulus over the solid solution series $Mg_2Si_{1-x}Sn_x$

Lower values of the recovery resistance are characteristic to materials whose ability to recover from localized deformation is high. Binary Mg_2Si and the solid solution get this characteristic through intrinsic or extrinsic strengthening of their lattice.

8.3. Influence of material synthesis method on microstructure and hardness

Sample preparation originally started with ball milled powder obtained through the same preparation as in [63, 73]. However, geometrical constraints for measurement of mechanical properties require larger samples. This in turn means larger batches of material synthesis and compaction. Two options were tried to fabricate this material, gas atomization and a hybrid melting-milling method, the latter being described in chapter 4.1 and employed heavily for the sample fabrication of this thesis.

Samples from gas atomization did not have optimized TE properties, but powder was readily available from a previous batch. 30 mm and 50 mm pellets were pressed and cut to long rods for testing in the IET. 30 mm samples proved to be unreliable as the frequencies produced were too high (due to the sample length being too short and thus, too stiff) that yielded unrealistically high values for Young's modulus because of

equipment limitations on sample size. However, from a 50 mm pellet a 43 x 12 x 3 mm³ sample was produced fitting for testing at both room and high temperature.

Using this information, it was clear that large samples were needed and thus, large amounts of powder would be needed. The melting route was selected due to the faster processing time and the better control of Mg loss during synthesis compared to gas atomization, albeit with a smaller batch size.

XRD characterization was performed on all samples. Diffractograms are presented in **Figure 8–3**. Samples pressed from gas atomized powder showed impurities of elemental Bi. This is probably the reason behind the poor TE performance achieved by the material. All other samples showed good purity without secondary phases not belonging to the Mg₂(Si,Sn) system.

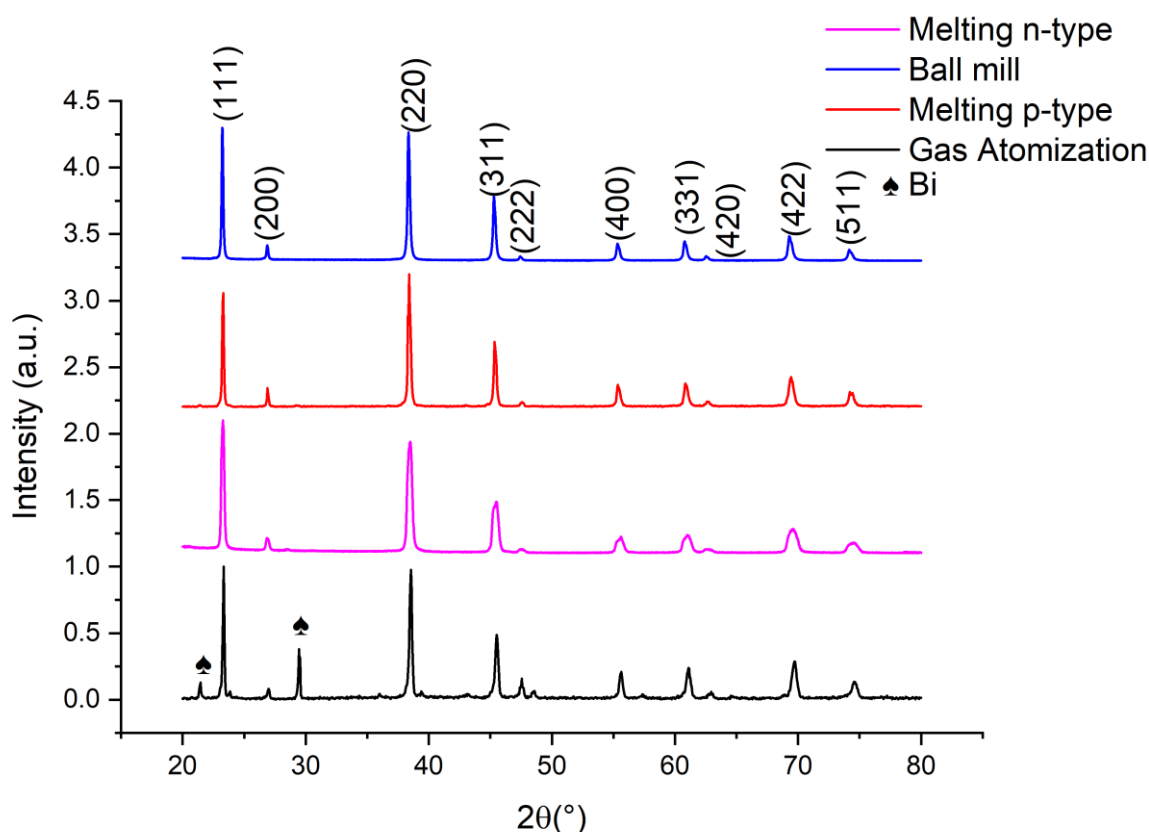


Figure 8–3 X-ray diffractograms from samples obtained by pressing powder synthesized by different methods

Grain size was also similar in all samples, since all samples were pressed for the same time (20 min) under a relatively high temperature (973 K). It is possible that smaller grains were coarsening into bigger ones. This would leave only grains in the ranges mentioned in **Table 8-2** present in the material.

Table 8-2 Summary of structural and mechanical data for material $Mg_2Si_{0.3}Sn_{0.665}Bi_{0.035}$ synthesized through different methods: ball milled samples following [60, 73] and melting samples following [118].

Synthesis methods	Grain size (μm)	Lattice parameter (\AA)	Young's modulus (GPa)	Density (g/cm^3)
Gas atomization	6 ± 3	6.60	78 ± 3	3.07
Ball milling	5 ± 2	6.61	-	3.10
Melting + Ball milling	7 ± 3	6.61	84 ± 1	3.09

As mentioned earlier, mechanical characterization was possible on the samples obtained from gas atomization and melting, but the samples obtained through ball milling could not be measured due to their smaller size. It can be seen that the gas atomization sample has a lower Young's modulus. Segregated Bi and lower density of the sample are probably the reasons behind this lower value.

Another point of comparison between the different synthesis methods was the Vickers Hardness of the material as shown in **Figure 8-4**

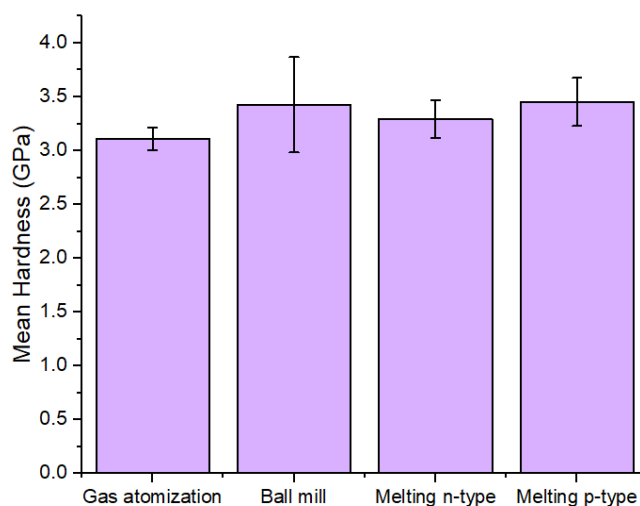


Figure 8-4 Vickers hardness of samples pressed from powder synthesized by different processes.

It can be seen that all materials, independent of the preparation method, have a similar hardness value. This is most likely due to the similar microstructure. It is particularly interesting to note that the gas atomization material did not exhibit different hardness

values compared to the other samples, in contrast to what the Young's modulus measurement showed.

Characterization through SEM imaging also provides information about the similarity between all samples. Si-rich areas are present in a similar pattern as shown in **Figure 8-5**

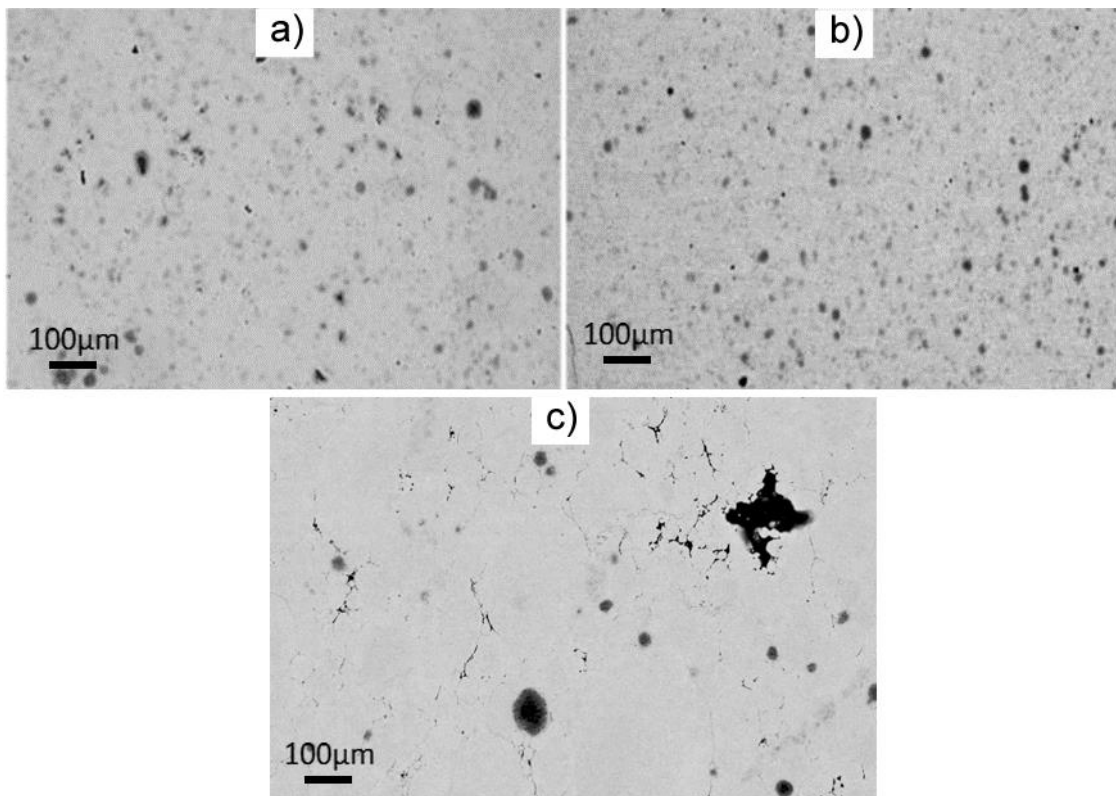


Figure 8-5 SEM backscatter images for $Mg_2Si_{0.3}Sn_{0.665}Bi_{0.035}$ samples synthesized by a) melting + milling, b) ball milling and c) gas atomization. All samples were compacted at 66 MPa and 700 °C for 20 min.

As can be seen from the pictures, the gas atomized powder was not completely densified as particle boundaries can still be seen with gaps between them. The Si-rich phases have a roughly similar size and distribution in a) and b), gas atomization sample shows larger, albeit fewer Si-rich regions.

Secondary phases outside the $Mg_2(Si,Sn)$ system are only present in material from the gas atomization process. This process also produces a sample with lower density compared to the other methods. However, hardness values do not seem to be affected by either the lower density or the secondary phases.

The dependence of mechanical properties on the synthesis parameters was not investigated in full depth. However, it was exemplarily shown here that quite different synthesis routes can yield similar microstructural properties and thus, similar Young's modulus and hardness. Such findings extend the conclusion from chapter 7 where it was shown that a change of carrier type results also only in a minor change of the mechanical response.

8.4. Mechanical modelling of a $\text{Mg}_2(\text{Si},\text{Sn})$ pn-couple considering the temperature dependence of the material properties

To identify the effect of the temperature dependence of mechanical material properties (E , G , CTE) on the mechanical response of a module, a simple model of a uni-couple was developed in SolidWorks.

The uni-couple consists of a pair of legs, joined together by a copper bridge. Additional copper contacts were added at the bottom side of the legs. The geometry of the model is kept similar to literature reports [7, 8, 119–121] and can be observed in **Figure 8–6**. The model is studied under the assumption that electrical current is not flowing through the assembly, thus Peltier and Joule heating effects are disregarded.

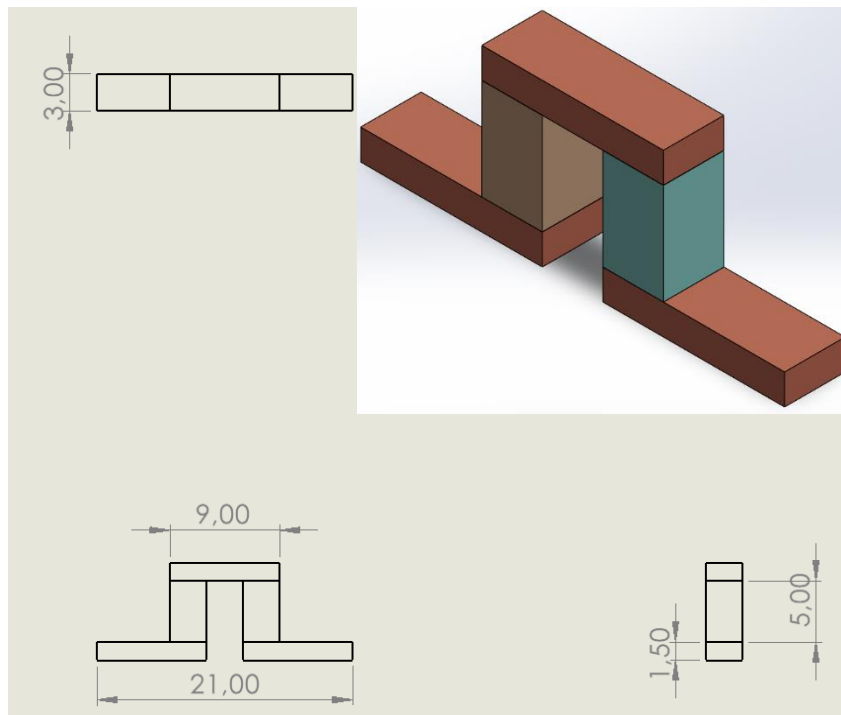


Figure 8–6 Dimensions in mm and 3D geometry of the model employed for FEM analysis, with the n-type on the left and p-type on the right.

In order to keep the model simple, both legs had exactly the same geometry. This is also common in real TE modules, even though having legs with the same geometry does not lead to an optimum in energy conversion if the thermoelectric properties (specifically zT) are different for the n and p-type material, as is the case for Mg_2X [7, 8, 119].

The mechanical data for the copper was taken from the SolidWorks library. These values correspond to a DIN copper alloy Cu-DHP. The mechanical data for the thermoelectric materials were taken from the results detailed in chapter 7. The thermoelectric legs were composed of $Mg_2Si_{0.3}Sn_{0.665}Bi_{0.035}$ for the n-type and $Mg_{1.97}Li_{0.03}Si_{0.3}Sn_{0.7}$ for the p-type. These compositions were chosen for their reported good thermoelectric properties [60, 77, 101, 102]. **Table 8-3** summarizes the data used for room temperature calculations.

Table 8-3 Mechanical data used in the model.

<i>Property</i>	<i>Young's modulus (GPa)</i>	<i>Poisson ratio</i>	<i>CTE (10^{-6} 1/K)</i>	<i>Thermal conductivity (W/mK)</i>	<i>Density (g/cm³)</i>
<i>N-type</i>	83,3	0,209	16,5	2,96	3,11
<i>P-type</i>	84,1	0,193	17,6	2,43	3,09
<i>Bridge (Cu-DHP)</i>	120	0,37	17	384	8,9

The raw data, fitting procedure and temperature dependent data for the thermoelectric materials is available in the Appendix 2.

The zero-stress condition for the model was set at 22 °C. The residual stress within the module after soldering is not taken into account here, these stresses were ignored in order to keep the model simple. However, in a real case, cooling down from the processing temperature, as well as solidification of the solder material will produce residual stress in the module.

The thermal boundary conditions were as follows: a temperature of 300 °C was set to the hot side of the assembly, while the cold side was kept at 22 °C. Temperature dependent thermal conductivity values for the TE material were used in all cases. The temperature profile obtained is shown in **Figure 8-7**.

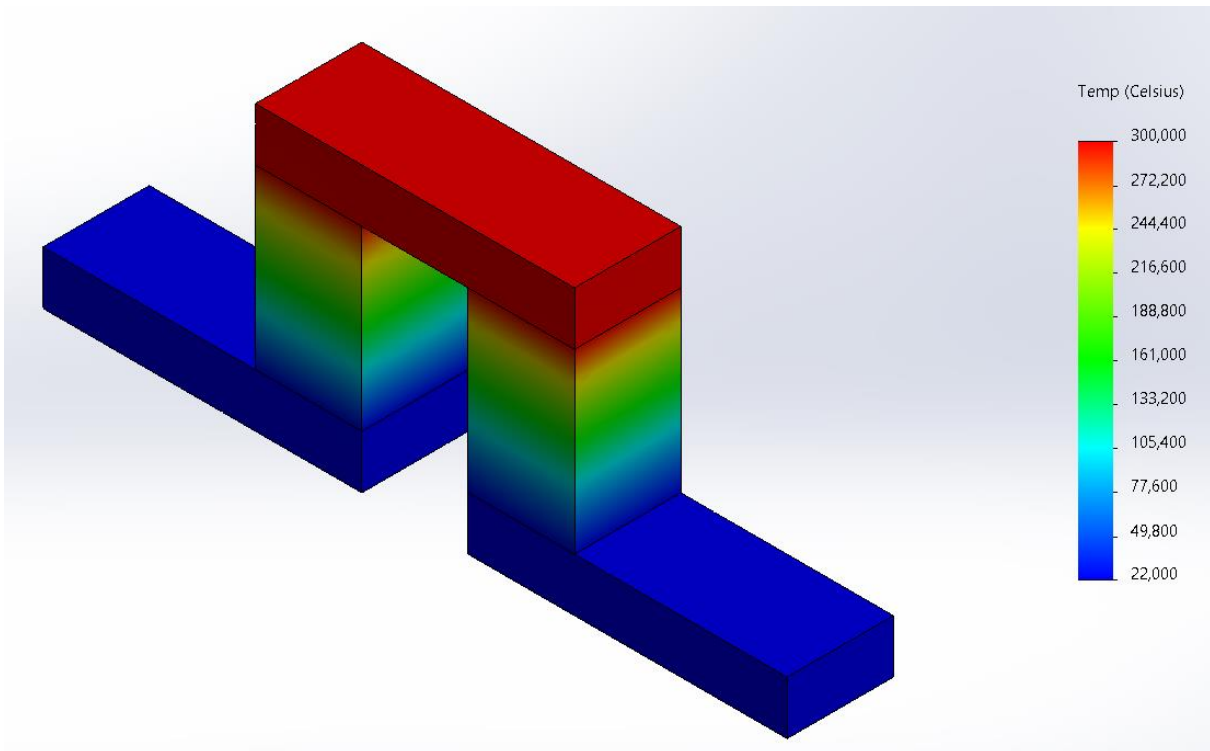


Figure 8–7 Temperature distribution used for the simulation

Five main cases were studied that were chosen to identify the effect of using temperature dependent data in comparison with constant room temperature and averaged properties.

The average property is estimated using the equation $\bar{A} = \frac{\sum_{T_c}^T A(T_i)}{\sum n_i}$

where A is any temperature dependent property and n_i the number of temperature points taken. The average was taken using 100 datapoints obtained using the equations for temperature dependent properties (see Appendix).

These conditions are summarized in **Table 8-4**

Table 8-4 Material properties employed for each of the 5 different cases studied, here E is the Young's modulus, CTE the coefficient of thermal expansion

Case	A	B	C	D	E
N-type E	Constant RT	Constant avg	Constant RT	T-dependent	T-dependent
N-type CTE			T-dependent	Constant RT	
P-type E			Constant RT	T-dependent	
P-type CTE			T-dependent	Constant RT	
Bridge	Constant				

Although case E is the closest to the real situation, adding cases A-D helps isolate the individual effects of certain properties, as well as a comparative tool to correlate with the literature process of constant property simulation.

While the TE module assembly with mechanical fixation by ceramic plates (e.g. Direct Bonded Copper (DBC)) on top and bottom side is practically quite common, several examples of assemblies with a DBC only on the cold side are found [121]. The model presented here corresponds to having no DBC on the hot side and the mechanical constraints will be chosen accordingly. The lower nodes in the model (cold side) were fixed in all 6 degrees of freedom, no translation or rotation was allowed. This is chosen to represent the copper contact being firmly bonded to an Al_2O_3 plate that does not expand. The upper nodes are left free, analogous to a plate-less thermoelectric module. A simple diagram showing these restraints is shown in **Figure 8-8**

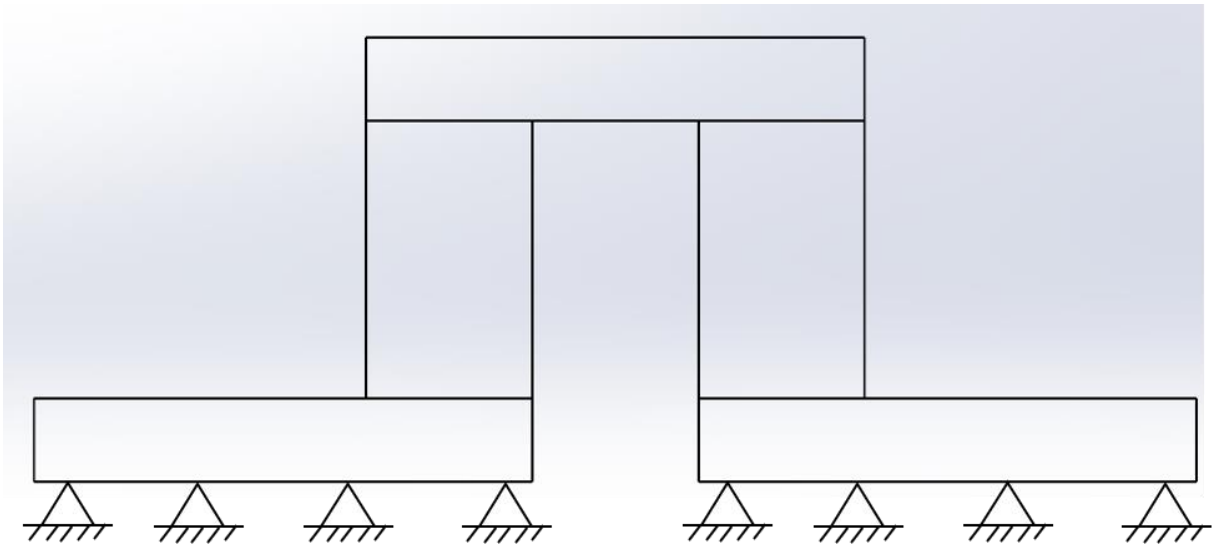


Figure 8–8 Diagram showing the model and the mechanical constraints

Meshing was done using the standard mesh type and an element size of 0.6 mm, comparable to previous studies where a size of 1 mm was chosen [120]. The mesh is shown in **Figure 8–9**.

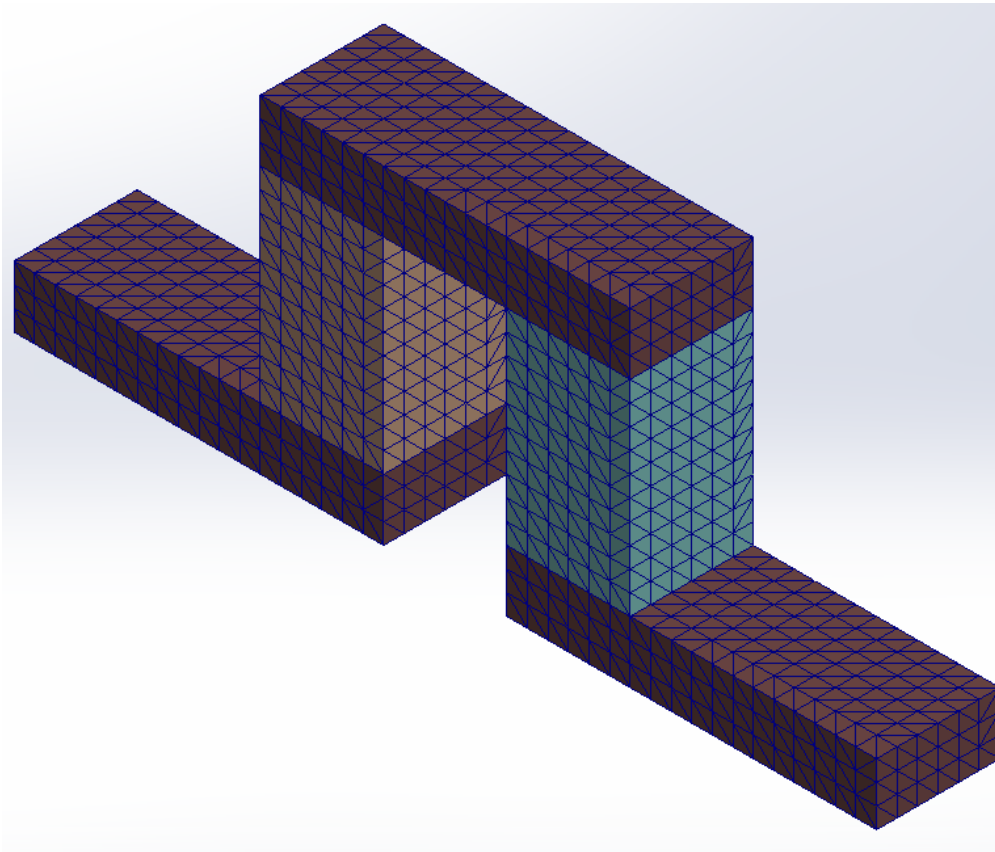


Figure 8–9 Meshed model

Only figures for cases A (all properties RT constant) and E (all T-dependent) are shown, the summary at the end displays also data for the other cases. Along with the von Mises equivalent stress, the maximum principal and shear stress in the xz plane are presented. This approach was initially proposed by Karri [7], where additional parameters besides von Mises stress were used to study TE module stability.

All the results presented next have the same exaggeration factor for deformation, 60.

The von Mises stress distribution for both presented cases is shown in **Figure 8–10**

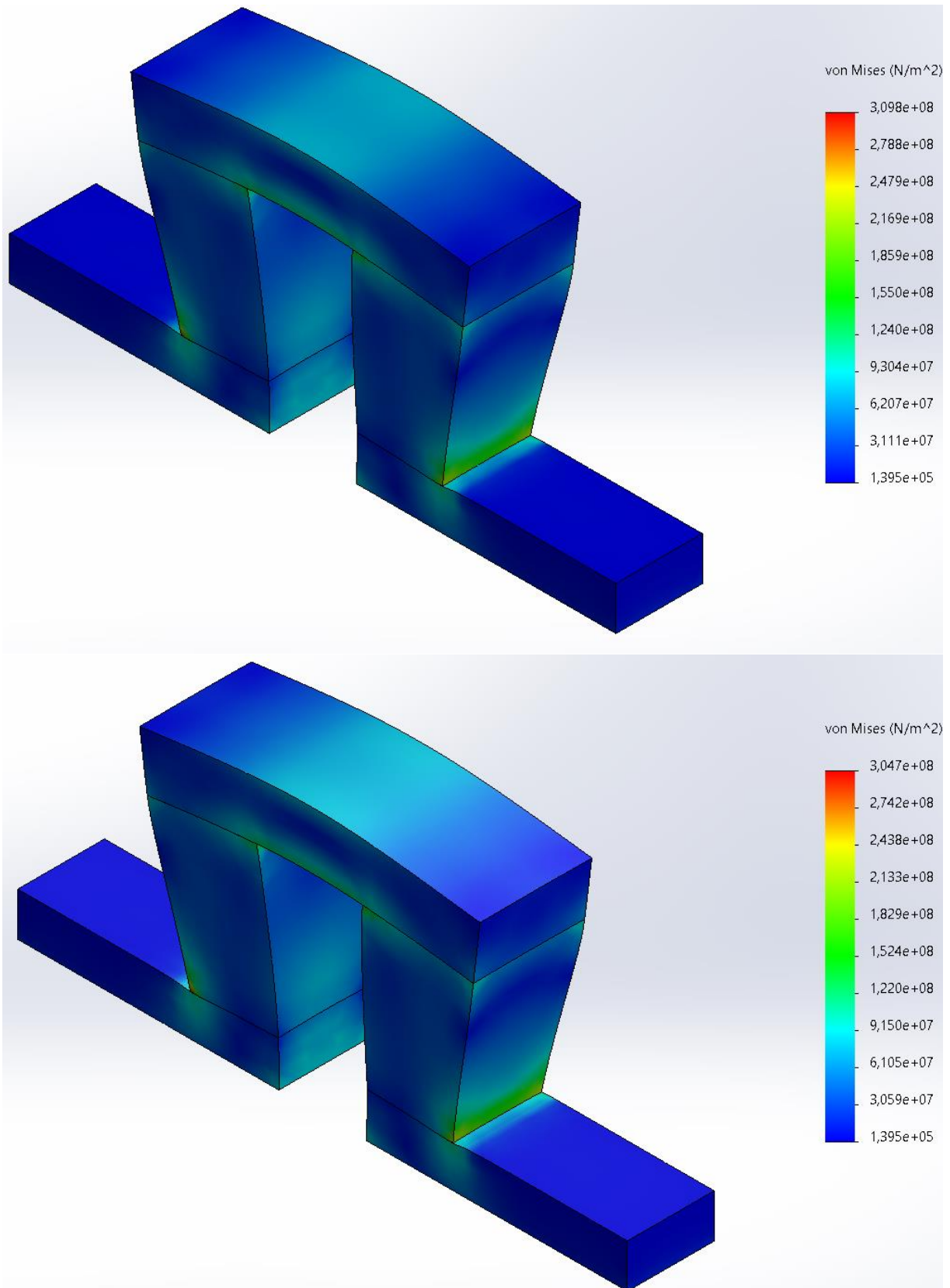


Figure 8–10 von Mises stress distribution for material properties a) all RT constant and b) all temperature dependent 25 – 300°C.

The stress distribution is similar in both cases, with the highest stress concentration happening around the area where the leg is in contact with the lower electrode. In this region, compressive stresses are caused by the expansion of the bridge on top of the legs.

The maximum first principal stress (which is the most positive of the three main stress values) is shown in **Figure 8–11**.

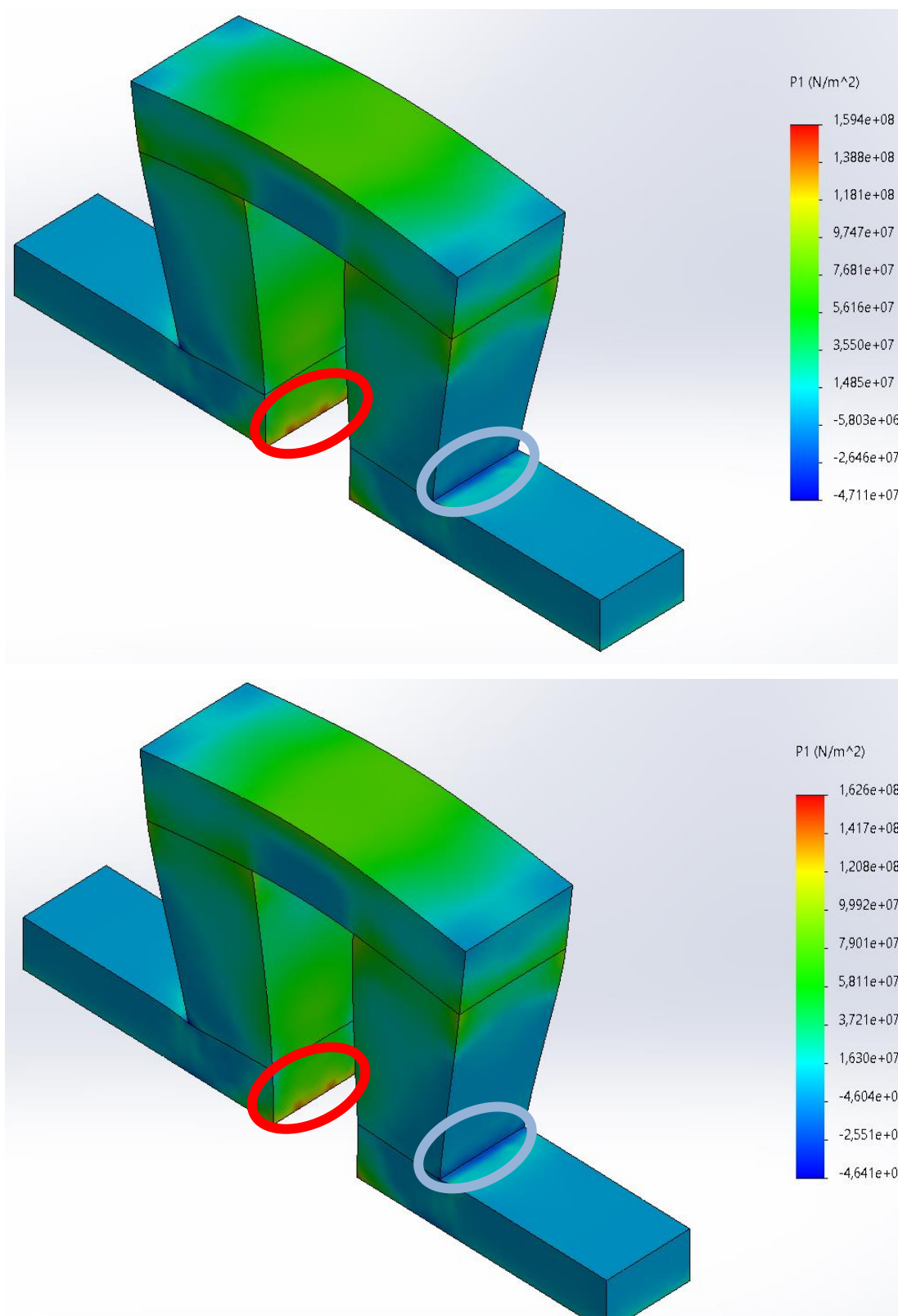


Figure 8–11 Distribution of the first principal stress for material properties a) all RT constant and b) all temperature dependent

The effect of the expanding bridge that pushes both legs apart from each other generates a high compressive stress on the outer lower edge (light blue circle) as well

as tensile stress on the inside part of the assembly near the alumina plate (red circle). The upper part of the bridge has also a higher tensile stress in comparison with the lower part of this same component. This is due to the bending caused by the thermal expansion.

The expansion of the bridge does not only happen in one direction only, transversal expansion is also happening and this will cause edge effects on the interface between the bridge and the thermoelectric leg. These effects are shown with the shear stress τ_{yz} along the xz plane in **Figure 8–12**.

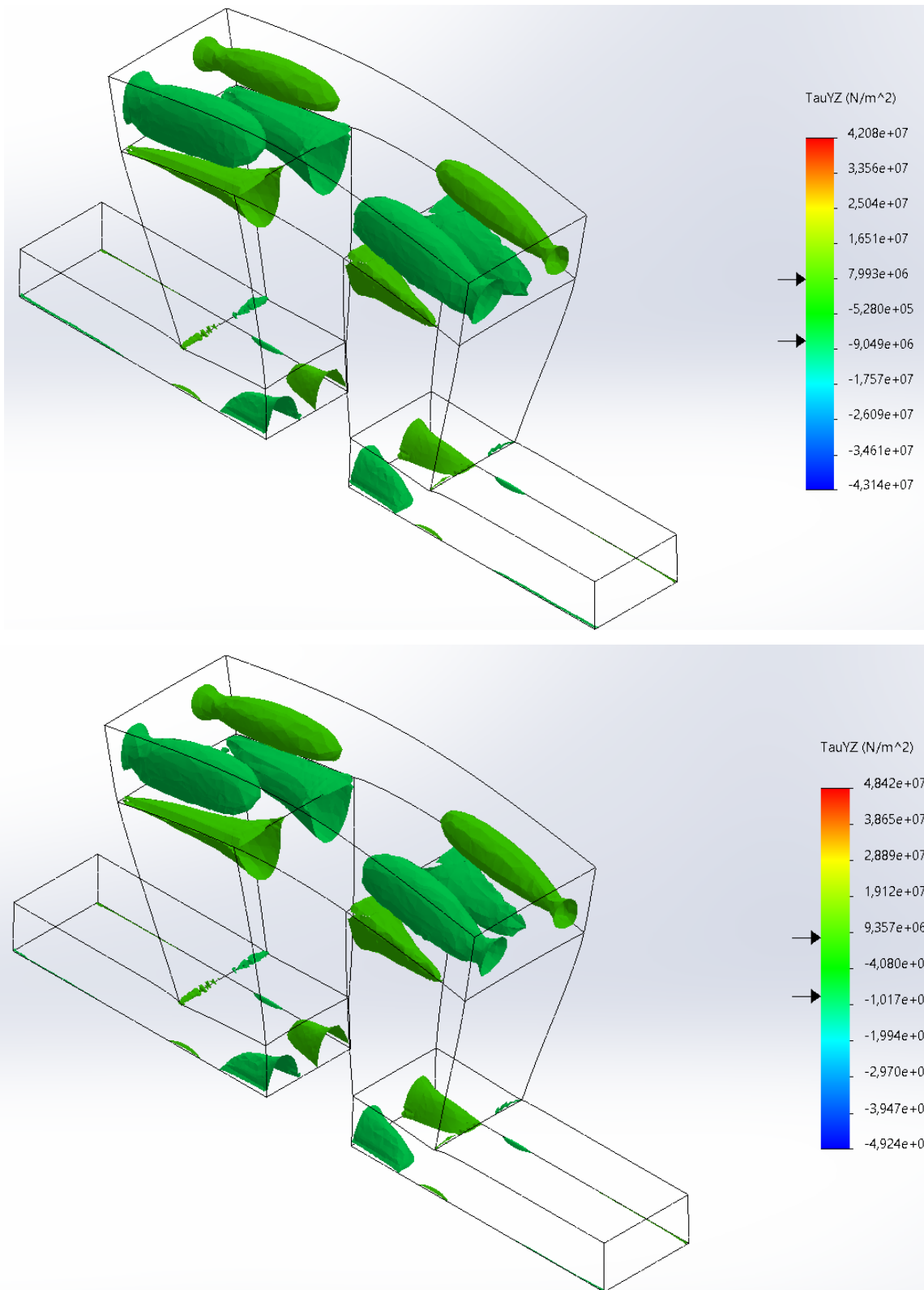


Figure 8–12 Cut view from the shear stress τ_{yz} for material properties a) all RT constant and b) all temperature dependent at 300°C

A cut version showing the shear stresses with an absolute value above 7.9×10^7 Pa along the xz plane shows a clear maximum towards the edge.

The shear stresses are lower when using constant mechanical properties compared to using temperature dependent values. This is partially caused by the increase of CTE in the thermoelectric legs while the copper bridges remain constant as shown in **Figure 8–13**.

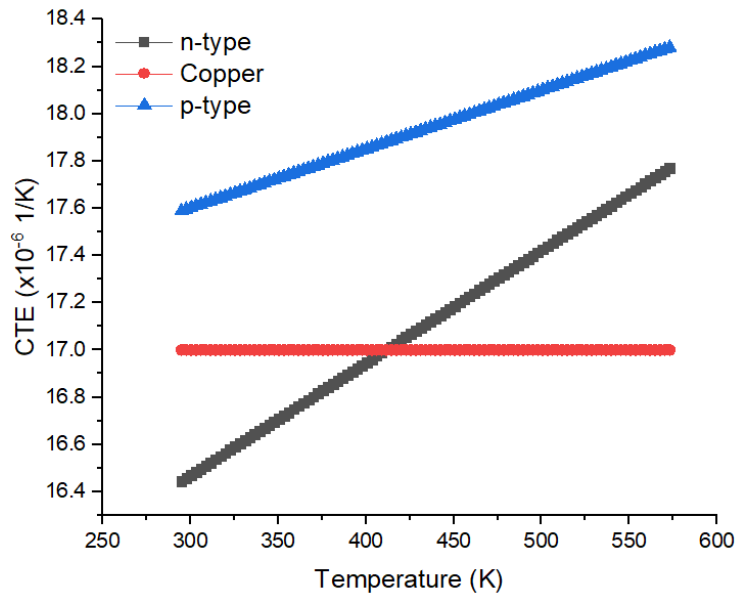


Figure 8–13 Comparison between the CTE for the thermoelectric legs and the copper bridge

The magnitude of these stresses is affected by the lateral size of the contact. Wider interfaces between TE leg and bridges, produced by larger cross section of the legs, will generate greater maximum shear stresses. This is because an element that has a greater initial length will expand more at the same temperature than a shorter one, bringing the difference in total displacement between bridge and leg further apart.

A mismatch between the CTE values between bridge and TE material will also influence this stress, as previously described, and could cause delamination or cracking, reducing TE performance and eventually destroy the device.

A final comparison between the maximum values for the von Mises stress, principal stress 1 and shear τ_{yz} between all the cases studied is shown in **Table 8-5**

Table 8-5 Maximum values for the von Mises equivalent stress, principal 1 stress and shear stress τ_{yz} for all cases

Case	von Mises (MPa)	Principal 1 (MPa)	Shear τ_{yz} (MPa)
a	310.0	160.0	48.0
b	301.9	160.3	37.4
c	306.8	164.0	37.8
d	301.7	158.0	41.7
e	304.7	162.0	37.5

The lowest stresses values can be found in case D, where the Young's modulus is allowed to vary with temperature and the CTE is left constant. In contrast, the maximum tensile stress is found in case C, where the CTE is allowed to vary with temperature and Young's modulus is left constant. This behavior answers to the temperature dependence of both properties, while the thermal expansion slightly increases with temperature, the Young's modulus decreases as shown in **Figure 8–14**.

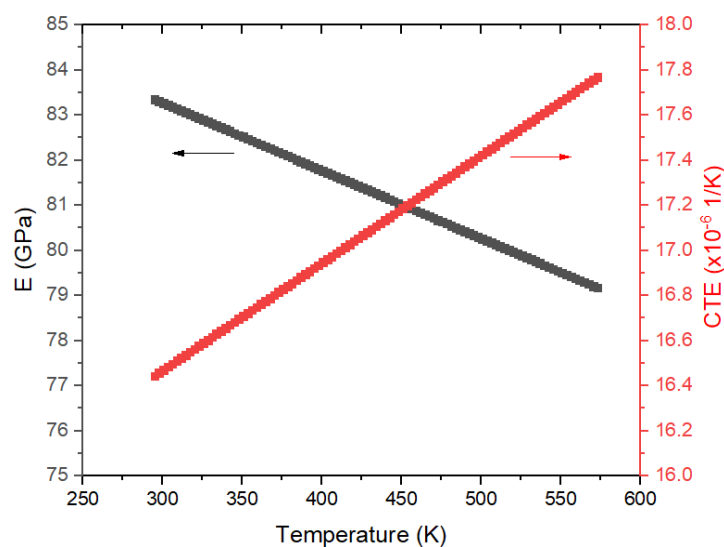


Figure 8–14 Temperature dependent Young's modulus and CTE for the n-type material showing the compensating mechanical effects at higher temperatures

This behavior corresponds to the analytical stress estimation done in chapter 7 (figure 7). The effect of the sinking Young's modulus is partially compensated by the rising

CTE in case E, which gives a similar value to room temperature and average constant values of cases A and B. However, when one of them is left constant, the compensation does not happen and smaller or bigger stresses (case C and D) can be seen.

Using average values (case B) compared to only room temperature values (case A) or temperature dependent values (case E) does not affect greatly the maximum stress values. Given the linear behavior of both properties, and the overall maximum difference between room and high temperature values (~10%), the average value differs 5% from constant room temperature values and has minimal influence on the result.

It is therefore a recommendation from this work that either temperature dependent data for both properties should be used, or constant values. Both these approaches give very similar values. However, using only one of them as temperature dependent can give variations of up to 10% in the computed stress and could lead to a faulty design.

It is a general trend in solid materials to increase in CTE and reduce in Young's modulus with increasing temperature [122], which makes this recommendation applicable to most materials, thermoelectric and metallic, for module assembly. The extent of the compensation between CTE and Young's modulus depends on every material, however.

Further work needs to be done in order to find accurate boundary conditions regarding mechanical coupling and residual stresses for the device under which to run the model, as well as to provide strength values of the materials used in the assembly to be able to assess whether or not these stresses/deformations can cause component failure. However, the ground work and initial database for such work was laid down with the information provided in this thesis.

9. Conclusions and outlook

The focus of this work is to provide a first insight into the mechanical properties of the $\text{Mg}_2\text{Si-Mg}_2\text{Sn}$ solid solutions, to fill the gap in the information needed for the design of a long-lasting module.

The samples chosen for this study were all prepared using parameters that provide the best TE properties with the best cost/effort ratio, in preparation for an upscaling to an industrial mass production process-. These samples are known to have regions with different Si/Sn ratio. Chapter 5 was dedicated to study the effect of Si/Sn ratio on the hardness and fracture toughness in the material, as well as to describe the effect of the local compositional variation in these properties.

It was found that local spots of Si-rich material act as toughening factors by introducing interfaces to the material, as well as providing strain fields to increase the hardness of the particular area in which they are present.

Chapter 6 was dedicated to the study of Young's and shear modulus in the solid solution. Values for the moduli were provided at both room and high temperature. These values were accurately described by a linear model and thus an interpolation formula to estimate the effective moduli for any material within the compositional range and temperature was provided.

Using this formula and the rapid determination of composition through SEM imaging, chapter 7 was dedicated to estimate Young's modulus for samples with different doping species and amount. A very good agreement between the predicted and observed elastic properties in the samples was found, despite the variation factors described in chapter 8.

Chapter 7 also presented the temperature dependent CTE for $\text{Mg}_{1.97}\text{Li}_{0.03}\text{Si}_{0.3}\text{Sn}_{0.7}$, $\text{Mg}_{2.06}\text{Si}_{0.3}\text{Sn}_{0.7}$, $\text{Mg}_{2.06}\text{Si}_{0.3}\text{Sn}_{0.6925}\text{Bi}_{0.0075}$, $\text{Mg}_{2.06}\text{Si}_{0.3}\text{Sn}_{0.665}\text{Bi}_{0.035}$. These values were in good agreement with literature and more importantly, were very similar. The material sensitivity to thermally induced stresses was presented as the product of the Young's modulus and the coefficient of thermal expansion $E \cdot \alpha$, finding similar values between the optimized n-type and the optimized p-type. These comparisons were expanded to other material systems like skutterudites. In this regard, $\text{Mg}_2(\text{Si},\text{Sn})$ materials showed

a similar potential to develop thermally induced stress compared to skutterudites and Bi_2Te_3 , with the added advantage of a low toxicity and cost.

The similarity of mechanical properties exhibited by the main candidates for an $\text{Mg}_2(\text{Si},\text{Sn})$ -only module suggests that such a device is mechanically feasible.

A gap in the information needed to better design thermoelectric modules was filled with the information provided in this work. However, further work is still needed in the characterization of mechanical properties of thermoelectric materials. Some suggestions to complement and enhance the information presented in this work will now be discussed.

9.1. Outlook

- Suggestion on determination of critical stress values

The information collected by this work can be used for modelling and design optimization using a mechanical simulation software. However, once the stresses are identified in the assembly, it is important to know if such a stress will damage the material.

Destructive testing is needed to provide information on the maximum tensile and compressive stresses to evaluate if the maximum stresses identified through FEM can damage the assembly.

Due to the brittle nature of the material, tensile testing is not recommended. Bending tests are better suited for such a material and indeed, literature results already published support this approach [93]. Such a test requires elongated samples, however the procedure detailed in this work for IET samples should fulfill the requirements of any bending test.

Compressive testing is also recommended, as restricted expansion in a material will cause compressive stress. In this case small diameter samples are better suited for such a test, as the force needed to collapse it will be smaller. The Direct Sinter Press method can produce 8 mm diameter samples, which are the best suited for compressive tests.

Note that in the case of testing done in DLR premises, a way to prevent powder spread in the laboratory needs to be provided in the means of a protective pouch or screen.

- **Suggestion on improving the boundary conditions for the FEM**

The boundary conditions in the simulation presented in this work do not represent the working conditions of many modules. Further work needs to be done on this to enhance the model and its usefulness.

Constant properties were used for copper. Being a metal, these properties will be strongly affected by temperature and this needs to be accounted for. Accurate data is needed for the correct alloy used in module assembly.

The zero-stress condition needs to be set to a realistic temperature. The module is assembled at 450 °C, however if the module operation is limited to 300 °C (due to thermal, mechanical or chemical stability), this should be the starting point. Cooling from this temperature to 25 °C will cause internal strain and residual stresses that need to be taken into account to accurately describe the real module with the model.

Although there exist modules without a cover plate on the hot side, most of them have such a component. The model presented in this work did not include a cover plate to keep simulations simple. A further developed model should include such a plate and a means to replicate the holding pressure on the hot side. This is particularly important if the model is a module with more than one uni-couple.

- **Suggestion on determination of thermal stability of mechanical properties**

Just as it has been previously reported for thermoelectric properties, mechanical properties can be expected to change after long time annealing. It is thus imperative to perform experiments to assess the thermal stability of mechanical properties after the samples have been thermally treated.

The effect of time, as well as of atmosphere and protective coating should be studied, since it is known that Mg loss within the material leads to degradation and eventually corrosion of the sample.

Several coatings have been tested in order to suppress degradation, however, experience within the research group has proven that BN slurry can be sufficient to keep the Mg loss at bay for the duration of the experimental trials. It is highly recommended to follow this approach.

Since one of the main objectives of our research is to provide a thermoelectric generator prototype to be used in space technology, it would be advantageous to know how the material behaves under vacuum.

A design of experiments using the 2^k full factorial approach is recommended as shown in **Table 9-1**.

Table 9-1 Proposed factors and levels for the annealing experiment

<i>Factor</i>	<i>Option 1</i>	<i>Option 2</i>
<i>Atmosphere</i>	Vacuum	Argon
<i>Coating</i>	BN coating	No coating
<i>Time (days)</i>	5	10
<i>Temperature (°C)</i>	300	600

Mechanical characterization, in the form of hardness tests and Young's modulus estimation through RUS is recommended as they can be done using small samples.

Microstructural characterization through XRD and SEM imaging is also beneficial to identify any possible change in microstructure and pinpoint the origin of any possible change to mechanical properties.

- **Suggestion on determining the thermal cycling resistance**

Additional to long term annealing, thermal cycling is an important factor in TE modules life expectancy.

Previous reports show a decrease up to 90% in thermoelectric properties after $\sim 10^4$ cycles. Mechanical performance after such testing has, however, not been reported.

If the materials undergo any sort of change during cycling, such as Mg loss or oxidation, this could impact the resistance of said material to the thermally and statically induced stresses related to expansion within the assembly.

It is recommended to perform thermal cycling using similar parameters to the annealing experiments. However, the time factor could be replaced by number of cycles.

An initial run to identify a possible number of cycles to failure can be implemented.

As with the annealing experiments, both mechanical and microstructural characterization are recommended to identify changes within the material.

10. References

Below are the references used for chapters 1 through 4, 8 and 9.

1. Rowe DM (1991) Applications of nuclear-powered thermoelectric generators in space. *Appl Energy* 40:241–271. [https://doi.org/10.1016/0306-2619\(91\)90020-X](https://doi.org/10.1016/0306-2619(91)90020-X)
2. Lee H (2016) *Thermoelectrics: Design and Materials*
3. Keser ÖF, İdare B, Bulat B, Okan A (2019) The Usability of PV-TEG Hybrid Systems on Space Platforms. In: 2019 9th International Conference on Recent Advances in Space Technologies (RAST). pp 109–115
4. Rowe DM (2006) General Principles and Basic Considerations. In: *Thermoelectrics Handbook Macro to Nano*, 1st ed. Taylor and Francis, Florida, pp 1–14
5. Rowe DM (2018) *Thermoelectrics Handbook: Macro to Nano*. CRC Press
6. Rowe DM, Min G (1998) Evaluation of thermoelectric modules for power generation. *J Power Sources* 73:193–198. [https://doi.org/10.1016/S0378-7753\(97\)02801-2](https://doi.org/10.1016/S0378-7753(97)02801-2)
7. Karri NK, Mo C (2018) Reliable Thermoelectric Module Design under Opposing Requirements from Structural and Thermoelectric Considerations. *J Electron Mater* 47:3127–3135. <https://doi.org/10.1007/s11664-017-5934-6>
8. Karri NK, Mo C (2018) Structural Reliability Evaluation of Thermoelectric Generator Modules: Influence of End Conditions, Leg Geometry, Metallization, and Processing Temperatures. *J Electron Mater* 47:6101–6120. <https://doi.org/10.1007/s11664-018-6505-1>
9. Sakamoto T, Iida T, Ohno Y, et al (2013) Stress Analysis and Output Power Measurement of an n-Mg₂Si Thermoelectric Power Generator with an Unconventional Structure. *J Electron Mater* 43:1620–1629. <https://doi.org/10.1007/s11664-013-2814-6>
10. Goldsmid HJ (1958) The Electrical Conductivity and Thermoelectric Power of Bismuth Telluride. *Proc Phys Soc* 71:633. <https://doi.org/10.1088/0370-1328/71/4/312>
11. Tritt T (2011) *Thermoelectric Phenomena, Materials, and Applications*. <https://doi.org/10.1146/ANNUREV-MATSCI-062910-100453>
12. Ren Z, Lan Y, Zhang Q (2017) *Advanced Thermoelectrics: Materials, Contacts, Devices, and Systems*. CRC Press, New York
13. Ioffe AF, Stil'bans LS, Iordanishvili EK, et al (1959) Semiconductor Thermoelements and Thermoelectric Cooling. *Phys Today* 12:42–42. <https://doi.org/10.1063/1.3060810>

14. Yang J (2004) Theory of Thermal Conductivity. In: Tritt TM (ed) Thermal Conductivity: Theory, Properties, and Applications. Springer US, Boston, MA, pp 1–20
15. Berman R (1980) Thermal Conduction in Solids
16. Heikes RR (1961) Thermoelectricity: science and engineering. New York, Interscience Publishers
17. Snyder GJ, Toberer ES (2008) Complex thermoelectric materials. *Nat Mater* 7:105–114. <https://doi.org/10.1038/nmat2090>
18. Zhang QH, Huang XY, Bai SQ, et al (2016) Thermoelectric Devices for Power Generation: Recent Progress and Future Challenges. *Adv Eng Mater* 18:194–213. <https://doi.org/10.1002/adem.201500333>
19. Skomedal G, Holmgren L, Middleton H, et al (2016) Design, assembly and characterization of silicide-based thermoelectric modules. *Energy Convers Manag* 110:13–21. <https://doi.org/10.1016/j.enconman.2015.11.068>
20. Inoue H, Yoneda S, Kato M, et al (2018) Examination of oxidation resistance of Mg₂Si thermoelectric modules at practical operating temperature. *J Alloys Compd* 735:828–832. <https://doi.org/10.1016/j.jallcom.2017.11.202>
21. Ni JE, Case ED, Schmidt RD, et al (2013) The thermal expansion coefficient as a key design parameter for thermoelectric materials and its relationship to processing-dependent bloating. *J Mater Sci* 48:6233–6244. <https://doi.org/10.1007/s10853-013-7421-7>
22. Barako MT, Park W, Marconnet AM, et al (2013) Thermal Cycling, Mechanical Degradation, and the Effective Figure of Merit of a Thermoelectric Module. *J Electron Mater* 42:372–381. <https://doi.org/10.1007/s11664-012-2366-1>
23. Ugural AC, Fenster SK (2003) Advanced Strength and Applied Elasticity. Pearson Education
24. Gould PL, Feng Y (2018) Introduction to Linear Elasticity, 4th ed. Springer International Publishing
25. Craig R Mechanics of Materials, 3rd ed. wiley
26. Gross D, Seelig T (2018) Fracture Mechanics: With an Introduction to Micromechanics, 3rd ed. Springer International Publishing
27. FUNG YC (1965) Foundations of Solid Mechanics
28. Kittel C (2004) Introduction to Solid State Physics
29. Norton RL Machine Design, 5th ed. Pearson

30. Gross D, Seelig T (2007) Klassische Bruch- und Versagenshypthesen. In: Bruchmechanik: Mit einer Einführung in die Mikromechanik. Springer, Berlin, Heidelberg, pp 41–50
31. Anderson TL, Anderson TL (2005) Fracture Mechanics: Fundamentals and Applications, Third Edition. CRC Press
32. Broberg KB (1999) Cracks and Fracture
33. E08 Committee Test Method for Linear-Elastic Plane-Strain Fracture Toughness K_{Ic} of Metallic Materials. ASTM International
34. Matsumoto RLK (1987) Evaluation of Fracture Toughness Determination Methods as Applied to Ceria-Stabilized Tetragonal Zirconia Polycrystal. J Am Ceram Soc 70:C-366-C-368. <https://doi.org/10.1111/j.1151-2916.1987.tb04921.x>
35. Anstis GR, Chantikul P, Lawn BR, Marshall DB (1981) A Critical Evaluation of Indentation Techniques for Measuring Fracture Toughness: I, Direct Crack Measurements. J Am Ceram Soc 64:533–538. <https://doi.org/10.1111/j.1151-2916.1981.tb10320.x>
36. Walley SM (2012) Historical origins of indentation hardness testing. Mater Sci Technol 28:1028–1044. <https://doi.org/10.1179/1743284711Y.0000000127>
37. DIN EN ISO 14577-1:2015-11, Metallische Werkstoffe_- Instrumentierte Eindringprüfung zur Bestimmung der Härte und anderer Werkstoffparameter_- Teil_1: Prüfverfahren (ISO_14577-1:2015); Deutsche Fassung EN_ISO_14577-1:2015. Beuth Verlag GmbH
38. Smith RL, Sandly GE (1922) An Accurate Method of Determining the Hardness of Metals, with Particular Reference to Those of a High Degree of Hardness. Proc Inst Mech Eng 102:623–641. https://doi.org/10.1243/PIME_PROC_1922_102_033_02
39. E28 Committee Test Method for Vickers Hardness of Metallic Materials. ASTM International
40. DIN EN ISO 6507-1:2018-07, Metallische Werkstoffe_- Härteprüfung nach Vickers_- Teil_1: Prüfverfahren (ISO_6507-1:2018); Deutsche Fassung EN_ISO_6507-1:2018. Beuth Verlag GmbH
41. Wachtman JB, Tefft WE, Lam DG, Apstein CS (1961) Exponential Temperature Dependence of Young's Modulus for Several Oxides. Phys Rev 122:1754–1759. <https://doi.org/10.1103/PhysRev.122.1754>
42. Rahemi R, Li D (2015) Variation in electron work function with temperature and its effect on the Young's modulus of metals. Scr Mater 99:41–44. <https://doi.org/10.1016/j.scriptamat.2014.11.022>

43. Taya M, Arsenault RJ (1989) *Metal Matrix Composites: Thermomechanical Behavior*. Butterworth-Heinemann Ltd, Oxford, England ; New York
44. Daviaud R, Filliatre C, Naslain R (1983) *Introduction aux matériaux composites*. CNRS, Paris
45. Eisenschitz R, London F (1930) Über das Verhältnis der van der Waalsschen Kräfte zu den homöopolaren Bindungskräften. *Z Für Phys* 60:491–527. <https://doi.org/10.1007/BF01341258>
46. Cverna F (2003) *Bagdade, S: AMS Ready Reference: Thermal Properties of Metals*. ASM International, Materials Park, Ohio
47. Liu X, Xi L, Qiu W, et al (2016) Significant Roles of Intrinsic Point Defects in Mg₂X (X = Si, Ge, Sn) Thermoelectric Materials. *Adv Electron Mater* 2:1500284. <https://doi.org/10.1002/aelm.201500284>
48. de Boor J, Compere C, Dasgupta T, et al (2014) Fabrication parameters for optimized thermoelectric Mg₂Si. *J Mater Sci* 49:3196–3204. <https://doi.org/10.1007/s10853-014-8023-8>
49. Fiameni S, Battiston S, Boldrini S, et al (2012) Synthesis and characterization of Bi-doped Mg₂Si thermoelectric materials. *J Solid State Chem* 193:142–146. <https://doi.org/10.1016/j.jssc.2012.05.004>
50. Huang ZW, Zhao YH, Hou H, Han PD (2012) Electronic structural, elastic properties and thermodynamics of Mg₁₇Al₁₂, Mg₂Si and Al₂Y phases from first-principles calculations. *Phys B Condens Matter* 407:1075–1081. <https://doi.org/10.1016/j.physb.2011.12.132>
51. Imai M, Isoda Y, Udono H (2015) Thermal expansion of semiconducting silicides β-FeSi₂ and Mg₂Si. *Intermetallics* 67:75–80. <https://doi.org/10.1016/j.intermet.2015.07.015>
52. Kasai H, Song L, Andersen HL, et al (2017) Multi-temperature structure of thermoelectric Mg₂Si and Mg₂Sn. *Acta Crystallogr Sect B* 73:1158–1163. <https://doi.org/10.1107/S2052520617014044>
53. Mito Y, Ogino A, Konno S, Udono H (2017) Influence of Humidity, Volume Density, and MgO Impurity on Mg₂Si Thermoelectric-Leg. *J Electron Mater* 46:3103–3108. <https://doi.org/10.1007/s11664-016-5182-1>
54. Nieroda P, Leszczynski J, Kolezynski A (2017) Bismuth doped Mg₂Si with improved homogeneity: Synthesis, characterization and optimization of thermoelectric properties. *J Phys Chem Solids* 103:147–159. <https://doi.org/10.1016/j.jpcs.2016.11.027>
55. Wang L, Qin XY, Xiong W, Zhu XG (2007) Fabrication and mechanical properties of bulk nanocrystalline intermetallic Mg₂Si. *Mater Sci Eng A* 459:216–222. <https://doi.org/10.1016/j.msea.2007.01.038>

56. Skomedal G, Burkov A, Samunin A, et al (2016) High temperature oxidation of Mg₂(Si-Sn). *Corros Sci* 111:325–333. <https://doi.org/10.1016/j.corsci.2016.05.016>
57. Davis LC, Whitten WB, Danielson GC (1967) Elastic constants and calculated lattice vibration frequencies of Mg₂Sn. *J Phys Chem Solids* 28:439–447. [https://doi.org/10.1016/0022-3697\(67\)90311-3](https://doi.org/10.1016/0022-3697(67)90311-3)
58. Li X, Xie H, Yang B, Li S (2020) Elastic and Thermodynamic Properties Prediction of Mg₂Sn and MgTe by First-Principle Calculation and Quasi-Harmonic Debye Model. *J Electron Mater* 49:464–471. <https://doi.org/10.1007/s11664-019-07682-w>
59. D. A. Pshenai-Severin MIF (2013) The Influence of Grain Boundary Scattering on Thermoelectric Properties of Mg₂Si and Mg₂Si_{0.8}Sn_{0.2}. *J Electron Mater* 42:. <https://doi.org/10.1007/s11664-012-2403-0>
60. Kamila H, Sankhla A, Yasseri M, et al (2019) Synthesis of p-type Mg₂Si_{1-x}Sn_x with x = 0-1 and optimization of the synthesis parameters. *Mater Today Proc* 8:546–555. <https://doi.org/10.1016/j.matpr.2019.02.052>
61. Orenstein R, Male JP, Toriyama M, et al (2021) Using phase boundary mapping to resolve discrepancies in the Mg₂Si–Mg₂Sn miscibility gap. *J Mater Chem A* 9:7208–7215. <https://doi.org/10.1039/D1TA00115A>
62. Yasseri M, Mitra K, Sankhla A, et al (2021) Influence of Mg loss on the phase stability in Mg₂X (X = Si, Sn) and its correlation with coherency strain. *Acta Mater* 208:116737. <https://doi.org/10.1016/j.actamat.2021.116737>
63. Yasseri M, Sankhla A, Kamila H, et al (2020) Solid solution formation in Mg₂(Si,Sn) and shape of the miscibility gap. *Acta Mater* 185:80–88. <https://doi.org/10.1016/j.actamat.2019.11.054>
64. Viennois R, Jund P, Colinet C, Tédénac J-C (2012) Defect and phase stability of solid solutions of Mg₂X with antiferroite structure. An ab-initio study. *AIP Conf Proc* 1449:49–52. <https://doi.org/10.1063/1.4731494>
65. Mao J, Kim HS, Shuai J, et al (2016) Thermoelectric properties of materials near the band crossing line in Mg₂Sn–Mg₂Ge–Mg₂Si system. *Acta Mater* 103:633–642. <https://doi.org/10.1016/j.actamat.2015.11.006>
66. Liu W, Tan X, Yin K, et al (2012) Convergence of Conduction Bands as a Means of Enhancing Thermoelectric Performance of n-Type Mg₂Si_{1-x}Sn_x Solid Solutions. *Phys Rev Lett* 108:166601. <https://doi.org/10.1103/PhysRevLett.108.166601>
67. Klobes B, de Boor J, Alatas A, et al (2019) Lattice dynamics and elasticity in thermoelectric Mg₂Si_{1-x}Sn_x. *Phys Rev Mater* 3:025404. <https://doi.org/10.1103/PhysRevMaterials.3.025404>

68. Dasgupta T (2019) High Thermoelectric Performance in $Mg_2(Si_{0.3}Sn_{0.7})$ by Enhanced Phonon Scattering. <https://doi.org/10.1021/acsaem.8b02148>
69. Mitra K, Goyal GK, Rathore E, et al (2018) Enhanced Thermoelectric Performance in Mg_2Si by Functionalized Co-Doping. *Phys Status Solidi A* 215:1700829. <https://doi.org/10.1002/pssa.201700829>
70. Tang X, Zhang Y, Zheng Y, et al (2017) Improving thermoelectric performance of p-type Ag-doped $Mg_2Si_{0.4}Sn_{0.6}$ prepared by unique melt spinning method. *Appl Therm Eng* C:1396–1400. <https://doi.org/10.1016/j.applthermaleng.2016.05.146>
71. Liu W, Chi H, Sun H, et al (2014) Advanced thermoelectrics governed by a single parabolic band: $Mg_2Si_{0.3}Sn_{0.7}$, a canonical example. *Phys Chem Chem Phys* 16:6893–6897. <https://doi.org/10.1039/C4CP00641K>
72. Gao P, Davis JD, Poltavets VV, Hogan TP (2016) The p-type $Mg_2Li_xSi_{0.4}Sn_{0.6}$ thermoelectric materials synthesized by a B_2O_3 encapsulation method using Li_2CO_3 as the doping agent. *J Mater Chem C* 4:929–934. <https://doi.org/10.1039/C5TC03692E>
73. Sankhla A, Patil A, Kamila H, et al (2018) Mechanical Alloying of Optimized $Mg_2(Si,Sn)$ Solid Solutions: Understanding Phase Evolution and Tuning Synthesis Parameters for Thermoelectric Applications. *ACS Appl Energy Mater* 1:531–542. <https://doi.org/10.1021/acsaem.7b00128>
74. Vivekanandhan P, Murugasami R, Kumaran S (2018) Microstructure and mechanical properties of magnesium silicide prepared via spark plasma assisted combustion synthesis. *Mater Lett* 231:109–113. <https://doi.org/10.1016/j.matlet.2018.08.017>
75. Bux SK, Yeung MT, Toberer ES, et al (2011) Mechanochemical synthesis and thermoelectric properties of high quality magnesium silicide. *J Mater Chem* 21:12259–12266. <https://doi.org/10.1039/C1JM10827A>
76. Farahi N, Prabhudev S, Botton GA, et al (2016) Nano- and Microstructure Engineering: An Effective Method for Creating High Efficiency Magnesium Silicide Based Thermoelectrics. *ACS Appl Mater Interfaces* 8:34431–34437. <https://doi.org/10.1021/acsaem.6b12297>
77. Farahi N, Stiewe C, Truong DYN, et al (2019) High efficiency $Mg_2(Si,Sn)$ -based thermoelectric materials: scale-up synthesis, functional homogeneity, and thermal stability. *RSC Adv* 9:23021–23028. <https://doi.org/10.1039/C9RA04800F>
78. Macario LR, Cheng X, Ramirez D, et al (2018) Thermoelectric Properties of Bi-Doped Magnesium Silicide Stannides. *ACS Appl Mater Interfaces* 10:40585–40591. <https://doi.org/10.1021/acsaem.8b15111>

79. de Boor J, Dasgupta T, Saparamadu U, et al (2017) Recent progress in p-type thermoelectric magnesium silicide based solid solutions. *Mater Today Energy* 4:105–121. <https://doi.org/10.1016/j.mtener.2017.04.002>
80. Nieroda P, Kolezynski A, Oszejca M, et al (2016) Structural and Thermoelectric Properties of Polycrystalline p-Type $Mg_{2-x}Li_xSi$. *J Electron Mater* 45:3418–3426. <https://doi.org/10.1007/s11664-016-4486-5>
81. Saparamadu U, de Boor J, Mao J, et al (2017) Comparative studies on thermoelectric properties of p-type $Mg_2Sn_{0.75}Ge_{0.25}$ doped with lithium, sodium, and gallium. *Acta Mater* 141:154–162. <https://doi.org/10.1016/j.actamat.2017.09.009>
82. Kamila H, Sahu P, Sankhla A, et al (2019) Analyzing transport properties of p-type Mg_2Si – Mg_2Sn solid solutions: optimization of thermoelectric performance and insight into the electronic band structure. *J Mater Chem A* 7:1045–1054. <https://doi.org/10.1039/C8TA08920E>
83. Rogl G, Grytsiv A, Gürth M, et al (2016) Mechanical properties of half-Heusler alloys. *Acta Mater* 107:178–195. <https://doi.org/10.1016/j.actamat.2016.01.031>
84. Rogl G, Rogl P (2017) Skutterudites, a most promising group of thermoelectric materials. *Curr Opin Green Sustain Chem* 4:50–57. <https://doi.org/10.1016/j.cogsc.2017.02.006>
85. He R, Gahlawat S, Guo C, et al (2015) Studies on mechanical properties of thermoelectric materials by nanoindentation. *Phys Status Solidi A* 212:2191–2195. <https://doi.org/10.1002/pssa.201532045>
86. Zhang L, Rogl G, Grytsiv A, et al (2010) Mechanical properties of filled antimonide skutterudites. *Mater Sci Eng B* 170:26–31. <https://doi.org/10.1016/j.mseb.2010.02.022>
87. Schmidt RD, Case ED, Giles J, et al (2012) Room-Temperature Mechanical Properties and Slow Crack Growth Behavior of Mg_2Si Thermoelectric Materials. *J Electron Mater* 41:1210–1216. <https://doi.org/10.1007/s11664-011-1879-3>
88. Milekhine V, Onsøien MI, Solberg JK, Skaland T (2002) Mechanical properties of $FeSi$ (ϵ), $FeSi_2$ ($\zeta\alpha$) and Mg_2Si . *Intermetallics* 10:743–750. [https://doi.org/10.1016/S0966-9795\(02\)00046-8](https://doi.org/10.1016/S0966-9795(02)00046-8)
89. Schmidt RD, Fan X, Case ED, Sarac PB (2015) Mechanical properties of Mg_2Si thermoelectric materials with the addition of 0–4 vol% silicon carbide nanoparticles (SiCNP). *J Mater Sci* 50:4034–4046. <https://doi.org/10.1007/s10853-015-8960-x>
90. Whitten WB, Chung PL, Danielson GC (1965) Elastic constants and lattice vibration frequencies of Mg_2Si . *J Phys Chem Solids* 26:49–56. [https://doi.org/10.1016/0022-3697\(65\)90071-5](https://doi.org/10.1016/0022-3697(65)90071-5)

91. Muthiah S, Singh RC, Pathak BD, Dhar A (2017) Mechanical properties of thermoelectric n-type magnesium silicide synthesized employing in situ spark plasma reaction sintering. *Mater Res Express* 4:075507. <https://doi.org/10.1088/2053-1591/aa76a8>
92. Gao P, Berkun I, Schmidt RD, et al (2014) Transport and Mechanical Properties of High-ZT $\text{Mg}_{2.08}\text{Si}_{0.4-x}\text{Sn}_{0.6}\text{Sbx}$ Thermoelectric Materials. *J Electron Mater* 43:1790–1803. <https://doi.org/10.1007/s11664-013-2865-8>
93. Gelbstein Y, Tunbridge J, Dixon R, et al (2014) Physical, Mechanical, and Structural Properties of Highly Efficient Nanostructured n- and p-Silicides for Practical Thermoelectric Applications. *J Electron Mater* 43:1703–1711. <https://doi.org/10.1007/s11664-013-2848-9>
94. Mejri M, Thimont Y, Malard B, Estournès C (2019) Characterization of the thermo-mechanical properties of p-type ($\text{MnSi}_{1.77}$) and n-type ($\text{Mg}_2\text{Si}_{0.6}\text{Sn}_{0.4}$) thermoelectric materials. *Scr Mater* 172:28–32. <https://doi.org/10.1016/j.scriptamat.2019.06.037>
95. Mejri M, Malard B, Thimont Y, et al (2020) Thermal stability of $\text{Mg}_2\text{Si}_{0.55}\text{Sn}_{0.45}$ for thermoelectric applications. *J Alloys Compd* 846:156413. <https://doi.org/10.1016/j.jallcom.2020.156413>
96. Skomedal G, Vehus T, Kanas N, et al (2019) Long term stability testing of oxide unicomple thermoelectric modules. *Mater Today Proc* 8:696–705. <https://doi.org/10.1016/j.matpr.2019.02.070>
97. Ebling D, Bartholomé K, Bartel M, Jäggle M (2010) Module Geometry and Contact Resistance of Thermoelectric Generators Analyzed by Multiphysics Simulation. *J Electron Mater* 39:1376–1380. <https://doi.org/10.1007/s11664-010-1331-0>
98. Erturun U, Erermis K, Mossi K (2014) Effect of various leg geometries on thermo-mechanical and power generation performance of thermoelectric devices. *Appl Therm Eng* 73:128–141. <https://doi.org/10.1016/j.applthermaleng.2014.07.027>
99. Mu Y, Chen G, Yu R, et al (2014) Effect of geometric dimensions on thermoelectric and mechanical performance for Mg_2Si -based thermoelectric unicomple. *Mater Sci Semicond Process* 17:21–26. <https://doi.org/10.1016/j.mssp.2013.08.009>
100. Jung I, Kang DH, Park W, et al (2007) Thermodynamic modeling of the Mg–Si–Sn system. <https://doi.org/10.1016/J.CALPHAD.2006.12.003>
101. Ayachi S, Castillo Hernandez G, Pham NH, et al (2019) Developing Contacting Solutions for $\text{Mg}_2\text{Si}_{1-x}\text{Sn}_x$ -Based Thermoelectric Generators: Cu and $\text{Ni}_{45}\text{Cu}_{55}$ as Potential Contacting Electrodes. *ACS Appl Mater Interfaces* 11:40769–40780. <https://doi.org/10.1021/acsami.9b12474>
102. Camut J, Pham NH, Nhi Truong DY, et al (2021) Aluminum as promising electrode for $\text{Mg}_2(\text{Si},\text{Sn})$ -based thermoelectric devices. *Mater Today Energy* 21:100718. <https://doi.org/10.1016/j.mtener.2021.100718>

103. Graff JS, Schuler R, Song X, et al (2021) Fabrication of a Silicide Thermoelectric Module Employing Fractional Factorial Design Principles. *J Electron Mater* 50:4041–4049. <https://doi.org/10.1007/s11664-021-08902-y>
104. Pecharsky VK, Zavalij PY (2009) Fundamentals of Diffraction. In: *Fundamentals of Powder Diffraction and Structural Characterization of Materials*. Springer US, Boston, MA, pp 133–149
105. Reed-Hill RE, Abbaschian R (1992) *Physical metallurgy principles*. PWS-Kent Pub., Boston
106. Yasserli M, Farahi N, Kelm K, et al (2018) Rapid determination of local composition in quasi-binary, inhomogeneous material systems from backscattered electron image contrast. *Materialia* 2:98–103. <https://doi.org/10.1016/j.mtla.2018.06.014>
107. Lloyd GE (1987) Atomic number and crystallographic contrast images with the SEM: a review of backscattered electron techniques. *Mineral Mag* 51:3–19. <https://doi.org/10.1180/minmag.1987.051.359.02>
108. Timoshenko S (1953) *History of strength of materials : with a brief account of the history of theory of elasticity and theory of structures*. New York : McGraw-Hill
109. Han SM, Benaroya H, Wei T (1999) DYNAMICS OF TRANSVERSELY VIBRATING BEAMS USING FOUR ENGINEERING THEORIES. *J Sound Vib* 225:935–988. <https://doi.org/10.1006/jsvi.1999.2257>
110. E28 Committee Test Method for Dynamic Youngs Modulus, Shear Modulus, and Poissons Ratio by Impulse Excitation of Vibration. ASTM International
111. Leisure RG, Willis FA (1997) Resonant ultrasound spectroscopy. *J Phys Condens Matter* 9:6001–6029. <https://doi.org/10.1088/0953-8984/9/28/002>
112. Migliori A, Sarrao JL, Visscher WM, et al (1993) Resonant ultrasound spectroscopic techniques for measurement of the elastic moduli of solids. *Phys B Condens Matter* 183:1–24. [https://doi.org/10.1016/0921-4526\(93\)90048-B](https://doi.org/10.1016/0921-4526(93)90048-B)
113. Satyala N, Krasinski JS, Vashaee D (2014) Simultaneous enhancement of mechanical and thermoelectric properties of polycrystalline magnesium silicide with conductive glass inclusion. *Acta Mater* 74:141–150. <https://doi.org/10.1016/j.actamat.2014.04.007>
114. Radovic M, Lara-Curzio E, Riestler L (2004) Comparison of different experimental techniques for determination of elastic properties of solids. *Mater Sci Eng A* 368:56–70. <https://doi.org/10.1016/j.msea.2003.09.080>
115. Ajit Prasad SL, Mayuram MM, Krishnamurthy R (1999) Response of plasma-sprayed alumina–titania composites to static indentation process. *Mater Lett* 41:234–240. [https://doi.org/10.1016/S0167-577X\(99\)00136-6](https://doi.org/10.1016/S0167-577X(99)00136-6)

116. Bao YW, Wang W, Zhou YC (2004) Investigation of the relationship between elastic modulus and hardness based on depth-sensing indentation measurements. *Acta Mater* 52:5397–5404. <https://doi.org/10.1016/j.actamat.2004.08.002>
117. Oliver WC, Pharr GM (1992) An improved technique for determining hardness and elastic modulus using load and displacement sensing indentation experiments. *J Mater Res*. <https://doi.org/10.1557/JMR.1992.1564>
118. Castillo-Hernandez G, Yasseri M, Klobes B, et al (2020) Room and high temperature mechanical properties of Mg₂Si, Mg₂Sn and their solid solutions. *J Alloys Compd* 156205. <https://doi.org/10.1016/j.jallcom.2020.156205>
119. Edwards M, Brinkfeldt K (2013) Thermo-mechanical modelling and design of SiGe-based thermo-electric modules for high temperature applications. In: 2013 14th International Conference on Thermal, Mechanical and Multi-Physics Simulation and Experiments in Microelectronics and Microsystems (EuroSimE). pp 1–11
120. Jia X, Gao Y (2014) Estimation of thermoelectric and mechanical performances of segmented thermoelectric generators under optimal operating conditions. *Appl Therm Eng* 73:335–342. <https://doi.org/10.1016/j.applthermaleng.2014.07.069>
121. Tewolde M, Fu G, Hwang DJ, et al (2016) Thermoelectric Device Fabrication Using Thermal Spray and Laser Micromachining. *J Therm Spray Technol* 25:431–440. <https://doi.org/10.1007/s11666-015-0351-y>
122. Ho CY, Taylor RE (1998) *Thermal Expansion of Solids*. ASM International
123. Yasseri M, Schüpfer D, Weinhold M, et al (2020) Comparing Raman mapping and electron microscopy for characterizing compositional gradients in thermoelectric materials. *Scr Mater* 179:61–64. <https://doi.org/10.1016/j.scriptamat.2020.01.002>

11. Appendix

11.1. Limitations on the use of the rapid compositional analysis in Mg_2X

In order to apply the rapid determination method developed by Yasseri *et al.* [106] EDX composition points for calibration of the grey-tone scale are needed. The original work details the process needed to estimate the spatial resolution for each EDX point. It is related to a specific gray value in the SEM picture. The process is done by hand and is of course subjected to human error. Additionally, there exists also the grey tone variation within a sample. As shown in **Figure 11–1**, even areas with a homogeneous color to the naked eye have a great variation within a small area. In this case a mean gray value of 230 is used, however values 210-251 are contained in the apparently uniform region.

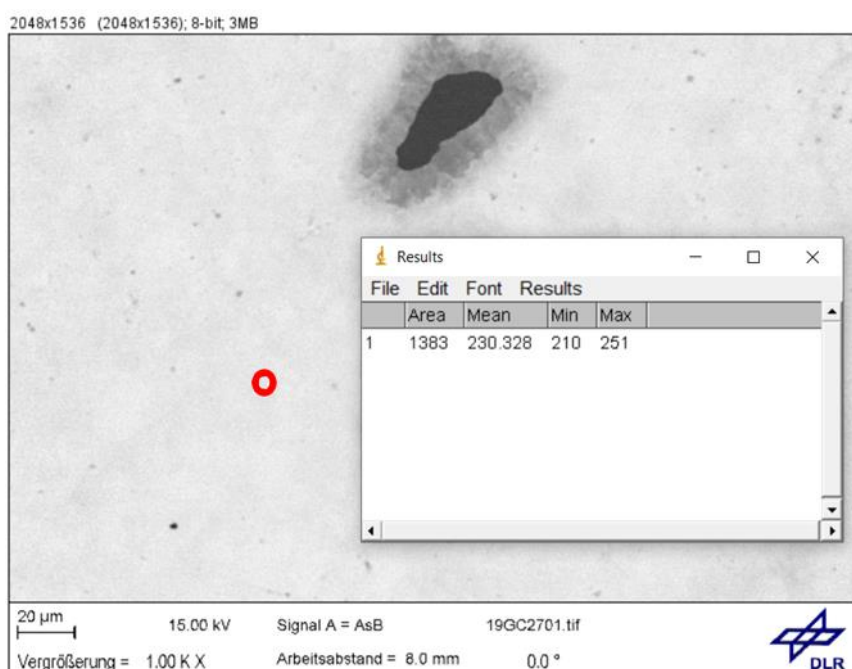


Figure 11–1 Exemplary image of a $Mg_2(Si,Sn)$ sample with a variety of gray values for a small area (red circle).

The fitting of said gray values to the backscatter coefficient is done in a tool developed in excel. Values within the variation shown in **Figure 11–1** are manually fed into the fitting to produce the best R^2 possible, equations with a goodness of fit below 0.95 are not used due to a low reliability for further analysis.

Furthermore, the equation found in the previous step is fed into a MATLAB script that estimates the local composition for each individual pixel in the picture.

The variation imposed by all these factors is however mitigated by the use of some good practices; namely adding EDX points close or within very identifiable spots on the SEM image, to avoid confusion when estimating the gray values, as well as avoid using low R^2 fitting. The accuracy of this quantification method is not 100% reliable but has a very good degree of agreement with EDX mapping, XRD phase quantification and Raman mapping [63, 106, 123].

11.2. Material properties used for simulation

n-type $\text{Mg}_2\text{Si}_{0.3}\text{Sn}_{0.665}\text{Bi}_{0.035}$

A linear fit was used for the Young's modulus measured, this is shown in **Figure 11–2**

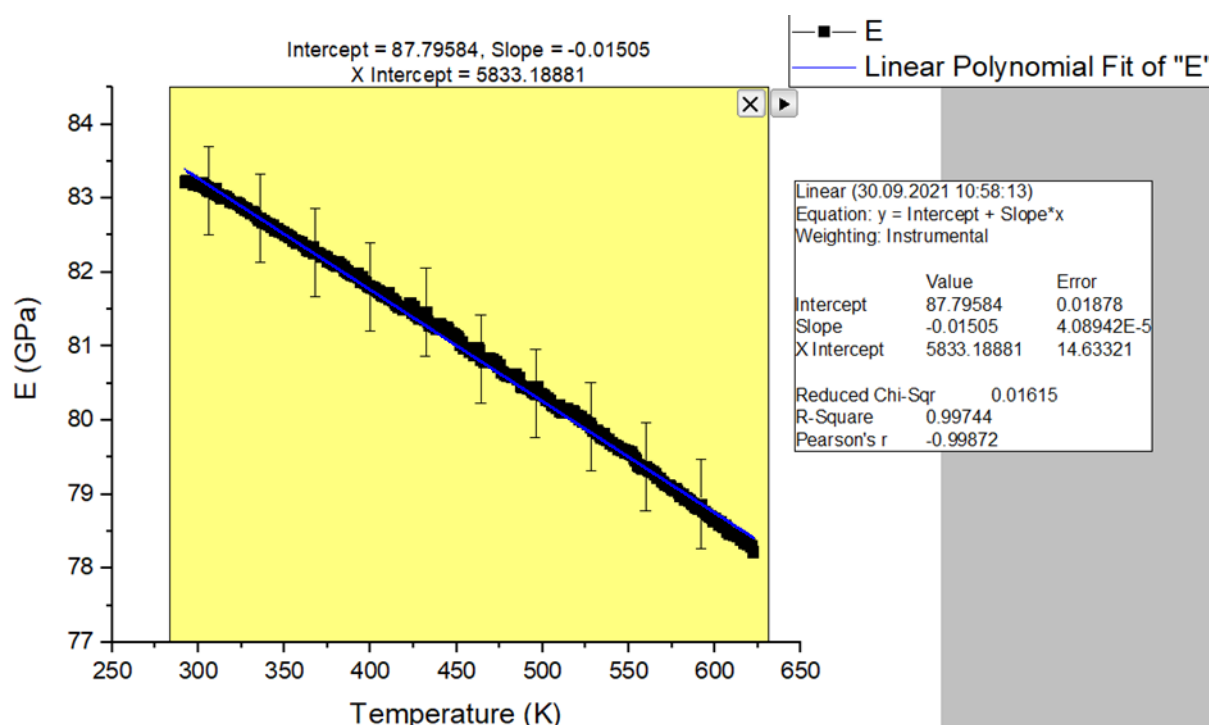


Figure 11–2 Raw data and fitting for the Young's modulus of n-type $\text{Mg}_2\text{Si}_{0.3}\text{Sn}_{0.7}$

The measurement of the coefficient of thermal expansion shows two distinctive areas as discussed in chapter 7. A linear fit was added to the linear part and extrapolation used for values at room temperature as shown in **Figure 11–3**. Spikes in the raw data stem from the calibration, most likely a movement of the sapphire standard.

As described in chapter 7, the CTE is usually reported as mean values. The mean value for the n-type $\text{Mg}_2(\text{Si},\text{Sn})$ is 16.810^{-6} 1/K. On the other hand, using the linear fit and extrapolation yields a value of $\text{CTE}(22\text{ }^\circ\text{C}) = 16.44 \times 10^{-6}$ 1/K.

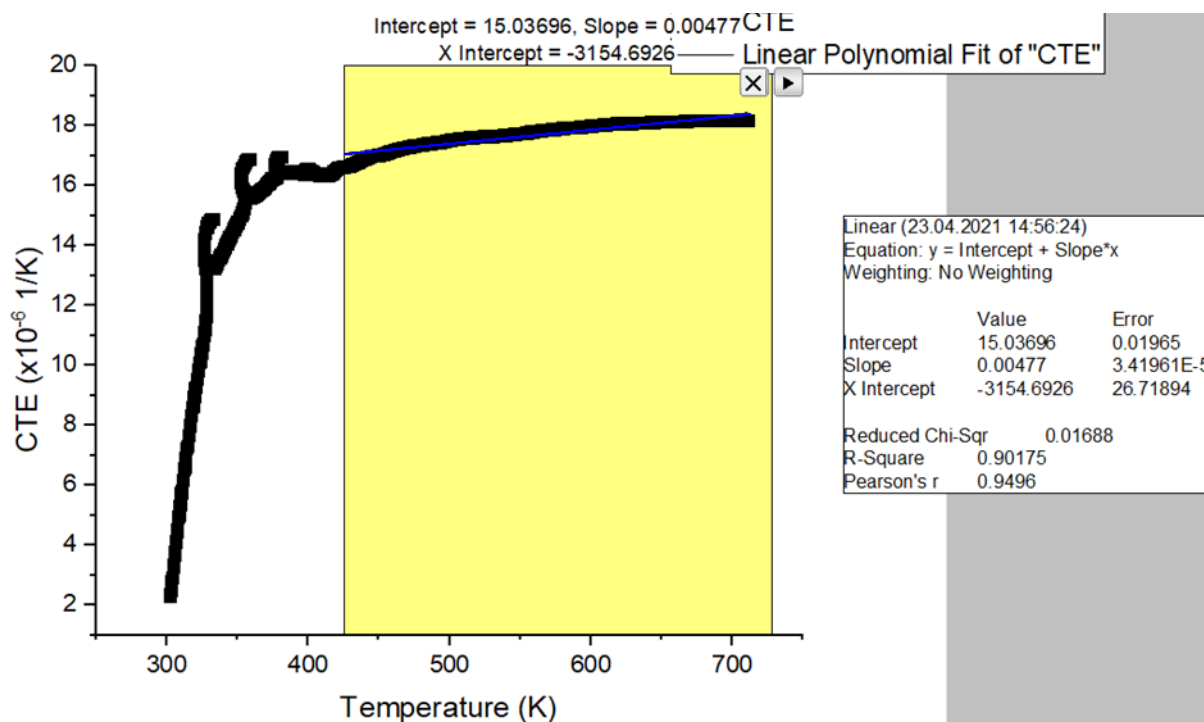


Figure 11–3 Raw data and fitting for the coefficient of thermal expansion of the n-type $\text{Mg}_2\text{Si}_{0.3}\text{Sn}_{0.7}$

Thermal conductivity was not measured on the same samples studied in this work, however the material for those samples came from the same batch of powder and pressed under the same conditions. It is therefore assumed that the properties are the same.

The fitting of thermal conductivity was done using a polynomial function of order 3.

Figure 11–4 shows the fit.

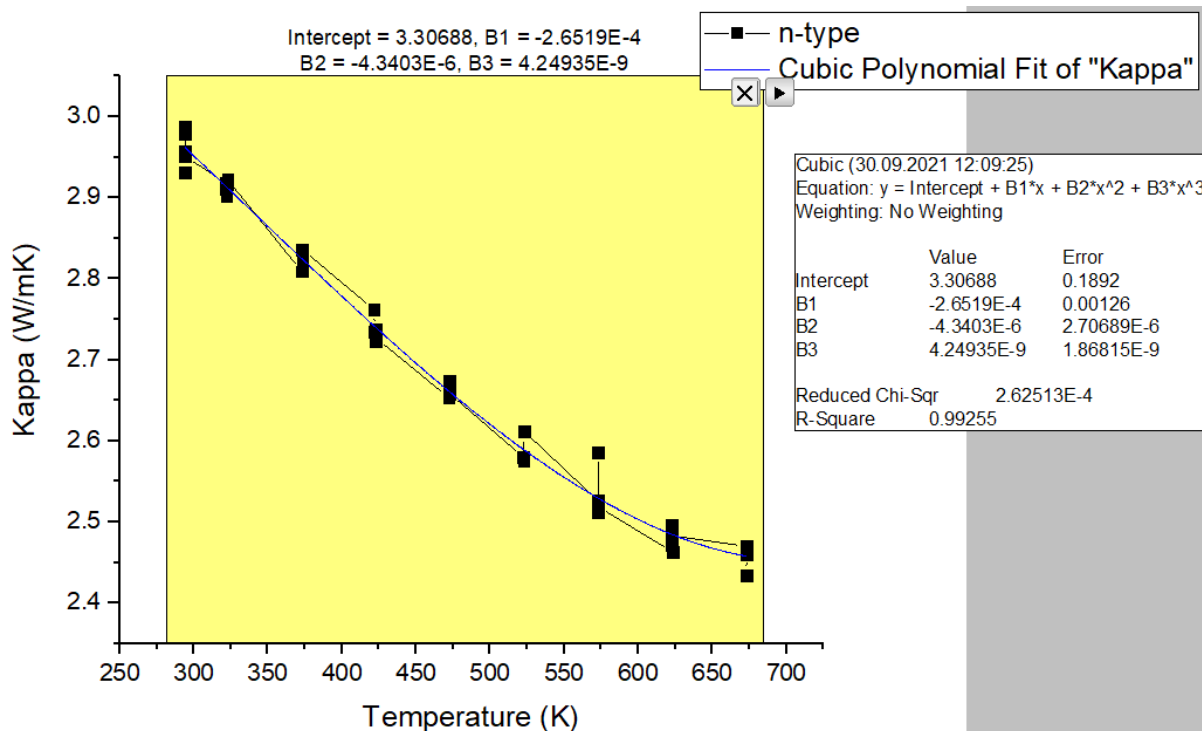


Figure 11-4 Raw data and fitting for the total thermal conductivity of the n-type $Mg_2Si_{0.3}Sn_{0.7}$

p-type $Mg_{1.97}Li_{0.03}Si_{0.3}Sn_{0.7}$

Similar to the n-type, the Young's modulus of the p-type thermoelectric material was fitted with a linear function shown in Figure 11-5.

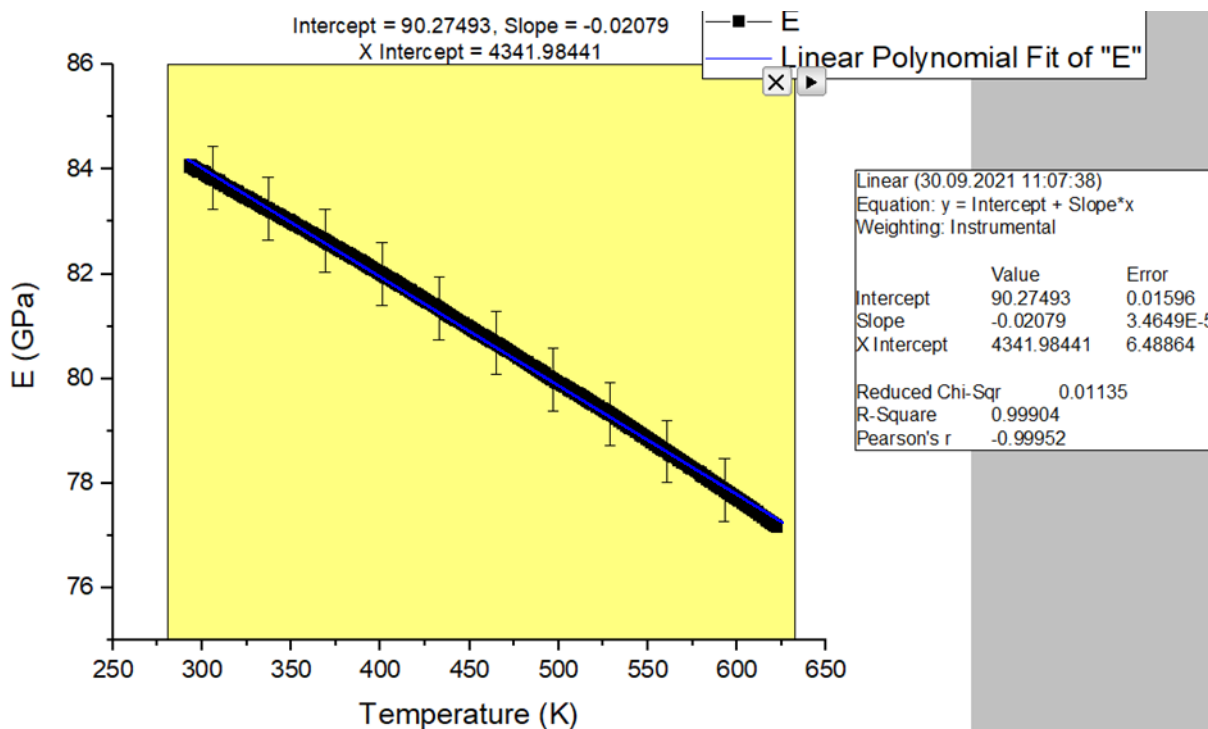


Figure 11-5 Raw data and fitting for the Young's modulus of the p-type $Mg_2Si_{0.3}Sn_{0.7}$

A linear fit and extrapolation were used for the p-type material as well. In this case the mean value for the p-type $\text{Mg}_2(\text{Si},\text{Sn})$ is $17.372 \times 10^{-6} \text{ 1/K}$, while $\text{CTE}(22^\circ\text{C}) = 17.588 \times 10^{-6} \text{ 1/K}$ is found using the extrapolation. These results are shown in **Figure 11-6**.

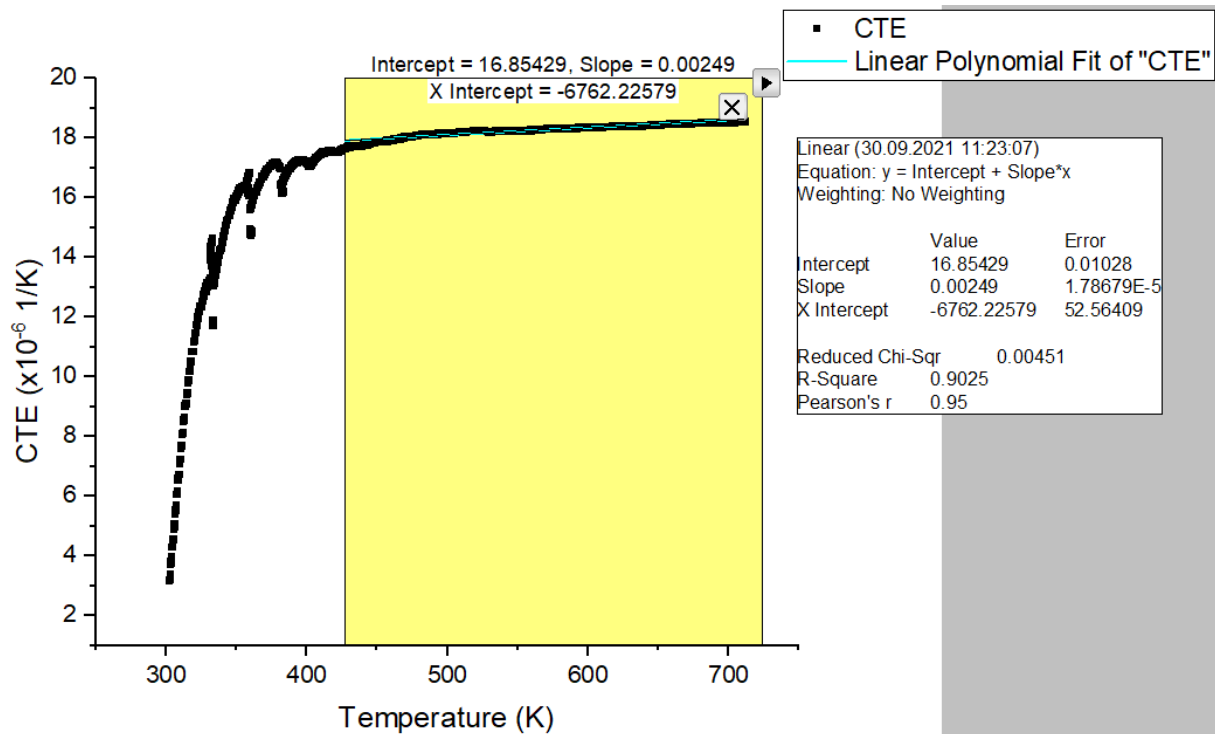


Figure 11-6 Raw data and fitting for the coefficient of thermal expansion of the p-type $\text{Mg}_2\text{Si}_{0.3}\text{Sn}_{0.7}$

The total thermal conductivity was fitted to a 3rd degree polynomial function as well. This process is illustrated by **Figure 11-7**

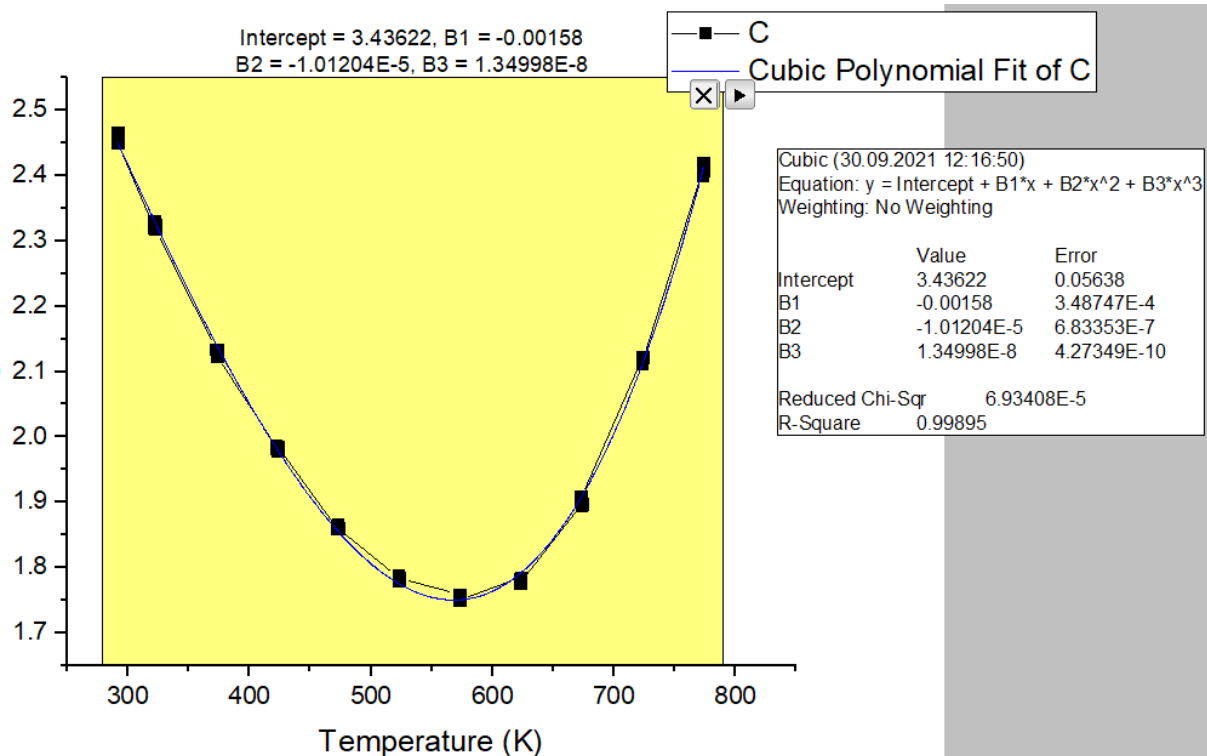


Figure 11-7 Raw data and fitting for the total thermal conductivity of the p-type $Mg_2Si_{0.3}Sn_{0.7}$

The functions used to fit the data in the temperature range 22 - 300 °C (295 - 573 K) are summarized in **Table 11-1**

Table 11-1 Equations used to fit data for the simulation, temperature values are given in Kelvin

Property	Equation for n-type	Equation for p-type
Young's modulus (GPa)	$E(T) = 87.80 - 0.015T$	$E(T) = 90.27 - 0.020T$
Coefficient of thermal expansion ($10^{-6}1/K$)	$CTE(T) = 15.037 + 0.0048 T$	$CTE(T) = 16.85 + 0.0025 T$
Thermal conductivity (W/mK)	$\kappa(T) = 3.31 - 2.66 \times 10^{-4}T - 4.34 \times 10^{-6}T^2 + 4.25 \times 10^{-9}T^3$	$\kappa(T) = 3.44 - 1.58 \times 10^{-3} T - 1.01 \times 10^{-5}T^2 + 1.35 \times 10^{-8}T^3$